

DETERMINATION OF THE FAR-INFRARED
PROPERTIES OF GALAXIES IN THE COMA
CLUSTER

Scot Hickinbottom

A thesis submitted in partial fulfilment of the requirements of
Liverpool John Moores University
for the degree of
Doctor of Philosophy.
August 2015

Declaration

The work presented in this thesis was carried out at the Astrophysics Research Institute, Liverpool John Moores University. Unless otherwise stated, it is the original work of the author.

While registered as a candidate for the degree of Doctor of Philosophy, for which submission is now made, the author has not been registered as a candidate for any other award. This thesis has not been submitted in whole, or in part, for any other degree.

Scot Hickinbottom
Astrophysics Research Institute
Liverpool John Moores University
IC2, Liverpool Science Park
146 Brownlow Hill
Liverpool
L3 5RF
UK

OCTOBER 16, 2015

Abstract

This thesis presents results from the deepest ever far-infrared study of the Coma cluster (Abell 1656), with the *Herschel* PACS and SPIRE instruments being used to observe the cluster at a wavelength range of 70-500 μm . These observations resulted in a catalogue consisting of 70 galaxies which were spectroscopically confirmed as Coma cluster members, from which far-infrared galaxy luminosity functions at 70, 100 and 160 μm were constructed. Additionally, the far-infrared properties of 68 of these galaxies were determined from spectral energy distribution fits across the full wavelength range. Finally, these galaxies were grouped by morphological type, resulting in 30 elliptical galaxies, 37 spiral galaxies and one with an unknown morphology. These results were then compared to other studies of both clusters and the field in order to ascertain the extent to which environmental processes affect galaxy evolution.

A comparison of the luminosity functions at 100 and 160 μm and the equivalent functions from the *Herschel* Virgo cluster survey Auld et al. (2013) showed similarities in both the functional form and the function parameters describing them. A further comparison of the Coma cluster luminosity functions at all three PACS wavelengths and various field galaxy luminosity functions was made, and again the forms and function parameters were consistent to within the errors. This would imply that the environmental processes thought to occur within the clusters do not have as great an effect on the galaxy population as initially thought.

The far-infrared properties derived from the spectral energy distribution fits were analysed by galaxy type. The early-types were found to have mean normalised dust masses, dust temperatures and total infrared luminosities of $\log_{10} \left(\frac{M_{dust}}{M_{stellar}} \right) = -4.19 \pm 0.1$,

$T = 24.7 \pm 0.5\text{K}$ and $\log_{10}L = 9.03 \pm 0.1L_{\odot}$ respectively. For the late-types the mean values were found to be $\log_{10}\left(\frac{M_{dust}}{M_{stellar}}\right) = -2.94 \pm 0.1$, $T = 23.4 \pm 0.5\text{K}$ and $\log_{10}L = 9.37 \pm 0.1L_{\odot}$.

When examining the derived dust masses as a function of stellar mass a bimodality can be seen, with those sources identified as being late-type spiral galaxies having a linear relation between the two mass components, whilst the early-type ellipticals have a near constant stellar mass for any given dust mass. When this trend is supplemented with data taken from CO observations of the molecular gas present in Coma cluster galaxies (Boselli et al., 1997; Lavezzi et al., 1999; Casoli et al., 1996), then it can be seen that eleven of the galaxies have molecular gas present within them, and thus contain the fuel needed for star formation processes to occur. Additionally, out of a possible eleven galaxies which had been identified via ultraviolet observations as currently undergoing a ram pressure stripping process (Smith et al., 2010), seven are seen within the sample and once again they sit in this late-type galaxy trend. Given ultraviolet wavelengths are a tracer of star formation, this would once again suggest that these processes are occurring in these galaxies, and therefore by extension in all of the galaxies present in this late-type trend. This trend is therefore likely to be the ‘star formation main sequence’ as previously observed in the infrared by Elbaz et al. (2011).

The dust masses and temperatures of the early- and late-types were then compared to *Herschel* studies of the Virgo (Auld et al., 2013) and Fornax (Fuller et al., 2014) clusters. In terms of the dust mass of a galaxy, the mean values for the early-types in the Coma and Virgo clusters were very similar. For the late-type galaxies the differences between the clusters are much larger, with the Virgo cluster having the highest mean dust mass, the Fornax cluster the lowest, and the Coma cluster lying in the middle of the two. In terms of the dust temperature, it can be seen that whilst the three clusters have differing mean values, the late-types of all three clusters have slightly lower mean dust temperatures than the early-types of the respective cluster. This result supports similar observational evidence obtained by ISO (Bendo et al., 2003) and the *Herschel* Reference Survey (Smith et al., 2012), both of which noted a small but no-

ticeable increase in dust temperature for early-type galaxies. This result seems at odds with the accepted idea that the dust in elliptical galaxies is heated by the old stellar population, which one would expect to be cooler than the dust that is heated by the hot young stars produced during star formation processes. However, if the emission in the early-type galaxies is as a result of dust produced by an AGB star population, then it is plausible that the observed temperatures will be higher than those seen from star formation regions.

Acknowledgements

Firstly, I would like thank my supervisor Phil James for his continued help and guidance during the entirety of my Ph.D., and for not firing me nearly as much as he should have done, especially given my complete ineptness at spelling and grammar. I am fully expecting to get this acknowledgments page back with numerous corrections and typographical errors, but I still have that ‘Get out of being fired free’ card, so I’m safe. Additional thanks go to the other members of my supervisory team, as well as the other members of the ARI who have contributed their time and knowledge to help improve the work I have completed; Chris Collins, Dave Carter, Ivan Baldry and Ian McCarthy.

Obviously, it is well known that all work and no hot beverages, makes a Ph.D. student go completely crazy, so I’d like to thank the ARI Tea Team for keeping me sane (or a close approximation to sane), especially during my writing up period; Rich, Andy, Caroline, Helen, Rob, Katie and Chris. You are nearly all perfectly adequate friends.

I’d also like to thank my parents for supporting me throughout my entire journey up to this point, I honestly don’t think I will have made it this far if it weren’t for your help and your continued belief in me. I promise I will stop being a lazy eternal student and go get a real job now.

Finally, I would like to thank my awesome and beautiful wife, Lucy, who has been there for me throughout my many years as a postgraduate student, and who more than anyone has pushed me to keep going when the stress and boredom of thesis writing set in. You are truly amazing, and I couldn’t have done this without you.

Thanks everyone. Theeveryone.

SCOT HICKINBOTTOM

OCTOBER 16, 2015

“The universe is big, it’s vast and complicated, and ridiculous. And sometimes, very rarely, impossible things just happen and we call them miracles.”

- The Doctor

Contents

Declaration	ii
Abstract	iii
Acknowledgements	vi
Contents	ix
List of Tables	xv
List of Figures	xvii
1 Introduction	1
1.1 Early- and late-type galaxies	2
1.2 Galaxy Colour-Magnitude Bimodality	2
1.3 The galaxy cluster environment	4
1.4 Physical processes within clusters	4
1.4.1 Ram-pressure stripping	5
1.4.2 Tidal forces	5
1.4.3 Galaxy harassment	6

1.4.4	Viscous stripping	7
1.4.5	Thermal evaporation	7
1.4.6	Galaxy starvation	7
1.5	Observations of star formation in clusters	8
1.5.1	Star formation tracers	8
1.5.2	The Coma cluster	9
1.5.3	The Virgo cluster	10
1.5.4	The Fornax cluster	12
1.6	Dust and far-infrared emission	12
1.7	Observational facilities	14
1.7.1	IRAS and <i>Spitzer</i>	14
1.7.2	<i>Herschel</i>	15
1.8	Thesis aims and layout	16
2	Observations and data reduction	18
2.1	<i>Herschel</i> observations	18
2.2	Data reduction	19
2.2.1	Data retrieval	19
2.2.2	Flagging and calibration	20
2.2.3	Deglitching	20
2.2.4	Final image production	21
2.3	Image analysis	22
2.3.1	Source extraction	22

2.3.2	Noise estimates	26
2.3.3	Completeness	26
2.3.4	Error calculation	28
2.3.5	Total number counts	30
2.4	Concluding remarks	33
3	Galaxy luminosity functions	34
3.1	Spectroscopic redshift selection	34
3.1.1	The spectroscopic catalogue	35
3.1.2	Identification of Coma cluster members	36
3.2	Schechter function fits	39
3.3	Comparisons with other luminosity functions	41
3.3.1	Comparison with the Virgo cluster	41
3.3.2	Comparison to the field galaxy luminosity function	42
3.4	Concluding remarks	46
4	Spectral energy distribution fitting analysis	49
4.1	The form of the fitting function	49
4.2	The far-infrared data	51
4.2.1	<i>Herschel</i> PACS data	51
4.2.2	<i>Herschel</i> SPIRE data	51
4.3	The fitting process	52
4.4	Quality of fits	53

4.5	Calculation of dust masses	55
4.6	Concluding remarks	57
5	Morphological and environmental analysis	58
5.1	Galaxy morphological classification	59
5.1.1	Hubble T-type classification	59
5.1.2	Galaxy Zoo classification	60
5.1.3	Sérsic index classification	62
5.1.4	Classification comparison	62
5.2	Comparison with HST/ACS survey	66
5.3	Galaxy morphology by location	71
5.4	Galaxy luminosity functions by morphology	71
5.5	Non-detection analysis	74
5.6	Comparison with the X-ray environment	79
5.6.1	Comparison with X-ray observations	79
5.6.2	Comparison with X-ray surface brightness profile	82
5.7	Comparison with UV observations	84
5.8	Comparison with CO observations	86
5.9	Concluding remarks	87
6	Analysis of galaxy properties	89
6.1	Comparisons of Coma cluster galaxy properties	90
6.1.1	Dust and stellar masses of the Coma cluster galaxies	90

6.1.2	Dust temperature of Coma cluster galaxies	96
6.1.3	Total infrared luminosity of Coma cluster galaxies	99
6.2	Effect of radial distance on galaxy properties	101
6.3	Comparisons with the Virgo and Fornax clusters	104
6.3.1	Comparison of galaxy dust masses	104
6.3.2	Comparison of galaxy dust temperatures	105
6.4	Comparison with the field	109
6.4.1	Comparison of galaxy dust temperatures	109
6.4.2	Comparison of galaxy dust and stellar mass properties	110
6.5	Concluding remarks	112
7	Scientific conclusions	113
8	Future work	117
8.1	Near-infrared observations	117
8.2	Comparisons with H α observations	118
8.3	Comparisons with other galaxy environments	118
8.4	Determination of the source of far-infrared emission in early-type galaxies	119
A	Spectral energy distributions and <i>Herschel</i> PACS images	121
B	Data table: measured parameters	157
C	Data table: derived parameters	160

List of Tables

3.1	Spectroscopic detection fractions for objects detected within each of the three <i>Herschel</i> PACS bands	37
3.2	Schechter luminosity function parameter values for Coma cluster galaxies in the three <i>Herschel</i> PACS bands	41
3.3	Schechter luminosity function parameter values for Virgo cluster galaxies in two of the <i>Herschel</i> PACS bands	44
3.4	Comparison of the number densities of the field and the Coma and Virgo cluster	46
5.1	The de Vaucouleurs and Hubble T-type classifications of the sample	60
5.2	Detection fractions of galaxy type by location	79
6.1	Statistical properties of the normalised dust masses	94
6.2	Statistical properties of the dust temperatures	97
6.3	Statistical properties of the total infrared luminosities	101
6.4	Comparison of the dust masses of Coma, Virgo and Fornax cluster galaxies	105
6.5	Comparison of the dust temperatures of Coma, Virgo and Fornax cluster galaxies	107

6.6	Comparison of the statistical properties of the dust temperature of various cluster and field surveys	110
6.7	Comparison of the statistical properties of the dust mass of various surveys	111
6.8	Comparison of the statistical properties of the normalised dust mass of various surveys	111

List of Figures

1.1	A three colour image of NGC 4911 (Object 70) taken with the HST/ACS	11
2.1	A map of the observed area created via the combination of the three wavelength band maps	23
2.2	Signal-to-Noise as a function of aperture diameter	24
2.3	Encircled energy fraction as a function of aperture diameter	25
2.4	Completeness curves of the 70 μm map	27
2.5	Completeness curves of the 100 μm map	28
2.6	Completeness curves of the 160 μm map	29
2.7	Total number counts from other <i>Herschel</i> surveys, compared to this study	31
2.8	Total number counts from other <i>Herschel</i> surveys, compared to this study with Coma members removed	32
3.1	<i>Herschel</i> 100 μm flux density versus <i>r</i> -band magnitude	39
3.2	Galaxy luminosity functions for all three <i>Herschel</i> PACS bands	40
3.3	Comparison of the Coma and Virgo luminosity functions	43
3.4	Comparison of the Coma and Field luminosity functions	45
3.5	Comparison of the Coma cluster and field galaxy samples	47

4.1	Plot of the flux density scaling factor as a function of temperature . . .	54
5.1	Histogram of the Galaxy Zoo-determined morphological types, for the Coma cluster catalogue	61
5.2	Comparison of T type and Galaxy Zoo morphology classifications . . .	63
5.3	Comparison of Galaxy Zoo morphology classifications and r -band Sérsic index	64
5.4	SDSS images of Coma cluster galaxies with discrepant morphological information	65
5.5	Comparison of HST/ACS and <i>Herschel</i> images for Object 2	67
5.6	Comparison of HST/ACS and <i>Herschel</i> images for Object 19	67
5.7	Comparison of HST/ACS and <i>Herschel</i> images for Object 27	68
5.8	Comparison of HST/ACS and <i>Herschel</i> images for Object 39	68
5.9	Comparison of HST/ACS and <i>Herschel</i> images for Object 40	69
5.10	Comparison of HST/ACS and <i>Herschel</i> images for Object 44	69
5.11	Comparison of HST/ACS and <i>Herschel</i> images for Object 46	70
5.12	Comparison of HST/ACS and <i>Herschel</i> images for Object 70	70
5.13	A three-colour image of NGC 4921 (Object 39) taken with the HST/ACS	72
5.14	Coma cluster member morphologies by location	73
5.15	Galaxy luminosity function at 70 μm , split by morphology	74
5.16	Galaxy luminosity function at 100 μm , split by morphology	75
5.17	Galaxy luminosity function at 160 μm , split by morphology	76
5.18	Images produced by a stacking analysis of various subsets of galaxies	77

5.19	Histogram of the number of SExtractor identified sources, grouped by sigma detection level	78
5.20	Contour map detailing X-ray emission in the region of the Coma cluster	80
5.21	X-ray sky background as a function of radial distance	81
5.22	Normalised dust mass as a function of the X-ray sky background . . .	82
5.23	Normalised dust mass as a function of the X-ray surface brightness . .	84
5.24	Normalised dust mass as a function of 100 μm flux, with UV observations highlighted	85
5.25	Normalised dust mass as a function of dust temperature, with UV observations highlighted	86
5.26	CO derived H_2 mass as a function of the far-infrared derived dust mass	87
6.1	Dust mass as a function of stellar mass, subset by galaxy morphology	91
6.2	Dust mass as a function of stellar mass, subset by galaxy location . . .	92
6.3	Dust mass as a function of stellar mass, with CO observations highlighted	93
6.4	Normalised dust mass as a function of stellar mass	93
6.5	Comparison of the derived and estimated dust masses for detected Coma cluster members	95
6.6	Histogram of the dust masses for the field galaxy and Coma cluster populations	95
6.7	Histogram of the normalised dust masses for the field galaxy and Coma cluster populations	96
6.8	Normalised dust mass as a function of dust temperature	97
6.9	Dust temperature as a function of the X-ray sky background	98
6.10	Dust temperature as a function of the X-ray surface brightness	99

6.11	Normalised dust mass as a function of total infrared luminosity	100
6.12	Total infrared luminosity as a function of dust temperature	102
6.13	Normalised dust mass as a function of cluster radial position	103
6.14	Total infrared luminosity as a function of cluster radial position	103
6.15	Temperature as a function of cluster radial position	104
6.16	Recovered dust mass as a function of the <i>Herschel</i> detected flux. . . .	106
6.17	Dust temperature as a function of stellar mass	108

Chapter 1

Introduction

The optical appearance of our universe is dominated by galaxies. Through various observations at multiple wavelengths, detailed knowledge has been determined regarding the contents of these galaxies thus giving insight into their internal dynamics and star formation histories. Additionally, computer simulations have provided an increasingly detailed picture regarding the formation of these galaxies through the interaction of baryonic matter with the dark matter dominated haloes.

However, there are still many questions that remain unanswered, one of the most fundamental of which is what processes dictate whether a galaxy is an early-type elliptical or a late-type spiral. This question is essentially asking why have some galaxies retained their gas, thus allowing for star formation processes to continue to the current epoch, whilst other galaxies have had theirs removed.

Some possible explanations for this include differences in the formation processes of the two types, or internal processes such as stellar explosions or black hole activity. One additional explanation for this is the effect of various environmental processes that are thought to act upon galaxies, and these will be the main focus of this thesis.

This introduction will present some essential background information on galaxies and galaxy clusters, outline the reasons for studying cluster galaxies at far-infrared wavelengths, and identify the key scientific questions to be addressed in this thesis.

1.1 Early- and late-type galaxies

Early-type, or elliptical, galaxies are triaxial systems, where all the stars orbit in various radial planes (Binney, 1976, 1978a,b). They contain little interstellar medium and as such they are associated with low star formation rates, and are thus dominated by old stellar populations. Elliptical galaxies are formed via major mergers of other galaxies in a hierarchical manner (Toomre, 1977). Major mergers are defined as a merger between galaxies of comparable sizes, with the resulting galaxy having significant structural differences when compared to the original merging galaxies.

Late-type, or spiral, galaxies are disk-shaped rotating systems with a central bulge (Kormendy, 1993), with approximately two-thirds of these galaxies having a bar structure protruding from this bulge (Sellwood & Wilkinson, 1993). These galaxies are rich in gas and interstellar medium with high rates of star formation, resulting in the majority of the stars being part of a young stellar population. These disk structures are formed when a system suffers a gravitational collapse, with the conservation of angular momentum preventing complete collapse and giving the galaxy a spiral structure (Hoyle, 1949).

1.2 Galaxy Colour-Magnitude Bimodality

It has long been established that there exists a relation between the colour of a galaxy and its morphological type, with early-types generally being redder than late-types (Holmberg, 1958; Roberts & Haynes, 1994). However, it is also possible to see bimodality in the properties of galaxies if their colour is plotted as a function of their absolute magnitude (Baldry et al., 2004). This results in two populations of galaxies; those occupying the ‘red sequence’ and those in the ‘blue cloud’. The underpopulated area between the two is defined as the ‘green valley’.

This bimodality is further reflected in the relation known as the ‘star formation main sequence’. This sequence contains only star forming galaxies and is a result of the

linear relationship between the star formation rate and the stellar mass. This trend is known to exist at both low redshifts ($z < 1$, Brinchmann et al. 2004; Salim et al. 2007) and high redshifts ($z \gtrsim 1$, Daddi et al. 2007), and has been observed at optical (Tasca et al., 2014), infrared (Elbaz et al., 2011) and radio (Karim et al., 2011) wavelengths. The location of galaxies relative to this main sequence can give an indication as to their own star forming processes. Galaxies that lie above this sequence, with a higher star formation rate for a given stellar mass, are said to be starburst galaxies (Rodighiero et al., 2011; Sargent et al., 2012; Atek et al., 2014) experiencing increased star formation activity but on a short timescale. Below the sequence are those galaxies which feature little to no star formation, typically elliptical galaxies (Wuyts et al., 2011) which have little to no gas to fuel star formation processes.

One issue that has yet to be fully answered is the process by which the gas-rich galaxies present in the ‘blue cloud’ are converted to the gas-depleted galaxies seen in the ‘red sequence’. Simulations of galaxy formation can mostly reproduce the results seen via observations; however without a suitable feedback mechanism, the simulated galaxies do not halt the star formation processes with the result being that their total stellar mass is a magnitude greater than that expected. Peng et al. (2010) suggest that there are two different feedback mechanisms that can be affecting the evolution of a galaxy, which they define as ‘mass quenching’ and ‘environment quenching’.

Mass quenching is most effective on isolated galaxies, as the star formation processes are halted due to the fuel required being removed from the system through either supernovae or active galactic nuclei (AGN). For example, the more massive galaxies tend to have more massive AGN which can result in an amount of energy much greater than the binding energy being fed into the galaxy (Bluck et al., 2011). This force can strip a galaxy of the gas needed for star formation and thus prevent further processes occurring.

The processes that drive environment quenching (which will be discussed in detail in Section 1.4) are much more pronounced in the extreme environment of a galaxy cluster due to the increased number of galaxy interactions and the increased mass of gas present in the core of clusters. This study will investigate the potential impact of

these processes by analysing this extreme galaxy cluster environment.

1.3 The galaxy cluster environment

A collection of numerous galaxies, held together by a mutual gravitational force, can be defined as either a group or a cluster, with the difference being down to a number of factors, none of which are well defined. In simple terms however one can define a group to be a collection of fewer than ten galaxies, compared to a cluster which would consist of tens to hundreds of galaxies.

These galaxy clusters play an important role in the evolution of the individual galaxies contained within them, and as such are an important source of data to aid our understanding of this ongoing evolution. It has been well documented that types of galaxies are strongly linked with the nature of their local environments, with a morphology-density relation being found (Dressler, 1980; Whitmore et al., 1993; Dressler et al., 1997; Baldry et al., 2006) such that early-type elliptical and lenticular galaxies are preferentially found in high-density cluster environments. Several processes have been identified for removing or depleting gas in cluster galaxies, through interaction between both the galaxies themselves and with the surrounding environment. These interactions act upon the contents of the individual galaxies and can have a great effect on the gas and dust content as well as the number of stars in the galaxy.

1.4 Physical processes within clusters

The evolution of galaxies is believed to be strongly affected by the cluster environment owing to the numerous interactions that occur, either between the galaxy and the cluster or between the galaxies themselves. These processes affect the galaxy in different ways depending on the nature of the interaction and the various properties of the galaxy, such as its mass, temperature and velocity. This section will detail a number of the more extensively studied processes thought to be driving galaxy evolution.

1.4.1 Ram-pressure stripping

One of the more important interactions that can occur in galaxy clusters is known as ram-pressure stripping. This is a process whereby the interstellar medium (ISM) is removed from a galaxy that is moving quickly through the hot and dense intergalactic medium (IGM) (Gunn & Gott, 1972). The ISM is removed if the ram pressure is greater than the gravitational force that is holding the gas to the galaxy disk (Boselli & Gavazzi, 2006), with various models concluding that such a process could occur on a timescale of a gigayear, which is approximately the amount of time it takes a galaxy to cross the cluster. This process is more efficient if the galaxy being stripped is face-on to the IGM with respect to its direction of motion, as opposed to it being edge-on (Abadi et al., 1999; Quilis et al., 2000; Vollmer et al., 2001). Additionally it can be shown that the process is more effective on galaxies which have higher velocities, such as those in a radial orbit of the cluster (Abadi et al., 1999; Quilis et al., 2000; Vollmer et al., 2001). In rich, dense clusters this process would occur more efficiently and would be a major environmental influence on galaxy evolution.

1.4.2 Tidal forces

Tidal forces are one type of interaction that can take place between the galaxies themselves, acting on the galaxy's gas, dust, stars and dark matter. The efficiency of this process is dependent on how strongly bound this matter is, with the HI gas on the outer edges being more easily removed than the molecular gas in the galaxy centre. This type of interaction results in an increase in star formation in the centre of the galaxy but a lesser increase in the disk, something which has been seen in both observations (Kennicutt et al., 1987) and simulations (Iono et al., 2004). However, perturbations of the individual galaxies as a result of these interactions are not very severe within the cluster environment. The reason for this is that while the number of interactions is high due to the high density of galaxies within the environment, the high relative velocities result in the interaction durations being short, of the order of 10^8 years (Boselli & Gavazzi, 2006). Identifying galaxies which are undergoing a process like this is difficult, as any

tidally disturbed material will not remain bound to the original galaxy, as one would see in field interactions, but rather it will become unbound from the galaxy, but remain bound within the cluster environment. This material is thought to be a possible source of the diffuse intergalactic light seen in clusters (Murante et al., 2007; Conroy et al., 2007).

It is also possible to have tidal forces that act between the galaxies and the potential well of the cluster itself. These forces can have a substantial effect on galaxy morphology, altering the size of the bulge and disk, as well as the thickness of the disk (Valluri, 1993). Simulated models have shown that these forces can also result in the acceleration of molecular clouds of disk galaxies towards the galaxy centre, with the kinetic pressure rise inducing star formation within the ISM. All this can have an effect on star formation, as there is an increase in the nuclear activity of the galaxies followed by a decrease in the amount of gas available for subsequent star formation.

1.4.3 Galaxy harassment

Moore et al. (1996) proposed that one of the driving forces behind the morphological evolution of galaxies in the cluster environment is the multiple high speed interactions that occur between the galaxies in a process called ‘galaxy harassment’. The strength of such a series of interactions is dependent on the frequency of collisions, the tidal field of the cluster and the potential within the colliding galaxies. The simulations of Moore et al. (1996) showed that this type of continuous interaction would cause the stellar component to heat up, whilst causing the gas to sink into the centre of the galaxy. The small disk galaxies affected by this process will initially be transformed into distorted spiral galaxies, before eventually evolving into the spheroidal systems seen to be common in cluster environments (Moore et al., 1998). In contrast this harassment process has less of an effect on the more massive objects within the cluster, with the end result being only a slight increase in star formation activity in the disk (Mihos, 2003).

1.4.4 Viscous stripping

Another process for removing gas from galaxies in the cluster environment is viscous stripping. The outer layers of the cold ISM of a galaxy are removed as the galaxy moves through the hot IGM due to a viscosity momentum transfer caused by the turbulent flow of the gas (Nulsen, 1982). This process only affects larger objects that are subject to a turbulent viscosity; smaller objects have a laminar viscosity and are thus less affected. This interaction occurs over a relatively short timescale and results in a galaxy with an asymmetric gas distribution, owing to the stripping predominantly affecting the leading side of the galaxy.

1.4.5 Thermal evaporation

Cowie & Songaila (1977) showed that gas can be removed from galaxies in a cluster through thermal evaporation. This occurs when the IGM has a higher temperature than the ISM at the point where the two meet, resulting in a rapid rise in ISM temperature. Subsequently, the ISM will evaporate if the gravitational attraction of the galaxy is not sufficiently high. The efficiency of this process is related to the temperature difference and, hence, the cluster density.

1.4.6 Galaxy starvation

Galaxy ‘starvation’ or ‘strangulation’ causes a spiral galaxy to change into a lenticular galaxy due to the star formation activity in the galaxy being halted (Larson et al., 1980). This occurs when the outer halo of a galaxy, and thus the source of the infalling gas that would fuel star formation, is removed. Over time the star formation processes in the galaxy would be suppressed due to a lack of gas, finally resulting in the processes stopping completely.

1.5 Observations of star formation in clusters

1.5.1 Star formation tracers

Ultraviolet (UV) observations of galaxies are frequently used to study their stellar and star formation properties (Boselli et al., 2001). UV light is a good star formation tracer as it is emitted directly by young massive stars, although the light is also absorbed and scattered by the presence of dust in the galaxies, hampering the UV observations and leading to the need for strong extinction corrections.

The H α luminosity of a galaxy is believed to be emitted when the interstellar medium is ionised by the ultraviolet radiation produced by the massive young stars in the galaxy. Stars with high masses ($M > 10M_{\odot}$) and short lifetimes ($\tau < 20\text{Myr}$) contribute the majority of the ionizing flux (Kennicutt, 1998a), and therefore the H α emission can be seen as a direct measurement of star formation. Due to the gas and dust that surround the stars in the galaxy, some of this flux is absorbed and re-emitted at longer wavelengths, specifically infrared, and thus an extinction correction is needed.

The re-emitted infrared light can be used as a tracer of the star formation rate by using the relation between this rate and the infrared luminosity as shown by Kennicutt (1998b). This relation is theoretical and is based on continuous starburst synthesis models produced by Leitherer & Heckman (1995), solar abundances and the Salpeter (1955) initial mass function (IMF). However, this relation does not hold as well in galaxy disks or early-type galaxies due to the dust being additionally heated by the older stellar population, and as such the relation only traces stellar populations with ages less than approximately 100Myr (Kennicutt, 1998b).

Thermal emission from the dust grains provides additional evidence about processes occurring within galaxies; the interstellar ionising field can heat dust to a low temperature, whereas hot dust implies heating via the process of star formation. This idea will be expanded upon in Section 1.6.

Radio observations are also used as tracers of star formation, as it is generally be-

lieved that the majority of the emission at these wavelengths is due to synchrotron radiation from electrons that have been accelerated by massive young stars undergoing supernovae explosions, with an additional component of thermal radiation from H_{II} (Biermann, 1976).

1.5.2 The Coma cluster

Studying rich galaxy clusters with these techniques is needed to help advance our knowledge of how the environment affects galaxy evolution. The best nearby candidate that fulfils this criterion is the Coma cluster (Abell 1656). The Coma cluster contains over 1500 galaxies (Abell, 1977), the majority of which are early-type lenticular and elliptical galaxies, and of which the very brightest are between the 12th and 14th magnitudes. Struble & Rood (1999) give a heliocentric redshift for the Coma cluster of $z = 0.0231$ which, when assuming a Hubble constant of $H_0 = 70 \text{ km s}^{-1} \text{ Mpc}^{-1}$ and a dark matter density of $\Omega = 0.25$, gives a distance of 98.5 Mpc. The Coma cluster is therefore the most massive and densely populated cluster in the local universe. In addition to this, the velocity dispersion of the cluster is 1.3 to 2 times larger than the nearer but less-rich clusters of Virgo and Fornax, resulting in a higher rate of galaxy-galaxy interaction. This means that the galaxies contained within it are subjected to a significantly different environment. It is classed as being near virialization in terms of its evolution (Colless & Dunn, 1996).

The Coma cluster has been studied at multiple wavelengths in the past. X-ray observations of the diffuse hot gas component by ROSAT (White et al., 1993) and XMM-Newton (Briel et al., 2001) revealed evidence of a separate infall substructure to the south west of the cluster centre. There have been near- and mid-infrared observations by IRAS (Saunders et al., 1990) and Spitzer (Jenkins et al., 2007; Bai et al., 2006), which probed the specifics of the individual galaxies within the cluster environment.

The Coma cluster has also been studied in detail by the Hubble Space Telescope Advanced Camera for Surveys (HST/ACS; Carter et al. 2008). This survey utilises the ACS Wide Field Camera and imaged 25 fields of 11.3 arcmin^2 mostly covering the

central regions, but with additional coverage of the southwest region. An example of the quality of the images produced by this survey is presented in Figure 1.1, which shows a three colour image of one of the brightest galaxies recovered in this *Herschel* study.

This *Herschel* far-infrared survey can be seen as expansion upon the work of the HST/ACS survey in terms of multiwavelength studies of the Coma cluster, as was mentioned within the time application proposal for this project.

1.5.3 The Virgo cluster

The Virgo cluster provides a useful source of comparison for this study. It is a very well studied galaxy cluster which primarily lies at a distance of 17 Mpc (Gavazzi et al., 1999). However, through the use of the GOLDMINE database (Gavazzi et al., 2003) one can see that there is evidence for substructure within the cluster, with groupings at 17, 23 and 32 Mpc. The Virgo cluster contains ~ 2000 optically catalogued galaxies (Binggeli et al., 1985) of both early- and late-types. It should be noted that this number is greater than that quoted for the Coma cluster (>1500 galaxies), despite the Coma cluster being a richer galaxy cluster. This is due to that fact that the Coma cluster lies approximately five times further away than the Virgo cluster, and as such a galaxy at a given luminosity will be 25 times dimmer in the Coma cluster. Therefore, there will be a great number of faint galaxies in the Coma cluster that contribute to the overall mass, but that cannot be easily observed.

The early-type galaxies in the Virgo cluster have a velocity dispersion of approximately 589 km s^{-1} , whereas late-type galaxies have a velocity dispersion of approximately 700 km s^{-1} (Binggeli et al., 1993). These authors also note that the Virgo cluster is not fully virialised, and so these values may be affected by substructures or infall velocities. For comparison, the Coma cluster has a velocity dispersion of 1008 km s^{-1} (Struble & Rood, 1999), and it is a well virialised environment, apart from the south west infall region. The Virgo cluster has been studied in detail at far-infrared wavelengths as part of the *Herschel* Virgo cluster Survey (HeViCS; Davies et al. 2010).



Figure 1.1: A three colour image of NGC 4911 (Object 70) taken with the HST/ACS.

These observations were carried out using the ESA *Herschel Space Observatory* (Pilbratt et al., 2010), using the Photodetector Array Camera and Spectrometer (PACS; Poglitsch et al. 2010) at 100 and 160 μm , as well as the Spectral and Photometric Imaging Receiver (SPIRE; Griffin et al. 2010) at 250, 350 and 500 μm .

1.5.4 The Fornax cluster

An additional means of comparison is provided by the Fornax cluster. This cluster lies at a distance of approximately 19 Mpc (Madore et al., 1999), though, as is the case for the Virgo cluster, there is evidence of substructure within the system. Drinkwater et al. (2001) showed that the Fornax system consists of two main parts in a similar arrangement to the Coma cluster: a main central region, and an infalling subcluster to the southwest. The Fornax cluster has also been observed at far-infrared wavelengths as part of the *Herschel* Fornax cluster Survey (HeFoCS; Davies et al. 2013), once again utilising the full range of wavelength available from the PACS and SPIRE instruments.

1.6 Dust and far-infrared emission

One of the important constituents of a galaxy is the interstellar dust. This dust originates in stars and comprises mostly of carbon, silicon and oxygen in various forms, including polycyclic aromatic hydrocarbons (PAHs). It is released into the ISM via stellar winds and supernovae where it plays a key role in star formation processes, acting as a base onto which hydrogen atoms can condense and thus form H_2 molecules (Hollenbach et al., 1971).

This dust obscures the light emitted from galaxies in the optical and ultraviolet wavelengths, however it is closely linked to the infrared emission, with at least 30 per cent of the energy emitted from stars being re-radiated in the infrared spectrum by this dust (Bernstein et al., 2002). At far-infrared wavelengths (8-1000 μm) it is this thermal emission from interstellar dust that dominates. This means that far-infrared emission

is a sensitive and powerful tracer of the evolutionary state of galaxies.

For late-type galaxies, dust emission principally traces star formation activity (Lonsdale Persson & Helou, 1987; Buat & Xu, 1996), with the dominant emission coming from dust thermalisation and re-radiation of energy from high-mass stars. In early-type galaxies, much or all of this emission is instead thought to arise from dust heated by the general radiation field of the older stellar population (Lonsdale Persson & Helou, 1987; Walterbos & Greenawalt, 1996), and hence far-infrared emission in these galaxies is an indicator primarily of the amount of interstellar medium they have retained. Alternatively, Asymptotic Giant Branch (AGB) stars can produce significant amounts of dust in stellar populations up to 1 Gyr old (Cassarà et al., 2013). This is long enough that it may be important even for apparently passive early-type galaxies with no current star formation (e.g. M32, see Jones et al., 2015).

The shape of the far-infrared spectral energy distribution and the total luminosity at these wavelengths thus give insight into both the cold dust content and the star-formation rate (Dunne et al., 2000; Kennicutt, 1998b; Kennicutt & Evans, 2012). For galaxies where there is no star formation, the dust properties are still important as they provide evidence in regards to the efficiency of the dust removal processes, such as ram pressure stripping (Cortese et al., 2010). In turn this information can improve our understanding of galaxy evolution in the cluster environment and the effect of the various galaxy interactions upon the morphology.

The absorption and scattering of infrared emission by dust particles has an effect on the observed spectrum of a given galaxy. The majority of the infrared flux emitted by a galaxy is by large grains of dust at a temperature of approximately 30 K, and thus is seen in a wavelength range of 60-100 μm (Boselli et al., 2003). However, the majority of the dust is colder, with temperatures less than 15 K, and as such the flux is seen at wavelength more than 100 μm (Bianchi et al., 1999). This difference can lead to complications in determining the mean dust temperature from spectral energy distributions, as it is dependent on the wavelengths with which the galaxy is observed.

The size of the dust grains is important when attempting to define a temperature of the

interstellar dust. Draine & Li (2001) showed that grains where radius $\gtrsim 20\text{nm}$, can be defined as having a steady, average temperature dependent on the incoming radiation. However, for grains where radius $\lesssim 5\text{nm}$ the same does not apply. In these cases the grains are small enough that an incoming photon will greatly increase the temperature of the grain for a brief moment, resulting in an irregular emission pattern (Sellgren, 1994). These extreme temperature variations cannot be easily accounted for and as such these effects are not considered in this study.

Additionally, when attempting to estimate the mass of dust responsible for the emission stemming from a galaxy, some assumptions need to be made regarding the nature of the dust; specifically the dust absorption coefficient. Draine (2003) provides a table of suitable values for various observing wavelengths, from which a value closely matching the observed peak of the spectral energy distribution should be assumed. However, a dust absorption coefficient value of $0.192\text{m}^2\text{kg}^{-1}$, corresponding to a wavelength of $350\text{ }\mu\text{m}$, results in a dust emission spectrum that closely matches that seen in both the Milky Way and in models for other galaxies.

1.7 Observational facilities

As mentioned in subsection 1.5.2, the Coma cluster has been observed at a number of wavelengths including studies in the infrared. These historical observations of infrared data provide a means of comparison with the current study, and as such it is important to understand how they compare with each other.

1.7.1 IRAS and *Spitzer*

The first space-based observations of the infrared sky were taken by the Infrared Astronomical Satellite (IRAS; Neugebauer et al., 1984). This telescope performed an all sky survey over the course of 10 months at four separate wavelengths: 12, 25, 60 and $100\text{ }\mu\text{m}$. These observations detected approximately 25,000 galaxies, of which

approximately half had been previously detected in the optical (Soifer et al., 1987a). These galaxies emit most strongly in the infrared, and were thus a new class of galaxy. Wang et al. (1991) optically identified 59 IRAS point sources within the Coma cluster. The *Spitzer Space Telescope* (SST; Werner et al., 2004) is an infrared telescope launched in 2003, and consists of three instruments: the Infrared Array Camera (IRAC), the Infrared Spectrograph (IRS) and the Multiband Imaging Photometer for Spitzer (MIPS). The MIPS instrument was used by Bai et al. (2006) to observe the Coma cluster at 24 and 70 μm , with the study looking at an area covering both the core and the south west infall region. From this an infrared luminosity function was produced for galaxies that were spectroscopically confirmed as Coma cluster members.

1.7.2 *Herschel*

The *Herschel Space Observatory* is a 3.5m infrared telescope launched on 14 May 2009 for a planned three year mission. Observations with the telescope ceased on 29 April 2013, when the instrument coolant ran out. *Herschel* maintained an orbit such that it resided at the second Lagrangian point, thus removing any issues with contamination from light from either the Earth or the Sun, both of which can be obscured with the telescope's sun shields. It observed at a wavelength range of 55 to 672 μm , thus covering a region that is closed off to ground-based astronomy. Onboard there are three instruments: Photodetector Array Camera and Spectrometer (PACS; Poglitsch et al., 2010), Spectral and Photometric Imaging Receiver (SPIRE; Griffin et al., 2010), and Heterodyne Instrument for the Far-Infrared (HIFI; de Graauw et al., 2010). The PACS photometry allows for a wavelength range of 60 to 210 μm , whilst the SPIRE photometry allows for a range of 200 to 670 μm .

The bolometer array of the PACS instrument consists of eight 16×16 pixel detectors arranged in a 4×2 grid, resulting in the 70 and 100 μm observations being completed with a 32×64 array, and the 160 μm observations being completed with a 16×32 array. The instrument was diffraction limited, with a resolution of 5 arcseconds and a field of view of 1.75×3.5 arcminutes.

For given observational area, the data were taken in a ‘snaked’ path. This method results in a small band of erroneous data around the edge of the observational area where the instrument has turned around, but this is accounted for in the data reduction.

1.8 Thesis aims and layout

This thesis aims to determine the physical properties of all the galaxies in the Coma cluster system that can be detected in the far-infrared, and then isolate and identify any trends within the system. These trends and data will then be used to attempt to answer a number of key questions regarding the Coma cluster and emission from cluster galaxies in the far-infrared, namely:

1. What type of galaxies dominate the far-infrared emission from the Coma cluster?
2. Is there far-infrared emission coming from galaxies with no evidence of star formation?
3. Are the optically brightest galaxies detected at these wavelengths?
4. What is the far-infrared luminosity function of the Coma cluster, and what sources contribute to the bright and faint ends?
5. How do the far-infrared properties vary with morphological type and other observational properties?

The structure of the thesis is as follows. Chapter 2 discusses the observations that were taken, along with the data reduction and source extraction processes. Chapter 3 covers the spectroscopic selection and the construction of luminosity functions, before comparing these functions to other available samples. Chapter 4 details the spectral energy fitting of the identified sources, and the calculation of the derivable parameters. Chapter 5 determines the best method of sorting the identified galaxies by morphological type, and investigates the cluster environment through X-ray, UV and CO observations. Chapter 6 takes the far-infrared properties determined for the sample

and investigates any potential trends both within the Coma cluster and when compared with other cluster environments. Chapter 7 summarises the scientific conclusions of the project, drawing together all of the various aspects. Finally, Chapter 8 discusses potential observations and analysis that could be completed to build on the results of this work. Additionally, there are three appendices; one containing plots of the spectral energy function of every identified source, and two containing tables of all object parameters, one observational and one derived.

Chapter 2

Observations and data reduction

This chapter will detail the observations taken for this research, the pipeline utilised for the data reduction, and the extraction of flux densities for all identified objects within the image. The original pipeline was produced by Edo Ibar, with the pipeline parameters specifically needed for these data being tested and determined by the author. All reduction of the PACS data presented in this thesis was performed by the author.

The content and results of this chapter have previously been published as part of Hickinbottom et al. (2014).

2.1 *Herschel* observations

The observations were carried out using the ESA *Herschel Space Observatory* (Pilbratt et al., 2010), using the Photodetector Array Camera and Spectrometer (PACS; Poglitsch et al., 2010) at 70, 100 and 160 μm , and then combined with data from the Spectral and Photometric Imaging Receiver (SPIRE; Griffin et al., 2010) at 250, 350 and 500 μm . The observational area was the core of the cluster and the south-west infall region, covering an area of 1.75 by 1.0 degrees. Two scans were performed with simultaneous imaging at 100/160 μm and another two at 70/160 μm , resulting in four separate scans being made. Within each pair, one scan was performed along the long

axis of the mapped area, and one along the short axis. The scans were performed at a speed of 20 arcsec/sec and the total integration time was 27.2 hours, equating to an effective integration time per pixel in the final map of approximately 40 seconds for 70 and 100 μm and 80 seconds for 160 μm . The OBSID for the scan containing the 70/160 μm maps is 1342224628/9, and for the scan containing the 100/160 μm maps it is 1342233085/6.

2.2 Data reduction

The data were reduced using a pipeline written in JYTHON (a PYTHON implementation written in JAVA) that was run within the *Herschel* Interactive Pipeline Environment (HIPE; Ott, 2010). The pipeline used follows a similar procedure to that described in Ibar et al. (2010), but with an improved cosmic-ray removal method.

2.2.1 Data retrieval

The raw data, or ‘level-0 data’ as it is also known, were first retrieved from the *Herschel* archive, and saved to the local drive. These data contain all the information needed for the complete reduction, combining both the science data and the necessary calibration data. The first check that needs to be performed on the data involves the checking of the astrometry. The *Herschel* satellite completes each scan by following a snaked path along the observed area, before moving and adjusting to its next target. As such it is possible for the raw data to contain readings from this adjustment phase, which are irrelevant to the study and could be of detriment to the data. In order to determine whether this had occurred with the data, a plot was constructed for each scan of the right ascension (RA) of the datapoints against the declination (Dec) of the datapoints. In this way it is possible to visualise any spatial outliers within the data, as they would lie outside of the grid of true points. For the scans where there were outliers present it was required that these points be removed before continuing.

Each of the bolometers on the instrument records the signal as a function of time in an object called a ‘frame’. These frames are analysed during the pipelined process. The telemetry, calibration and housekeeping data are extracted from the frames.

2.2.2 Flagging and calibration

This next stage is mostly user-independent and involves the removal of known errors in the data, and calibration of the data. During ground based tests of the instrument, certain bolometers were identified as being defective. In order to remove the data that were retrieved by these bolometers it is necessary to use the command ‘photFlag-BadPixels’. There is an additional command of ‘photFlagSaturation’ which removes any saturated pixels. These processes result in a 2-3 per cent loss in coverage of the bolometers and as such the effective integration time is reduced, however this reduction is minimal.

The final four commands complete the astrometric calibration of the data by assigning the correct units and coordinates to the pixels. The first of these is ‘convertChopper2Angle’ which takes the position of the chopper controlling the secondary mirror, and from that determines the angle of the mirror and thus defines a reference pixel for the maps from the line of sight of the spacecraft relative to the line of sight of the PACS instrument. This is then used by ‘photAddInstantPointing’ to determine the sky coordinates of the centre of the bolometer and add this to the frames table along with the position angle. The ‘photRespFlatfieldCorrection’ then converts the raw bolometer signals to physical units, specifically volts. Finally the last command assigns a right ascension and declination value to each pixel in the bolometer array.

2.2.3 Deglitching

The data is subject to erroneous signal values called ‘glitches’, the main source of which are cosmic rays that have impacted on the bolometer array causing spikes in the signal. There are two types of glitches that are present in the PACS data: single

pixel/frame glitches and multi-pixel/frame glitches.

The single pixel/frame glitches appear in just one read-out of the time line and affect only one bolometer of the array. They can be seen on the display of the data timeline as a single point lying well above or below the average values. To remove these glitches a second level deglitching task was used. The first level deglitching techniques work by removing extreme values within each detector pixel, and as such work over the timeline. In contrast, the second level deglitching process acts on the map pixels, and hence works over the spatial plane. The reason for utilising this difference is because the telescope moves as it scans the sky, and thus any single detector pixel will contain data from numerous parts of the sky. If one uses the map pixels instead, then all the signal contributions to any one pixel will be approximately the same, and so any glitched values can be easily detected and removed via the process of sigma-clipping. For these data a cut off of 5 sigma was used, with any value outside of this range being classed as erroneous and therefore being removed.

The multi-pixel/frame glitches are characterised by a sudden peak (or dip) in signal that greatly differs from the average, followed by exponential decrease (or increase) over a given time period that differs for each individual glitch. These glitches are normally caused by an especially energetic particle impacting the array and thus affecting a subsection of the array for an extended period of time. These glitches are not fully removed with the deglitching task, but can be reduced in part via the use of a high pass filter process, as explained in subsection 2.2.4.

2.2.4 Final image production

This final stage is an iterative one that can be repeated as many times as is necessary to achieve the desired final map. It comprises of performing a high pass filter task, joining the two scan orientations together, and then projecting the image. A mask is then made of the map, which is used during the high pass filter task of the next iteration of the pipeline.

The high pass filter task is used to remove the $1/f$ noise, and requires that the parameter ‘hpfradius’ is chosen carefully, so that it does not affect sources in the map. If the radius is too small, then the process will remove flux density from the centres of sources. If the value is too large, then the process would not properly remove the $1/f$ noise. This removal of flux density can be seen in especially bright sources via the presence of dark side lobes orientated in the direction of the scan. The use of a masking process when applying the high pass filter is sufficient to reduce this problem, and after several iterations of the imaging process the side lobes are removed completely. A value of 15 arcsec was used for the high pass filter radius, as this returned the best result out of the feasible values tested.

This process was repeated until the projected map did not differ significantly from the previous iteration. This process results in two different types of sources detected within the map, those which were masked before producing the final version of the map, and those which were not masked and were therefore subject to the high-pass filtering. These two types of sources will be referred to as masked and unmasked sources respectively.

The projection resulted in the 160 μm maps having a pixel size of 6.4 arcsec, while the 70 and 100 μm maps both have a pixel size of 3.2 arcsec. The 160 μm map was resampled during the final image production so that it had the same pixel size as the maps taken at the other two wavelengths.

2.3 Image analysis

2.3.1 Source extraction

The data were then analysed using the automatic image detection algorithm SExtractor (Bertin & Arnouts, 1996), in order to determine the number of sources present in each of the three maps. SExtractor works by identifying groups of contiguous pixels, where each individual pixel lies above a given threshold. Additionally, it works to deblend

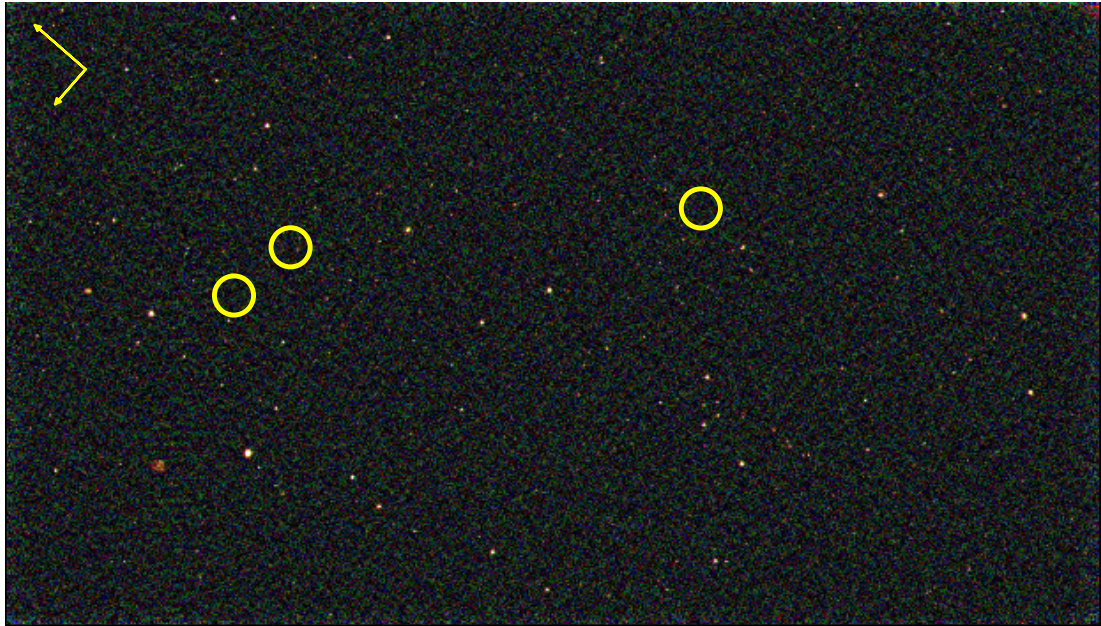


Figure 2.1: A map of the observed area created via the combination of the three wavelength band maps. Blue, green and red represent the 70, 100 and 160 μm maps respectively. The three yellow rings denote the location of the three brightest galaxies in the Coma Cluster; NGC 4889, NGC 4874 and NGC 4839 (from left to right). These are not seen in the *Herschel* maps, and are presented for visual reference only. The final map covers an area of sky measuring 1.75 by 1.0 degrees.

nearby sources, by assessing whether a nearby source is above a certain fraction of the flux density of the surrounding area. The values used for the detection threshold, the minimum contiguous pixels, and the deblending contrast fraction were 1.3σ , 6 and 0.01 respectively. As a secondary flux density limit, it was required that each source as a whole was detected at a five sigma level relative to the rms noise (as determined in subsection 2.3.2). The background level is consistent with zero across the map, as is to be expected due to the nature of the high pass filter process. Additionally, any sources that were located at the very edges of the maps were discarded due to the increased levels of noise in those regions.

The nature of the PSF of a point source is such that some flux density will be contained within the elongated wings of the source and thus lie outside the aperture used for measurement. However, it is not possible to simply increase the aperture diameter to such a degree that it encloses the entire source, as this would increase the amount of noise that is within the aperture and thus decrease the signal-to-noise ratio. Conversely,

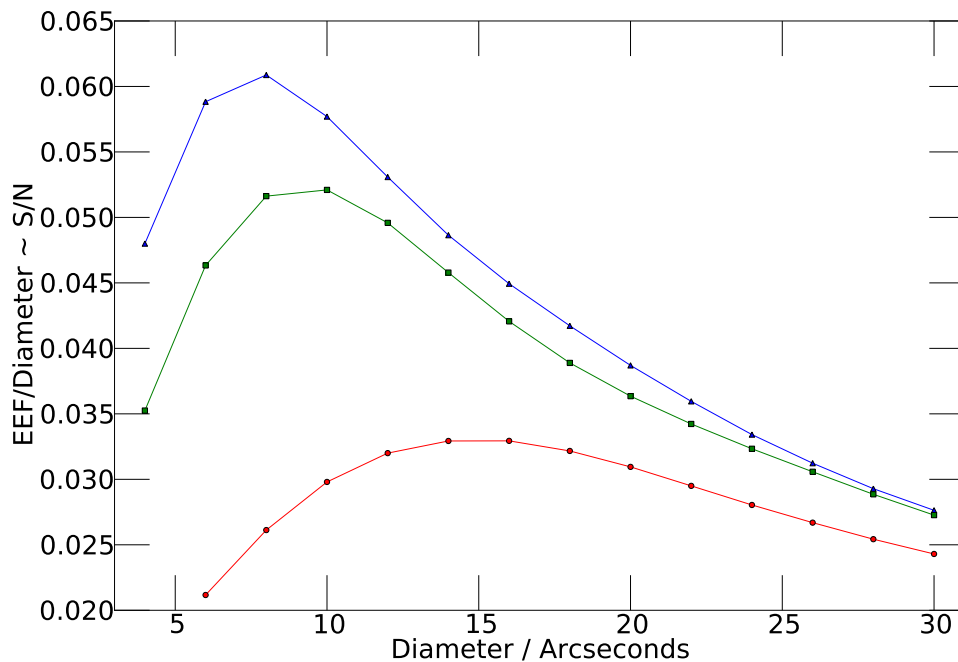


Figure 2.2: Signal-to-noise as a function of aperture diameter for the three PACS wavelengths. The blue triangles, green squares and red circles represent the 70, 100 and 160 μm data respectively.

a smaller aperture diameter might have a higher signal-to-noise ratio, but would not contain all of the flux density, and would thus need a correction, based on the encircled energy fraction, to account for the missing flux density. The values of the encircled energy fraction were determined by Balog et al. (2014). Therefore, there is an optimum aperture size that maximizes the signal-to-noise ratio for point sources, but minimises the correction needed to produce the total flux density.

Figures 2.2 and 2.3 show the signal-to-noise and the encircled energy fractions as a function of aperture diameter for each of the three wavelengths utilised by the PACS instrument. These figures are reproduced from the PACS Observers Manual¹, but with updated values of the encircled energy fraction as taken from Balog et al. (2014). The aperture diameter that resulted in the highest value of signal to noise whilst also having a encircled energy fraction of at least 60 per cent was deemed to be the optimum value.

¹http://herschel.esac.esa.int/Docs/PACS/html/pacs_om.html

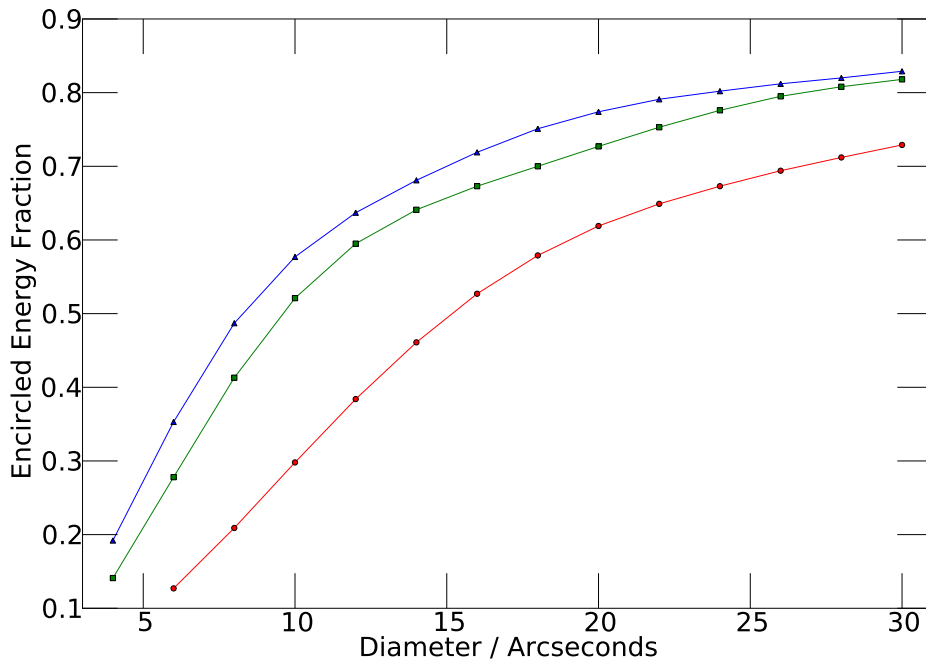


Figure 2.3: Encircled energy fraction as a function of aperture diameter for the three PACS wavelengths. The blue triangles, green squares and red circles represent the 70, 100 and 160 μm data respectively.

For the 70, 100 and 160 μm sources, the optimum aperture diameters are therefore 12, 14 and 20 arcseconds. These values correspond to encircled energy fractions of 63.7, 64.1 and 61.9 per cent for the 70, 100 and 160 μm point sources respectively. For unmasked sources this encircled energy fraction will be too large due to the removal of flux density during the high-pass filter process. Therefore a secondary set of corrections was determined by comparing the final flux density of sources with the unprocessed map flux density of the same sources and taking an average of the difference between them. This yielded encircled energy fractions for unmasked point sources of 59.9, 59.7 and 54.4 per cent at 70, 100 and 160 μm respectively. The final catalogue contains a combination of both masked and unmasked sources, with the appropriate correction being applied to each one.

The apertures and corrections described above are appropriate for point sources, but in the case of extended objects this method is not viable. An object with this catalogue is defined as being extended if the full width at half maximum (FWHM) of the object is

greater than $\sqrt{2}$ multiplied by the FWHM of the PACS PSF. Thus an object is considered to be extended if it has a FWHM greater than 2.47, 2.96 and 4.86 pixels in the 70, 100 and 160 μm maps respectively.

For sources which have been classified as being extended, the aperture utilised has a diameter of 24 pixels (76.8 arcseconds). This value was chosen as it fully encircles the most extended sources found within the maps, and hence no correction needs to be applied to the resulting measured flux.

2.3.2 Noise estimates

The root mean square noise for the final maps was determined by the random placing of 10,000 apertures of the optimum size (see Section 2.3.1), and measuring the counts enclosed within them. These numbers were then binned and fitted to a Gaussian curve. The root mean square of this curve is then determined, and corrected to account for the encircled energy fraction, resulting in root mean square noise values of 5.7, 6.7 and 7.9 mJy at 70, 100 and 160 μm respectively.

2.3.3 Completeness

The completeness of the data was determined in order to ascertain how many sources had been missed during the source extraction process. Completeness curves were determined for each wavelength band by inserting fake sources, 100 at a time, into the maps before running the SExtractor algorithm as described in subsection 2.3.1 in order to see how many sources were recovered at a flux density greater than the five sigma limit. This was done 25 times for each brightness level between 4 mJy and 1 Jy, with intervals of 0.1 dex.

The fake source was constructed by stacking a number of bright point sources, and then scaling the flux density of the object accordingly. This process was completed twice with two separate fake sources; once for masked sources, and once for unmasked sources. This was done to account for sources that were not masked at any point during

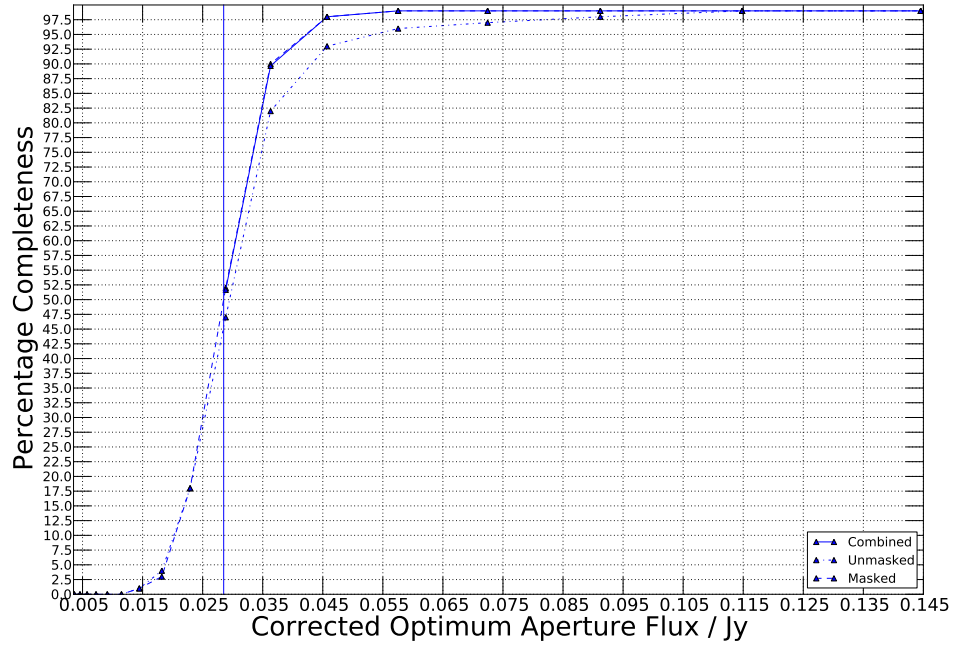


Figure 2.4: Curves of the $70\ \mu\text{m}$ completeness versus the corrected aperture flux density, for masked and unmasked sources, as well as a combination of the two determined via the use of Equation 2.1. The vertical line corresponds to the five sigma noise limit for the map at this wavelength of 28.5 mJy.

the high pass filter process, and as such have a different PSF. The total completeness was determined for each magnitude bin by combining the masked and unmasked completeness using the following equation:

$$C = \frac{c_m c_u (n_m + n_u)}{c_u n_m + c_m n_u} \quad (2.1)$$

Here, c_m and c_u are the masked and unmasked completenesses, and n_m and n_u are the number of masked and unmasked sources in the bin. This results in a 50 (80) per cent completeness of 28.5, 34.5 and 42.0 (34.4, 42.2 and 52.3) mJy for the 70, 100 and 160 μm maps respectively.

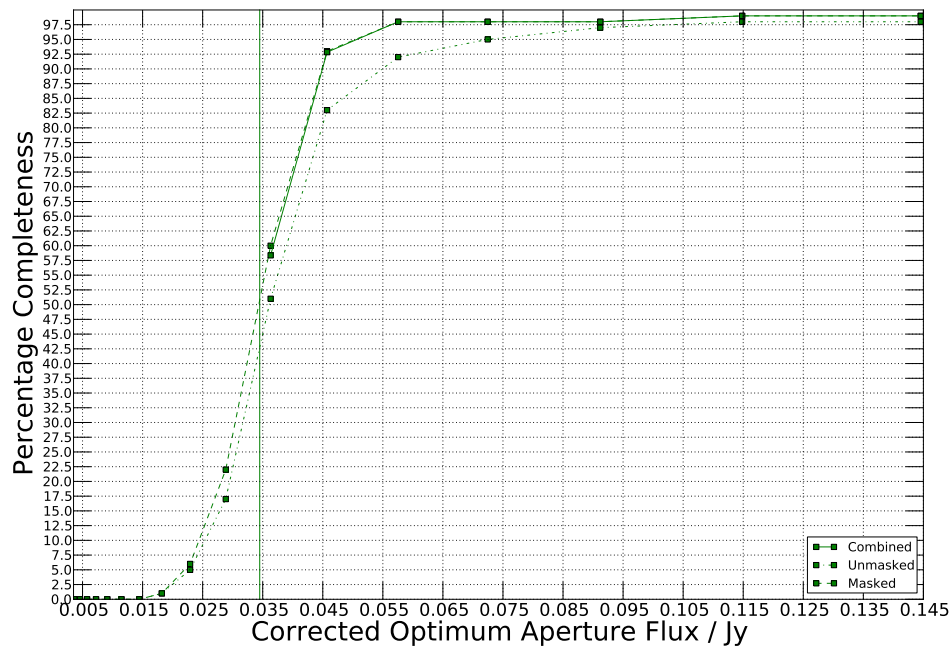


Figure 2.5: Curves of the $100\ \mu\text{m}$ completeness versus the corrected aperture flux density, for masked and unmasked sources, as well as a combination of the two determined via the use of Equation 2.1. The vertical line corresponds to the five sigma noise limit for the map at this wavelength of 33.5 mJy.

2.3.4 Error calculation

The error on the retrieved flux densities comes from two sources: the instrument calibration and the source extraction process. The calibration of the PACS photometer was detailed in Balog et al. (2014), with the end result being that the absolute calibration accuracy is limited by the uncertainty of the standard models used, giving an error on the flux density of 5 per cent.

The second source of error, the source extraction process, is determined using the same fake sources utilised for the completeness calculations as described in subsection 2.3.3. For each wavelength, and at each brightness level, the flux densities of the individual fake sources were measured, and compared to the known input flux density to give a fractional difference. The standard deviations of the differences were calculated and the resulting values plotted against the corresponding brightness level. A curve of best

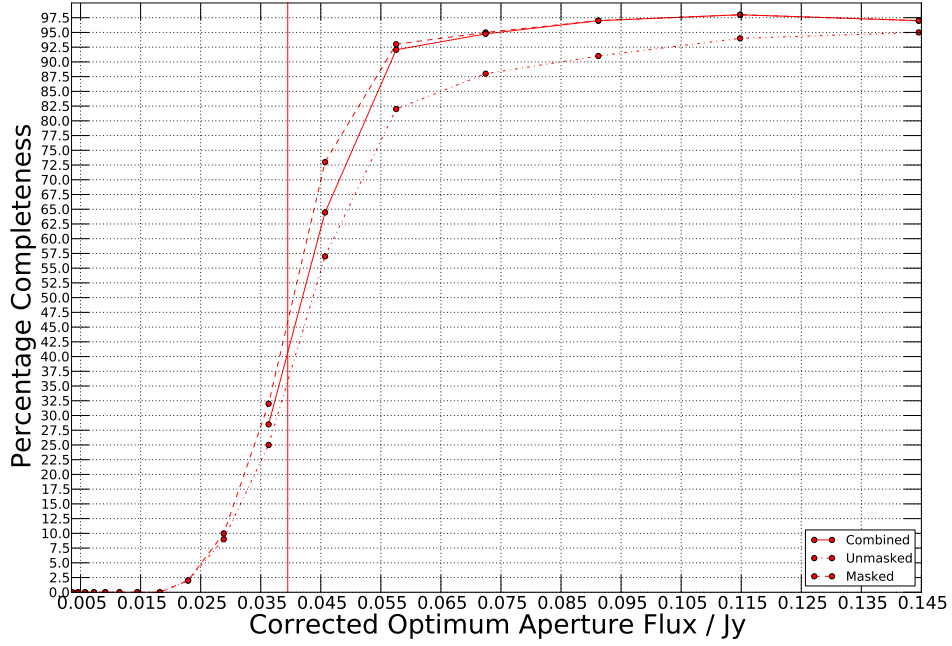


Figure 2.6: Curves of the $160\ \mu\text{m}$ completeness versus the corrected aperture flux density, for masked and unmasked sources, as well as a combination of the two determined via the use of Equation 2.1. The vertical line corresponds to the five sigma noise limit for the map at this wavelength of $39.5\ \text{mJy}$.

fit was then fitted to the points in order to determine a relation between source flux density and the fractional error on its measurement. This curve has the form $y = ax^b$, where x is the source flux density and a and b are constants. The equations for each of the three wavelength maps are shown in Equations 2.2, 2.3 and 2.4.

$$E_{70} = 0.0115 \times S_{Jy}^{-0.8915} \quad (2.2)$$

$$E_{100} = 0.0130 \times S_{Jy}^{-0.9287} \quad (2.3)$$

$$E_{160} = 0.0106 \times S_{Jy}^{-1.1598} \quad (2.4)$$

These two sources of error are then added together in quadrature to give the final

fractional error on the flux density of a given source, where the instrument calibration dominated for the brighter sources and the source extraction error dominates for the dimmer sources.

2.3.5 Total number counts

This process results in the detection of 201, 370 and 507 sources above the 5σ limit, in the 70, 100 and 160 μm maps respectively. The numbers of these confirmed sources as a function of flux density in the 100 and 160 μm maps were compared directly to recent results from the *Herschel* Astrophysical Terahertz Large Area Survey (H-ATLAS: Eales et al. 2010) and the PACS Evolutionary Probe (PEP: Lutz et al. 2011), as described in Rigby et al. (2011) and Berta et al. (2010). This comparison is shown in Figure 2.7. The numbers of sources from the Coma data have been corrected for incompleteness, as determined via the method described in subsection 2.3.3. The excess of sources at the bright end is to be expected, given the presence of a rich galaxy cluster in the mapped area. To confirm this point, a plot of the same data, but with spectroscopically confirmed Coma members removed, shows no such excess as seen in Figure 2.8. The faint end of the data is consistent with previous studies to within the respective errors.

The Coma Cluster was also surveyed to shallower depths using *Herschel* at 100 and 160 μm by the H-ATLAS survey (Eales et al., 2010). There was a match of 153 and 231 sources between the maps to within a distance equal to the optimum aperture radius for the 100 and 160 μm maps respectively. Good agreement was found between the flux densities of these sources down to the 100mJy noise limit of the maps (Smith 2013, private communication).

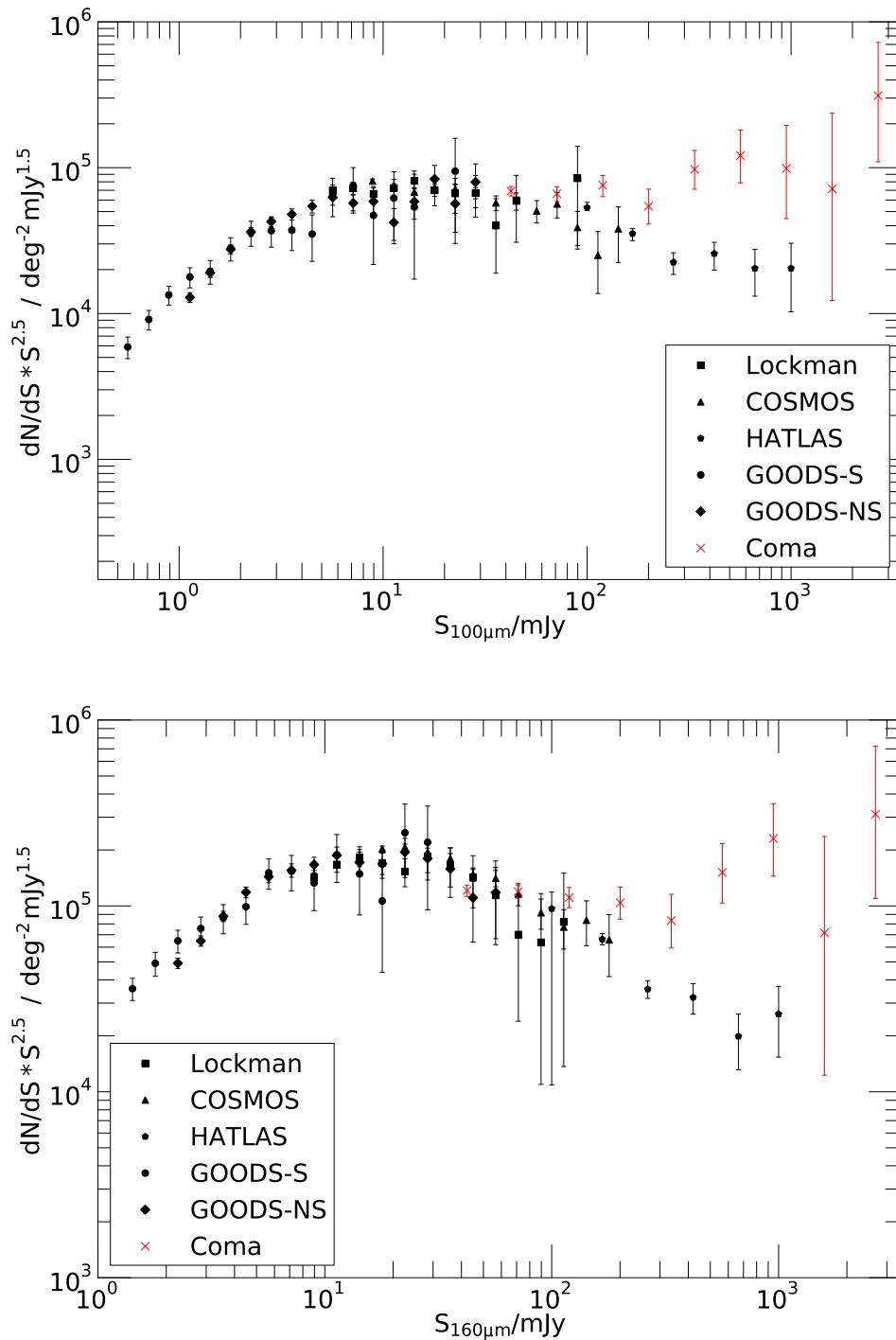


Figure 2.7: A comparison of *Herschel* Coma source number counts to the H-ATLAS and PEP data at the same wavelength. The top plot shows the $100 \mu\text{m}$ sources, whilst the bottom plot shows the $160 \mu\text{m}$ sources. The data for the Lockman and COSMOS fields were taken from Berta et al. (2010). The GOODS field data were taken from Magnelli et al. (2013). GOODS-S refers to the deep scan of the south field only, whereas GOODS-NS is the data from a shallower scan of both the north and south fields.

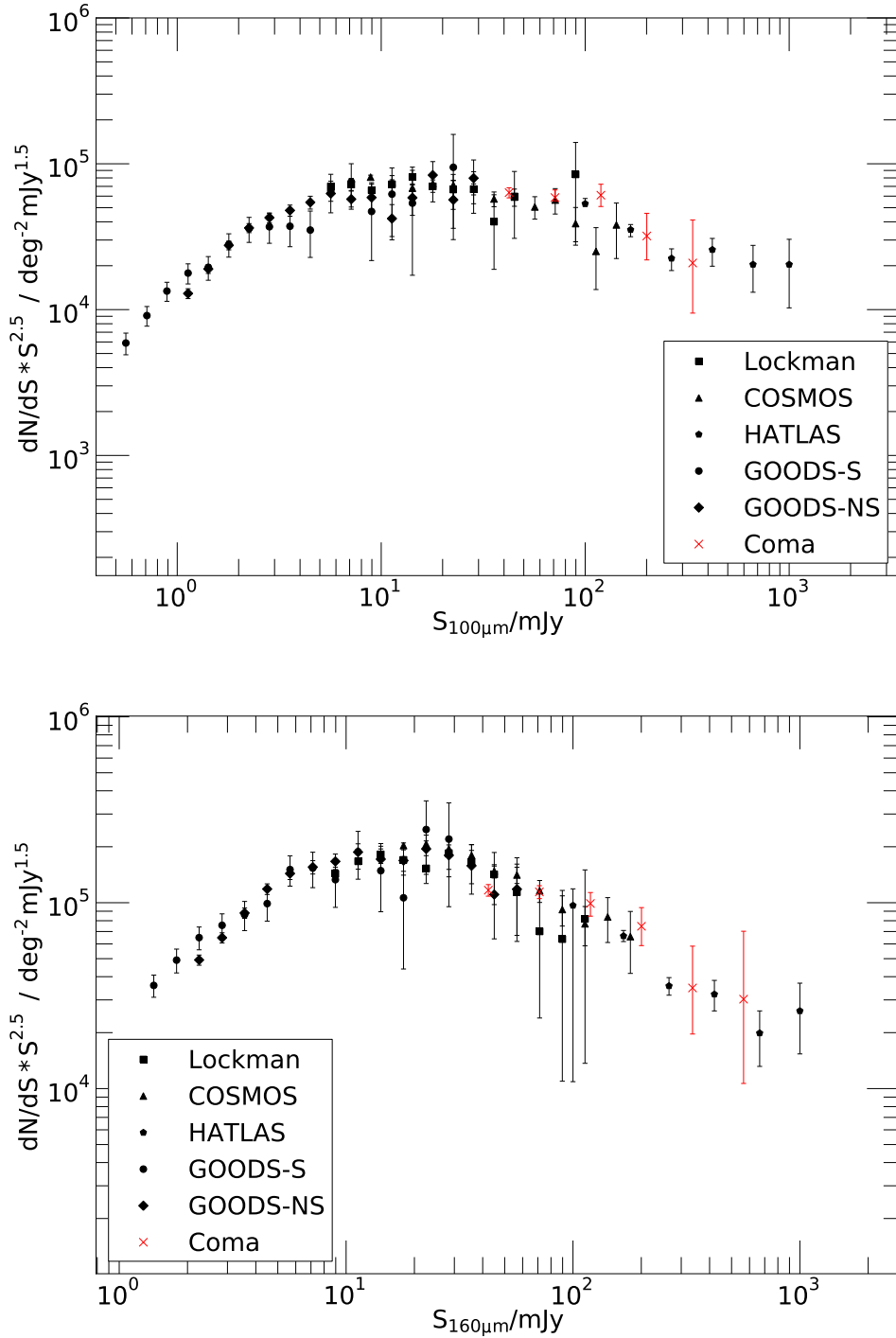


Figure 2.8: A comparison of *Herschel* Coma source number counts to the H-ATLAS and PEP data at the same wavelength, however those sources which are spectroscopically confirmed to be members of the Coma Cluster have been removed. The top plot shows the 100 μm sources, whilst the bottom plot shows the 160 μm sources. The data for the Lockman and COSMOS fields were taken from Berta et al. (2010). The GOODS field data were taken from Magnelli et al. (2013). GOODS-S refers to the deep scan of the south field only, whereas GOODS-NS is the data from a shallower scan of both the north and south fields.

2.4 Concluding remarks

In this chapter, the reduction of the raw data through to the extraction of individual sources in each of the three wavelength maps has been described. This process resulted in the detection of 201, 370 and 507 sources in the 70, 100 and 160 μm wavelength maps. It was found that the flux densities were consistent in the cases where these sources had been detected by other studies.

In the next chapter these sources will be compared to a spectroscopic catalogue of the Coma cluster in order to determine the true cluster members sources. These cluster sources are then used to construct galaxy luminosity functions in each of the three wavelength bands.

Chapter 3

Galaxy luminosity functions

Having reduced the data and subsequently produced a list of detected objects in the map area, it is necessary to then determine which of these can be spectroscopically confirmed to lie within the region of the Coma cluster. This chapter details this process and uses the resulting catalogue, combined with *Herschel* photometry, to produce far-infrared luminosity functions. These are then compared to the luminosity trends of the field and the Virgo cluster. The Hectospec section of the spectroscopic catalogue was provided by David Carter.

The content and results of this chapter have previously been published as part of Hickinbottom et al. (2014).

3.1 Spectroscopic redshift selection

A number of the detected sources in the maps will be foreground or background objects, and have no relation to the Coma cluster. In order to determine which sources are true Coma cluster members, spectroscopic redshifts are required for all the sources.

3.1.1 The spectroscopic catalogue

Data for the Hectospec catalogue were obtained with the fibre multi-object spectrograph Hectospec (Fabricant et al., 2005) at the Multi-Mirror Telescope (now MMT) on the nights of 12-15 April 2007, with additional queue observations being made on subsequent nights. The proposal was PA-07A-0260 (PI: Ann Hornschemeier). These observations used a 270 lines mm^{-1} grating blazed at ~ 500 nm to provide a dispersion of 0.121 nm^{-1} over a useful wavelength range of 380-890 nm. A total of 20 fibre configurations were observed with an integration time of one hour each and 200 fibres of each configuration were assigned to the redshift survey.

Targets for the redshift survey were selected from a parent catalogue of galaxies with Petrosian magnitudes $r < 21.3$, within which the higher priority targets were those with $r < 20.3$, those within the footprint of the *HST* Survey (Carter et al., 2008), within the *XMM-Newton* survey (Briel et al., 2001), and those identified with radio sources from the VLA survey (Bravo-Alfaro et al., 2000, 2001). No colour selection criteria were applied.

The data reduction and the estimation of the redshifts had been performed in a standard manner using the Hectospec data reduction pipeline HSRED¹. A second redshift estimate was derived for galaxies in the redshift survey sample using the IRAF cross-correlation task XCSAO. Each spectrum was then inspected visually by two separate members of the HST survey team to resolve discrepancies between HSRED and XCSAO redshifts and to assess the quality and reliability of the measured redshifts.

The Hectospec catalogue was augmented by redshifts from the NASA/IPAC extragalactic database² and an unpublished catalogue by M.M. Colless and A.M. Dunn (private communication). The final catalogue is approximately 50 per cent complete at $r = 20.3$. Incompleteness is due to the lack of spectra for some galaxies because of fibre proximity constraints, and the inability to obtain reliable redshifts for the faintest galaxies.

¹<http://www.astro.princeton.edu/~rcool/hsred/>

²<http://ned.ipac.caltech.edu/>

Owing to the nature of the Hectospec observations, the catalogue does not cover the entirety of the *Herschel* observational area. For this reason it was necessary to supplement the redshift catalogue with that of SDSS data release 10 (Ahn et al., 2014), specifically the ‘SpecObj’ catalogue to ensure the objects had associated spectroscopic measurements. The Hectospec catalogue classes a source as being within the Coma cluster if the redshift lies in the range of 0.0099 to 0.0333, therefore the same criteria were applied to the SDSS catalogue to produce a final complete spectroscopic catalogue for the area observed. This final spectroscopic catalogue is defined as the parent catalogue for these observations.

A second catalogue was constructed that consisted of objects within the observational area, but with spectroscopic measurements that placed them outside the range associated with the Coma cluster. This catalogue will allow for a more meaningful analysis of the far-infrared detected objects that are not part of the Coma cluster.

3.1.2 Identification of Coma cluster members

Any source in the *Herschel* catalogue that could be matched to a member within this spectroscopic catalogue, within a distance equal to the optimum aperture radius for the given wavelength, was classified as a true Coma cluster member. This matching radius definition was chosen as it allowed for differences in centroiding with a source. A test of plausibly larger values showed no effect on the returned number of matches. From this process it was determined that the data contain 53, 68 and 56 cluster members in the 70, 100 and 160 μm maps respectively. In total there are 70 individually identified sources, with 49 sources being common to all three wavelength bands. Of these 70 sources, four sources were identified that were unique to the SDSS spectroscopic catalogue and six that were unique to the Hectospec spectroscopic catalogue. The remainder of the sources are present in both catalogues.

For each wavelength the remaining far-infrared detected sources were compared to the catalogue of objects spectroscopically confirmed to lie outside of the Coma cluster; this returned 86, 147 and 199 galaxies in the 70, 100 and 160 μm maps respectively.

Wavelength (μm)	Total Far-infrared detections	Redshift within Coma cluster	Redshift outside Coma cluster	Unknown redshift
70	201	24.9%	42.8%	32.3%
100	370	17.3%	39.7%	43.0%
160	507	10.5%	39.3%	50.3%

Table 3.1: Detection fractions for objects detected within each of the three *Herschel* PACS bands for each of the three redshift categories: redshifts within the Coma cluster, redshifts outside the Coma cluster and unknown redshifts.

This leaves 65, 159 and 255 objects remaining within the 70, 100 and 160 μm maps respectively, that have been detected at far-infrared wavelengths, but do not have an associated spectroscopic measurement placing them either within or outside the Coma cluster.

Table 3.1 shows the fraction of objects that lie within the three spectroscopic groups: within Coma, outside Coma, and unknown. It can be seen that the fraction that are spectroscopically confirmed as lying outside of the Coma cluster is approximately constant across the three wavelength bands. However, the fraction that lie within the Coma cluster declines with increasing wavelength, with the opposite being true for those with no spectroscopic information.

The 70 identified Coma cluster members were then matched to the SDSS photometry catalogue in order to obtain u -, g -, r -, i - and z -band magnitudes for each one. It was possible to find photometric data for those sources for which SDSS spectroscopic data are unavailable, because the magnitude limit of the two SDSS catalogues is different: the SDSS spectroscopy catalogue limit is 17.77 in r , compared to 22.2 in r for the SDSS photometric catalogue. Figure 3.1 shows the infrared flux densities of the 68 sources identified in the 100 μm map against their r -band magnitudes. It can be seen that all the sources have r -band magnitudes much brighter than the limiting magnitudes of the SDSS and Hectospec catalogues. This shows that the limiting magnitude of the spectroscopic surveys is unlikely to have a significant effect on the number of identifiable sources within our catalogue, and that it is probable that all Coma members within our *Herschel* sample have been identified. Ball et al. (2006) determine a value

of $M^* = -20.49$ in the SDSS r -band for their sample of galaxies. This gives a value of L^* equal to 14.47, therefore as the sources lie around this value, it is not only the most massive and luminous galaxies that are being observed.

The Coma Cluster has previously been observed at far-infrared wavelengths using *IRAS*. The observations found 41 galaxies within 4.2 degrees of the cluster centre, of which 26 were confirmed to be members from their velocities (Wang et al., 1991). Of these 26 confirmed Coma Cluster members found by *IRAS*, only four lie within our survey region. All four sources match to sources in our *Herschel* catalogue to within 1 arcmin, which is the approximate limiting resolution of the *IRAS* survey. There is a good flux density agreement between *Herschel* and *IRAS* for these four sources at 100 μm , however they each have a lower flux density as determined by *Herschel*, with the difference ranging from 8 to 22 per cent. This is most likely due to the *IRAS* flux density being contaminated by other nearby sources due to the large *IRAS* point spread function.

Observations of this region at 24, 70 and 160 μm have also been completed using the Spitzer Space Telescope (Edwards & Fadda, 2011). A positional match of the Spitzer catalogue with the results of this *Herschel* study gives 66 sources at 24 μm , 21 at 70 μm and 15 at 160 μm . A comparison of the flux densities of sources observed at 70 and 160 μm shows that the Spitzer study recovers consistently higher values. However, the Spitzer study utilised apertures with radii of 15 and 20 arcsec for the 70 and 160 μm maps respectively. These are significantly larger than the apertures used for the *Herschel* study, and so the disagreement between the flux densities of the two studies is due to this difference.

The far-infrared flux densities measured at each PACS wavelength, along with their respective errors, for each of the 70 spectroscopically confirmed Coma cluster members are presented in Appendix B.

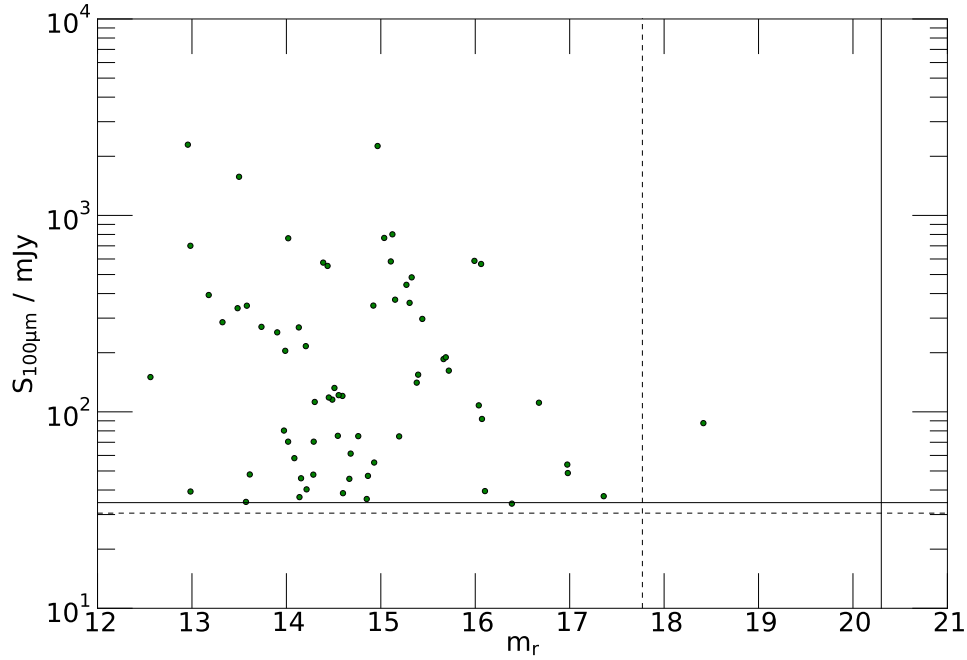


Figure 3.1: The 100 μm flux density against the r -band magnitude, for confirmed Coma cluster members. The dashed and solid vertical lines indicate the limiting magnitudes of SDSS (17.77) and Hectospec (20.3) respectively. The dashed and solid horizontal lines indicate the 30 and 50 per cent completeness levels respectively.

3.2 Schechter function fits

Having produced a catalogue of cluster members at each of the three PACS wavelengths, it is now possible to construct a far-infrared luminosity function for each catalogue, as shown in Figure 3.2. The numbers in each bin have been corrected for completeness as per the discussion in subsection 2.3.3. The errors in the numbers were determined via the use of low number statistics, as detailed in Gehrels (1986).

Schechter (1976) showed that galaxy numbers as a function of luminosity can be fitted using three parameters; ϕ^* , a normalisation parameter proportional to the number density of sources, L^* , the characteristic luminosity at which a rapid change in the slope of the function is seen, and α , a dimensionless parameter which gives the slope of the function at luminosities less than L^* . This function is shown in the equation below.

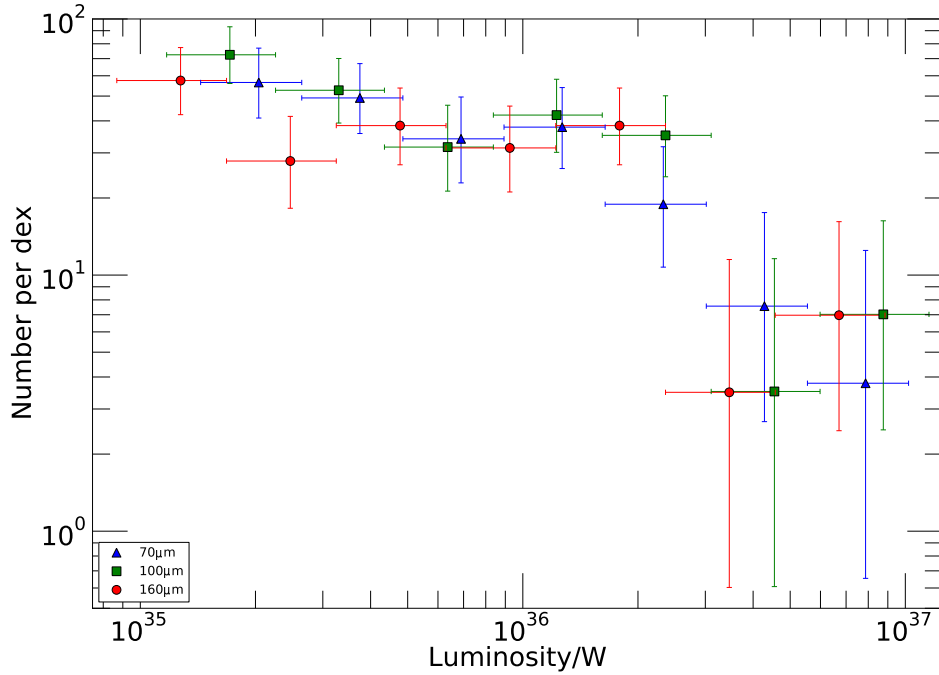


Figure 3.2: Galaxy luminosity functions for confirmed Coma cluster members with the 70, 100 and 160 μm functions being denoted by blue triangles, green squares and red circles respectively. These functions follow the form given in Equation 3.1, with the parameters listed in Table 3.2.

$$\phi(L)d \log L = \phi^* \ln 10 \left(\frac{L}{L^*} \right)^{\alpha+1} \exp \left(\frac{-L}{L^*} \right) d \log L \quad (3.1)$$

A maximum likelihood method (Marshall et al., 1983) was used to fit Schechter parameters to the data at each wavelength independently, with the resulting values being presented in Table 3.2. A Schechter fit was chosen as the extra free parameter in the fits used by Saunders et al. (1990) and Soifer et al. (1987b) results in the function being unable to converge on a singular set of values, and produces non-physical results for the data.

Wavelength	$\log_{10}\phi^*$ dex ⁻¹	$\log_{10}L^*$ W	α
70 μm	$1.30^{+0.23}_{-0.32}$	$36.46^{+0.27}_{-0.20}$	$-1.07^{+0.27}_{-0.25}$
100 μm	$1.21^{+0.23}_{-0.30}$	$36.62^{+0.27}_{-0.20}$	$-1.19^{+0.20}_{-0.19}$
160 μm	$1.38^{+0.19}_{-0.25}$	$36.35^{+0.22}_{-0.18}$	$-0.93^{+0.23}_{-0.22}$

Table 3.2: The Schechter luminosity function parameter values calculated for Coma cluster galaxies in the three *Herschel* bands.

3.3 Comparisons with other luminosity functions

3.3.1 Comparison with the Virgo cluster

The shape of the Schechter luminosity function is such that it is dominated by the low luminosity objects, with a drop off at the high luminosity end brighter than some intrinsic luminosity. Davies et al. (2010) showed the far-infrared luminosity function for Virgo cluster galaxies, as derived from the HeViCS data. They showed that at all observed wavelengths there was evidence of an additional turnover at lower luminosities. Further evidence of this was seen with the HeViCS catalogue of bright galaxies (Davies et al., 2012). If this trend is real, then it would imply that the cluster environment significantly suppresses the low luminosity population. However, Auld et al. (2013) reanalysed the data and presented far-infrared flux densities of optically selected Virgo cluster galaxies at 100 and 160 μm . This study found a different trend that more closely resembled the Schechter luminosity function.

The data presented in Auld et al. (2013) were used to determine new luminosity functions for Virgo and compare them to the equivalent data in the present study in order to ascertain if Virgo shows a turnover as well as for comparison with the Coma cluster luminosity function. The 100 and 160 μm bands were used as they are the only wavelengths common to both studies. For the purposes of deriving the luminosities for the Virgo sample, the assumptions made in Auld et al. (2013) that all Virgo cluster galaxies lie at one of three distances, 17, 23 or 32 Mpc, are taken to be correct. For the purposes of this study, only those Virgo sources which lie at 17 and 23 Mpc and have a

measured flux density greater than the noise limit are used. This sample corresponds to that used by the latest HeViCS analysis (Auld et al., 2013). Analysis of the data shows that the inclusion of those sources at 32 Mpc, and the assumption that all sources lie at 17 Mpc, have little effect on the derived parameters.

Figure 3.3 shows the 100 and 160 μm data, and it can be seen that the more extensive Virgo data now has a form more closely resembling a Schechter function, and as such is closely matched in shape to the Coma data. Schechter parameters are given for the Virgo data in Table 3.3 to allow for comparison with the Coma data values. The number of sources, as denoted by the parameter ϕ^* , cannot be compared directly as it is not applicable to the study of clusters. The other derived parameters for the Virgo cluster are consistent, within the errors, with those derived for the Coma cluster. A steeper value for α than that given by Auld et al. (2013) is found, however this is due to the luminosity cut applied to the dataset: if all viable sources are included then similar values are recovered.

The Virgo cluster has a r_{200} radius value of 1.08 Mpc or 3.9° at an adopted distance of 16.1 Mpc (Urban et al., 2011). Arnaud et al. (2005) showed that the r_{200} radius value can be adopted as the virial radius for Virgo, even though the cluster is not virialised. The HeViCS observations therefore cover an area out to over twice the equivalent virial radius. In comparison the virial radius of the Coma cluster is 1.7° or 2.9 Mpc (Łokas & Mamon, 2003), with the *Herschel* observations covering an area out to approximately this distance. The Virgo observations therefore cover a greater area outside of the core environment relative to the Coma observations. Thus there is the potential for an inherent bias in the observations if there is a correlation between properties of the galaxy and their distance from the cluster centre. This effect will be discussed in further detail in Section 6.2.

3.3.2 Comparison to the field galaxy luminosity function

The 70 μm data and best-fitting luminosity function are plotted in Figure 3.4, along with the field galaxy luminosity function at 70 μm from the *Spitzer* Wide-area Infra-

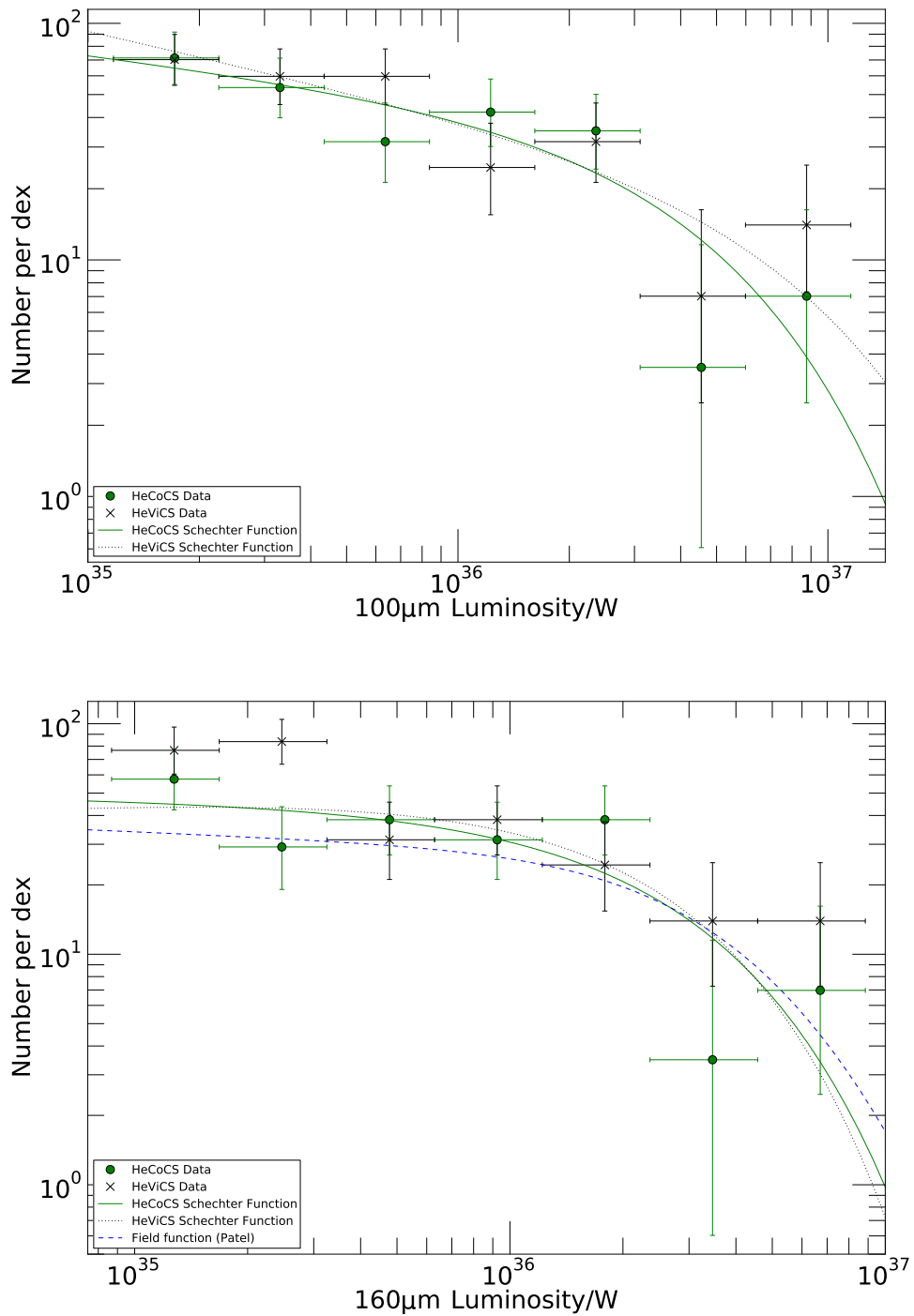


Figure 3.3: A comparison of the Coma and HeViCS luminosity functions. The upper plot shows the 100 μm data and the lower plot shows the 160 μm data. The Coma data are presented as green circles, and the HeViCS data are presented as black crosses. The solid green line shows the Schechter function fit for the Coma data, using the parameters presented in Table 3.2. The dotted black line shows the Schechter function fit for the Virgo data of Auld et al. (2013), using the parameters presented in Table 3.3. In the plot of the 160 μm data, the dashed blue line shows the field luminosity function as derived by Patel et al. (2013).

Wavelength	$\log_{10}\phi^*$ dex ⁻¹	$\log_{10}L^*$ W	α
100 μm	$0.94^{+0.26}_{-0.35}$	$36.92^{+0.33}_{-0.23}$	$-1.35^{+0.15}_{-0.15}$
160 μm	$0.91^{+0.28}_{-0.37}$	$36.83^{+0.34}_{-0.24}$	$-1.40^{+0.16}_{-0.14}$

Table 3.3: The Schechter luminosity function parameter values calculated for the two bands of the Virgo cluster data.

red Extragalactic survey (SWIRE; Patel et al. 2013) and a fit of the Coma data to the luminosity function derived from field galaxies at 60 μm as taken from Saunders et al. (1990) and converted to 70 μm assuming an M82-like spectral energy distribution. The luminosity functions presented by Patel et al. (2013) use the functional form of Saunders et al. (1990). Both field galaxy luminosity functions have been scaled vertically to fit the Coma cluster data, and good agreement is seen. Kolmogorov-Smirnov tests were run to compare the luminosity distribution of the cluster members with that predicted by the field luminosity functions after the correction for incompleteness, as detailed in subsection 2.3.3. It is found with a probability of 90 and 89 per cent respectively that the 70 μm sample is drawn from the same parent distribution as the Patel et al. (2013) and Saunders et al. (1990) luminosity functions. Patel et al. (2013) also derive a field luminosity function at 160 μm and a probability of 49 per cent that the Coma galaxy luminosities at this wavelength are drawn from this distribution is found. This result confirms that of Bai et al. (2006, 2009), who used mid-infrared and optical data to derive a total infrared luminosity function. They found an agreement between the Coma cluster and field luminosity functions constructed in this way.

In order to compare the number density of the field and cluster galaxies, it is necessary to apply a scaling factor to the data so that the two samples are representative of a volume of space that contains a comparable mass in galaxies, taking into account the high density of the Coma cluster region. This is done by using the definition of the R_{200} radius to calculate the much larger volume of an average field region containing the same mass in galaxies. Additionally, the Coma cluster numbers have been scaled up to account for the surveyed area being smaller than the full area within a radius of R_{200} . Figure 3.5 shows a comparison of the 70 and 100 μm Coma cluster galaxy

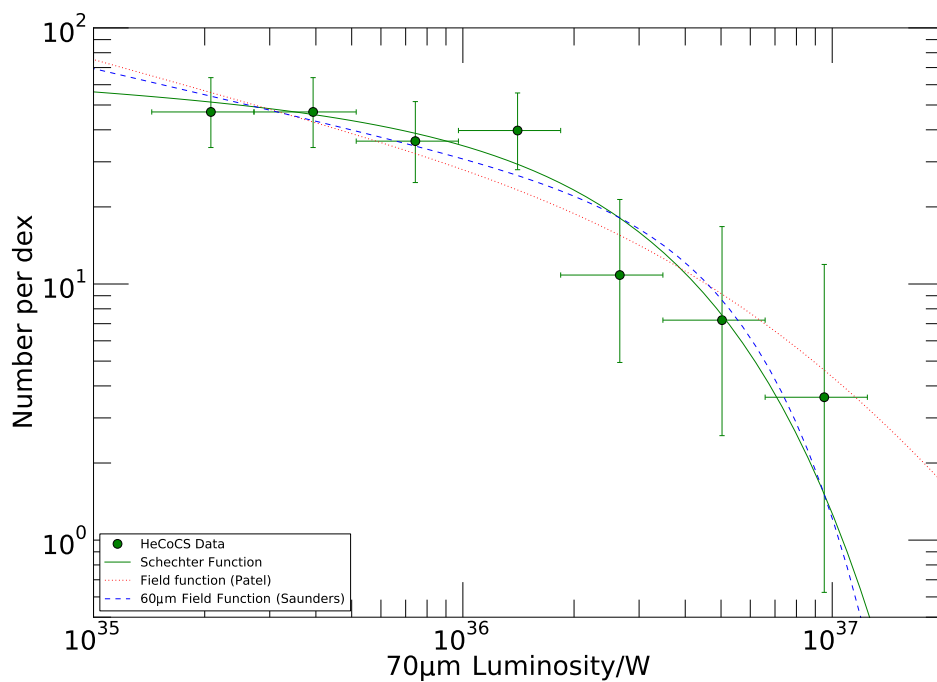


Figure 3.4: A comparison of the Coma and field luminosity functions determined at 70 μ m. The Coma data are presented as green circles. The solid green line shows the Schechter function fit for the Coma data, using the parameters presented in Table 3.2. The dashed blue line shows the fit of the Coma data to the luminosity function derived from field galaxies at 60 μ m as taken from Saunders et al. (1990) and converted to 70 μ m assuming an M82-like spectral energy distribution. The dotted red line shows the field luminosity function as derived by Patel et al. (2013).

Wavelength	$\log_{10}\phi^*$		
	Coma	Virgo	Field
70 μm	-2.86	–	-2.32
100 μm	-2.95	-2.71	–
160 μm	-2.78	-2.74	-2.43

Table 3.4: Comparison of the number densities of the field and the Coma and Virgo cluster.

sample with the 60 and 90 μm field galaxy sample, as presented by Gruppioni et al. (2013). The scaling has been applied by compressing the field galaxy sample down to a sphere with a radius equal to the R_{200} value for the Coma cluster. The result is that whilst the functional forms were similar for the two environments, the actual number density is greater in the field. Thus, while the shape of the luminosity function is approximately unchanged by the cluster environment, the number density of far-infrared emitting galaxies is strongly suppressed.

This difference can also be seen by comparing the number density, $\log_{10}\phi^*$, of the field and the Coma and Virgo clusters, as presented in Table 3.4. The values for the two clusters have been scaled to match the density of the field, so that the numbers are consistent across all three environments. It can be seen that as the density of the environment decreases, from Coma to Virgo to the field, the value of $\log_{10}\phi^*$ increases.

3.4 Concluding remarks

In this chapter the luminosity functions of the galaxies in the Coma and Virgo clusters were compared against each other and with that of galaxies in the field. The Virgo cluster data show a clear lack of turnover at the faint end, and thus more closely match the Schechter function form of the Coma cluster data. This would imply that there is no further need for the original explanation given in Davies et al. (2010) regarding a selective stripping process within the cluster environment.

A comparison between the luminosity functions of field galaxies and Coma and Virgo

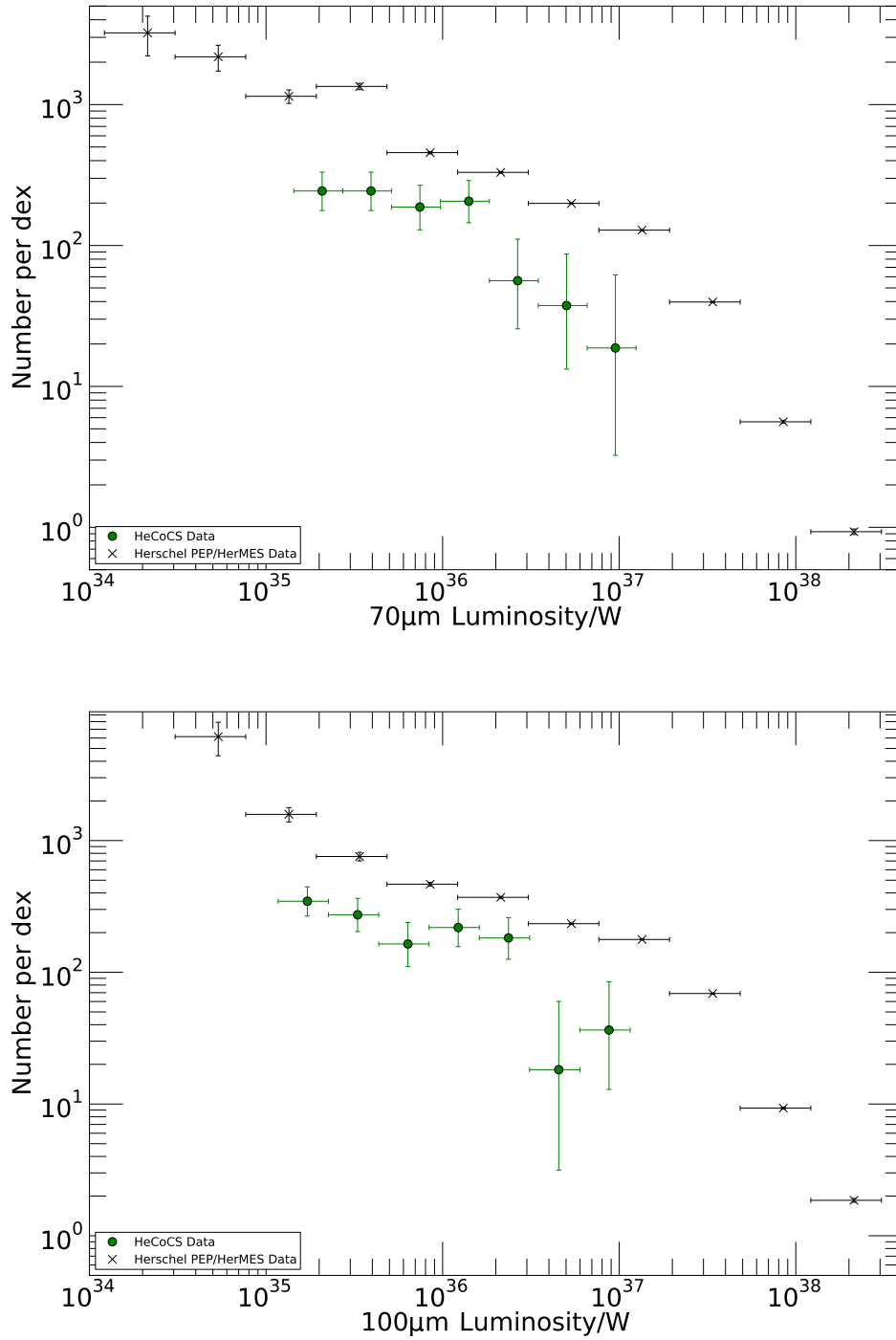


Figure 3.5: Comparison of the Coma cluster and field galaxy samples. The upper plot shows the 60/70 μm data and the lower plot shows the 90/100 μm data.

cluster galaxies, shows that all three follow the same shape. This is surprising as strong gas stripping within the cluster environment is expected from both theoretical and observational studies. However, an environmental effect is seen, in that the overall number density for galaxies within the cluster is much less than that seen within the field environment, once a correction has been made for the overall density contrast of the cluster.

One potential source of ambiguity within this comparison regards the nature of the galaxies that make up the faint end of the far-infrared luminosity function. The same features would be seen if these galaxies were dwarf galaxies or if they were large galaxies that had had their gas stripped. This possible issue will be addressed in Section 5.4 after determining the morphological types of the galaxies in the sample.

Chapter 4

Spectral energy distribution fitting analysis

Chapter 3 detailed the identification of the 70 sources within our map that are in the Coma cluster region. This chapter will describe the process of taking the flux density measurements from the three PACS instrument bands and combining them with flux density measurements in the three SPIRE bands in order to perform a spectral energy distribution fit for each object. This will provide temperatures, dust masses and total infrared luminosities for all of the 70 sources. The SPIRE data were reduced, analysed and provided by Chris Fuller of the University of Cardiff.

4.1 The form of the fitting function

A spectral energy distribution gives the observed flux density of a source as a function of the observed wavelength. When observing in the far-infrared, the flux density stems from thermal emission emitted by dust. Hildebrand (1983) showed that this distribution can be well described by a Planck function with a modified power law relation with frequency. A two temperature black body model would consist of one temperature to describe the cold dust, which will dominate the emission at wavelengths longer than 100 μm , and one to describe the warm dust. These two temperatures would trace

the interstellar medium that is heated by the general stellar population, and star formation regions respectively. As such a multi-temperature model would describe the physical system more accurately, but fitting such a model can result in a degenerate fit, and as a result the modified, single-temperature black body model is adopted, which takes the form:

$$S_\lambda = \frac{\kappa_{abs} M_{dust} B(\lambda, T_{dust})}{D^2} \quad (4.1)$$

Here, $B(\lambda, T_{dust})$ is the Planck function, which is given by:

$$B(\lambda, T_{dust}) = \frac{2hc}{\lambda^3} \frac{1}{\exp\left(\frac{hc}{\lambda k_B T_{dust}}\right) - 1} \quad (4.2)$$

In this form S_λ is the flux density at a given wavelength (λ) in Jansky, M_{dust} is the dust mass in kilograms, T_{dust} is the dust temperature in Kelvin, D is the distance to the source in metres, and κ_{abs} is the dust absorption coefficient, which has a wavelength dependence given by:

$$\kappa_{abs} = \kappa_{abs}(\lambda_0) \left(\frac{\lambda_0}{\lambda}\right)^\beta \quad (4.3)$$

Equation 4.1 is rearranged in order to combine the various constants into one for ease of fitting, resulting in the function used during the fitting process being:

$$S_\lambda = \frac{A}{\lambda^{3+\beta} \left[\exp\left(\frac{14404.5}{\lambda_{\mu m} T_{dust}}\right) - 1 \right]} \quad (4.4)$$

The function has two parameters that are varied to minimize the scatter about the fitted function; the temperature, T_{dust} , and the emissivity parameter, β . Additionally there is a flux density scaling factor that controls the normalisation of the function and includes a number of constants which takes the following form:

$$A = \frac{2hcM_{dust}\lambda_0^\beta\kappa_{abs}(\lambda_0)}{D^2} \quad (4.5)$$

4.2 The far-infrared data

4.2.1 *Herschel* PACS data

As previously described in Section 2.1 the PACS observations consist of measurements at three wavelengths (70, 100 and 160 μm) resulting in three independent maps on which the source detection process was completed. Of the 70 individual sources detected in the maps, only 49 were common to all three maps. Therefore, there are 21 sources which have only been detected in one or two of the individual maps. In those circumstances apertures were placed at the known detection locations in the remaining maps in order to recover a measurement at all three wavelengths. This can result in a flux density measurement that is negative, and as such it is not possible to determine an error on the measurement using the method described in subsection 2.3.4; thus, an upper limit equal to the five sigma detection limit is used instead.

4.2.2 *Herschel* SPIRE data

The three PACS flux density measurements are supplemented by a further three measurements at 250, 350 and 500 μm taken with the SPIRE instrument. These data were produced and provided by collaborators at Cardiff University, specifically Chris Fuller, using a similar method to that presented by Auld et al. (2013). This method requires an optical catalogue of known source positions and sizes, from which suitable apertures can be constructed with which to measure the far-infrared emission. The optical catalogue was based on the Main Galaxy Sample within the SDSS spectroscopic survey (Strauss et al., 2002), which requires a 5 sigma detection with an r -band magnitude detection brighter than $m_r \leq 17.77$, along with other size and flag requirements. The resulting catalogue contains 754 spectroscopically confirmed galaxies within the limits

of the Coma cluster, which are then used to construct a catalogue of SPIRE measurements.

A positional match was then completed between the SPIRE and PACS catalogues, in order to obtain a full range of flux densities. However, for a number of the 70 identified sources there was not a confirmed SPIRE observation, and thus no measurement was taken. In these cases an aperture was placed on the SPIRE maps at the known position and a flux density measurement taken. In some cases there was no significant detection of flux density in the aperture, but it provided an upper limit on the measurement and thus allowed for a true fit to be determined. The end result is that all 70 sources have flux density measurements or upper limits at six different wavelengths.

4.3 The fitting process

The form to be fitted has three parameters to minimize, namely the temperature, the emissivity parameters and the flux density scaling factor. However, many previous studies, e.g. (Davies et al., 2010), have fixed the emissivity index, β , at a value of two. The reasoning behind this value is that it reproduces the far-infrared/sub-millimetre dust emission in the Milky Way. In turn, these models have been used to replicate the dust emission spectral energy distributions seen in several other galaxies (Draine, 2003; Draine et al., 2007). For these reasons and in order to make meaningful comparisons with the *Herschel* studies of Virgo and Fornax, the same parameter value is adopted for this study. This same argument is applied to the dust absorption coefficient, κ_{abs} , which is used in the calculation of the dust mass in Section 4.5. The value used is $0.192\text{m}^2\text{kg}^{-1}$, as taken from Draine (2003).

Due to the nature of the spectral energy function, the flux densities measured at a wavelength of $70\ \mu\text{m}$ are sensitive to the hottest dust component most closely associated with star formation processes, and as such the measurements may be higher than expected and thus lie above the fitted curve. For this reason it is necessary to determine if a better fit is recovered when using the $70\ \mu\text{m}$ flux density only as an upper

constraint, or when using all six wavelengths equally.

For the former, the fitting process is completed in two stages; firstly all the flux density data points, with the exception of the 70 μm datapoint, are fitted to the function given in Equation 4.4, from which values for the temperature and the combined constant are determined. The data are then fitted a second time, using the returned parameters from the first fit as the starting point for the process, but with an additional upper constraint being applied by the 70 μm datapoint. This method was then compared to fitting all the wavelengths to the Equation 4.4, with all six datapoints being treated normally.

In the majority of cases these two methods of fitting return similar results, with the fitted parameters being within a few percent of one another. In a small number of cases where the errors on the flux densities are greater, the fits are more divergent, but it can be seen that the method of fitting all six wavelengths returns a more reliable result, with fewer extreme outliers in the derived temperatures. The spectral energy fits for each object, along with a cut-out of the map at each object's location in each of the three PACS bands, are presented in Appendix A.

Additionally, there is 24 μm *Spitzer* data available for all but four of the identified sources (Edwards & Fadda, 2011), however once again observations at these wavelengths can be dominated by a small fractional component of the galaxy that is closely associated with star formation processes. Therefore, as this point will often lie far above the expected curve, this point is not fitted in either method, but it has been included on the final plots for comparison purposes.

4.4 Quality of fits

Of the 70 spectral energy fits, it was found that the returned temperature values of two of the objects (Objects 8 and 23) are unphysical values that lie below absolute zero, therefore these are deemed as being poor fits and will not be included in future calculations.

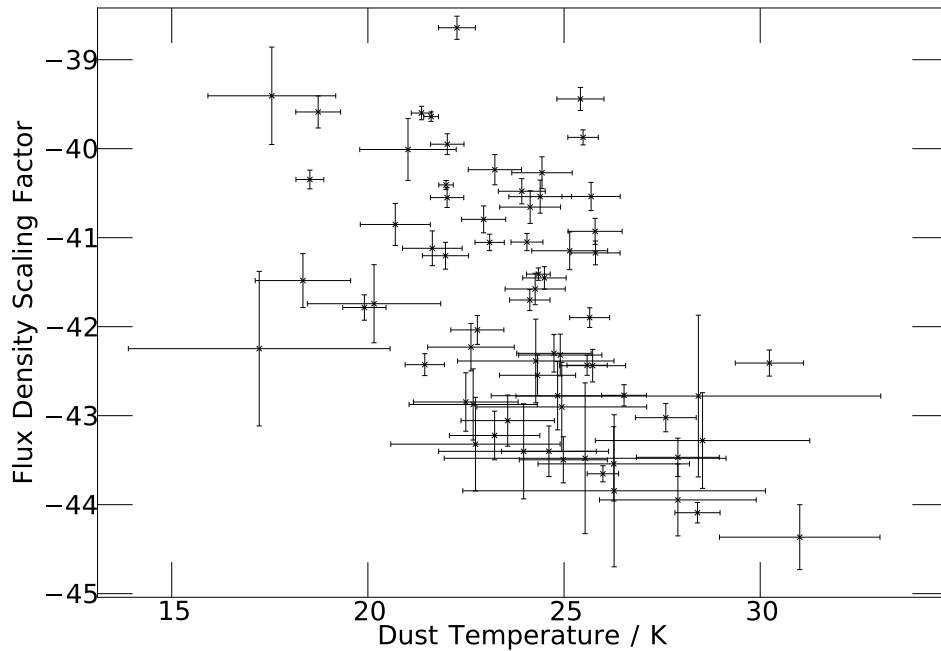


Figure 4.1: The flux density scaling factor of the temperature for the 68 spectroscopically confirmed Coma cluster galaxies which return a physical spectral energy fit.

As previously stated in Section 4.3, the spectral energy function to which the data are fitted has two free parameters which are minimised: the flux density scaling factor and the temperature. If this scaling factor is plotted as a function of temperature it is possible to see any potential degeneracy between the two fitted parameters. Figure 4.1 shows that these parameters have only a weak negative correlation, with the high temperature sources generally having lower dust masses. This slight degeneracy is reflected in those sources with the highest temperatures tending to have larger errors on both parameters. This trend cannot be entirely ruled out, however as the correlation is only weak is it not considered an issue for this study.

The range of fitted temperatures for the 68 Coma cluster galaxies, was found to be $T = 17.2 - 31.0\text{K}$, with a mean value of $T = 24.0\text{K}$ and a standard deviation of $T = 2.78\text{K}$. The median lies at $T = 24.3\text{K}$, and is thus in close agreement with the mean. Having determined values for all the parameters, it is then possible to calculate the total infrared luminosity of each source by integrating the final fitted function within a range

of 8-1000 μm . This results in a range of values from $L_{IR} = 1.5 \times 10^8 - 2.5 \times 10^{10}L_{\odot}$, with a mean of $L_{IR} = 3.2 \times 10^9L_{\odot}$ and a standard deviation of $L_{IR} = 4.7 \times 10^9L_{\odot}$. The median was found to be $L_{IR} = 1.5 \times 10^9L_{\odot}$.

One other source of potential degeneracy is that three physical properties (dust mass, temperature and total infrared luminosity) are determined from a fitting process where there are only two free parameters utilised (the flux scaling factor and temperature). These two parameters are used to directly calculate the dust mass and the temperature respectively, however the total infrared luminosity is determined via the integration of the final function, and as such the final value is dependent on the combination of the previous two properties.

In Chapter 6 these values will be analysed further after grouping the objects by morphological type, allowing for a comparison with other far-infrared studies of cluster and field populations.

4.5 Calculation of dust masses

The dust masses are calculated via a rearrangement of Equation 4.5, to give:

$$M_{dust} = \frac{AD^2}{2hc\lambda_0^\beta \kappa_{abs}(\lambda_0)} \quad (4.6)$$

Draine (2003) presents a table of κ_{abs} values for various wavelengths; standard literature practice is to use the value corresponding to 350 μm , i.e. $0.192\text{m}^2\text{kg}^{-1}$, as discussed in Section 4.3. The distance to the Coma cluster (and hence to all 70 galaxies studied here) is taken to be 98.5 Mpc, as discussed in subsection 1.5.2. As part of the fitting process, upper and lower errors are returned for the fitted parameters. Therefore an error on the dust mass values was determined by taking the maximum and minimum values of the flux density scaling factor, A , and calculating the corresponding dust masses. The difference between these values and the central value gave the positive and negative error respectively.

When calculating the mass of the dust present within a system, it is necessary to make some assumptions regarding the physical nature of the dust in relation to the far-infrared emission being observed. One such property that needs to be considered is the opacity of the dust at the wavelengths being utilised.

The opacity of the dust determines the amount of emission that can be seen from the galaxy. If the dust is optically thick, then the emission is internally absorbed and less is seen by the observer, and conversely optically thin dust allows the emission through more easily. For the purposes of this investigation, the dust is assumed to be optically thin, implying that all the flux is being recovered. However, if this assumption is incorrect, and the dust is in fact optically thick, then computing the dust masses in this way will result in the total mass being underestimated. This is because there would be a large fraction of dust from which emission cannot be seen and thus it would not be included in the calculation.

In order to make comparisons between different sources, it is useful to normalise the dust masses by dividing by the stellar mass of the source. For this work, stellar masses inferred from optical observations are utilised. A relation of this type takes a baseline assumption regarding a mass-to-light ratio, which in most cases is taken from population synthesis modelling or simulation of optical data. This relation is then supplemented with an assumption regarding the colour of the object. The stellar masses for this work were calculated using the relation derived by Taylor et al. (2011), shown below as Equation 4.7, using magnitudes from SDSS data release 10, as described in Section 3.1.2.

$$\log \left(\frac{\mathcal{M}_*}{\mathcal{M}_\odot} \right) = 1.15 + 0.7(g - i) - 0.4M_i \quad (4.7)$$

In this form the stellar and solar mass are given by \mathcal{M}_* and \mathcal{M}_\odot , with the absolute magnitude of the object in the i -band being given by M_i . Taylor et al. (2011) assert that this provides a relation accurate to 0.1 dex, i.e. an uncertainty of approximately 26 per cent. An error of 30 per cent is used in subsequent calculations in order to account for uncertainties in this mass modeling process and for inaccuracies in the

optical magnitudes. This error is then added in quadrature to the error on the dust mass to give the total error on the normalised dust mass.

When performed for the 68 galaxies with valid spectral energy distribution fits, these calculations give a range of dust masses of $\log_{10}(M_{dust}) = 5.43 - 7.92$, with a median value of $\log_{10}(M_{dust}) = 6.55$, where M_{dust} is measured in solar masses. The normalised dust mass range of these same sources is found to be between a minimum of $\log_{10}\left(\frac{M_{dust}}{M_{stellar}}\right) = -5.12$ and a maximum of $\log_{10}\left(\frac{M_{dust}}{M_{stellar}}\right) = -2.19$, with a median value of $\log_{10}\left(\frac{M_{dust}}{M_{stellar}}\right) = -3.49$. The dust masses and normalised dust masses will be analysed as a function of environment and other galaxy properties in Chapter 6.

4.6 Concluding remarks

In this chapter the spectral energy distributions of the 70 spectroscopically confirmed Coma cluster galaxies were fitted with a modified black body function. From this, with the addition of stellar masses derived from SDSS observations, the temperatures, total infrared luminosities and normalised dust masses of 68 of these galaxies were determined. These values are presented in Appendix C. In order to gain a greater insight to any trends that may be seen in regards to these parameters and enable an analysis to be completed in terms of gas stripping and galaxy transformation, the galaxies themselves need to be classified into either early or late types. This process will be detailed in Chapter 5.

Chapter 5

Morphological and environmental analysis

Having identified various properties of the 70 Coma cluster galaxies in our sample, it is beneficial to group the galaxies into early- and late-type galaxy groups. In general it is assumed that the far-infrared emission stems from different processes in each of these groups. In late-type (spiral) galaxies it is believed that the process of star formation is taking place, creating many young, hot stars, which heat the surrounding dust, that in turn can be observed in the far-infrared. By contrast, early-type (elliptical) galaxies are believed to be much more passive, with little star formation, and the far-infrared emission is probably dominated by residual heating of the dust by the older stars. These assumptions are generally well established, however there is still doubt as to the amount of star formation that continues to occur in elliptical galaxies. For this reason it is useful to test these assumptions and measure, in both the cluster core and the infall region, the relative fractions of emission stemming from star formation processes and from passively heated dust.

The first requirement of such a test is to be able to reliably classify the detected galaxies as early- or late-types. The classification of a galaxy can be determined either via the identification of the morphology of the galaxy, or the determination of the optical intensity profile across its radius. This chapter will detail how both of these methods

were completed and compared in order to best identify the source of the far-infrared emission in each source.

The research presented in this chapter has made use of the NASA/IPAC Extragalactic Database (NED) which is operated by the Jet Propulsion Laboratory, California Institute of Technology, under contract with the National Aeronautics and Space Administration.

The *XMM-Newton* observations of the Coma cluster were completed and provided by Alexis Finoguenov.

5.1 Galaxy morphological classification

In order to identify the most reliable method of obtaining galaxy morphology information about the identified sources, three types of classification were investigated; classifications from the NASA/IPAC Extragalactic Database (NED), morphology probabilities from the Galaxy Zoo public science catalogue, and the form of the optical light profile. Data from methods were compiled from relevant databases and then compared in order to determine the best morphologies to use for the purposes of dissecting galaxy properties by morphology class.

5.1.1 Hubble T-type classification

The positions of the 70 identified sources were inputted into NED, which provided morphological classifications for 62 sources. The returned morphologies were taken from the de Vaucouleurs system (de Vaucouleurs, 1959), which assigns a galaxy into one of four basic types; ellipticals, lenticulars, spirals and irregulars. It also provides information on the presence of bars, rings or spiral arms within the galaxy. This classification was then converted into a numerical value using a simplified version of the Hubble stage T value. These values range from $T = -6$ to $T = 11$, and allow the morphological classifications to be plotted more easily. The corresponding de Vaucouleurs

and Hubble T-types are shown in Table 5.1.

de Vaucouleurs class	E	S0	S0/a	Sa	Sab	Sb	Sbc	Sc	Sdm	Irr	Pec
Hubble T-type	-5	-2	0	1	2	3	4	6	8	10	11
Number of Sources	12	22	6	6	1	5	2	3	1	3	1

Table 5.1: The de Vaucouleurs and Hubble T-type classifications of the 62 sources for which morphological data are available.

5.1.2 Galaxy Zoo classification

Galaxy Zoo (Lintott et al., 2008) is a public science programme that uses input from many members of the general public to identify the basic morphology of numerous SDSS galaxies. The result is a number of probabilities regarding various physically identified features of the object. Here, just two of these are used; the probability of the object being a spiral galaxy, and the probability of the object being an elliptical galaxy. From this, a singular probability value was calculated by taking the difference between the two probabilities such that a final value of -1 implies that the object is an elliptical, and a value of 1 implies a spiral. For the purposes of this investigation, it is taken that objects with values greater (less) than 0.5 (-0.5) are spirals (ellipticals). Morphological classifications for 66 sources were found in the Galaxy Zoo catalogue, and by using the definition described above there are 25 ellipticals and 21 spirals in the sample, with the remainder having uncertain types.

Figure 5.1 shows two histograms of the Galaxy Zoo morphologies; the values for the spectroscopic parent catalogue, and the values of the confirmed Coma cluster members. This shows that the detection fraction of late-type spirals is highest, which is to be expected as they tend to be the brightest objects. However, the increase in the detection fraction at the extreme elliptical end is more surprising, but again is due to these being the brightest galaxies of this type.

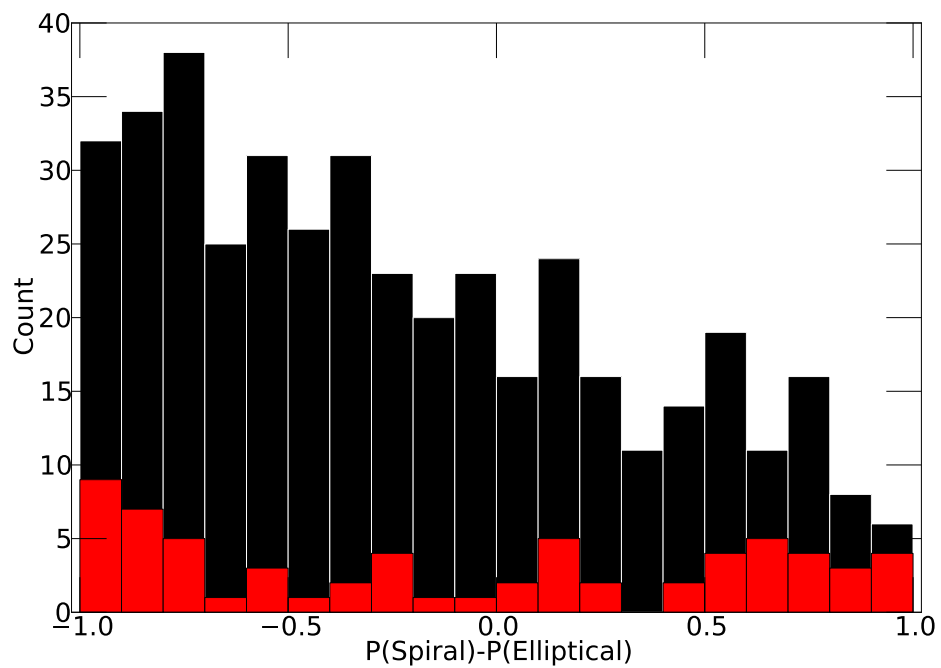


Figure 5.1: A histogram of the Galaxy Zoo determined morphology of the Coma cluster catalogue. The morphology is given as a difference in the probabilities of a given source being identified as a spiral and as an elliptical. The black bars represent the values determined for all the members of the spectroscopic catalogue which had a match to the Galaxy Zoo catalogue. The red bars represent the 66 confirmed Coma cluster members with Galaxy Zoo morphological information.

5.1.3 Sérsic index classification

Sérsic (1963) demonstrated that the intensity of a galaxy can be described as a function of radius, using the form:

$$\ln I(R) = \ln I_0 - kR^{\frac{1}{n}} \quad (5.1)$$

Here, I_0 is the value of the intensity at a radius, R , of zero. The Sérsic index, n , describes the curvature of the profile and takes a value between $0.5 < n < 10$. A value of four gives the de Vaucouleurs profile (de Vaucouleurs, 1948), often taken as best describing giant elliptical galaxies, and a value of one gives an exponential profile that better fits spiral galaxy disks.

The NYU Value-Added Galaxy Catalogue (NYU-VAGC; Blanton et al., 2005) details various parameters derived from imaging and spectroscopy of galaxies within the SDSS DR7 catalogue. Included within this catalogue are Sérsic index values derived for each of the five SDSS bands, as described by Blanton et al. (2005). A positional match between this catalogue and the *Herschel* detected sources finds 68 matches. For the purposes of classification we use the Sérsic index as derived in the r -band, as this band is less affected by dust or star formation than the short wavelength bands.

The values for these 68 sources lie in the range $0.973 < n_r < 5.903$. A study by Shen et al. (2003) found that the boundary between early and late-type galaxies can be defined as being at a Sérsic index of $n = 2.5$. By this definition there are 36 ellipticals and 32 spirals in the sample, with 2 being undefined.

5.1.4 Classification comparison

Comparisons between these differing morphologies are needed in order to ascertain whether they are in agreement, and to determine which is the best definition of morphology to use if there is any significant differences. Figure 5.2 shows the comparison between the classifications based on the galaxy morphology: the T type morphologies

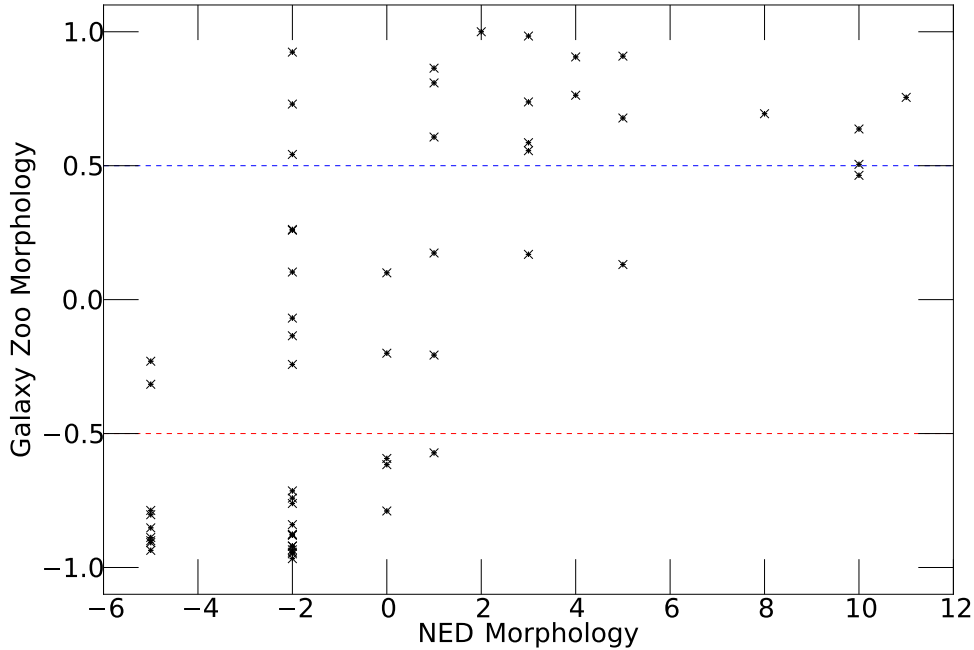


Figure 5.2: A comparison between the T type morphologies taken from NED and the morphological probabilities taken from the Galaxy Zoo catalogue for all Coma cluster members that had identifications present in both methods. The blue (red) dashed line represents the point above (below) which sources are defined as being a spiral (elliptical) according to the Galaxy Zoo criterion defined in subsection 5.1.2.

and the Galaxy Zoo probabilities. There is a general agreement such that there are no Galaxy Zoo identified spirals with a T type less than -2 (S0) and no Galaxy Zoo identified ellipticals with a T type greater than 1 (Sa). From this it possible to create an almost complete list of morphologies for the Coma cluster galaxies by using the T type information to complete the Galaxy Zoo definitions by sorting those without Galaxy Zoo probabilities into spirals and ellipticals. This process leaves only six sources that have no morphology information from either catalogue.

A comparison between the Galaxy Zoo probabilities and the Sérsic index values is shown in Figure 5.3. Of the 68 galaxies for which spectral energy distributions could be fitted, 64 have both Sérsic index values and Galaxy Zoo probabilities. It can be seen that there is good agreement for the Galaxy Zoo defined ellipticals, with the majority of sources having high Sérsic index values. However, there are six Galaxy Zoo defined

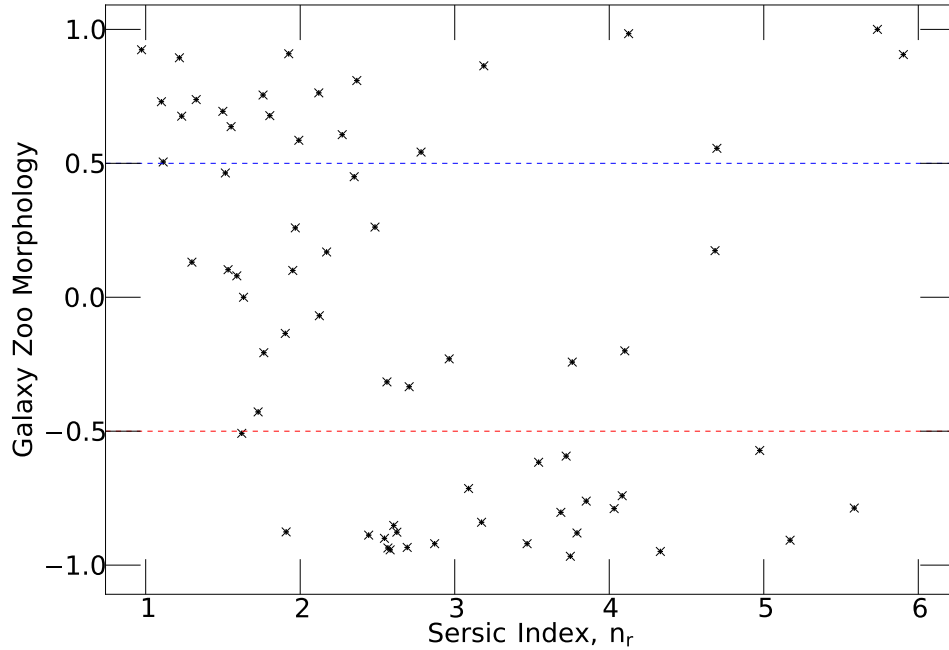


Figure 5.3: A comparison between the Sérsic index values taken from the r -band SDSS image and the morphological probabilities taken from the Galaxy Zoo catalogue for all Coma cluster members that had identifications present in both methods. The blue (red) dashed line represents the point above (below) which sources are defined as being a spiral (elliptical) according to the Galaxy Zoo criterion defined in subsection 5.1.2.

spirals with high Sérsic index values, which would imply they are ellipticals.

In order to determine the source of the discrepancy, images of these six sources were taken from SDSS and the morphology examined by eye: these images are presented in Figure 5.4. Object 14 is deemed to be a lenticular galaxy, and thus the Sérsic index value, implying it is an elliptical, is deemed to be correct in terms of the early- and late-type split. For the other five objects, the galaxies look like spiral galaxies thus implying the Galaxy Zoo morphology is correct. In three of these cases, NED identifies the galaxy as hosting an AGN, which is a plausible explanation for the galaxy having an anomalously higher Sérsic index value. It is therefore feasible that the other galaxies could have similar issues.

The Sérsic index was determined to be the best way to assign the identified galaxies into the two classes of morphology, due to it being a quantified parameter based on

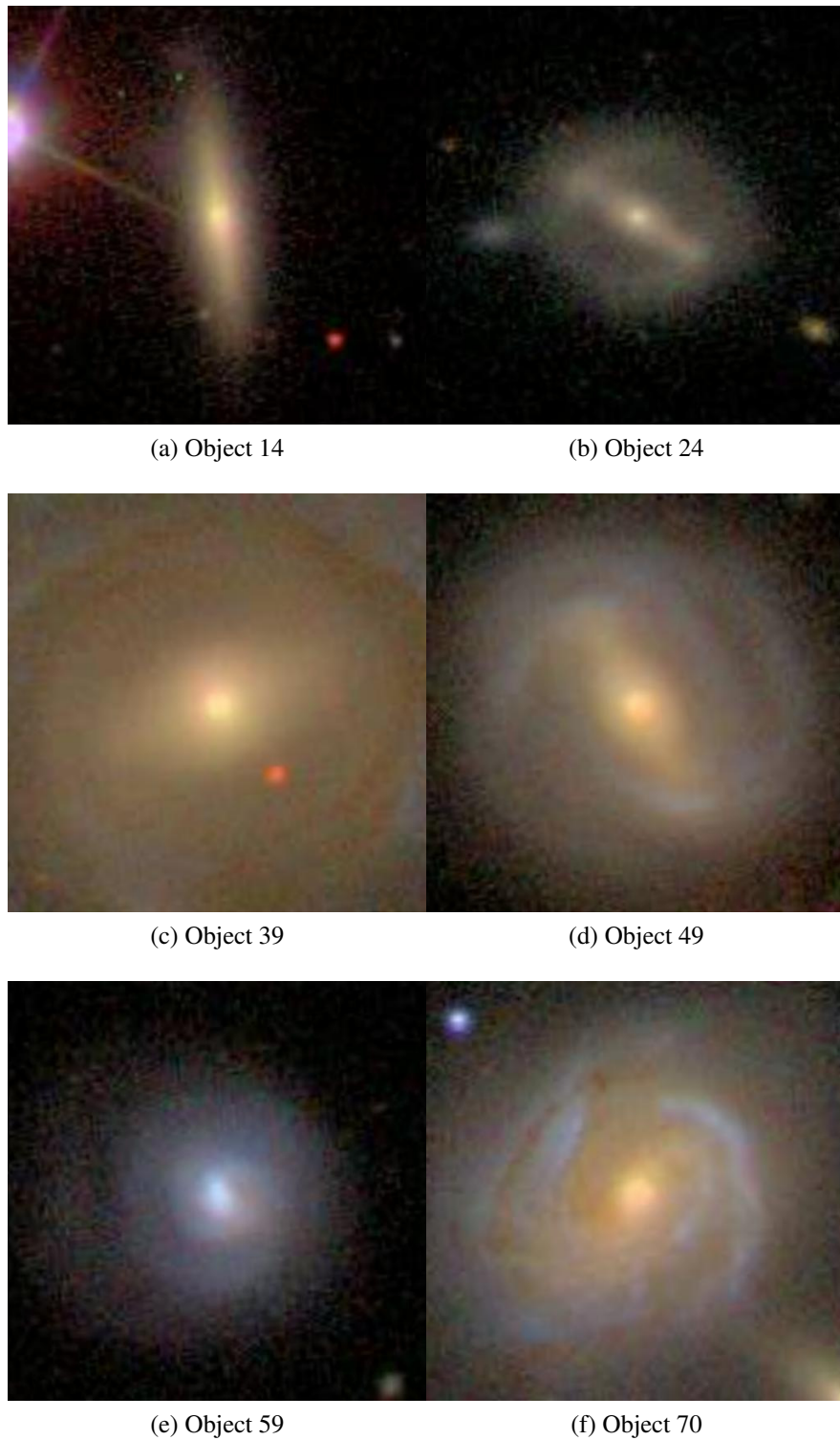


Figure 5.4: SDSS images of the six Coma cluster galaxies with a Galaxy Zoo probability implying a spiral morphology, but with a high Sérsic index value implying an elliptical morphology.

a physical measurement of the galaxy. However, in the six cases where there was a discrepancy with the Galaxy Zoo morphology, a visual inspection was completed to determine the best morphology to use. For the remainder of this work, the galaxy morphologies will be based on this combination of Sérsic index values and Galaxy Zoo probabilities. When this process is applied to the sample of 68 galaxies that have valid spectral energy distribution fits, it defines the sample as consisting of 37 spiral galaxies, 29 elliptical galaxies, and two lacking both a Sérsic index value and a Galaxy Zoo probability, thus making their morphologies unknown.

In order to increase the effectiveness of the data set, the two galaxies which lack both a Sérsic index value and a Galaxy Zoo probability were investigated further so that it could be determined to which morphological group they belong. The Hubble T -type of both objects is given by NED as $T = -5$, thus making them ellipticals. However, a visual inspection of the two objects revealed that whilst one (Object 4) was a clearly elliptical in shape and morphological appearance, the other (Object 28) was too faint for a true conclusion to be reached. Therefore, whilst the final catalogue was updated reflect the elliptical nature of Object 4, Object 28 remains unclassified.

5.2 Comparison with HST/ACS survey

As previously mentioned in subsection 1.5.2, the Coma cluster was observed using the Hubble Space Telescope Advanced Camera for Surveys (HST/ACS). A search of the archival data for this project returns eight images that match with galaxies in the *Herschel* catalogue. Comparisons of the *Herschel* images at all three wavelength bands and the HST/ACS image for these eight objects are presented in Figures 5.5 to 5.12. It should be noted that the HST/ACS images are orientated at an angle rotated relative to the *Herschel* images by approximately 49 degrees clockwise.

One of the objects that is detected with the HST/ACS is a part of the group discussed previously that have contradicting morphologies between the Galaxy Zoo probabilities and the Sérsic index values. A three colour optical image, presented in Figure 5.13,

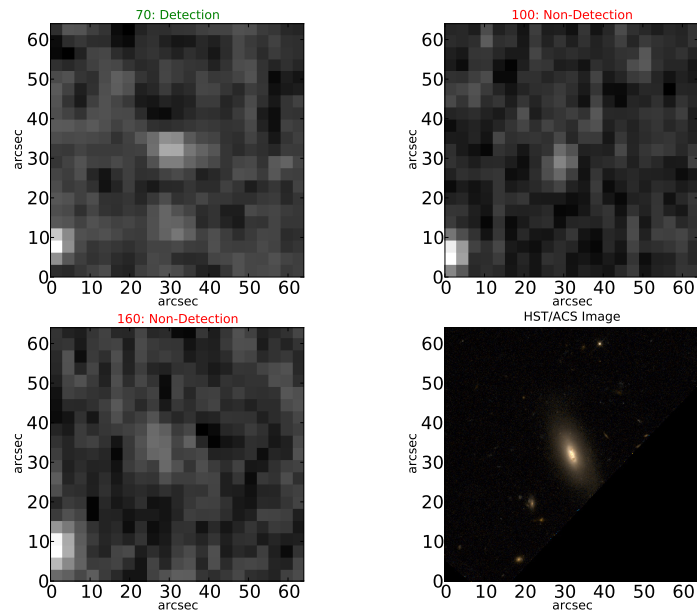


Figure 5.5: Comparison of HST/ACS and *Herschel* images for Object 2: $T = 26.28\text{K}$, $\log_{10} \left(\frac{M_{dust}}{M_{\odot}} \right) = 5.66$

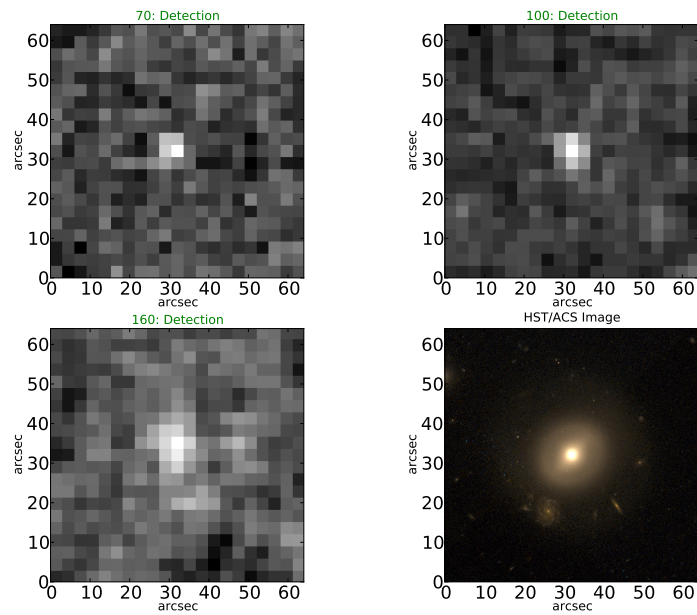


Figure 5.6: Comparison of HST/ACS and *Herschel* images for Object 19: $T = 20.16\text{K}$, $\log_{10} \left(\frac{M_{dust}}{M_{\odot}} \right) = 6.57$

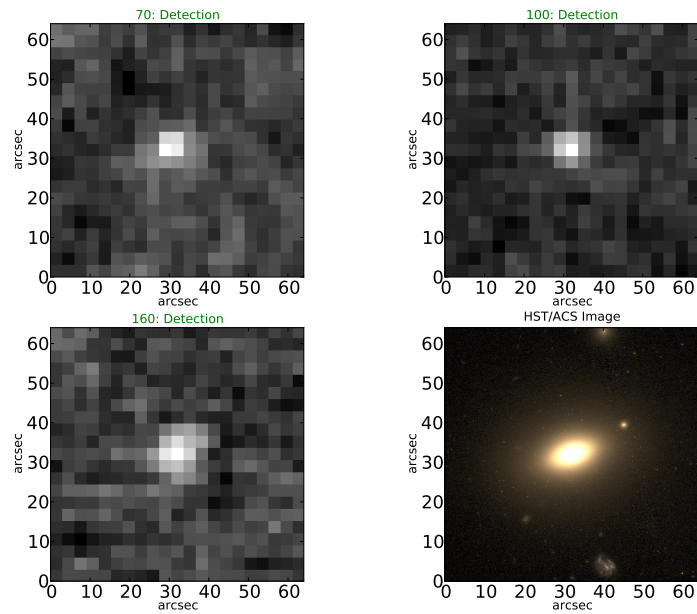


Figure 5.7: Comparison of HST/ACS and *Herschel* images for Object 27: $T = 24.32\text{K}$, $\log_{10}\left(\frac{M_{dust}}{M_{\odot}}\right) = 6.22$

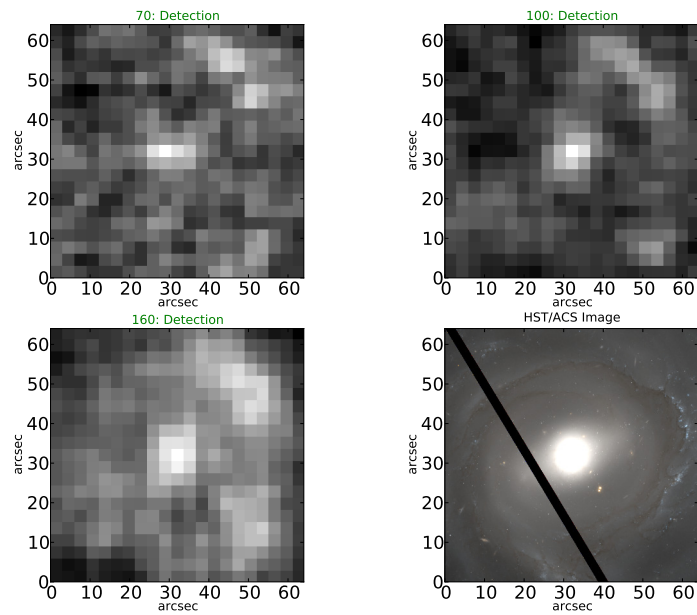


Figure 5.8: Comparison of HST/ACS and *Herschel* images for Object 39: $T = 17.55\text{K}$, $\log_{10}\left(\frac{M_{dust}}{M_{\odot}}\right) = 7.59$

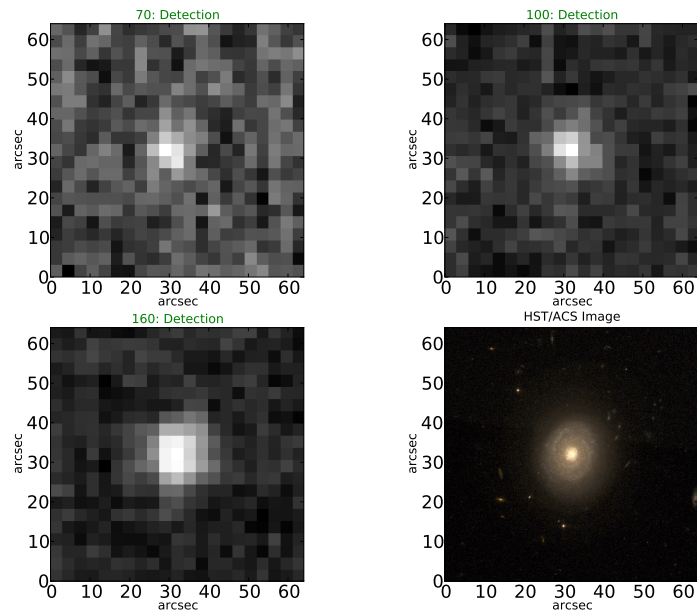


Figure 5.9: Comparison of HST/ACS and *Herschel* images for Object 40: $T = 21.64\text{K}$, $\log_{10} \left(\frac{M_{dust}}{M_{\odot}} \right) = 6.84$

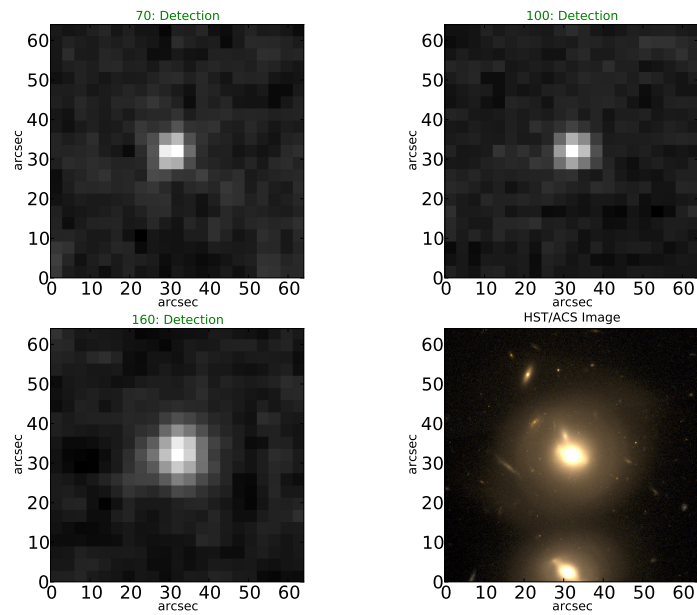


Figure 5.10: Comparison of HST/ACS and *Herschel* images for Object 44: $T = 24.26\text{K}$, $\log_{10} \left(\frac{M_{dust}}{M_{\odot}} \right) = 6.64$

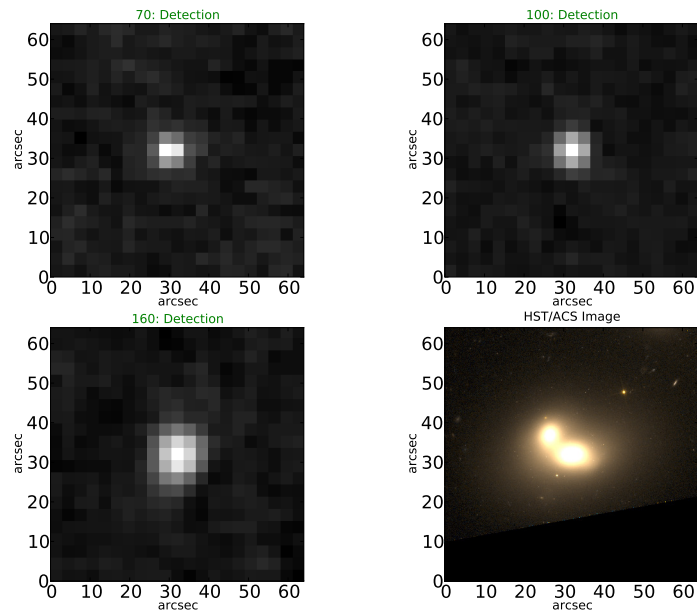


Figure 5.11: Comparison of HST/ACS and *Herschel* images for Object 46: $T = 24.50\text{K}$, $\log_{10} \left(\frac{M_{dust}}{M_{\odot}} \right) = 6.70$

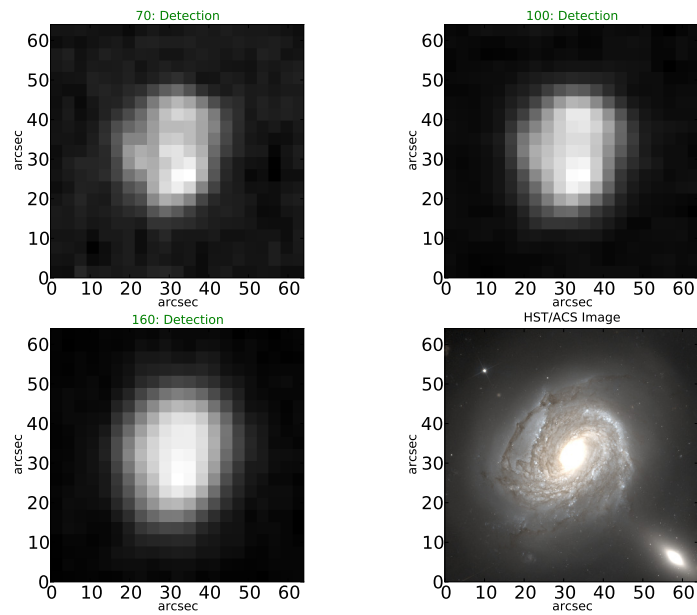


Figure 5.12: Comparison of HST/ACS and *Herschel* images for Object 70: $T = 22.27\text{K}$, $\log_{10} \left(\frac{M_{dust}}{M_{\odot}} \right) = 7.92$

provides further evidence that this galaxy should be defined as a spiral; in agreement with the Galaxy Zoo probability.

5.3 Galaxy morphology by location

Having determined the morphologies of most of the galaxies within the sample, it is advantageous to know if there is a trend between morphological type and location with the cluster environment. Figure 5.14 shows the location of all the 68 galaxies with valid spectral energy distributions, with different marker styles to identify the spiral, elliptical and unknown galaxies as per the Sérsic index and Galaxy Zoo classifications described in subsection 5.1.3.

As was previously mentioned in Section 2.1, the observational area of this study covered the core of the Coma cluster, as well as a region of infalling galaxies to the south west. If the local cluster environment has a strong effect on the evolution of a galaxy, it would be reasonable to assume that the morphological types present in these two regions would depend on the differing processes that would occur. This can be clearly seen in Figure 5.14, as the infall region mostly consists of spiral galaxies, with the core region being dominated by the elliptical galaxies.

5.4 Galaxy luminosity functions by morphology

In Section 3.2 the galaxy luminosity function was derived for each of the three wavelength bands observed by PACS presented in Figure 3.2. Now that the morphological type of each of the galaxies has been established, it is possible to redetermine these luminosity functions, but with the galaxies split into the two groupings; ellipticals and spirals. Spiral galaxies tend to be larger and brighter than elliptical galaxies when observed in the far-infrared, and as such one would expect them to dominate the function at the bright end, with their numbers decreasing as the luminosity decreases, whilst the inverse occurs to the number of ellipticals.

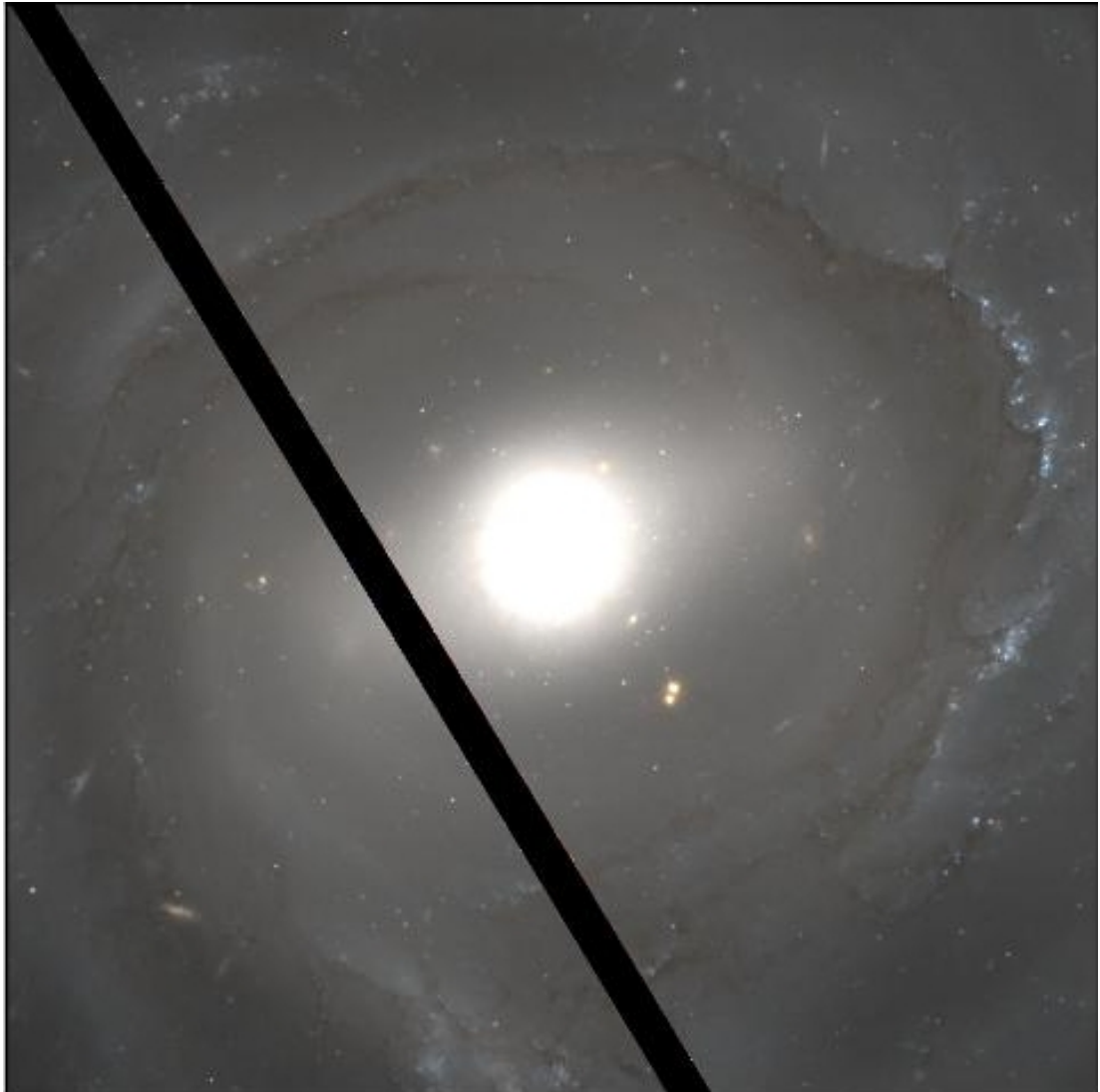


Figure 5.13: A three-colour image of NGC 4921 (Object 39) taken with the HST/ACS, clearly showing that it should be defined as a spiral galaxy.

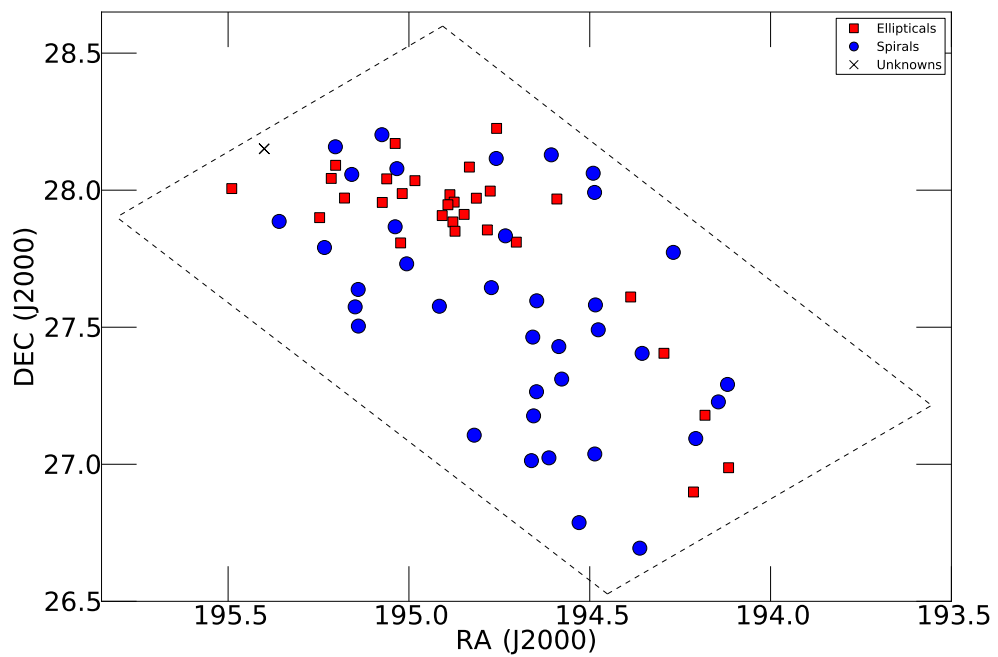


Figure 5.14: Locations of the 68 Coma cluster members with valid spectral energy distributions, with the points differentiated according to their final morphologies determined as explained in subsection 5.1.4. Ellipticals, spirals and unknown galaxies are designated by red squares, blue circles and black crosses respectively. The black dashed line shows the limit of the area observed by the PACS instrument for this study.

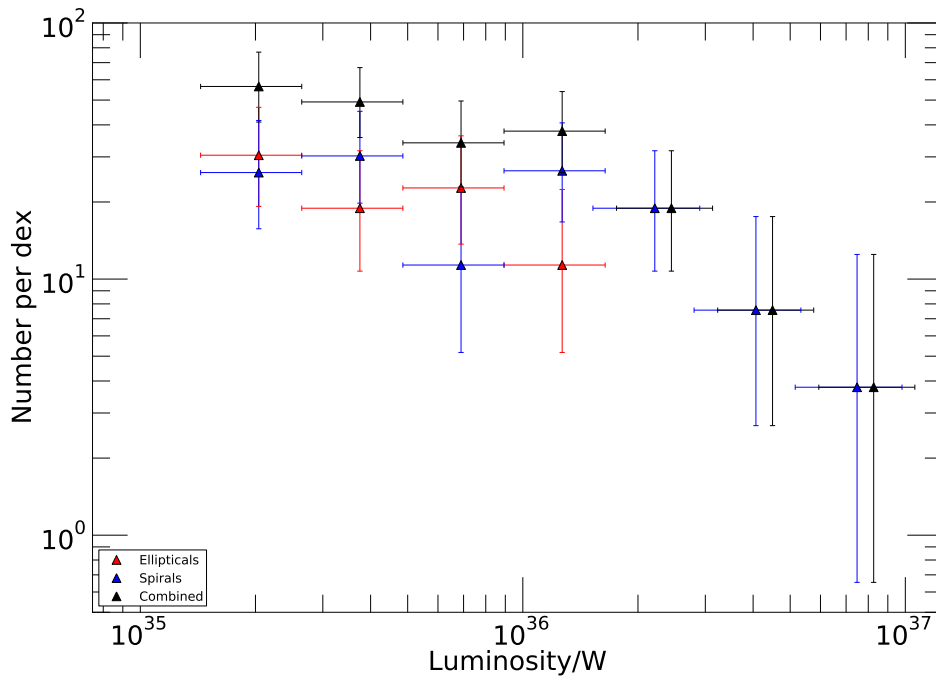


Figure 5.15: Galaxy Luminosity Function at $70\ \mu\text{m}$, split by morphology. Where the luminosity bin for the combined total consists of just one morphological type, a small arbitrary offset in luminosity is applied for clarity.

These new galaxy luminosity functions are presented in Figures 5.15, 5.16, 5.17. The function for the $100\ \mu\text{m}$ wavelength map shows evidence of the low luminosity end being dominated by the ellipticals; this trend is not seen as strongly in the 70 and $160\ \mu\text{m}$ wavelength maps. The brighter luminosity end is dominated by the spirals in all three wavelengths.

5.5 Non-detection analysis

There will be a number of sources within each map that were not detected during the source extraction process as their individual flux density will be less than the five sigma detection limit. If these objects were stacked and the flux densities summed together then the total flux density may be greater than the detection limit, which would imply the presence of other sources which have low-level emission.

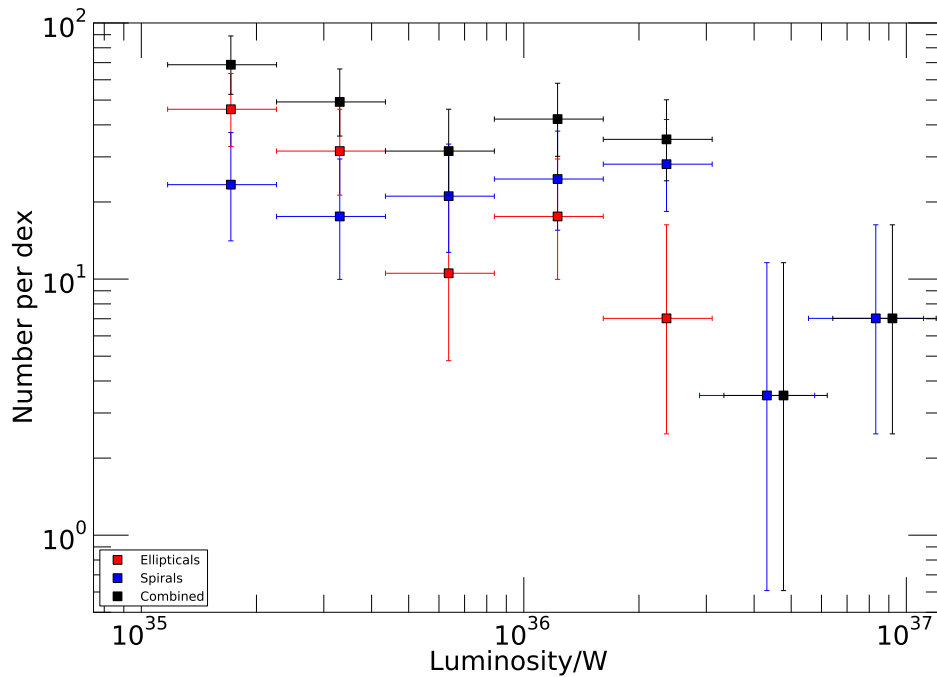


Figure 5.16: Galaxy Luminosity Function at $100\ \mu\text{m}$, split by morphology. Where the luminosity bin for the combined total consists of just one morphological type, a small arbitrary offset in luminosity is applied for clarity.

An analysis was completed using the parent catalogue that was constructed in subsection 3.1.1, to see if it is possible to find a detection at the remainder of the parent catalogue positions through a process of stacking cut-outs of the map at those positions. This was completed for four different subsets of undetected objects: all those in the parent catalogue (673 objects), those with Sérsic index information (400 objects), those classified as elliptical objects (163 objects), and those classified as spiral objects (237 objects). The four stacked images are shown in Figure 5.18, and it can be clearly seen that there is no clear detection in any of these subsets. This was confirmed via the use of an aperture measurement that showed no significant flux above the noise levels.

This result seems unusual in that one would expect there to be a number of sources that are below the five sigma detection threshold, but that still have a significant enough flux that when stacked they can be seen. Figure 5.19 shows the sigma detection of each of the sources identified by the SExtraction process (as described in subsection 2.3.1) in the $100\ \mu\text{m}$ map. It can be seen that the number of sources peaks at around five sigma.

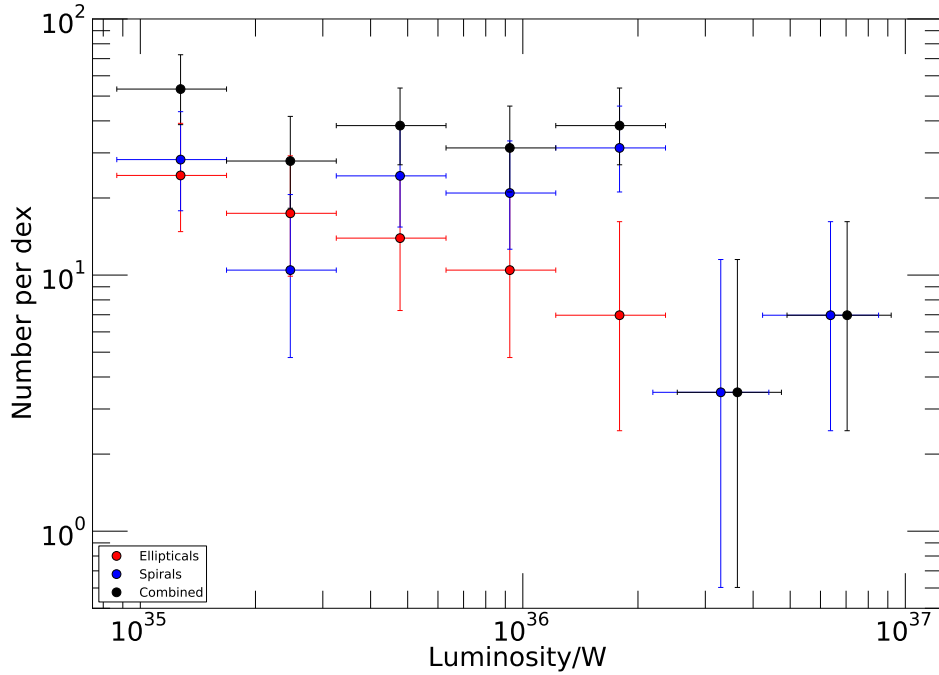


Figure 5.17: Galaxy Luminosity Function at $160\ \mu\text{m}$, split by morphology. Where the luminosity bin for the combined total consists of just one morphological type, a small arbitrary offset in luminosity is applied for clarity.

The steady decline for values higher than this is understandable, as there are greater numbers of dim objects than there are bright objects. However, the turnover at around three to four sigma is due to an effect of the map production process. As described in subsection 2.2.4, the production of the final map involves a high pass filtering process to remove the $1/f$ noise, which would have the side effect of removing flux from the centre of the source if it has not been masked. This mask is made automatically by the pipeline, and will act on any pixel with a value over three sigma, relative to all the non-zero pixels in the map. Given the nature of this mask making process, combined with the source extraction criteria of needing a minimum number of contiguous pixels, it is likely that this turnover is a result of these fainter sources not having been masked during the production of the map, and thus their flux has been reduced by the high pass filter process to a level where they are not detected.

This effect will not affect the identified Coma cluster sources, as their flux is sufficiently high as to assure that the mask was applied to them during the map production,

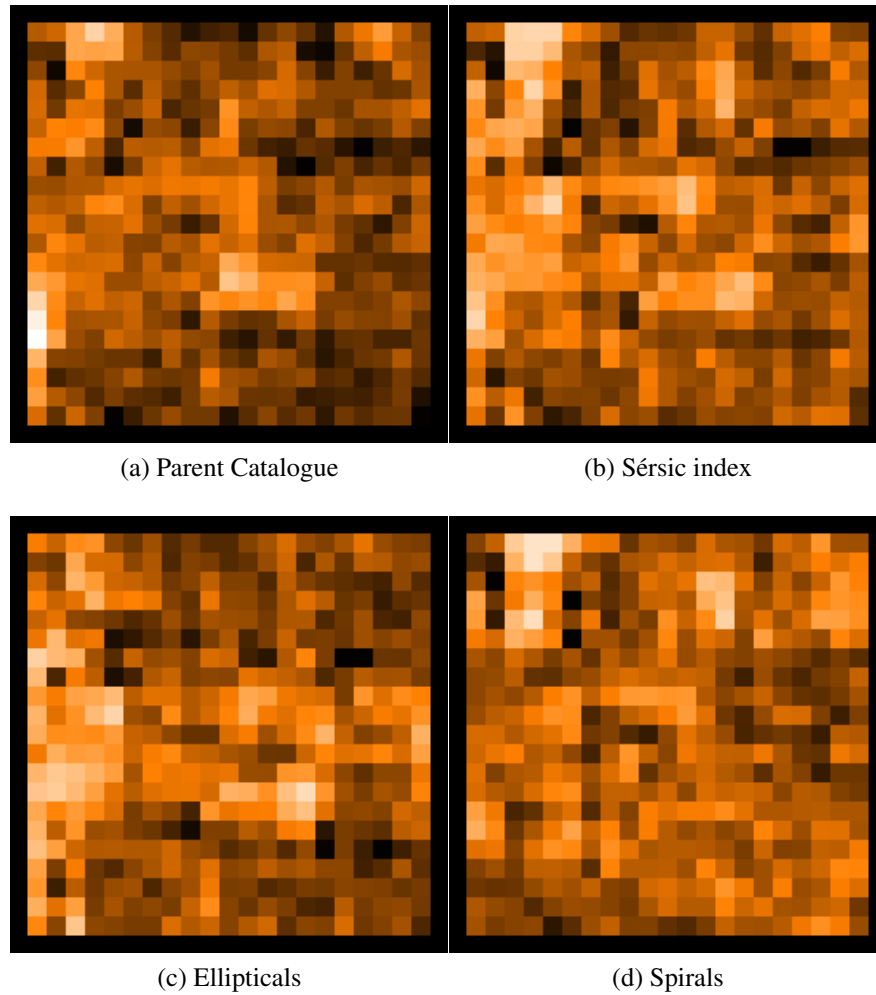


Figure 5.18: Four images showing the results of a stacking analysis of the 100 μm map at the known locations of different subsets of galaxies: all those in the parent catalogue, those with Sérsic index information, those classified as elliptical objects, and those classified as spiral objects. In all four cases the images show no significant increase in flux indicative of a detection of the combined flux of those objects.

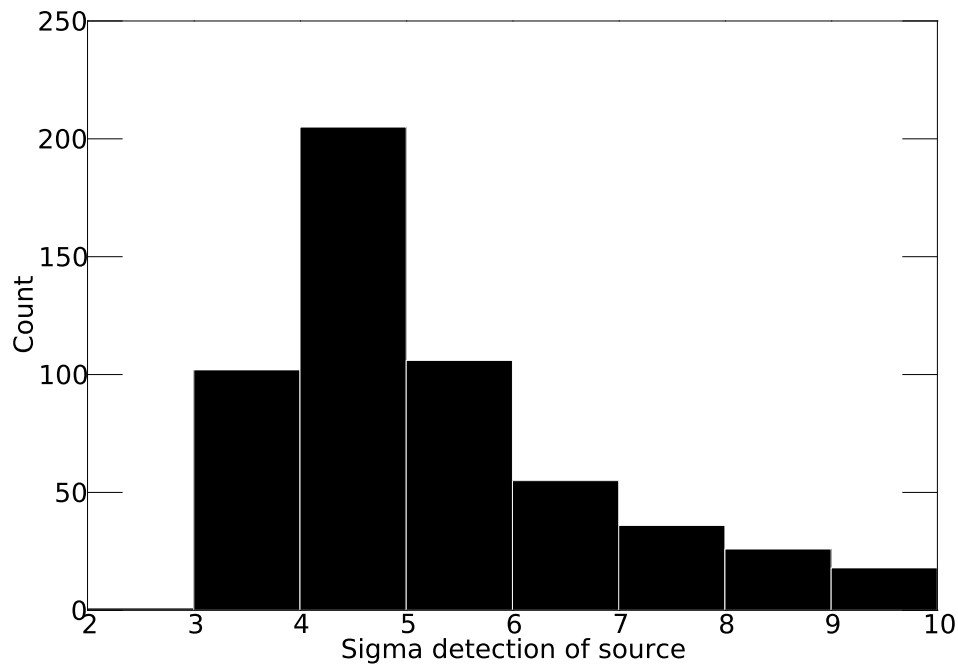


Figure 5.19: Histogram of the number of SExtractor identified sources in the 100 μm map, grouped by sigma detection level.

but it does provide a reasonable explanation for the lack of sources present in the non-detection stacking analysis.

Additionally, an analysis was made of the fraction of sources that were detected by *Herschel* compared to the parent catalogue, with sources categorised by both morphological type and location within the cluster. The results are presented in Table 5.2. It can be seen that the detection fraction in the core of the cluster is approximately the same as seen with the cluster as a whole, though the fraction of spirals detected is slightly lower. In the infall region however, the spirals have a slightly greater detection fraction when compared to the total. However, due to the low numbers involved in these statistics these differences are marginal when the errors are taken in to account.

Region	Ellipticals (Parent)	Ellipticals (<i>Herschel</i>)	Spirals (Parent)	Spirals (<i>Herschel</i>)
Total cluster	194	30 ($15.5^{+3.3}_{-2.8}\%$)	272	37 ($13.6^{+2.6}_{-2.2}\%$)
Core	156	25 ($16.0^{+3.8}_{-3.1}\%$)	175	18 ($10.3^{+3.0}_{-2.4}\%$)
Infall	38	5 ($13.2^{+8.9}_{-5.7}\%$)	97	19 ($19.6^{+5.6}_{-4.5}\%$)

Table 5.2: The detection fraction of early- and late-type galaxies split by Coma cluster location.

5.6 Comparison with the X-ray environment

Another component of a galaxy cluster is the intracluster medium. This is present in the cluster centre and consists mainly of ionized hydrogen and helium, and contains most of the baryonic material in the cluster. This material is important in regards to studies of the galaxy cluster environment, as it is the medium responsible for the ram-pressure stripping process. This material can be seen via its high level emission in X-ray bands.

5.6.1 Comparison with X-ray observations

X-ray observations of the Coma cluster area over a range of 0.8 – 2keV were taken using the *XMM-Newton Observatory* (Jansen et al., 2001) as part of the EPIC/PN observations (Briel et al., 2001), with the resulting map being provided for this study by Alexis Finoguenov. These observations cover the core and the infall area out to the limits of the X-ray emission. Figure 5.20 shows a contour map of the X-ray emission, with the locations of the detected *Herschel* sources marked as well. The core of the Coma cluster can be seen to have a high level of diffuse X-ray emission, with a number of peaks of emission surrounding the core. The infall region also has an area of diffuse X-ray emission, however compared to the core it is not as extensive nor is it as intense

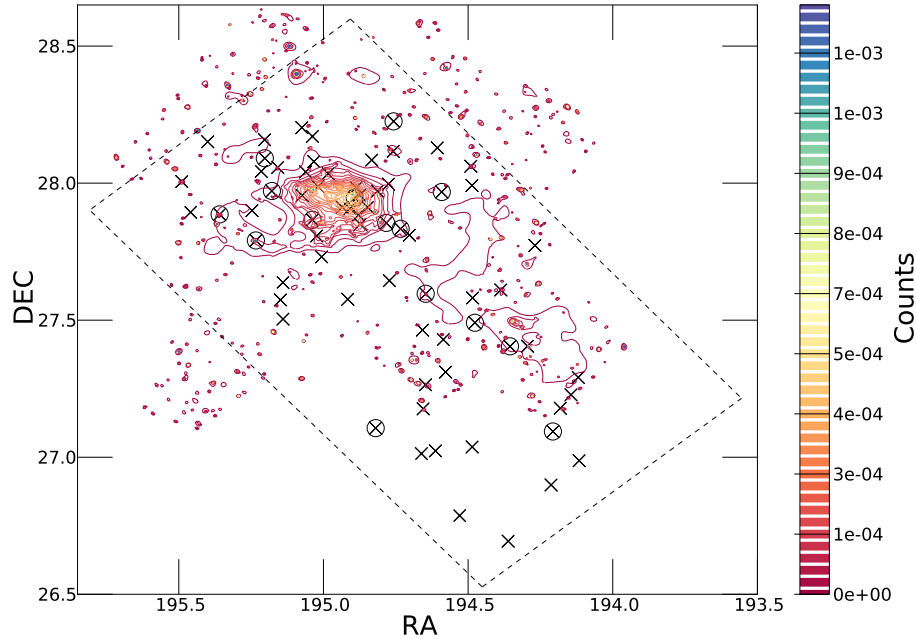


Figure 5.20: This contour map details the X-ray emission in the region of the Coma cluster as observed by *XMM-Newton* over a range of $0.8 - 2\text{keV}$. The locations of the *Herschel* detected galaxies are marked by black crosses, with those that have been identified as AGN being surrounded by a black circle.

in value. There are a number of the *Herschel* detected sources that have been identified via NED as being AGN, and it can be seen in Figure 5.20 that some, but not all, of these correspond to areas of peaked X-ray emission.

It is useful to identify which sources lie within areas of high X-ray emission due to the galaxy containing a source of X-ray emission, and which are surrounded by the intracluster medium. This difference was determined by placing an annulus around the galaxy position and measuring the sky background. If X-ray emission at a given position is due to the presence of an X-ray source in the galaxy, such as an AGN, then the surrounding background sky value will be low. However, if the X-ray emission is due to the intracluster medium, then the background sky will also be high.

Mahajan et al. (2010) compared $24\ \mu\text{m}$ *Spitzer* to the *XMM-Newton* EPIC/PN observations, and noted that there were virtually no star-forming galaxies in the core of the Coma cluster where the diffuse X-ray emission peaks. They state that this observation

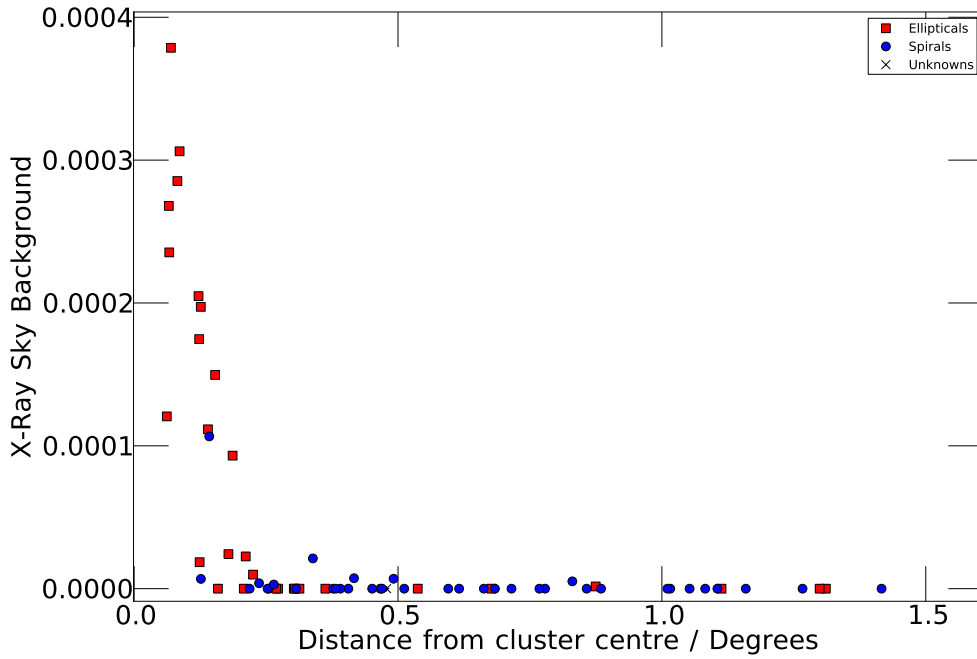


Figure 5.21: X-ray sky background as a function of radial distance.

supports the idea that the properties of a galaxy are affected by the changes in environment that occur on the outskirts of the cluster. Figure 5.21 shows the X-ray background value as a function of radial distance, and shows the location of the *Herschel* detected sources. When combined with the galaxy locations by morphological type presented in Figure 5.14, it is clear that elliptical galaxies make up the majority of the *Herschel* detected sources that are present in the area surrounded by the diffuse X-ray emission of the cluster core. This would seem to support the idea put forward by Mahajan et al. (2010) regarding the effect of environment on cluster galaxy properties.

The X-ray sky background was also plotted against the normalised dust mass, as shown in Figure 5.22, and shows two groupings of sources. The first, and largest, group are those with a low X-ray background flux, i.e. X-ray background counts $< 5 \times 10^{-5}$. These sources have a large range of normalised dust masses, with a mean value of $\log_{10} \left(\frac{M_{dust}}{M_{stellar}} \right) = -2.85$, and a median value of $\log_{10} \left(\frac{M_{dust}}{M_{stellar}} \right) = -3.14$. In comparison those sources with a higher X-ray sky background (X-ray background counts $> 5 \times 10^{-5}$) have a lower mean of $\log_{10} \left(\frac{M_{dust}}{M_{stellar}} \right) = -4.06$ and median of

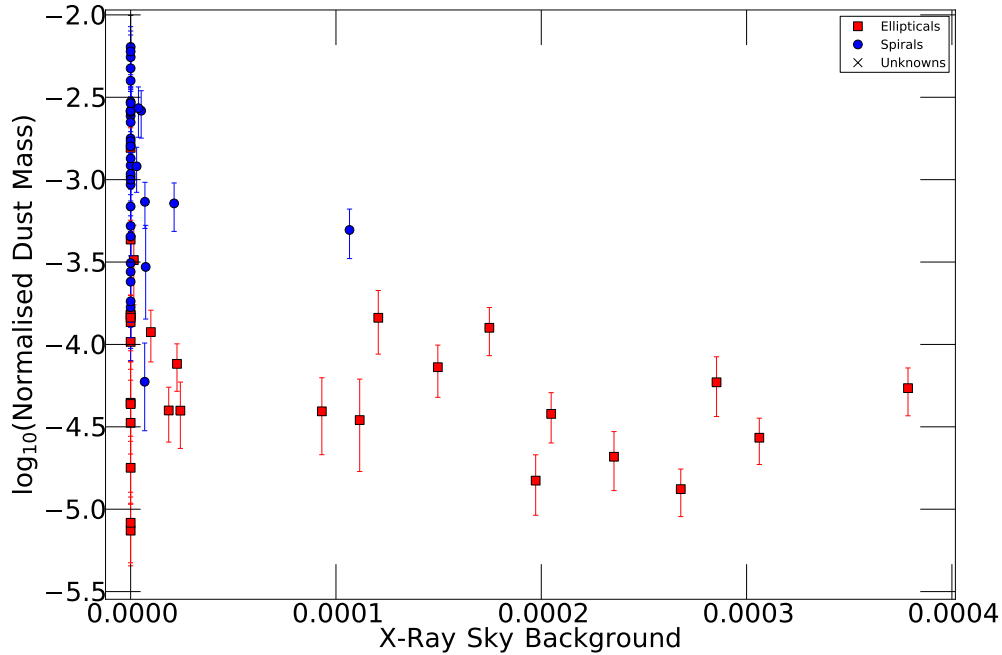


Figure 5.22: Normalised dust mass as a function of the X-ray sky background, subset by morphology.

$\log_{10} \left(\frac{M_{dust}}{M_{stellar}} \right) = -4.41$, taken from a much smaller range of normalised mass.

These numbers show that those galaxies that are in an area of high gas density have a lower normalised dust mass, which one would expect as a result of ram-pressure stripping processes, though there is a great deal of scatter on the data. More surprisingly, it can be seen that there is no trend within the group with X-ray background counts $> 5 \times 10^{-5}$ with the Spearman's rank correlation coefficient of this group being determined as $\rho = -0.412$. This is despite the fact that as the density of the gas increases, any dust stripping processes should be more pronounced and thus should lead to the normalised dust mass decreasing.

5.6.2 Comparison with X-ray surface brightness profile

Using the method described above there are a number of sources for which the measured X-ray flux is zero. In order to increase the dynamic range of the X-ray mea-

surements a X-ray surface brightness profile can be utilised. Simionescu et al. (2013) presented results from *Suzaku* observations of the Coma cluster, and constructed several X-ray surface brightness profiles along various azimuths from the cluster centre. A polynomial fit was applied to the data presented in Figure 3 of Simionescu et al. (2013), thus providing a relation between a normalised measure of the X-ray surface brightness, S_{X-ray} measured in counts, and the distance of the object from the X-ray centre of the cluster, r measured in arcminutes. The relation takes the form:

$$S_{X-ray} = 36.520 \times r^{-1.969} \quad (5.2)$$

From this relation it is possible to estimate the X-ray surface brightness at the location of every *Herschel* detected source, and compare the measured counts with the normalised dust masses, as shown in Figure 5.23. Once again two distinct populations can be seen, more so in normalised dust mass. In order to quantify this difference, a two dimensional Kolmogorov-Smirnov test was completed between the two morphological groups. This test assesses whether the distributions of two populations differ, but utilises two variables for each population as opposed to the single variable utilised in the standard test. It was found that the results of the 2-D tests were as expected when compared to the results obtained with the standard test. The 2-D Kolmogorov-Smirnov test returned a result of $D = 0.8126$ and $P = 5.28 \times 10^{-8}$.

The split in the X-ray measurement is less pronounced, with more of an overlap between the two. However, there is a clear trend, with galaxies with a lower normalised dust mass residing nearer to the high gas density core of the cluster. Within each morphological group there is no evidence of any trend, with Spearman's rank correlation coefficients of $\rho_E = -0.357$ and $\rho_S = -0.183$, despite the fact that one would expect dust stripping processes to be more efficient as the density of the gas increases.

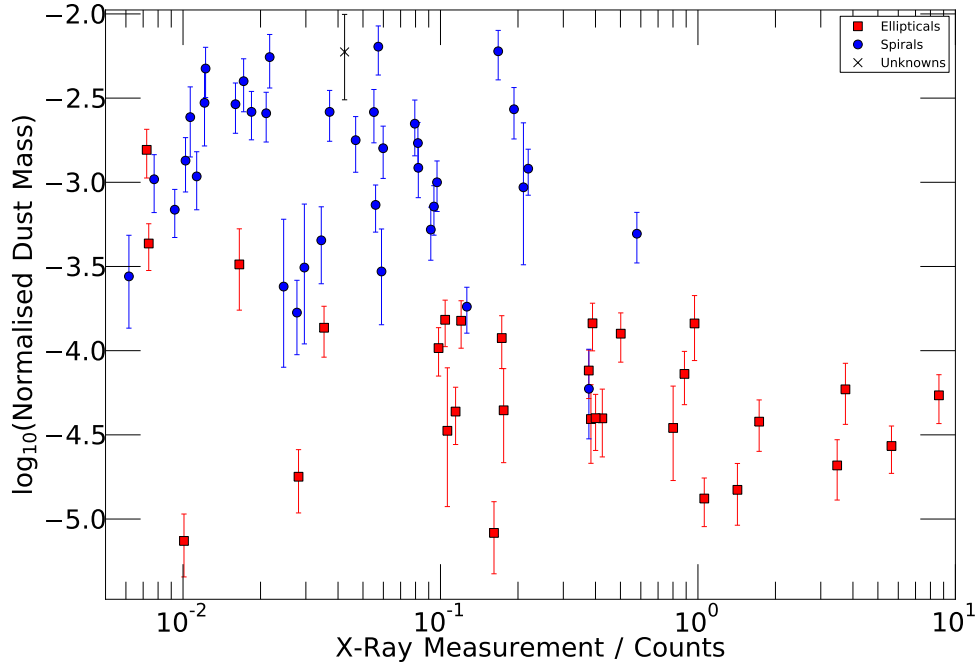


Figure 5.23: Normalised dust mass as a function of the X-ray surface brightness derived from a fitted power-law profile, subset by morphology.

5.7 Comparison with UV observations

The ultraviolet radiation emitted from a galaxy can be used a direct tracer of the star formation processes that are taking place within it. Smith et al. (2010) used the Galaxy Evolution Explorer (*GALEX*; Bianchi & *GALEX* Team 1999), to examine those galaxies within the Coma cluster whose ultraviolet emission suggested that ram-pressure stripping process were currently taking place. Viable sources were required to have a Hectospec spectroscopic redshift within the Coma cluster range, a ultraviolet measured colour below the limit of $\text{NUV-}i < 4$, and to be visually identified as having evidence of stripping processes occurring. These criteria result in 13 sources within their sample, of which 11 exist within the observational area of this *Herschel* study. A positional match of these 11 sources shows that seven are within the *Herschel* detected catalogue, and all are clearly identified as spiral galaxies as per the criteria stipulated in subsection 5.1.4.

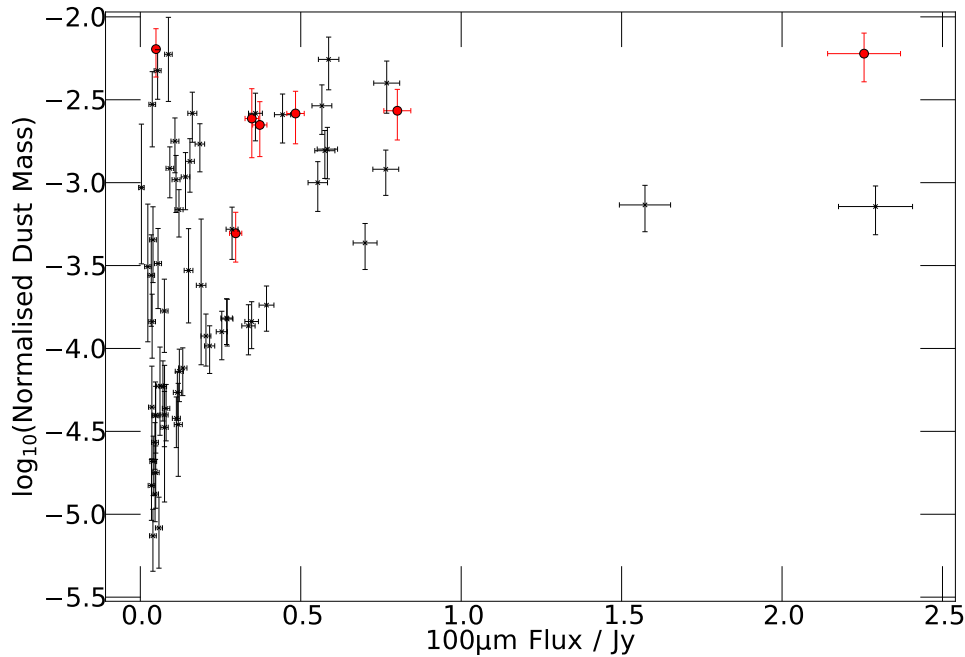


Figure 5.24: Normalised dust mass as a function of $100\ \mu\text{m}$ flux, with the seven sources that match with the UV observations denoted as red circles.

Figure 5.24 presents an examination of the $100\ \mu\text{m}$ flux of these seven sources, and shows that they are some of the brightest sources in the *Herschel* catalogue. One source stands out as having a much lower $100\ \mu\text{m}$ flux, however, it has a NUV-*i* colour of 1.20 mag which is near to the lower limit of the *GALEX* sample. This source also has a magnitude which lies close to the Hectospec detection limit used for both this *Herschel* study and the UV observations. This would seem to suggest that the lack of other detections with low infrared emission is due to limitations in ultraviolet observations and possibly the visual inspection criteria that were applied.

The far-infrared emission stemming from the dust in these galaxies could be as a result of one of two heating sources: the star formation processes that were induced by the stripping process, or from the shock wave produced by the stripping mechanism itself. Figure 5.25 shows the normalised dust masses as a function of the dust temperatures, and it can be seen that whilst the sources have high normalised dust masses, their temperatures are around average for the sample and show no clear indication of their

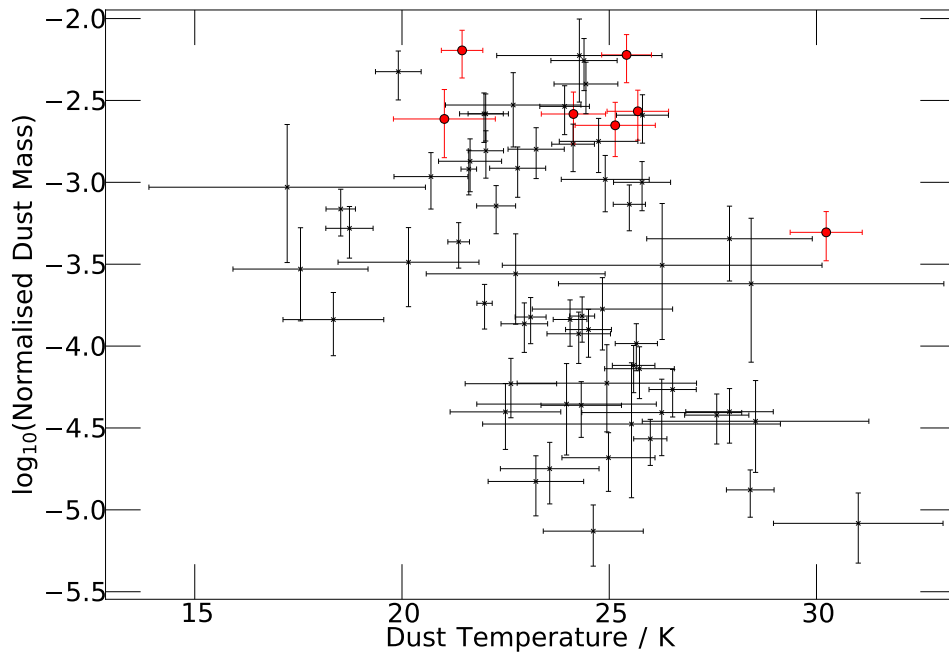


Figure 5.25: Normalised dust mass as a function of dust temperature, with the seven sources that match with the UV observations denoted as red circles.

stemming from a different source. The source with the slightly higher dust temperature when compared to the rest of the ultraviolet sources is the only one of the *Herschel* sources that lies in an area of high x-ray emission (X-ray background counts $> 5 \times 10^{-5}$), as can be seen in Figure 5.22 where it is the only spiral galaxy (denoted by the blue circle) in this region.

5.8 Comparison with CO observations

The molecular gas content of a galaxy can be traced through observations of the CO emission lines. Studies of the CO emission of galaxies in the Coma cluster were completed by Boselli et al. (1997), Lavezzi et al. (1999) and Casoli et al. (1996), which produced line velocities for the J(0-1) excitation as well as estimations of the mass the H_2 gas present in each galaxy. Figure 5.26 shows the CO derived H_2 mass as a function of the far-infrared derived dust masses for the eleven objects present in both

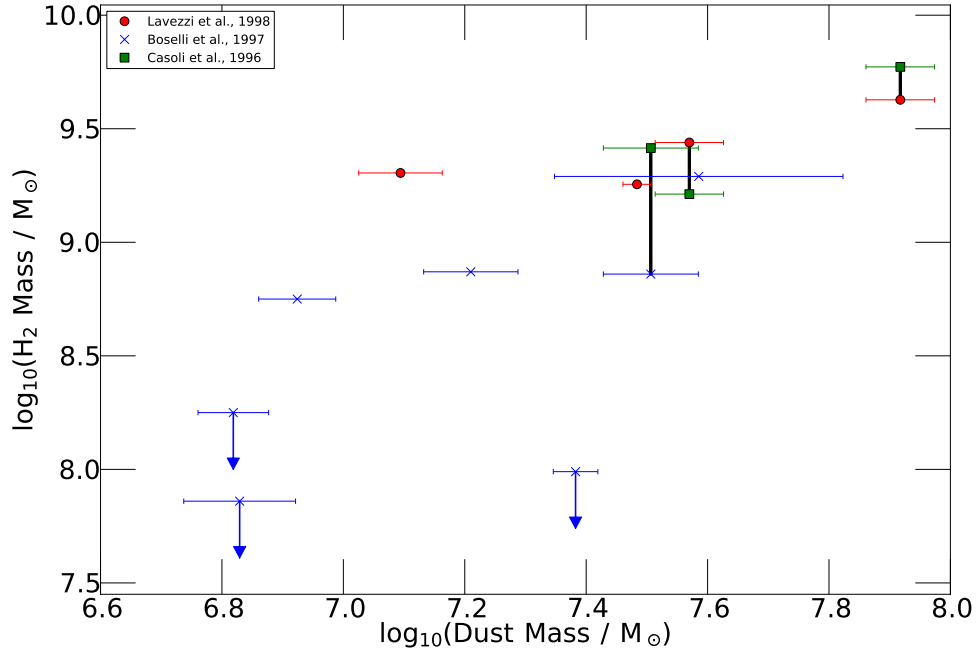


Figure 5.26: CO derived H₂ mass as a function of the far-infrared derived dust mass. The black lines join points representing the same *Herschel* detected source, but with differing H₂ masses taken from two literature sources. The arrows denote that the H₂ masses are upper limits, as described by Boselli et al. (1997).

this *Herschel* study and at least one of the CO studies. The data show a clear trend of increasing gas mass mass with respect to the dust mass, which would simply imply that the most massive galaxies are massive in all respects. It can be seen that three of the points are defined as upper limits on the H₂ mass, as described by Boselli et al. (1997). One of these points appears to have a low gas mass with respect to the derived dust mass, which is well defined as can be seen from the error bars.

5.9 Concluding remarks

In this chapter the morphologies and surrounding environment have been determined for the identified Coma cluster members, by supplementing the *Herschel* data with optical, ultraviolet and X-ray observations.

By combining morphological probabilities from the Galaxy Zoo project with Sérsic indices taken from SDSS observations, it was found that the sample of 68 Coma cluster galaxies with valid spectral energy distribution fits consists of 37 late-type spirals, 30 early-type ellipticals and one with an unknown morphology.

The possibility of drawing further data from the maps through a source stacking process was investigated, however there was no clear evidence of any low level emission being present. This lack of dim galaxies was deemed to be due to the high pass filter process during the initial map production.

The sample was then compared to X-ray observations of the cluster core and infall region, with the aim of identifying any trends within the sample with respect to the intergalactic medium. It was found that the sources with high level of X-ray emission surrounding them, are located in the centre of the cluster and have lower normalised dust masses relative to the those with low levels of surrounding emission.

When compared with ultraviolet observations of Coma cluster galaxies currently thought to be undergoing the process of ram pressure stripping, it was found that of the eleven UV observed sources within the observational area of this *Herschel* study, seven were detected in the far-infrared. A comparison was also made with observations of the CO J(0-1) emission for ten objects, and found a positive correlation between the dust mass and the molecular gas mass within the galaxy.

Chapter 6 will combine the morphological information that has been determined for the Coma cluster galaxies with the physical properties that were calculated in Chapter 4 in an attempt to ascertain if there are any trends or correlations present within the sample.

Chapter 6

Analysis of galaxy properties

There are two main sources of the far-infrared emission that is detected with *Herschel*: the dust thermalisation and re-radiation of energy from high mass stars or from dust that is heated by the older stellar population. The established theory states that of these two sources of emission, the former is found in late-type spiral galaxies, and the latter in the early-type elliptical galaxies. These two morphological types are subject to differing levels of star formation based on the amount of dust and gas that is present within a galaxy of each type. As the observed far-infrared wavelengths principally traces the dust within a galaxy, an analysis of the physical properties of these two groups could provide insight on the impact of the cluster environment on a given galaxy and the processes that occur within it.

Chapters 4 detailed how the total infrared luminosity, dust mass and dust temperature were determined for the detected Coma cluster galaxies. Chapter 5 determined the morphological type of each galaxy based on a combination of the Sérsic indices and the Galaxy Zoo probabilities. This chapter will combine this information and go through each of the physical parameters and isolate any trends within them by grouping the galaxies by morphological type. Any difference between the trends for early- and late-type galaxies could further the present understanding of the relationship between galaxies and their surrounding environment.

6.1 Comparisons of Coma cluster galaxy properties

6.1.1 Dust and stellar masses of the Coma cluster galaxies

The total mass of a galaxy contains both a stellar mass and a dust mass component, the ratios of which will differ for early- and late-type galaxies. Any differences between the trends of the two morphological types would give an indication of the effect of the environmental processes present in the cluster that drive the evolution of the galaxies from early- to late-type. Figure 6.1 presents a comparison of these two mass components for the sample, but subset by morphological type.

This plot clearly exhibits signs of bimodality within the sample, though the two trends do seem to reach a convergence point at a value of around $\log_{10} \left(\frac{M_{\text{stellar}}}{M_{\odot}} \right) = 11.0$, and $\log_{10} \left(\frac{M_{\text{dust}}}{M_{\odot}} \right) = 7.5$. The upper trend consists mostly of elliptical galaxies, whilst the lower trend contains the majority of the spirals; the implication being that ellipticals tend to have a higher stellar mass for a given dust mass. The ellipticals that have been detected cover a large range in dust mass, but have a near constant stellar mass, with no real correlation as such. Conversely, the spirals show a near one-to-one correlation. This would seem to replicate the ‘star formation main sequence’ that had previously been observed in the infrared by Elbaz et al. (2011).

When the sample is grouped by morphological type the 2-D Kolmogorov-Smirnov test returns $D = 0.8523$ and $P = 6.81 \times 10^{-9}$, thus confirming that there is a highly significant difference between the two populations.

Figure 6.2 shows the same relations, however this time the identified objects have been subset by location within the cluster. A clear split can be seen here also, however this separation is not as clearly defined as with the morphological trends. The elliptical sequence is dominated by core galaxies, whereas most of the infall galaxies are in the spiral sequence, though there are still some core galaxies present in this trend. The average stellar mass of objects in the core is high, as the values are dominated by the clump of objects in the elliptical trend. When the sample is grouped in this way, the 2-D Kolmogorov-Smirnov test returns $D = 0.5189$ and $P = 0.009$, showing that whilst

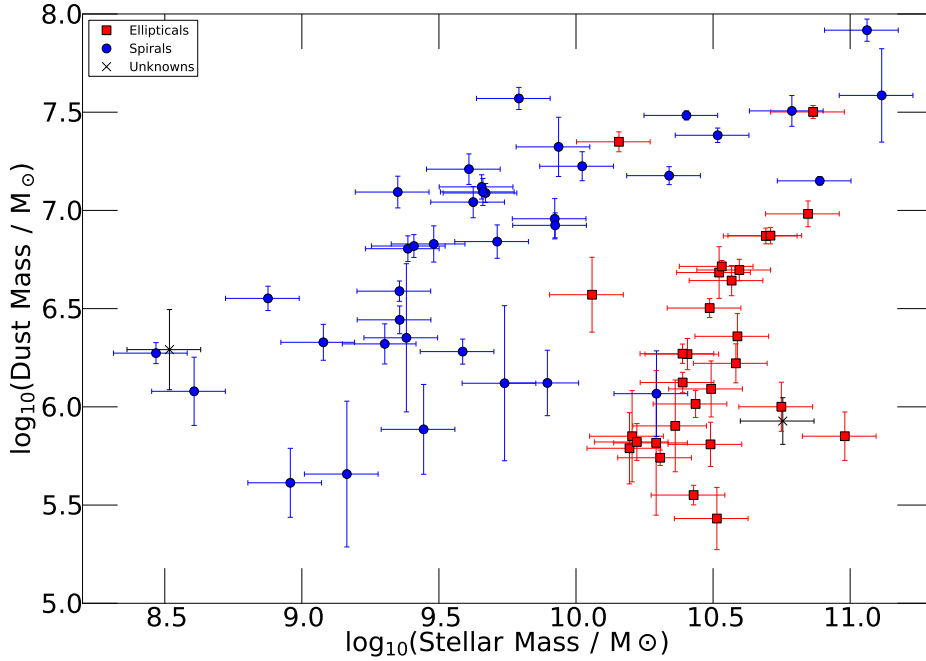


Figure 6.1: Dust mass as a function of stellar mass, subset by galaxy morphology.

the sample still shows a clear difference between the two populations, the difference is not as strong as when the sample is grouped by morphological type.

One way to test this assumption that the upper trend consists of star-forming galaxies is to ascertain the location of those galaxies that were deemed as having molecular gas by CO observations, as identified in Section 5.8. Given that molecular gas is the fuel for star formation processes, one would expect all eleven of the CO identified galaxies to be spirals and to lie in the upper trend. Figure 6.3 highlights the eleven sources and shows that all of them do lie in this upper trend, and thus provides evidence that this group consists of star-forming galaxies.

Additionally, it was shown in Section 5.7 that seven of the galaxies within the *Herschel* sample are detected via UV observations (Smith et al., 2010). The sources in this UV catalogue were selected as they have been identified as currently undergoing ram pressure stripping processes. This would suggest that they should also be host to star formation processes, and thus provide a further test of the nature of the bimodality trend seen with *Herschel*. The seven galaxies are all identified as being late-types,

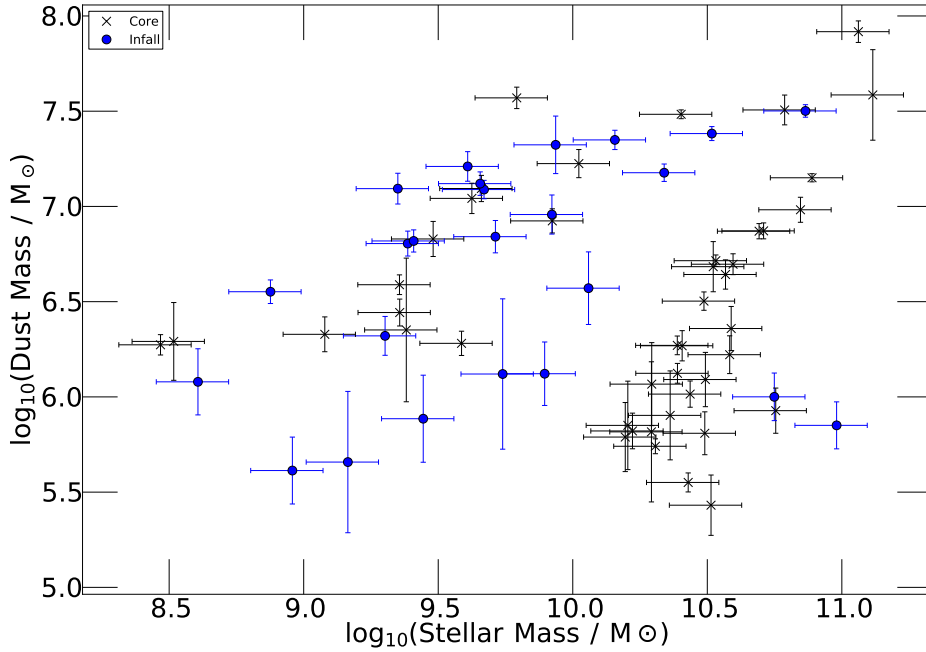


Figure 6.2: Dust mass as a function of stellar mass, subset by the location of the galaxy within the cluster (core or infall region).

and lie in the upper trend, further indicating that this trend is made up of star-forming galaxies.

Figure 6.4 depicts the normalised dust mass as a function of stellar mass, and shows the bimodal trend a little more clearly. It can be seen that the ellipticals have a low normalised dust mass and a high stellar mass, whilst the spirals have a high normalised dust mass which stays approximately constant over a large stellar mass range.

The statistical properties of the normalised dust masses are presented in Table 6.1. As there are signs of bimodality in the sample, a Kolmogorov-Smirnov test of the two morphological types was completed on the normalised dust masses. This test returned values of $D = 0.8695$ and $P = 0.0$, confirming that these are two separate populations.

To judge the role of environment in regards to the mass fractions of the detected galaxies, it is useful to compare the sample with a field sample. In this case the sample used consists of the objects detected within the observational area, but with spectroscopic redshifts that places them outside of the Coma cluster. The dust masses of these

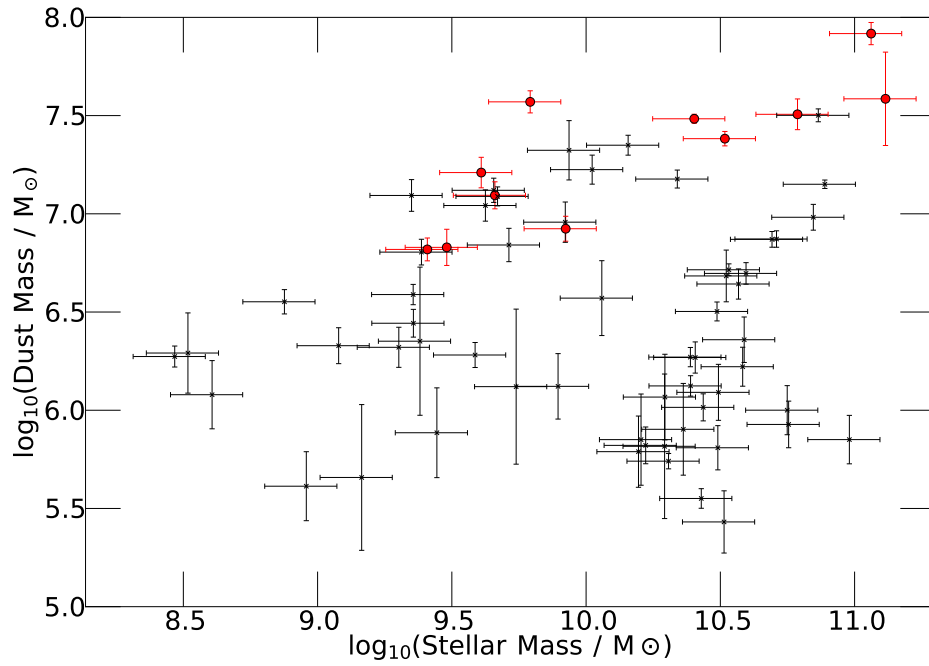


Figure 6.3: Dust mass as a function of stellar mass, with the eleven sources that match with the CO observations denoted as red circles.

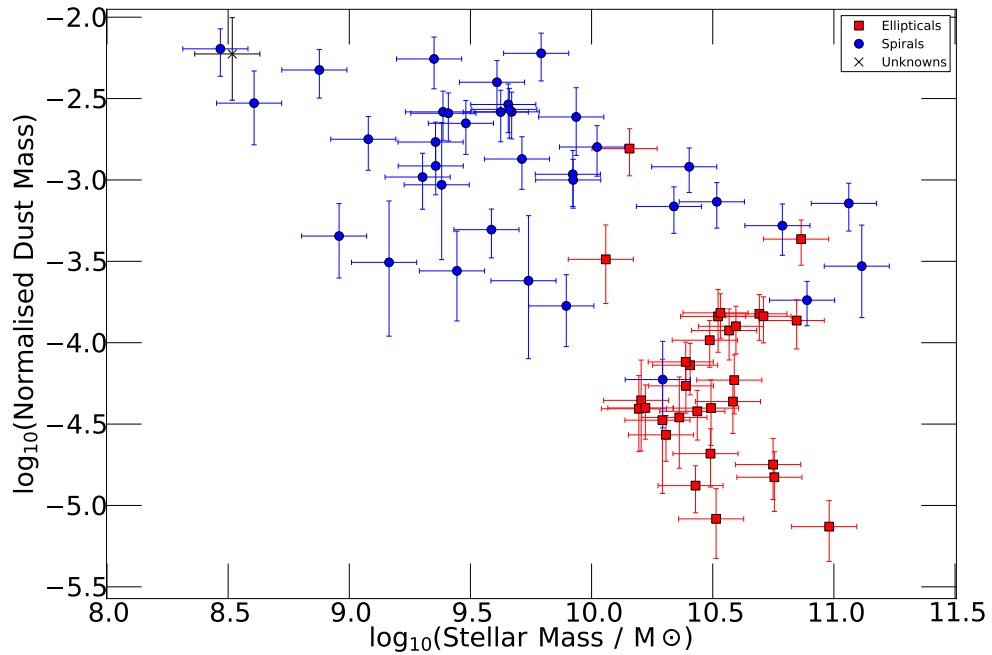


Figure 6.4: Normalised dust mass as a function of stellar mass, subset by galaxy morphology.

Group	Mean	Standard Deviation	Standard Error	Median
Spiral	-2.94	0.48	0.08	-2.91
Elliptical	-4.19	0.50	0.09	-4.27

Table 6.1: The statistical properties of the two morphological populations in regards to the normalised dust mass, $\log_{10} \left(\frac{M_{dust}}{M_{stellar}} \right)$.

objects are estimated by substituting the measured $100 \mu\text{m}$ flux and the mean dust temperature of the cluster sample into a rearrangement of Equation 4.4 to determine A , as given below:

$$A = S_{\lambda} \lambda^{3+\beta} \left[\exp \left(\frac{14404.5}{\lambda_{\mu\text{m}} T_{dust}} \right) - 1 \right] \quad (6.1)$$

This value can then be substituted into Equation 4.6 in order to return the dust mass estimate. The reliability of this method was tested by using it to derive dust masses for the known Coma members detected in the $100 \mu\text{m}$ map, and comparing the estimate to the derived values, as shown in Figure 6.5. It can be seen that the estimated dust masses are in agreement with the derived dust masses, as can further be seen with the Spearman's rank correlation coefficient for the sample, $\rho = 0.8495$.

Figure 6.6 shows a comparison of the dust masses of those objects within the *Herschel* detected Coma cluster catalogue and the estimated dust masses for the field galaxy sample. It can be seen that the dust masses of the field galaxies peak at a much higher value than those of the Coma cluster galaxies. Figure 6.7 shows the same samples but this time plotting their normalised dust masses, with the stellar masses of the field galaxies having been determined using the same method described in Section 4.5. Once again it can be seen that the peak of the field galaxy population lies at a greater value than the Coma cluster population. This would suggest that the surrounding environment of a galaxy has a definite effect on the physical properties of the galaxy.

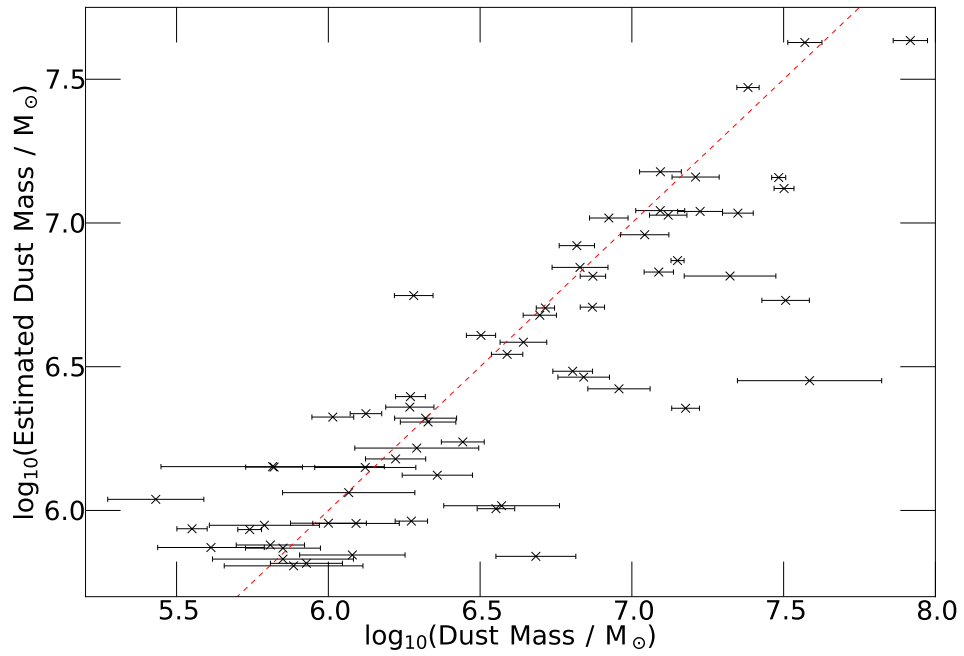


Figure 6.5: Comparison of the derived and estimated dust masses for detected Coma cluster members. The red dashed line shows a one-to-one correlation for comparison.

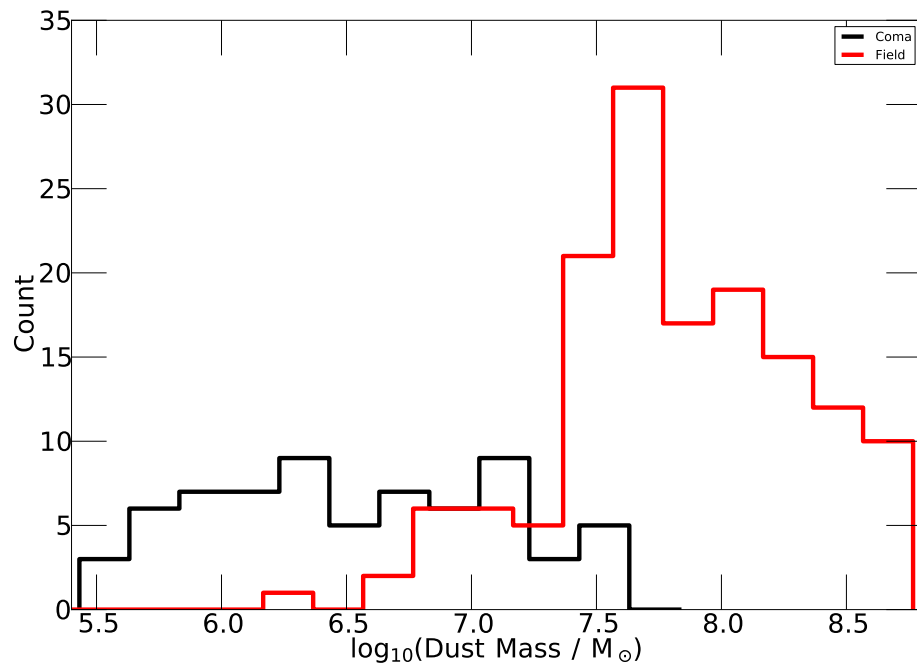


Figure 6.6: Histogram of the dust masses for the field galaxy and Coma cluster populations.

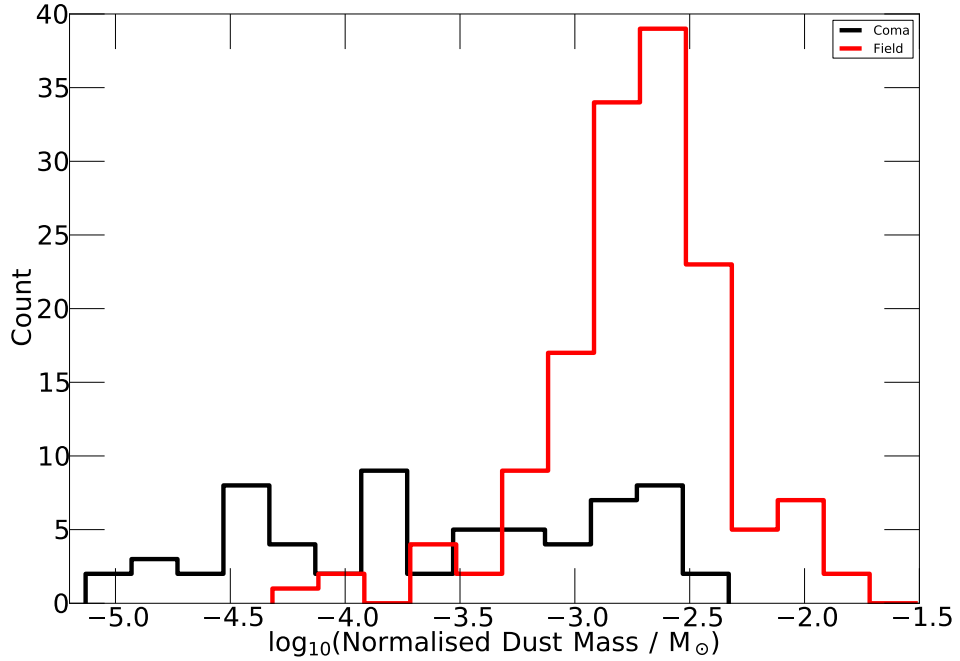


Figure 6.7: Histogram of the normalised dust masses for the field galaxy and Coma cluster populations.

6.1.2 Dust temperature of Coma cluster galaxies

Having found two separate populations within our galaxies in regards to their normalised dust mass, it is useful to determine if this bimodality is seen in any other galaxy properties. The first property that will be analysed is the dust temperature of the galaxies.

If the normalised dust mass is plotted with respect to temperature, as shown in Figure 6.8, the population split in normalised dust mass can be seen, however no such population difference appears to be present in terms of the dust temperature.

However, if one examines the statistical properties presented in Table 6.2 then a slight difference, greater than the standard error, can be seen between the temperature of the morphological types. A Kolmogorov-Smirnov test of the two populations returns $D = 0.2526$ and $P = 0.215$, and thus shows that there is only a marginal difference between the two populations.

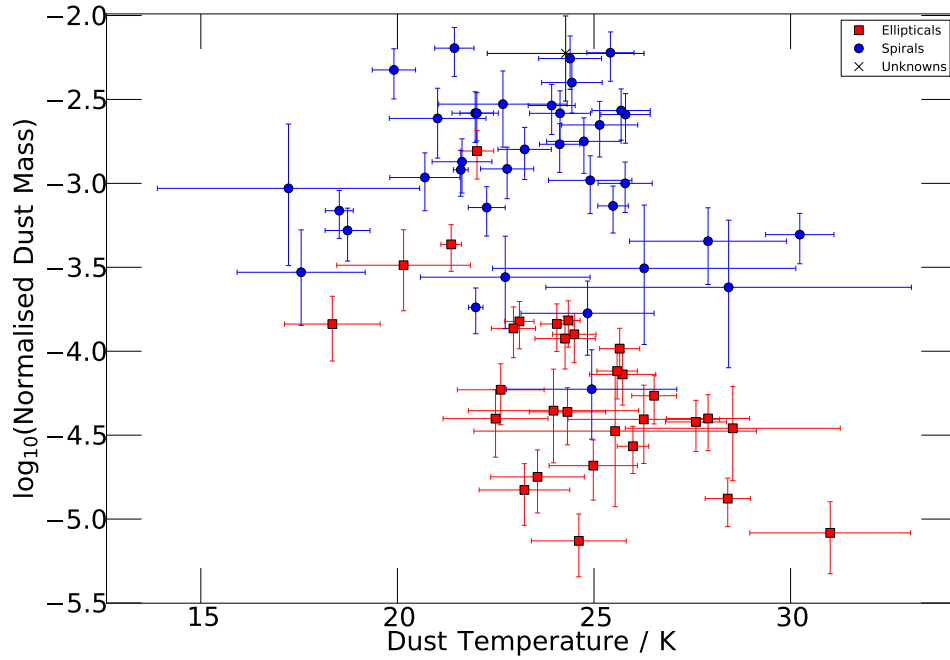


Figure 6.8: Normalised dust mass as a function of dust temperature, subset by galaxy morphology.

Group	Mean	Standard Deviation	Standard Error	Median
Spiral	23.37	2.86	0.47	23.92
Elliptical	24.70	2.59	0.48	24.50

Table 6.2: The statistical properties of the two morphological populations in regards to the derived dust temperatures, T , measured in Kelvin.

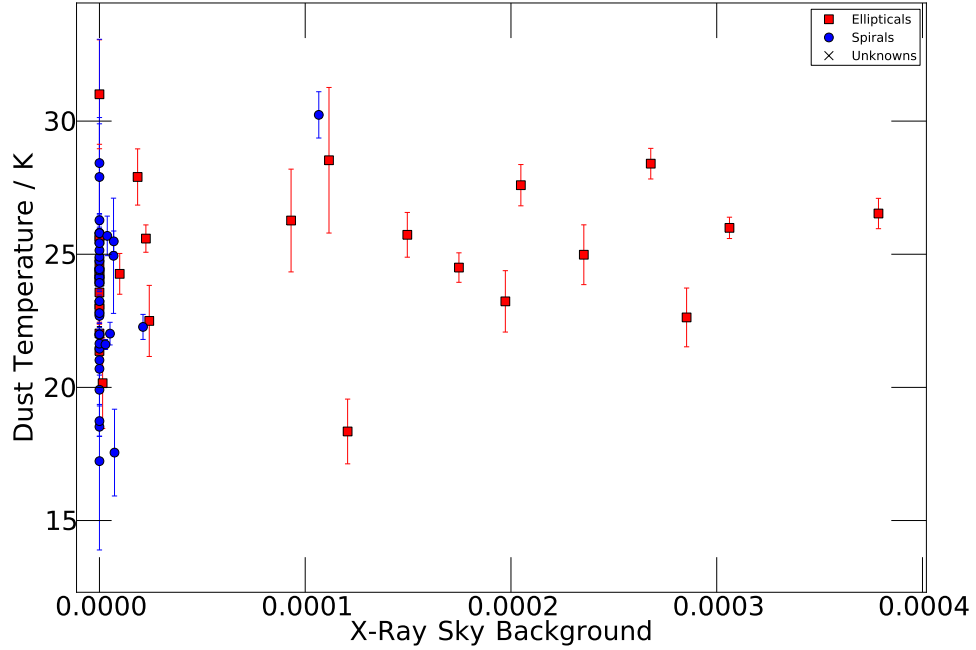


Figure 6.9: Dust temperature as a function of the X-ray sky background, subset by morphology.

One possible explanation for the higher dust temperature in the elliptical galaxies is that this dust could be heated by the surrounding X-ray emitting gas. However, no correlation between the X-ray background counts and the dust temperatures can be seen, as shown in Figure 6.9, which argues against this explanation. The Spearman's rank correlation coefficients of the two morphological groups are $\rho_E = 0.305$ and $\rho_S = 0.080$.

This lack of correlation is still evident when the X-ray surface brightness measurements are utilised for comparison against the dust temperature, with Spearman's rank correlation coefficients of $\rho_E = 0.379$ and $\rho_S = 0.177$.

Alternatively, it may be that the emission from the detected early-type galaxies is due to recently created dust from AGB stars. There are currently no published predictions for the far-infrared properties that would result from this mechanism, but the models of Cassarà et al. (2013) peak in the mid-infrared range, and thus it is plausible that the emission resulting from AGB stars leads to a higher dust temperature than that seen from star forming regions. However, only the youngest populations with the highest

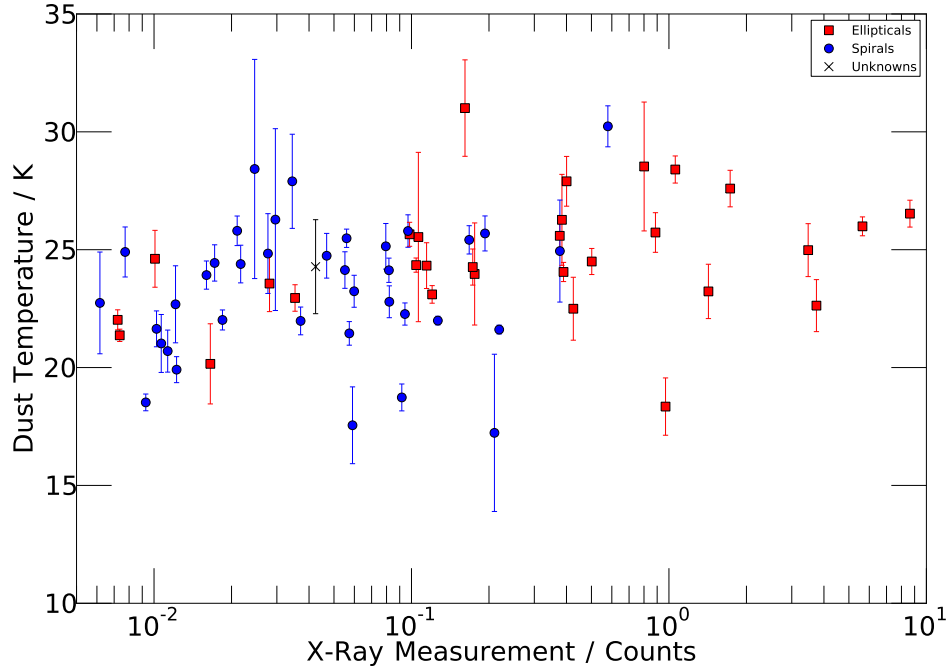


Figure 6.10: Dust temperature as a function of the X-ray surface brightness derived from a fitted power-law profile, subset by morphology.

metallicities modelled by Cassarà et al. (2013) produce any significant emission at the wavelengths of interest to this thesis. This may account for the non-detection of the optically brightest elliptical galaxies in the Coma cluster.

6.1.3 Total infrared luminosity of Coma cluster galaxies

The total infrared luminosity of a galaxy is determined by integrating the spectral energy distribution for a given galaxy over a wavelength range of 8-1000 μm .

Figure 6.11 shows the relation between the normalised dust mass and the total infrared luminosities of the objects within the sample. It can be clearly seen that there is a much larger range present in the normalised dust mass for the lower values of the total infrared luminosity. If there were objects present to increase the normalised dust mass range at the high luminosity end, these objects would have to be very bright and have large values of stellar mass, and as such it is not that surprising that this decreased

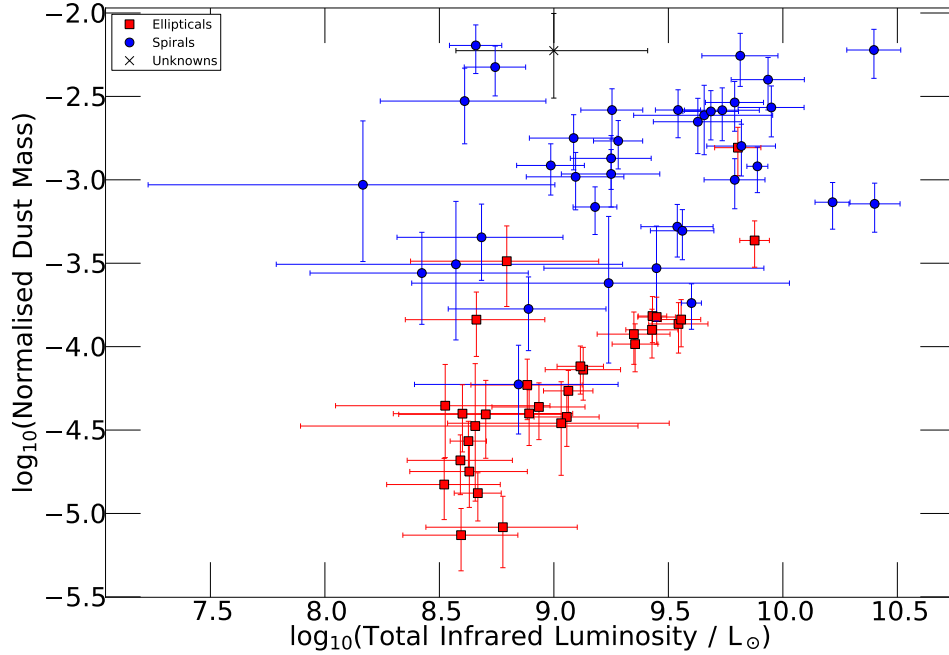


Figure 6.11: Normalised dust mass as a function of total infrared luminosity, subset by galaxy morphology.

range trend exists. The elliptical objects have low values for both parameters, with the spirals dominating at the extreme end of the scale.

The trends seen in Figure 6.11 do not show any obvious signs of bimodality within the total infrared luminosities for the two groups, and the statistics presented in Table 6.3 appear to support this. The mean and median values of both morphological types are consistent to within a single standard deviation. However, a Kolmogorov-Smirnov test of these values returns a result of $D = 0.3653$ with $P = 0.019$. This would appear to suggest that there is some slight difference, though it is not as obvious as that seen with the normalised dust masses.

Figure 6.11 does seem to show evidence of a trend between the two parameters for the elliptical galaxies, with those with the brightest luminosity also having the highest normalised dust masses. The Spearman's rank correlation coefficient of this trend being given as $\rho_E = 0.765$. Therefore, it would seem to be the case that the main factor that determines the far-infrared luminosity of these elliptical galaxies is the efficiency

Group	Mean	Standard Deviation	Standard Error	Median
Spiral	9.37	0.54	0.09	9.49
Elliptical	9.03	0.39	0.07	8.93

Table 6.3: The statistical properties of the two morphological populations in regards to total infrared luminosity, $\log\left(\frac{L}{L_{\odot}}\right)$.

of the stripping process acting upon them.

As a final means of comparison between the sources, the total infrared luminosities are shown as a function of the dust temperatures in Figure 6.12. These two parameters show no signs of correlation (Spearman’s rank correlation coefficient $\rho = -0.058$), which would imply that the infrared emission radiated by the dust in a given galaxy is independent of the dust temperature itself.

6.2 Effect of radial distance on galaxy properties

As previously discussed in subsection 3.3.1 there is a possible bias in the results when comparing to the Virgo cluster due to differences in how far the observations extend from the cluster centre.

In order to determine whether this bias is present within these data, the three galaxy properties previously investigated (normalised dust mass, dust temperature and total infrared luminosity) are each plotted as a function of distance from the cluster centre. This radial distance is defined as the difference between the coordinates of the source and the coordinates of the centre of the Coma cluster as given by NED.

Figure 6.13 shows how the normalised dust mass changes with distance from the cluster centre. This shows a slight positive trend, with those galaxies with higher dust fractions being detected on the edges of the cluster, however this is to be expected as the infall region is dominated by spiral galaxies, which have been shown to have higher normalised dust masses. The Spearman’s rank correlation coefficient of the

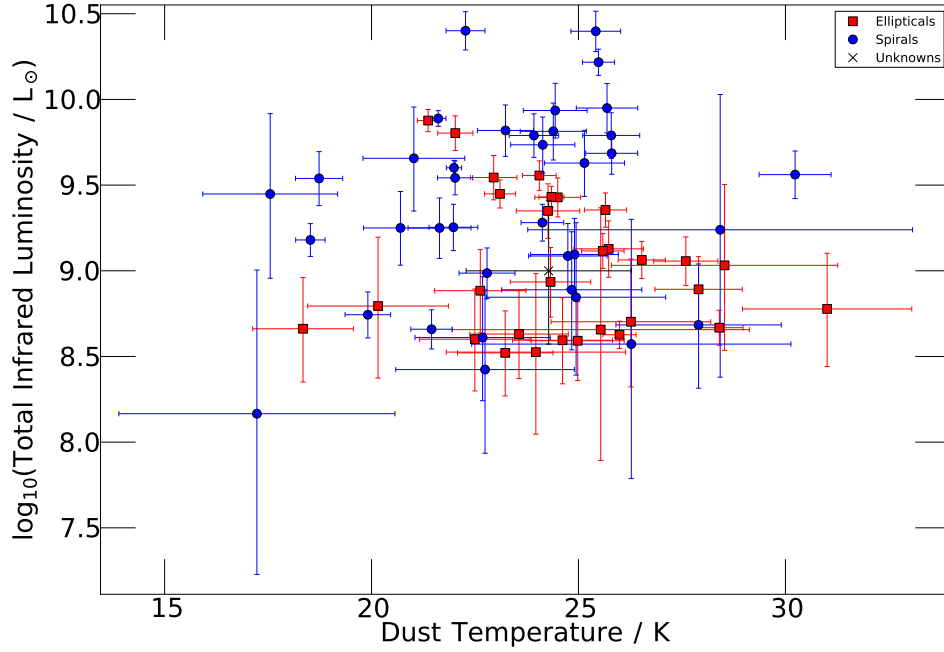


Figure 6.12: Total infrared luminosity as a function of dust temperature, subset by galaxy morphology.

whole sample is $\rho = 0.560$, whilst the values for the two morphological groups are $\rho_E = 0.299$ and $\rho_S = 0.176$.

In Figure 6.14 the radial trend for the total infrared luminosity can be seen, and it shows a slight trend for increasing luminosity with distance, with those at a distance further than ~ 0.4 degrees being around $0.5 L_\odot$ higher. However, this trend is only marginal, and there are a number of points with errorbars larger than this difference. The Spearman's rank correlation coefficient of the whole sample is $\rho = 0.201$, whilst the values for the two morphological groups are $\rho_E = 0.316$ and $\rho_S = -0.291$.

Figure 6.15 shows the radial trends are shown for the dust temperature and there is no clear indication of any trend. This would suggest that the sample has no biases in regards to this property, as the value remains unchanged within a distance equal to the virial radius of the cluster. The Spearman's rank correlation coefficient of the whole sample is $\rho = -0.363$, whilst the values for the two morphological groups are $\rho_E = -0.341$ and $\rho_S = -0.179$.

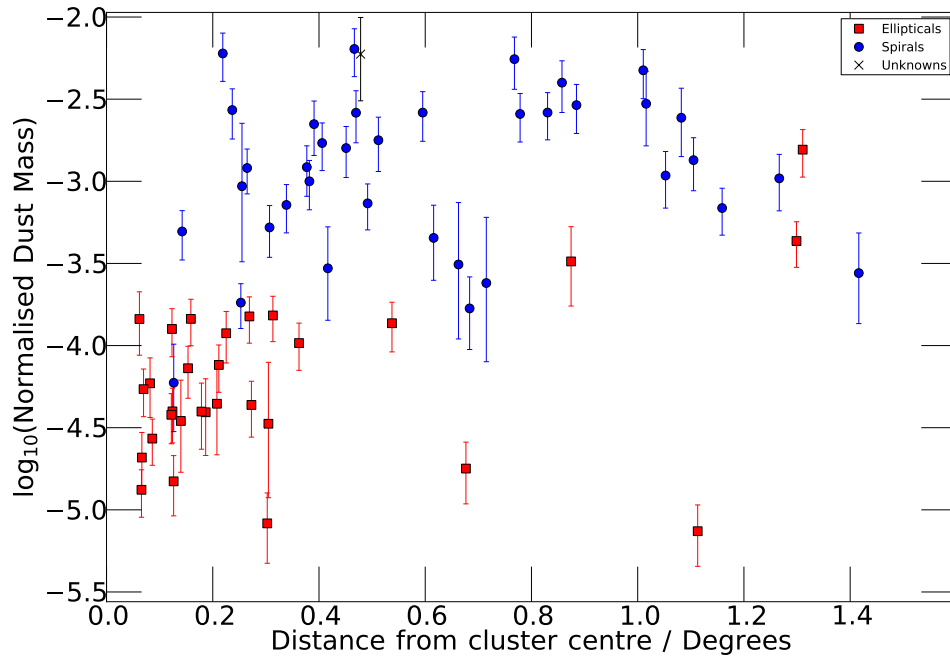


Figure 6.13: Normalised dust mass as a function of cluster radial position

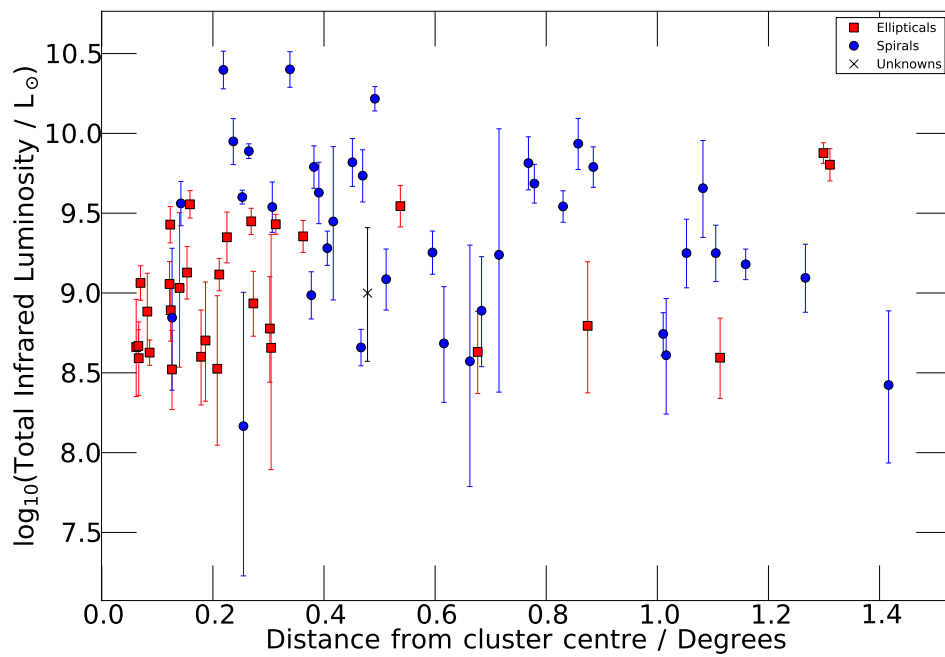


Figure 6.14: Total infrared luminosity as a function of cluster radial position

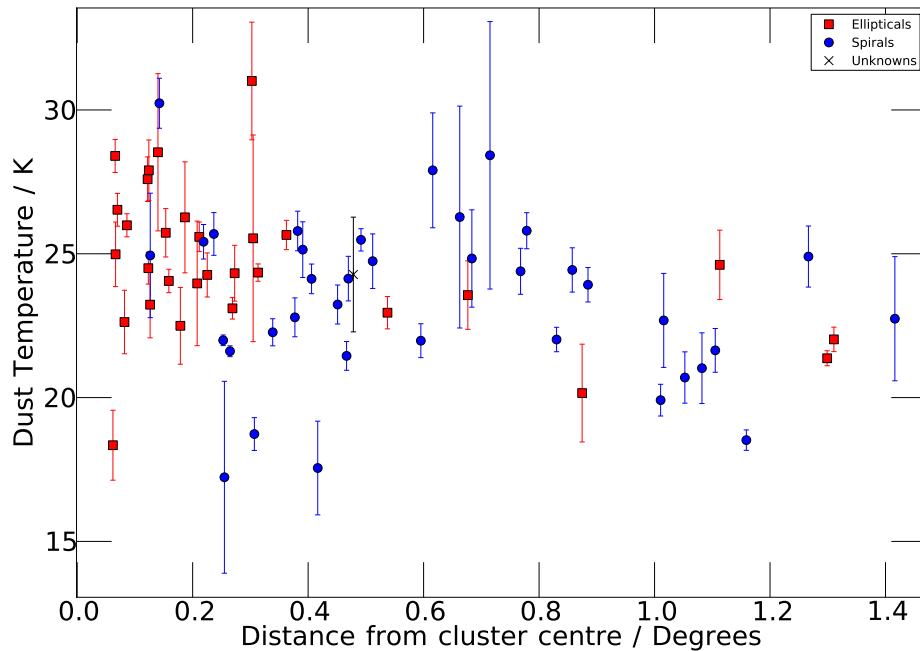


Figure 6.15: Temperature as a function of cluster radial position

6.3 Comparisons with the Virgo and Fornax clusters

As described in subsections 1.5.3 and 1.5.4, far-infrared *Herschel* observations of the Virgo and Fornax clusters have been taken and the far-infrared properties of the galaxies were presented by Auld et al. (2013) and Fuller et al. (2014) respectively. These works present ranges and mean values for the dust masses and temperatures for both the elliptical and spiral galaxies in the samples and as such provide a useful comparison for the present study. The values for the three clusters are shown Tables 6.4 and 6.5.

6.3.1 Comparison of galaxy dust masses

A similar range for the dust masses is seen in both the spiral and the ellipticals across all three clusters. In this case of the elliptical galaxies, the mean dust masses for the Coma and Virgo clusters are very similar, with the value for the Fornax cluster being

slightly lower, though consistent to within the standard errors. For the spiral galaxies, the values vary with differences greater than the standard error. The Virgo cluster has the highest mean dust mass, and the Fornax cluster the lowest, with the Coma cluster lying in the middle of the two.

		Dust mass range, $\log_{10} \left(\frac{M_{dust}}{M_{\odot}} \right)$	Dust mass mean, $\log_{10} \left(\frac{M_{dust}}{M_{\odot}} \right)$
Ellipticals	Coma	5.4 - 7.5	6.3 ± 0.1
	Virgo	5.4 - 7.0	6.3 ± 0.3
	Fornax	5.4 - 6.6	5.8 ± 0.2
Spirals	Coma	5.6 - 7.9	6.8 ± 0.1
	Virgo	5.2 - 8.1	7.1 ± 0.1
	Fornax	5.5 - 8.2	6.5 ± 0.2

Table 6.4: Comparison of the dust mass ranges and means for Coma, Virgo and Fornax cluster galaxies, separated by morphological type.

It should be noted that the lower limit of the dust mass range seen in the Coma cluster is likely due to the detection limits of the survey. Figure 6.16 shows how the recovered dust mass varies as a function of the *Herschel* detected flux at each of the three wavelengths. This clearly shows that the lower limit of the range of the dust mass seen, denoted by the horizontal black lines, is limited by the 5σ detection limit of the flux, shown as vertical lines for each wavelength band. However, given the Coma cluster lies at greater distance than the other two clusters, one would expect that Coma cluster would therefore have higher dust mass values as only the most massive and brightest galaxies would be observed, yet this trend is not seen as the Virgo cluster mean dust masses are higher.

6.3.2 Comparison of galaxy dust temperatures

The statistical trends seen when comparing the dust temperatures of the cluster galaxies differ slightly between the three clusters. For the spiral galaxies the overall range is shifted up for the Coma cluster. Additionally, the mean temperature of Coma cluster

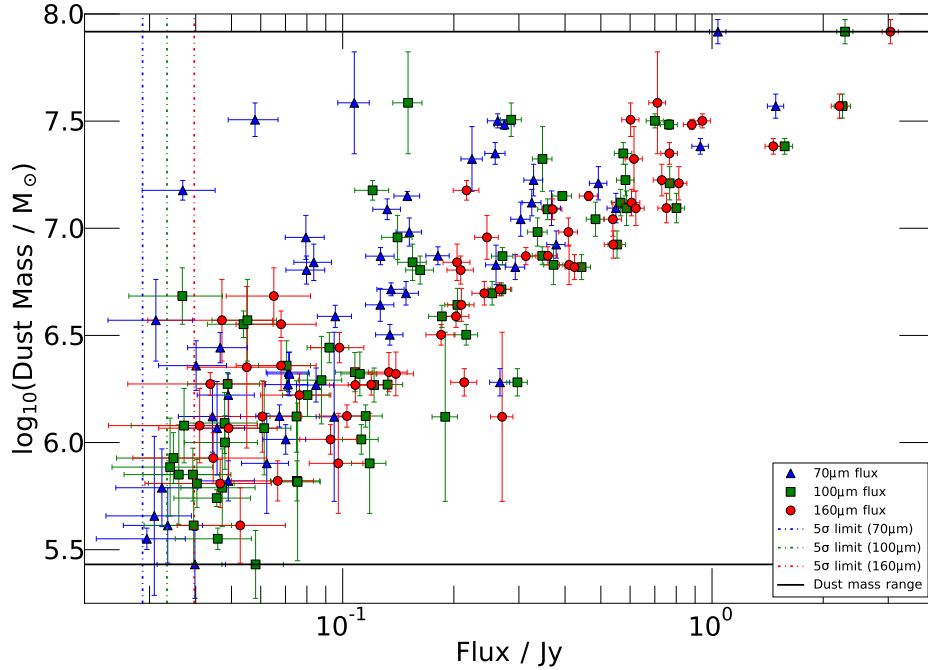


Figure 6.16: Recovered dust mass as a function of the *Herschel* detected flux at all three of the PACS wavelength bands. The coloured vertical lines denote the 5σ detection limit for each band, and the black horizontal lines show the upper and lower limits of the recovered dust mass.

spirals is higher, and thus lies more than one standard deviation away from the other cluster values. The elliptical galaxies have a similar minimum temperature in all three clusters, but the range is larger for the Coma cluster. The mean temperature of the elliptical galaxies in the Coma cluster is once again greater than that of the other clusters, though the difference is slightly less than seen with the spiral galaxies.

A possible explanation for the Coma cluster having the highest dust temperatures compared to the other two clusters is that the greater distance of the Coma cluster results in a sample biased to more massive galaxies. To investigate this, figure 6.17 shows the dust temperature as a function of the stellar mass for the sample of Coma cluster galaxies. It can be seen that there is no clear trend between the two properties, both when considering the sample as a whole or looking at the two morphological types separately. This is confirmed by the Spearman's rank correlation coefficients, which gives a values of $\rho = -0.099$, -0.354 and -0.208 for all galaxies, the ellipticals and the

		Dust temperature range, K	Dust temperature mean, K
Ellipticals	Coma	18.3 - 31.0	24.7±0.5
	Virgo	16.2 - 25.9	21.1±0.8
	Fornax	14.9 - 25.8	20.8±1.8
Spirals	Coma	17.2 - 30.2	23.4±0.5
	Virgo	12.9 - 26.4	19.4±0.2
	Fornax	11.2 - 23.7	17.5±1.0

Table 6.5: Comparison of the dust temperature ranges and means for Coma, Virgo and Fornax cluster galaxies, separated by morphological type.

spirals respectively. Thus, the higher mass of the Coma cluster galaxies should not result in the higher dust temperatures that are found.

One trend that remains constant across all three clusters is the fact that the elliptical group has a warmer average dust temperature than the spiral group. This difference is only a few degrees at most, but the fact that it is seen in all three would suggest that it is a true physical property. Additional evidence for this difference can be seen in the results presented by Bendo et al. (2003) and Smith et al. (2012).

Bendo et al. (2003) presented the dust properties of 71 galaxies that were part a catalogue produced by the *Infrared Space Observatory* (ISO; Kessler et al. 1996). These galaxies were grouped by morphological type, with 11 being identified as ellipticals or lenticular, and the remainder being spirals of various types. The spectral energy distribution was fitted with a number of black body functions with differing emissivities, however in all cases it was found that the returned dust temperature for the elliptical and lenticular group was approximately 3K higher than those returned for any of the spiral type groups.

The work by Smith et al. (2012) determined the dust properties of 62 early-type galaxies as part of the *Herschel* Reference Survey (HRS; Boselli et al. 2010). Within this sample, 31 had confirmed detections with the SPIRE instrument at 250 μm , with 24 being morphologically classified as lenticular galaxies (S0 and S0a) and 7 as ellipti-

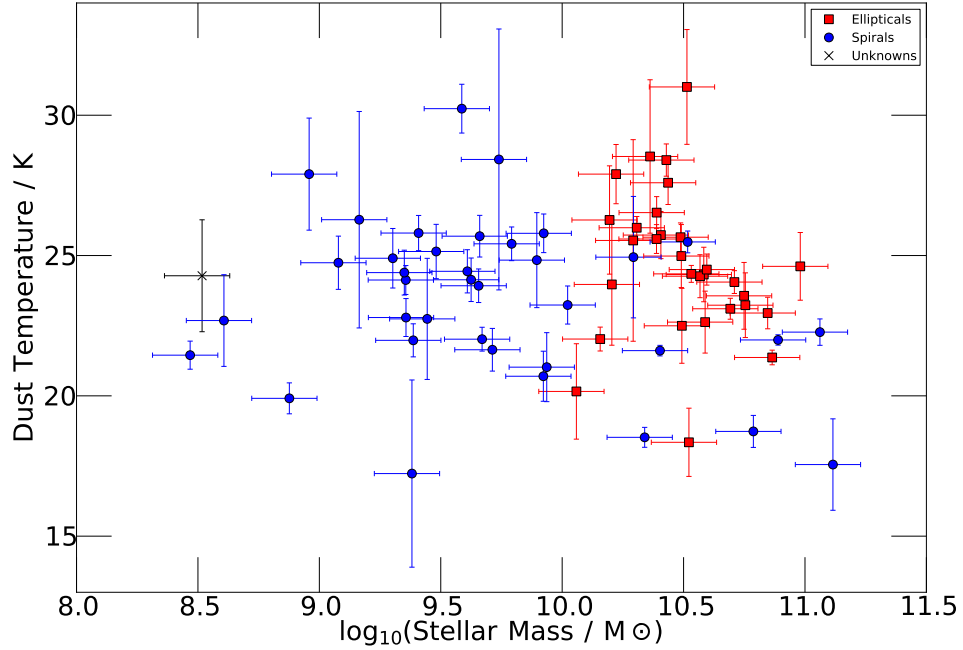


Figure 6.17: Dust temperature as a function of stellar mass, subset by galaxy morphology.

cal. These galaxies returned an average dust temperature of $T = 23.9 \pm 0.8\text{K}$; higher than the dust temperature of the Virgo and Fornax cluster spiral galaxies, though approximately the same as the Coma cluster spiral galaxies.

From the evidence presented in Table 6.5 it would be reasonable to assume that the three clusters exhibit similar galaxy properties, regardless of morphological type, with the elliptical galaxies having consistently higher dust temperatures than the spiral galaxies. This is the opposite of what one would expect if the dust in elliptical galaxies is only being heated by the old stellar population, and thus further analysis of this effect would be needed to fully understand the underlying cause. It is worth noting however that the statistical difference exhibited between the two clusters is potentially due to the small numbers involved in the comparison. Additionally, the observations of the Coma cluster resulted in 66 galaxies from which spectral energy distribution fits are good enough to determine dust mass and temperature values, and for which Sérsic index information is available to determine the morphology. In comparison, the HeViCS analysis produced a sample of 140 galaxies, and the HeFoCS analysis

produced 22 galaxies. This difference will partially be due to the fact that the Coma cluster is further away than both the Virgo or Fornax clusters, and as such the *Herschel* Coma observations will not be able to reach the faint absolute luminosities that were possible with the HeViCS and HeFoCS studies.

6.4 Comparison with the field

An additional comparison can be made between the infrared properties of the cluster galaxies and those of field galaxies. The normalised dust masses, dust masses and dust temperatures of field galaxy samples were presented as part of the *Herschel*-ATLAS Phase-1 Limited-Extent Spatial Survey (HAPLESS; Clark et al., 2015), the *Herschel* Reference Survey (HRS; Boselli et al., 2010), and the *Planck* Early Release Compact Source Catalogue (*Planck* ERCSC; Clemens et al., 2013).

6.4.1 Comparison of galaxy dust temperatures

Clark et al. (2015) derived dust temperatures for field galaxies from HAPLESS and HRS data, as well as presenting dust temperatures derived from Planck data by Clemens et al. (2013). These three surveys utilised two temperature components, each radiating as a modified black body, when constructing the spectral energy distributions, and as such are not directly comparable to the temperatures derived in the present study. However, it is noted by Clark et al. (2015) that the weighted mean of the cold and warm dust temperatures returns a value that is not significantly different to the cold dust component temperature. Clemens et al. (2013) also states that whilst a warm dust component is required in order to fit the data, the emission is dominated by the cold dust component. Therefore, the cold dust temperatures will be utilised for this comparison with the three cluster environments.

Table 6.6 presents the range and median of the dust temperatures for galaxies with the three cluster and three field samples. It can be seen that whilst the ranges of the

Survey	Dust temperature range, K	Dust temperature median, K
Coma	17.2 - 31.0	24.3±0.3
Virgo	12.9 - 26.4	19.4±0.2
Fornax	11.2 - 25.8	17.3±1.0
HAPLESS	9.2 - 25.6	14.6±0.6
HRS	–	18.5
<i>Planck</i>	–	17.7

Table 6.6: Comparison of the statistical properties of the dust temperature of the Coma, Virgo and Fornax clusters, and the field galaxy samples of HAPLESS, HRS and *Planck*.

three clusters and the HAPLESS sample are similar, the median dust temperature of the Coma cluster is significantly higher than that of any of the field samples. The median dust temperatures of the Virgo and Fornax clusters however are in agreement with the field surveys. This difference between the Coma cluster and the field could be as a result of the difference in method when determining the dust temperature, as a single temperature modified black body fit was utilised for the present study. It should also be noted that the field values are biased to low temperatures as only the cold dust component is considered. Even with these caveats however, the Coma cluster galaxies stand out in all comparisons as having unusually warm dust.

6.4.2 Comparison of galaxy dust and stellar mass properties

Clark et al. (2015) also present dust, stellar and normalised dust masses determined for the field galaxies in their sample. In addition to this the median dust, stellar and normalised dust masses are presented for the HRS and *Planck* surveys. Table 6.7 presents the statistical properties of the dust masses across the various surveys. It can be seen that the median values are in close agreement for all the surveys, except for that of the *Planck* survey which is slightly higher. However, a large galaxy that has had most of its dust removed could have the same dust mass as a much smaller dust rich galaxy. Therefore, the sizes of the galaxies can only really be compared between the

Survey	Dust mass range, $\log_{10} \left(\frac{M_{dust}}{M_{\odot}} \right)$	Dust mass median, $\log_{10} \left(\frac{M_{dust}}{M_{\odot}} \right)$
Coma	5.4 - 7.9	6.6 ± 0.1
Virgo	5.2 - 8.1	6.7 ± 0.1
Fornax	5.4 - 8.2	6.8 ± 0.2
HAPLESS	5.3 - 8	6.7 ± 0.1
HRS	–	6.7
<i>Planck</i>	–	7.6

Table 6.7: Comparison of the statistical properties of the dust mass of the Coma, Virgo and Fornax clusters, and the field galaxy samples of HAPLESS, HRS and *Planck*.

Survey	Normalised dust mass, $\log_{10} \left(\frac{M_{dust}}{M_{stellar}} \right)$		
	Minimum	Maximum	Median
Coma	-5.1	-2.2	-3.5 ± 0.1
Fornax	-4.9	-1.3	-3.0 ± 0.2
HAPLESS	-3.7	-1.1	-2.3 ± 0.1
HRS	–	–	-2.9
<i>Planck</i>	–	–	-2.6

Table 6.8: Comparison of the statistical properties of the normalised dust mass of the Coma cluster, and the field galaxy samples of HAPLESS, HRS and *Planck*.

various surveys by comparing the normalised dust mass.

The normalised dust masses are not presented for the Virgo cluster survey, but are available for the Fornax cluster survey as well as the three field surveys. The median values, as well as the ranges where they are available, are presented in Table 6.8. It can be seen that the median value for the Coma cluster galaxies is significantly lower than that of any of the field galaxy surveys, but is reasonably close to that of the Fornax cluster. This means that whilst the field galaxies have similar dust masses to those galaxies found in the cluster environments, they have lower stellar masses. Therefore, the galaxies found within the cluster environment are much larger, but have had a lot of their dust mass removed through the physical processes described in Section 1.4.

6.5 Concluding remarks

In this chapter we have seen the presence of two separate populations within the Coma cluster sample, the early- and late-types, and find that they have distinctly different mass and temperature properties. It can be seen that the elliptical galaxies have slightly higher dust temperatures than the spiral galaxies; the opposite of what one would expect given the assumptions about the dust heating mechanisms involved in the two types.

Similarities are seen when each of these two groups is compared to similar studies of the Virgo and Fornax clusters, suggesting that the effect of the rich, virialised environment of the Coma cluster is less substantial than previously assumed.

Additionally, the galaxy properties of the three cluster environments were compared to those of galaxies in the field. It was seen that the dust temperatures are mostly consistent across the various surveys, though the Coma cluster stands out with a higher median value. In regards to the mass properties of the galaxies, the dust masses are similar across all environments, however the normalised dust masses for the cluster galaxies are lower than those of the field. This would suggest that galaxies in cluster environments are larger than those found in the field, but have had large fractions of their dust removed through various processes.

Chapter 7

Scientific conclusions

This study has detailed the reduction and subsequent analysis of the deepest ever far-infrared observations of the Coma cluster using the *Herschel* PACS instrument. The resulting flux densities, when combined with data from the *Herschel* SPIRE instrument, allowed for the construction of far-infrared spectral energy distribution fits across a wavelength range of 70-500 μm for each of the 70 spectroscopically confirmed Coma cluster members. From these fits, the far-infrared properties of 68 of these members were determined, specifically the dust temperature, the dust mass and the total infrared luminosity. These 68 galaxies were then defined as either early- or late-types, through a combination of their Sérsic index values and their Galaxy Zoo defined morphologies, resulting in 67 galaxies in the sample to compare: 30 early-types and 37 late-types. These results were then compared to other studies of both clusters and the field in order to ascertain the extent to which environmental processes affect galaxy evolution.

The flux densities measured using the PACS instrument at 70, 100 and 160 μm were compared to previous far-infrared studies in order to determine if they are accurate. A positional match with the catalogue produced through observations by IRAS (Wang et al., 1991) resulted in four matched sources measured at 100 μm . The *Herschel* recovered flux densities are dimmer than those recovered by IRAS, though this is likely due to the larger point spread function of the IRAS instrument. A similar match with the 70 and 160 μm flux densities recovered by Spitzer (Edwards & Fadda, 2011) found

21 and 15 matches with the *Herschel* catalogue respectively. These flux densities were again higher than those recovered by *Herschel*, however, the apertures utilised in the Spitzer study were significantly larger than those used in the present study.

Far-infrared galaxy luminosity functions were constructed for each of the three PACS bands (70, 100, 160 μm), with all three being found to take the form of a Schechter function. The galaxy luminosity functions produced at 100 and 160 μm were compared with equivalent functions produced by Auld et al. (2013) as part of the *Herschel* Virgo cluster survey (HeViCS). The data of both the Coma and Virgo clusters take the form of a Schechter function, with the function parameters of the two being consistent to within the associated errors. This means that the galaxy populations of the two clusters are similar, despite the fact that the Coma cluster is a much more virialised system.

Additionally, comparisons of the Coma cluster luminosity functions at 70 and 160 μm were made with similar functions of field galaxies from data taken by IRAS (Saunders et al., 1990) and Spitzer (Patel et al., 2013). These field galaxy functions showed good agreement to the *Herschel* data, as confirmed by Kolmogorov-Smirnov tests. This result confirms that of Bai et al. (2006, 2009), which used mid-infrared and optical data to derive a total infrared field luminosity function and found a good agreement between this function and that of the Coma cluster.

A statistical analysis of the far-infrared properties of the galaxies in the sample was then completed for the early- and late-types separately. The early-types were found to have mean normalised dust masses, dust temperatures and total infrared luminosities of $\log_{10} \left(\frac{M_{dust}}{M_{stellar}} \right) = -4.19 \pm 0.1$, $T = 24.70 \pm 0.5\text{K}$ and $\log_{10} (L) = 9.03 \pm 0.1L_{\odot}$ respectively. For the late-types the mean values were found to be $\log_{10} \left(\frac{M_{dust}}{M_{stellar}} \right) = -2.94 \pm 0.1$, $T = 23.37 \pm 0.5\text{K}$ and $\log_{10} (L) = 9.37 \pm 0.1L_{\odot}$.

When examining the derived dust masses as a function of stellar mass a bimodality can be seen, with those sources identified as being late-type spiral galaxies having a linear relation between the two mass components, whilst the early-type ellipticals have a near constant stellar mass for any given dust mass. The late-type trend is therefore likely to be the ‘star formation main sequence’ as previously observed in the infrared

by Elbaz et al. (2011), while the early-type trend may be a result of passive heating of the dust by the older stellar population. In order to test this hypothesis a comparison is made with observations of CO and UV emission from the galaxies, to determine which galaxies have fuel for, and direct stellar emission from, forming stellar populations.

Observations of the CO emission present in Coma cluster galaxies were completed by Boselli et al. (1997), Lavezzi et al. (1999) and Casoli et al. (1996). The results of these three studies were then combined, and the resulting list of galaxies compared to the galaxies in the *Herschel* sample. This comparison resulted in eleven galaxies with detection of both far-infrared and CO emission. All eleven of these galaxies lie in the late-type trend as expected. Additionally, out of a possible eleven galaxies which had been identified via ultraviolet observations as currently undergoing a ram pressure stripping process (Smith et al., 2010), seven are seen within the sample and once again they sit in this late-type galaxy trend. These results support the hypothesis that the late-type trend consists of star forming galaxies. The other side of this analysis is that none of the galaxies identified as being early-type were detected by either the CO or ultraviolet observations. This confirms that whatever is powering the far-infrared emission from the early-type galaxies is not seen to be related to recent star formation processes, but star formation within approximately 1 Gyr leading to an AGB population may be a good explanation.

The dust masses and temperatures of the early- and late-types were then compared to *Herschel* studies of the Virgo (Auld et al., 2013) and Fornax (Fuller et al., 2014) clusters. In terms of the dust mass of a galaxy, the mean values for the early-types in the Coma and Virgo clusters were very similar, with the Fornax cluster value being slightly lower, but within the standard error of the other two. For the late-type galaxies, the differences between the clusters are much larger, with the Virgo cluster having the highest mean dust mass, the Fornax cluster the lowest, and the Coma cluster lying in between the other two. In terms of the dust temperature, it can be seen that whilst the three clusters have differing mean values, the late-types of all three clusters have slightly lower mean dust temperatures than the early-types of the respective cluster. This result supports similar observational evidence obtained by ISO (Bendo et al.,

2003) and the *Herschel* Reference Survey (Smith et al., 2012), both of which noted a small but noticeably higher dust temperature for early-type galaxies. This result seems at odds with the accepted idea that the dust in elliptical galaxies is heated by the old stellar population, which one would expect to be cooler than the dust that is heated by the hot young stars produced during star formation processes.

In order to summarise this thesis, it is useful to return to the questions posed in Section 1.8 as part of the introduction, and briefly detail the answers that have been determined for each.

1. Surprisingly, all types of galaxy are seen via the far-infrared emission from the Coma cluster.
2. There is evidence of far-infrared emission coming from the elliptical early-type galaxies with no evidence of star formation.
3. The optically brightest galaxies, namely the three large ellipticals NGC 4889, NGC 4874 and NGC 4839, are not detected at these wavelengths. The brightest galaxies seen in this *Herschel* sample are the brightest spirals, which themselves are still optically bright.
4. The far-infrared luminosity function of the Coma cluster follows the form of a Schechter function, with large number of dim galaxies and a small number of bright galaxies.
5. It has been discovered that there is a bimodality within the galaxy sample when comparing the dust and stellar masses of the two morphological types. A comparison of other observational properties shows that one group consists of star forming late-type spiral galaxies with a higher normalised dust mass, and the other consists of passive early-type elliptical galaxies with a lower normalised dust mass, but a marginally higher dust temperature.

Chapter 8

Future work

The data presented in this study can be built upon by future studies in order to further understand the processes that are occurring within the rich cluster environment, and to provide possible explanations for some of the trends seen. In this chapter, some potential ideas for this future work will be briefly detailed, covering the types of observations required, as well as how the results would relate to those of the current study.

8.1 Near-infrared observations

One possible improvement to the previously described work, would be to determine the stellar masses of the detected galaxies through measurements of their near-infrared emission. These data are already available via *K*-band observations that were taken with Wide Field Infrared Camera (WFCAM), which is mounted on the United Kingdom Infrared Telescope (UKIRT). The advantage of using near-infrared observations to determine the stellar masses is that unlike with optical observations, the *K*-band luminosity of a galaxy is less affected by recent star formation and as such provides a more accurate estimate for the mass of the old stellar population (Broadhurst et al., 1992; Kauffmann & Charlot, 1998).

8.2 Comparisons with H α observations

Domínguez Sánchez et al. (2012) found that there was good agreement between the star formation rate determined from H α observations (zCOSMOS; Lilly et al. 2009) and the rate determined from *Herschel* infrared observations, specifically the PEP survey. A comparison of the star formation rates of far-infrared and H α emission stemming from galaxies in the Coma cluster could be completed in order to ascertain if this agreement holds in the cluster environment and to determine the fraction of optically visible and deeply dust-embedded star formation. Additionally, if the H α and far-infrared emission itself correlates for a given source, it would imply that the far-infrared emission from the dust is due to star formation processes.

8.3 Comparisons with other galaxy environments

In Section 6.3, a comparison was drawn between the Coma cluster and *Herschel* observations of the Virgo and Fornax clusters. This comparison provided a useful insight into potential similarities of the three clusters, however the numbers produced can only be used as a starting point for the comparisons due to limitations of the observations. The Coma cluster is approximately five times further away than the Virgo and Fornax clusters, and as such the observations of the Coma cluster will not be as deep in terms of absolute luminosity as the other two, even with the same instrumentation being used. For this reason, flux limits would have to be applied to the HeViCS and HeFoCS catalogues in order to produce an equivalent sample for comparison with the Coma cluster catalogue.

In Section 3.3, similarities were seen between the luminosity functions of the Coma and Virgo clusters, as well as with that of field galaxies. This would imply that the various processes that shape galaxy evolution within the cluster environment do not have as strong an effect as initially assumed. An investigation into the far-infrared properties of field galaxies, similar to that completed in Chapters 6, could provide insight into this scenario by assessing whether any of the trends seen in Chapter 6,

including the bimodality of the mass components by morphological type, are replicated in field galaxy samples.

8.4 Determination of the source of far-infrared emission in early-type galaxies

The nature of the far-infrared emission stemming from the early-type elliptical galaxies is as yet not fully understood, and requires further investigation. The initial belief that the dust within these galaxies is heated by the background stellar population is a possibility, though this idea does not explain why these elliptical galaxies have a higher dust temperatures than the spiral galaxies.

One possible explanation is that the dust is heated by the X-ray emitting gas of the intracluster medium, as the elliptical galaxies tend to lie in areas of strong X-ray background. However, not all of the elliptical galaxies lie in such areas, and of those that do there is seemingly no correlation between the strength of the X-ray emitting gas and the dust temperature, as shown in Figure 6.9.

Another source of this emission could be active galactic nuclei (AGN) within the core of the galaxy. These AGN could quench star formation in the galaxy by forcibly removing the gas in the galaxy that fuels the star formation processes, though there are only 15 galaxies within the *Herschel* sample that are identified by NED as hosting an AGN, of which only 6 are elliptical galaxies. There could be more ellipticals that are hosting AGN that have yet to be detected due to them being obscured by the dust that is present in the galaxy. Further observations would be required in order to determine if this is a realistic possibility.

Finally, if the far-infrared emission from early-type galaxies is due to a population of AGB stars, then one would expect the detected galaxies to have had more recent star formation than the undetected galaxies. Potential evidence for this idea could be seen if one were to compare the star formation histories of both the detected and undetected

galaxies.

Appendix A

Spectral energy distributions and *Herschel* PACS images

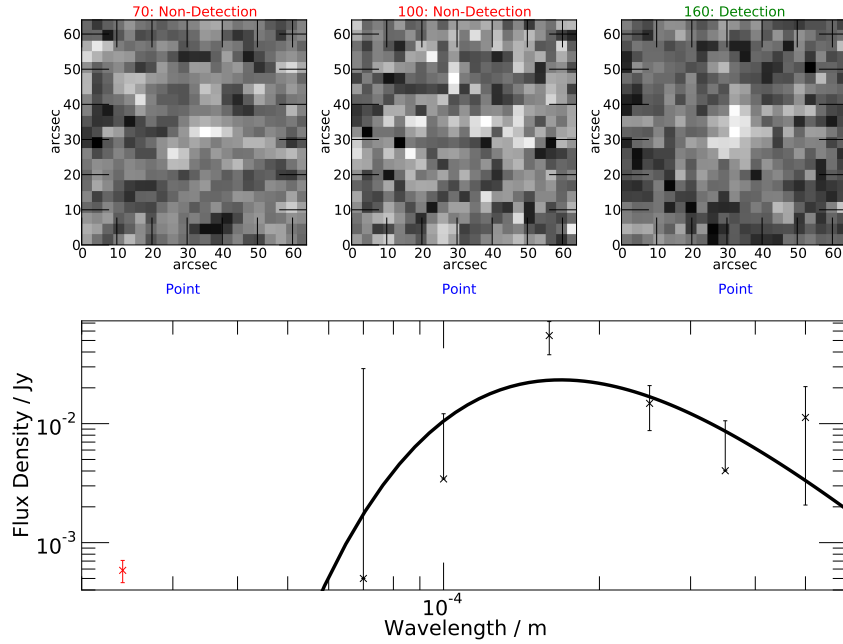


Figure A.1: Object 1: $T = 17.2\text{K}$, $\log_{10} \left(\frac{M_{Dust}}{M_{\odot}} \right) = 6.4$, $\log_{10} \left(\frac{M_{*}}{M_{\odot}} \right) = 9.4$

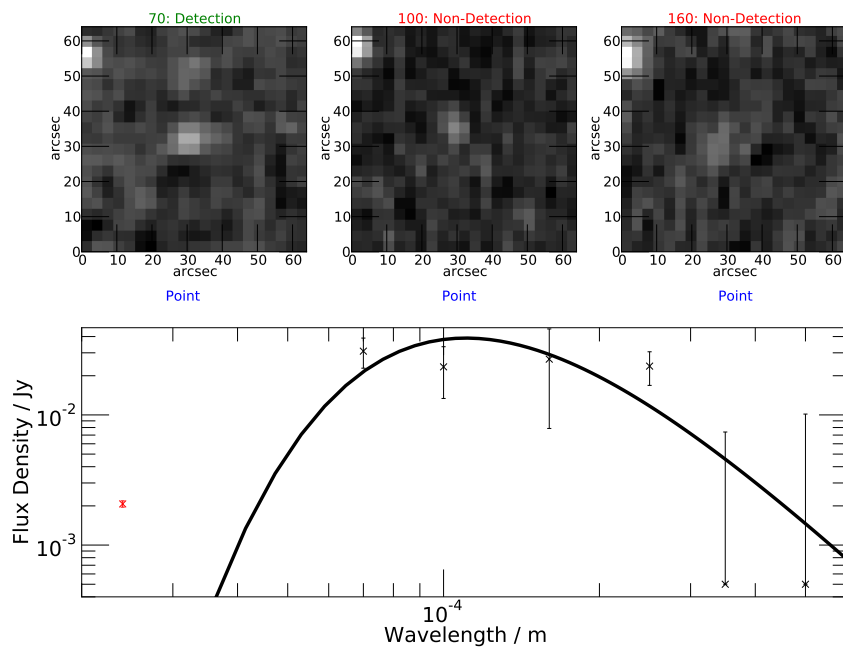


Figure A.2: Object 2: $T = 26.3\text{K}$, $\log_{10} \left(\frac{M_{Dust}}{M_{\odot}} \right) = 5.7$, $\log_{10} \left(\frac{M_{*}}{M_{\odot}} \right) = 9.2$

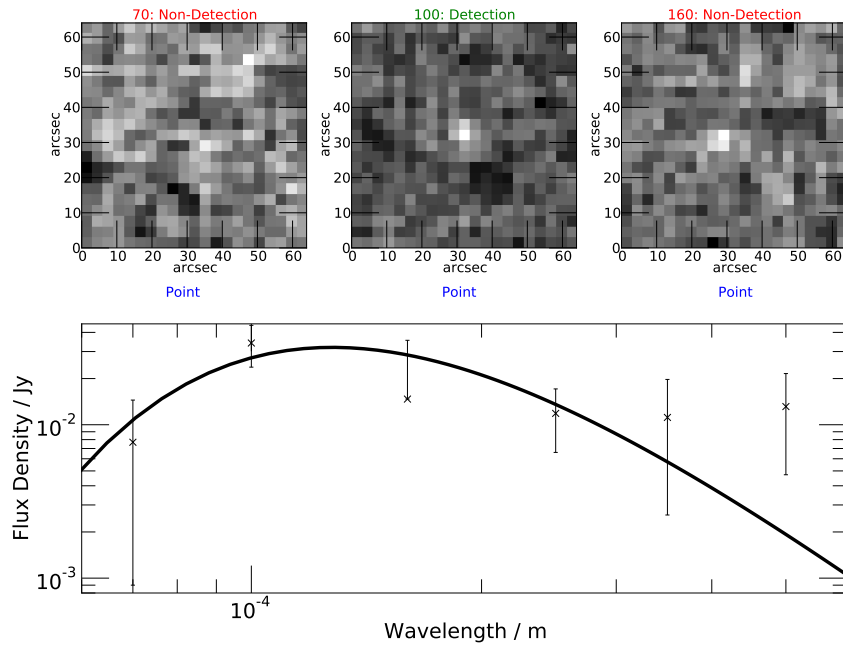


Figure A.3: Object 3: $T = 22.7\text{K}$, $\log_{10} \left(\frac{M_{Dust}}{M_{\odot}} \right) = 5.9$, $\log_{10} \left(\frac{M_{*}}{M_{\odot}} \right) = 9.4$

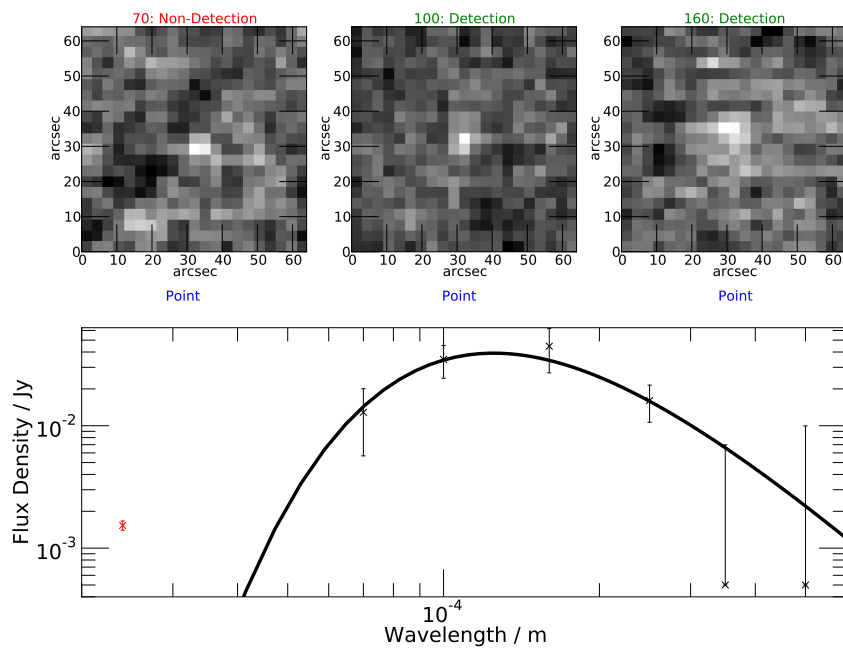


Figure A.4: Object 4: $T = 23.2\text{K}$, $\log_{10} \left(\frac{M_{Dust}}{M_{\odot}} \right) = 5.9$, $\log_{10} \left(\frac{M_{*}}{M_{\odot}} \right) = 10.8$

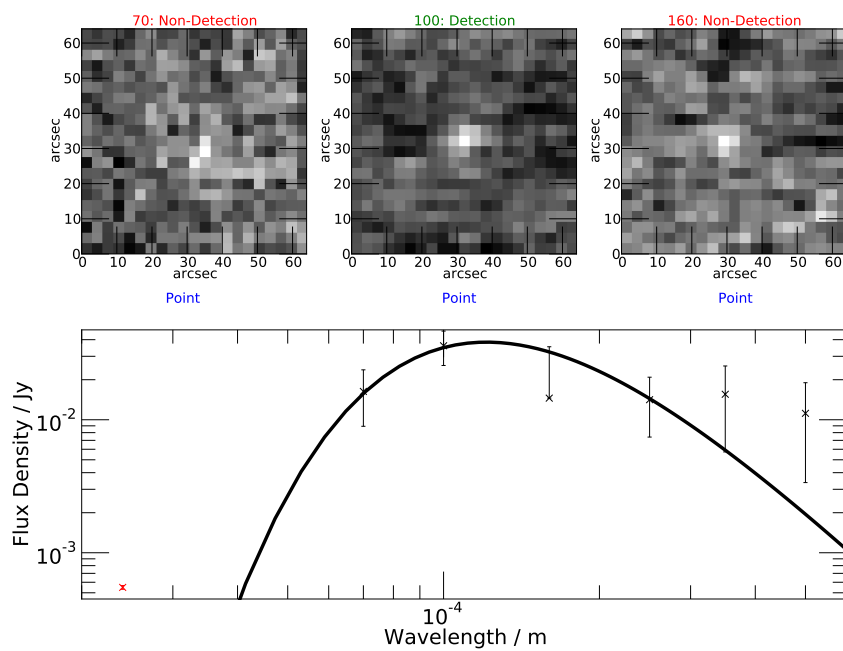


Figure A.5: Object 5: $T = 24.0\text{K}$, $\log_{10} \left(\frac{M_{Dust}}{M_{\odot}} \right) = 5.9$, $\log_{10} \left(\frac{M_{*}}{M_{\odot}} \right) = 10.2$

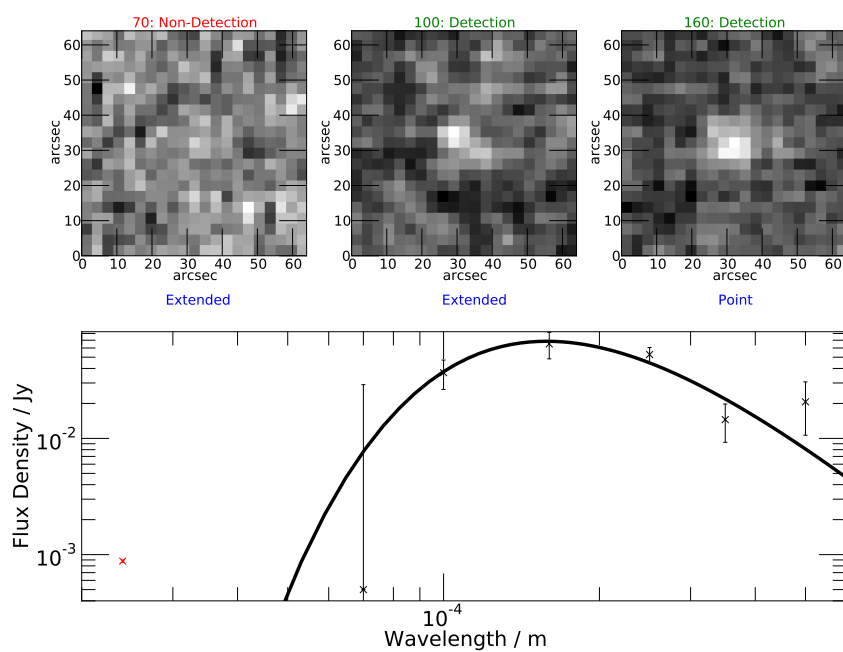


Figure A.6: Object 6: $T = 18.3\text{K}$, $\log_{10} \left(\frac{M_{Dust}}{M_{\odot}} \right) = 6.7$, $\log_{10} \left(\frac{M_{*}}{M_{\odot}} \right) = 10.5$

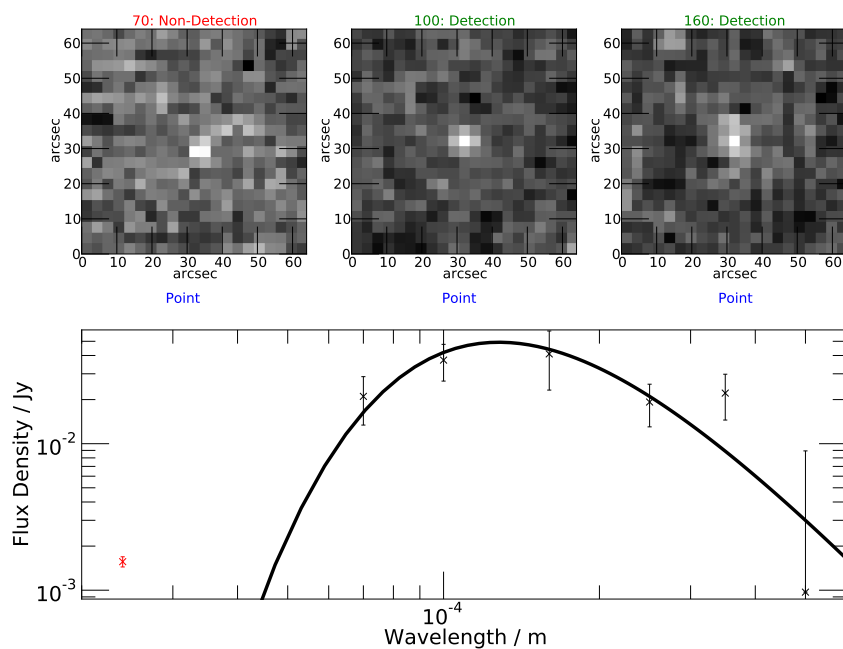


Figure A.7: Object 7: $T = 22.7\text{K}$, $\log_{10} \left(\frac{M_{Dust}}{M_{\odot}} \right) = 6.1$, $\log_{10} \left(\frac{M_{*}}{M_{\odot}} \right) = 8.6$

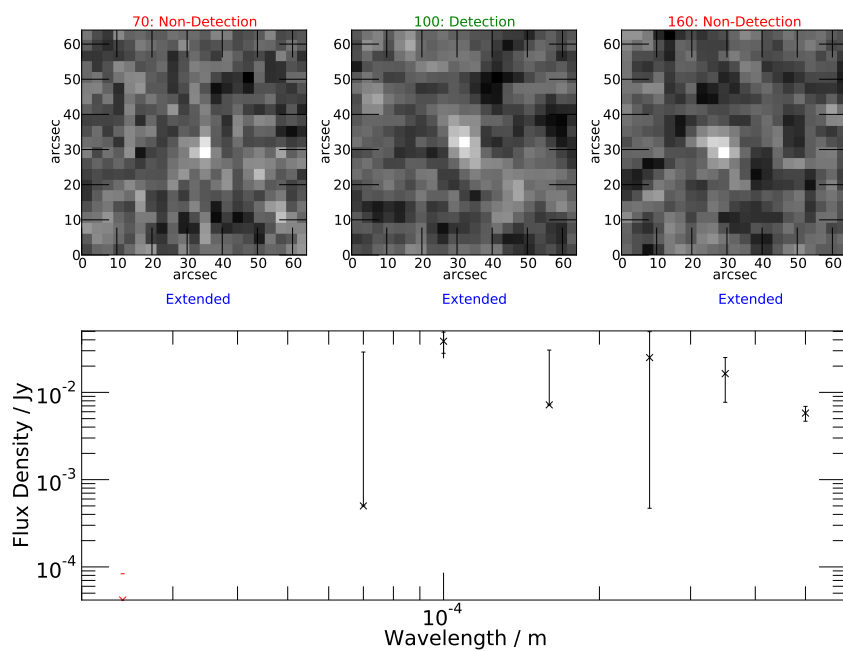


Figure A.8: Object 8: No constraint on fit, therefore no parameters can be derived.

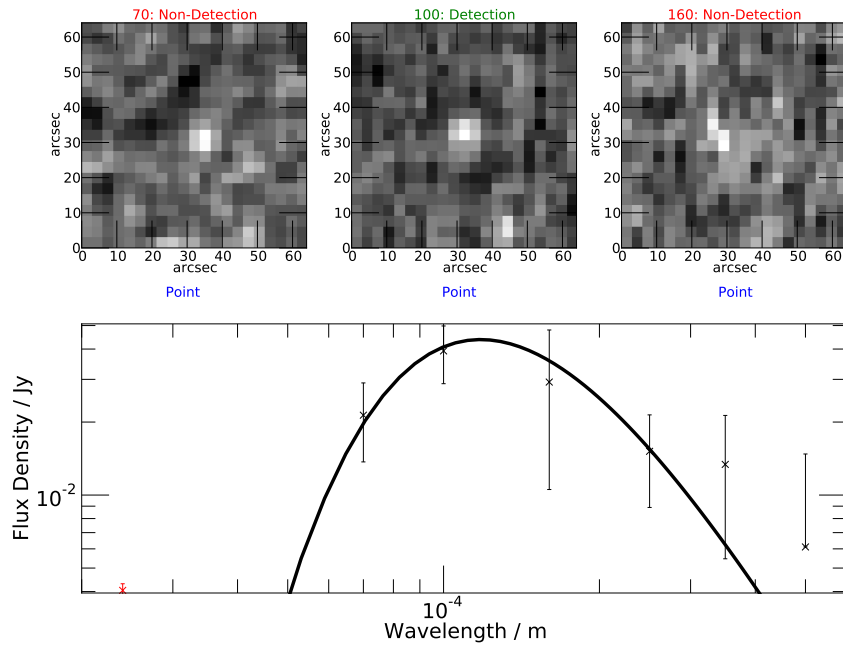


Figure A.9: Object 9: $T = 24.6\text{K}$, $\log_{10} \left(\frac{M_{Dust}}{M_{\odot}} \right) = 5.9$, $\log_{10} \left(\frac{M_{*}}{M_{\odot}} \right) = 11.0$

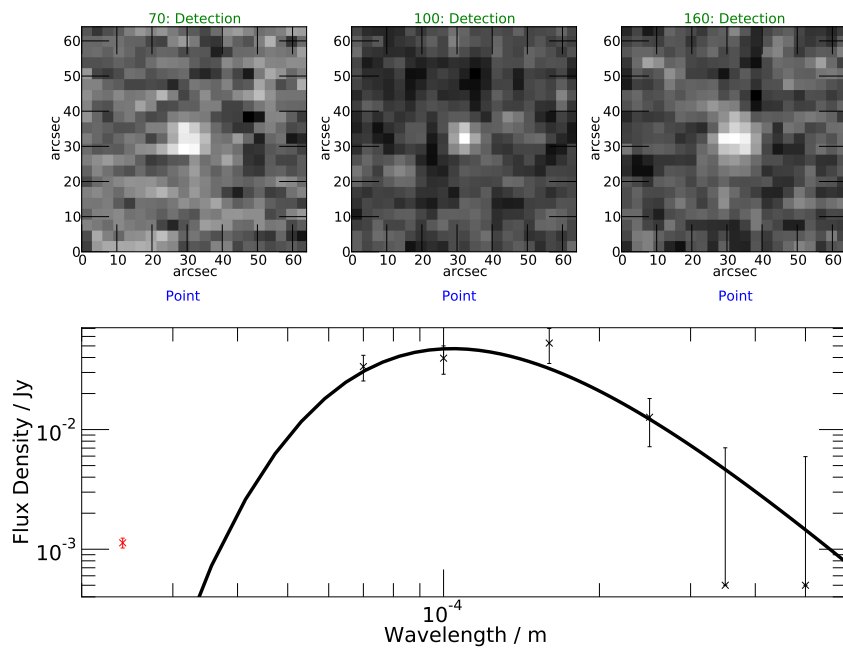


Figure A.10: Object 10: $T = 27.9\text{K}$, $\log_{10} \left(\frac{M_{Dust}}{M_{\odot}} \right) = 5.6$, $\log_{10} \left(\frac{M_{*}}{M_{\odot}} \right) = 9.0$

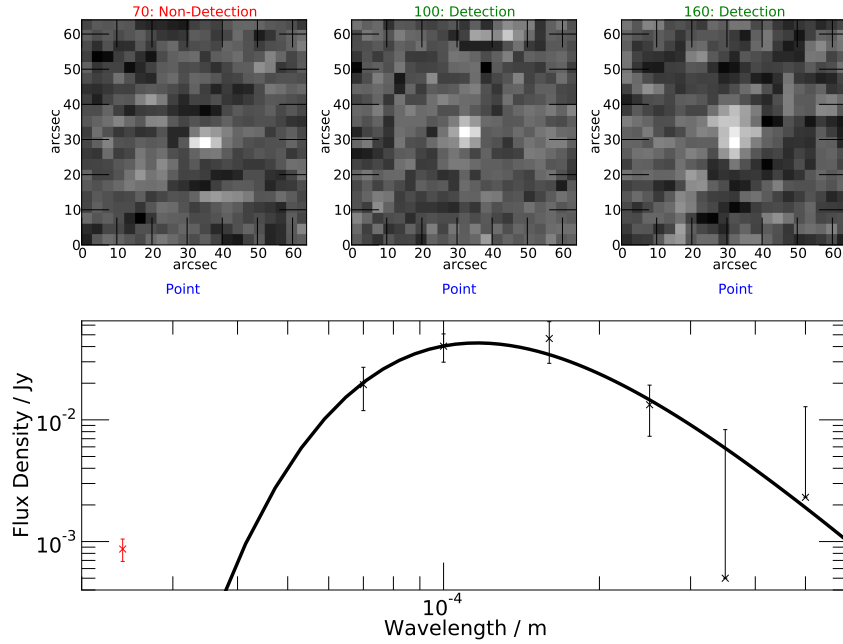


Figure A.11: Object 11: $T = 25.0\text{K}$, $\log_{10} \left(\frac{M_{Dust}}{M_{\odot}} \right) = 5.8$, $\log_{10} \left(\frac{M_{*}}{M_{\odot}} \right) = 10.5$

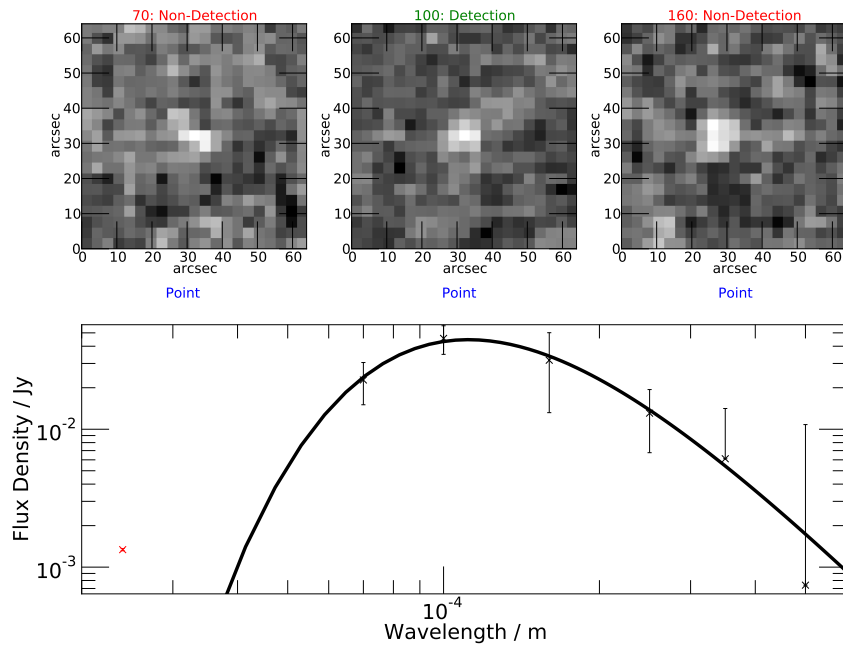


Figure A.12: Object 12: $T = 26.0\text{K}$, $\log_{10} \left(\frac{M_{Dust}}{M_{\odot}} \right) = 5.7$, $\log_{10} \left(\frac{M_{*}}{M_{\odot}} \right) = 10.3$

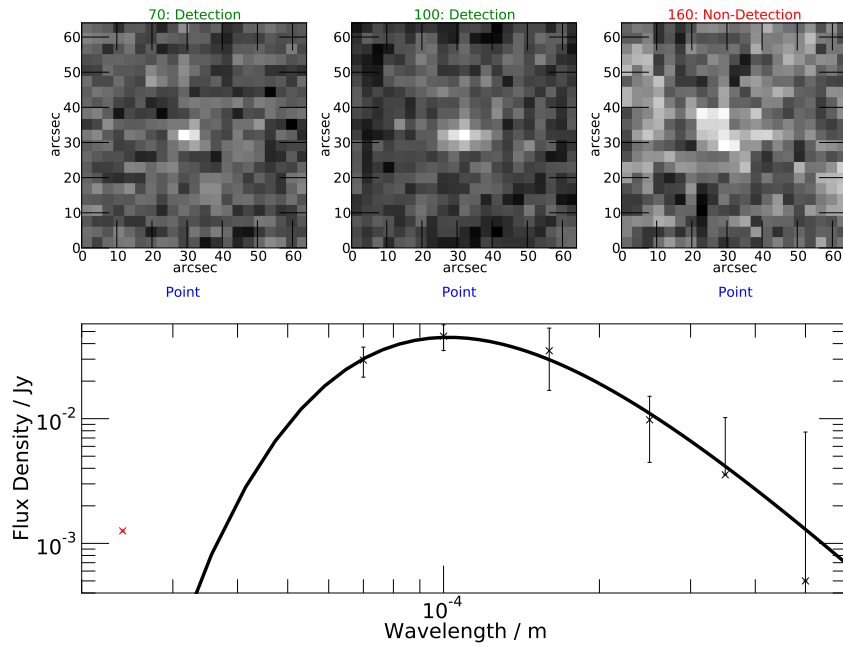


Figure A.13: Object 13: $T = 28.4\text{K}$, $\log_{10} \left(\frac{M_{Dust}}{M_{\odot}} \right) = 5.6$, $\log_{10} \left(\frac{M_{*}}{M_{\odot}} \right) = 10.4$

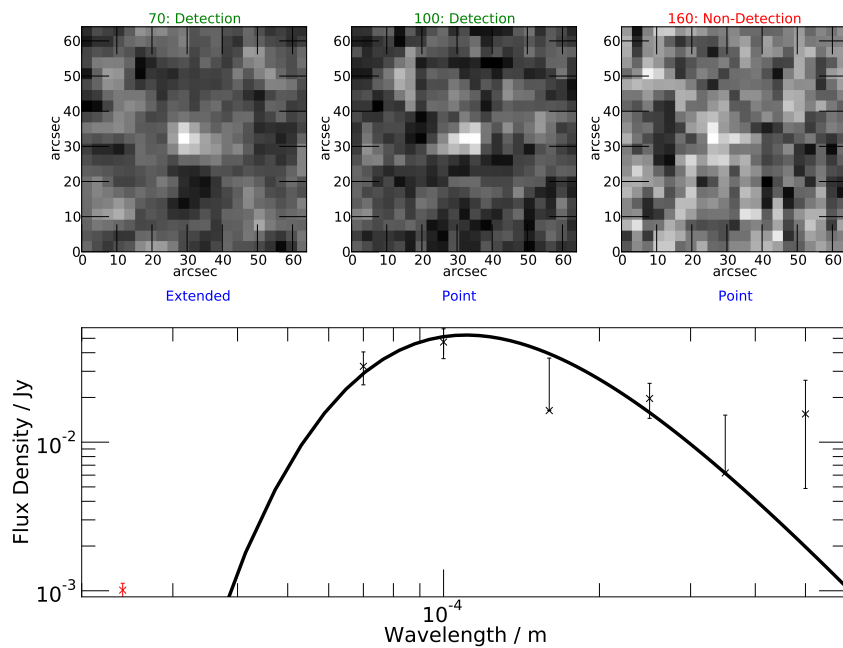


Figure A.14: Object 14: $T = 26.3\text{K}$, $\log_{10} \left(\frac{M_{Dust}}{M_{\odot}} \right) = 5.8$, $\log_{10} \left(\frac{M_{*}}{M_{\odot}} \right) = 10.2$

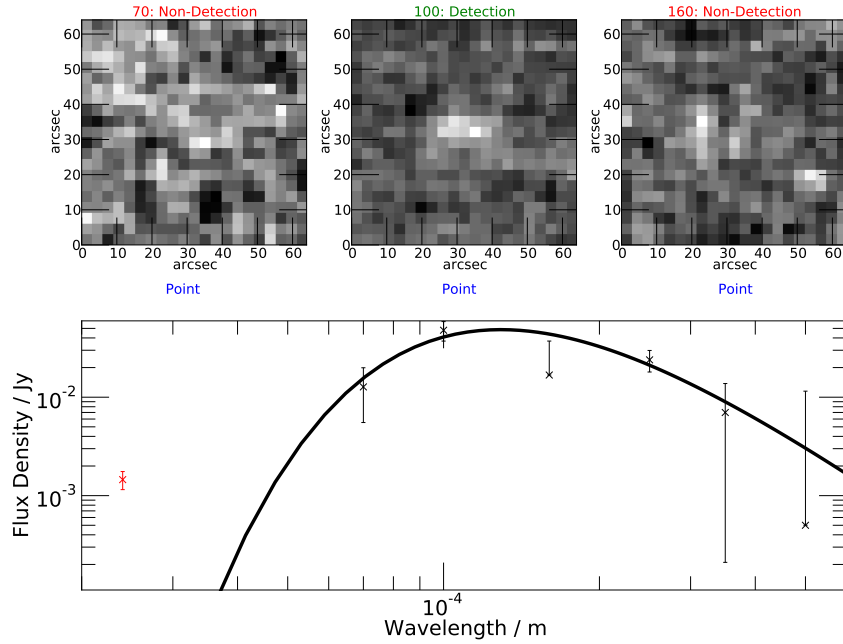


Figure A.15: Object 15: $T = 22.5\text{K}$, $\log_{10} \left(\frac{M_{Dust}}{M_{\odot}} \right) = 6.1$, $\log_{10} \left(\frac{M_{*}}{M_{\odot}} \right) = 10.5$

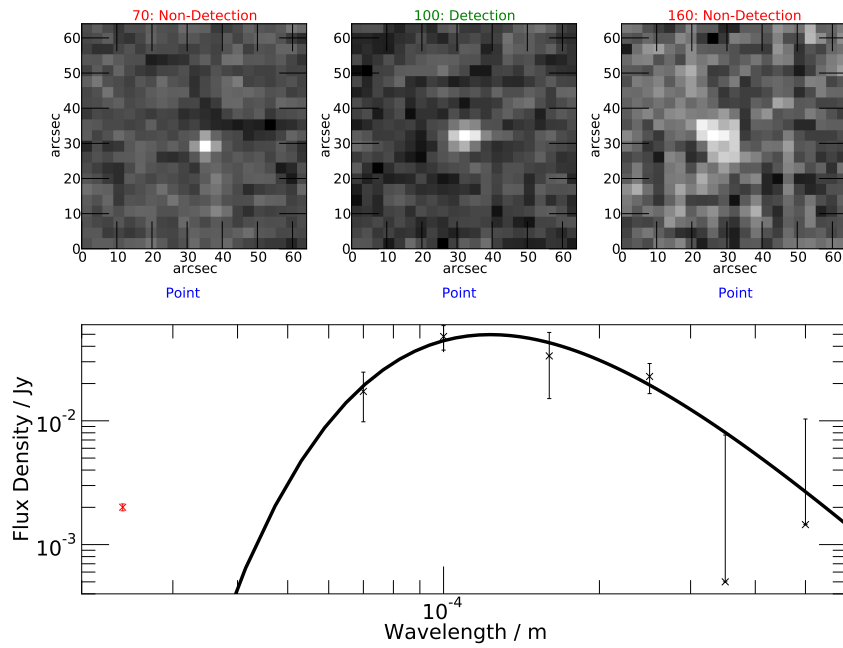


Figure A.16: Object 16: $T = 23.6\text{K}$, $\log_{10} \left(\frac{M_{Dust}}{M_{\odot}} \right) = 6.0$, $\log_{10} \left(\frac{M_{*}}{M_{\odot}} \right) = 10.7$

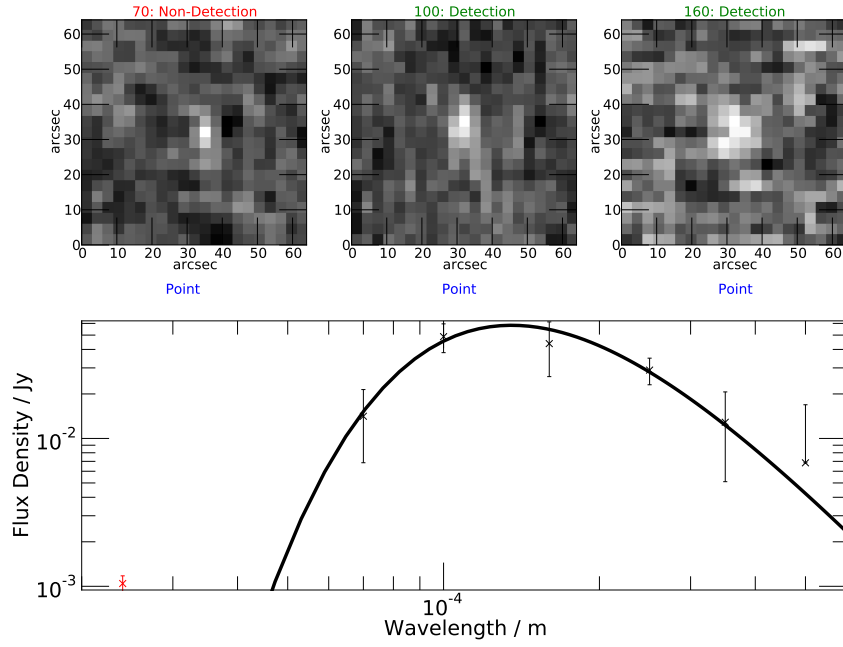


Figure A.17: Object 17: $T = 21.4\text{K}$, $\log_{10} \left(\frac{M_{Dust}}{M_{\odot}} \right) = 6.3$, $\log_{10} \left(\frac{M_{*}}{M_{\odot}} \right) = 8.5$

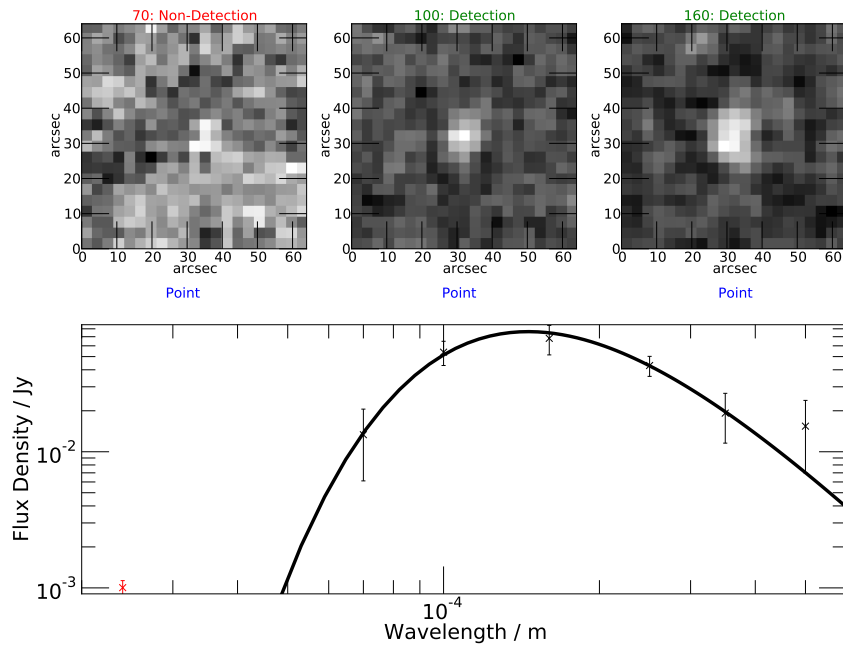


Figure A.18: Object 18: $T = 19.9\text{K}$, $\log_{10} \left(\frac{M_{Dust}}{M_{\odot}} \right) = 6.6$, $\log_{10} \left(\frac{M_{*}}{M_{\odot}} \right) = 8.9$

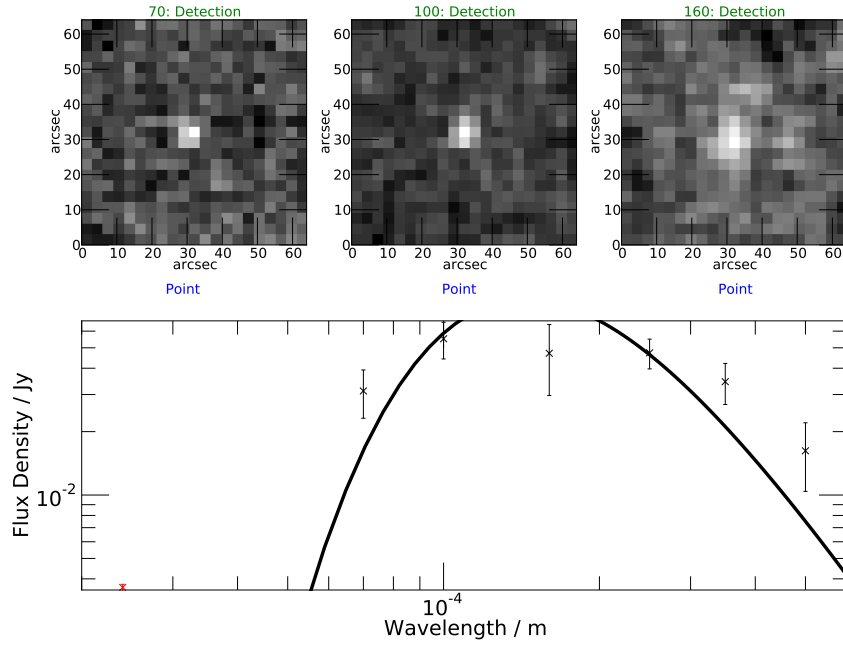


Figure A.19: Object 19: $T = 20.2\text{K}$, $\log_{10} \left(\frac{M_{Dust}}{M_{\odot}} \right) = 6.6$, $\log_{10} \left(\frac{M_{*}}{M_{\odot}} \right) = 10.1$

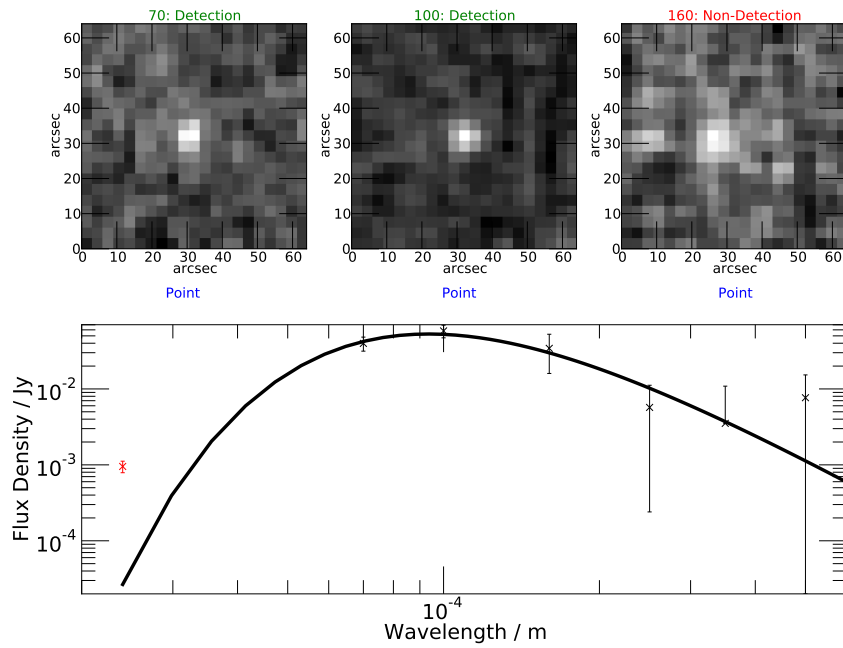


Figure A.20: Object 20: $T = 31.0\text{K}$, $\log_{10} \left(\frac{M_{Dust}}{M_{\odot}} \right) = 5.4$, $\log_{10} \left(\frac{M_{*}}{M_{\odot}} \right) = 10.5$

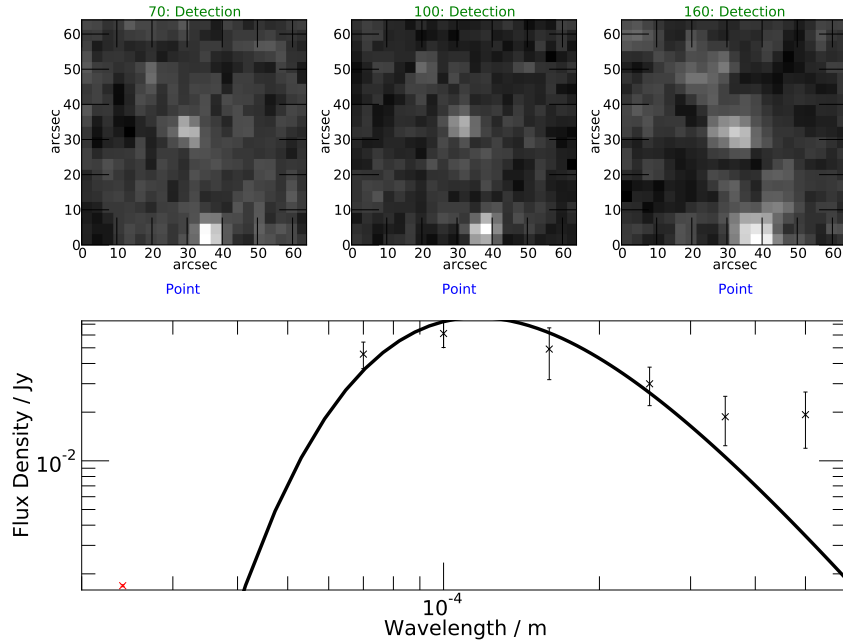


Figure A.21: Object 21: $T = 24.9\text{K}$, $\log_{10} \left(\frac{M_{Dust}}{M_{\odot}} \right) = 6.1$, $\log_{10} \left(\frac{M_{*}}{M_{\odot}} \right) = 10.3$

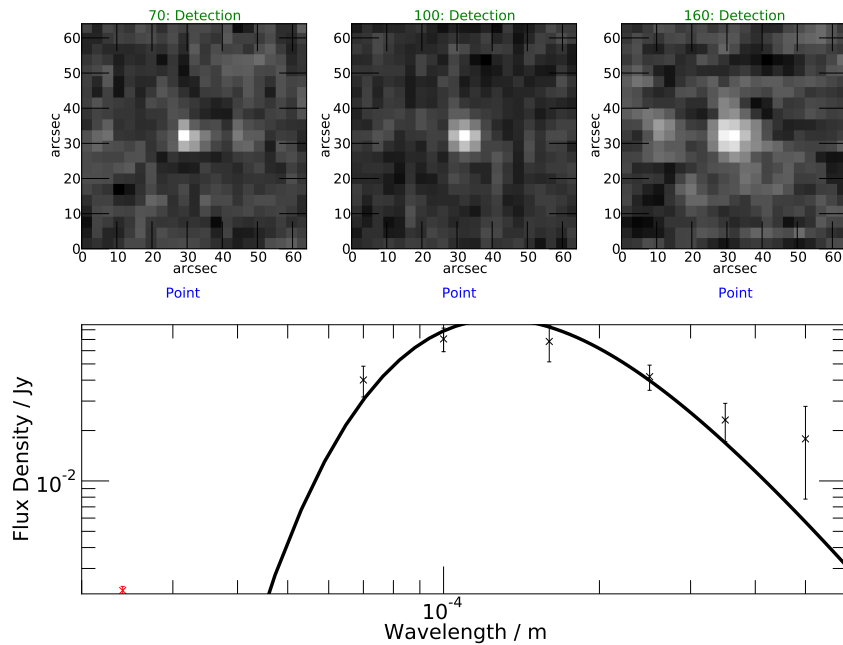


Figure A.22: Object 22: $T = 22.6\text{K}$, $\log_{10} \left(\frac{M_{Dust}}{M_{\odot}} \right) = 6.4$, $\log_{10} \left(\frac{M_{*}}{M_{\odot}} \right) = 10.6$

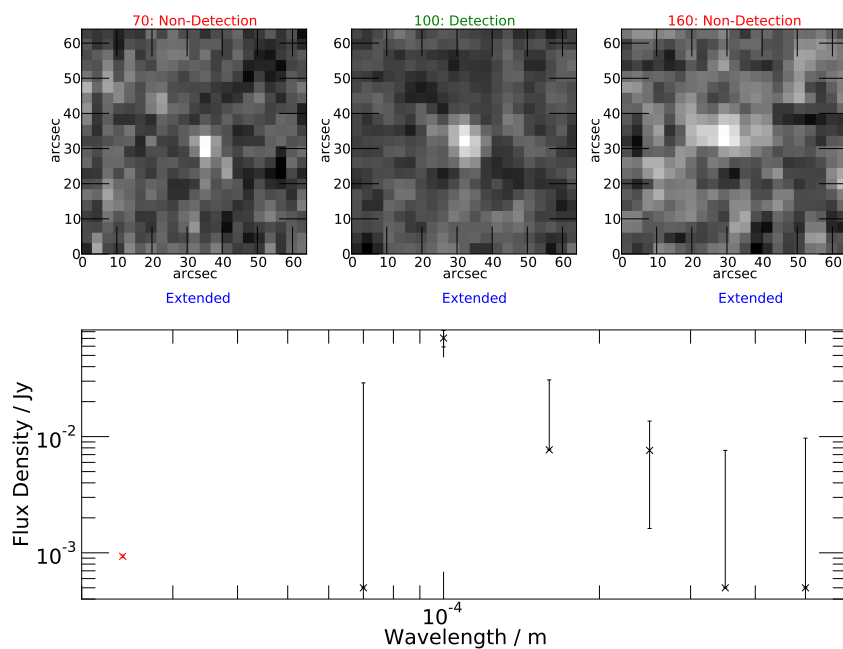


Figure A.23: Object 23: No constraint on fit, therefore no parameters can be derived.

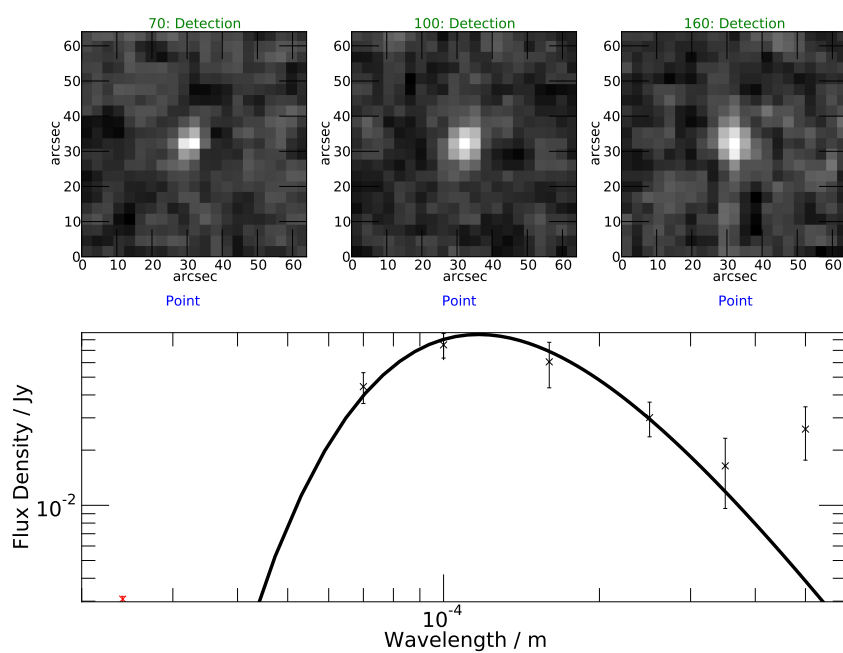


Figure A.24: Object 24: $T = 24.8\text{K}$, $\log_{10} \left(\frac{M_{Dust}}{M_{\odot}} \right) = 6.1$, $\log_{10} \left(\frac{M_{*}}{M_{\odot}} \right) = 9.9$

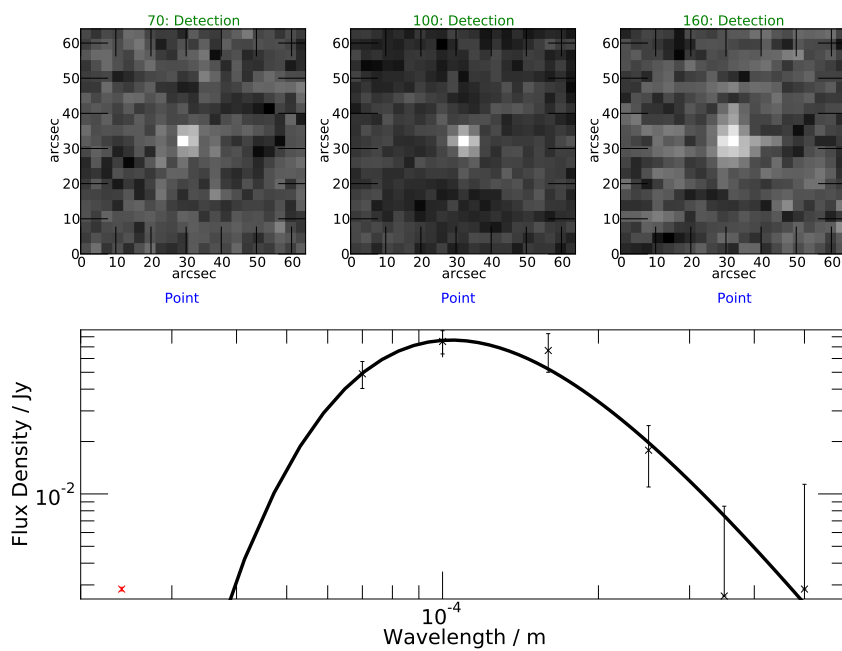


Figure A.25: Object 25: $T = 27.9\text{K}$, $\log_{10} \left(\frac{M_{Dust}}{M_{\odot}} \right) = 5.8$, $\log_{10} \left(\frac{M_{*}}{M_{\odot}} \right) = 10.2$

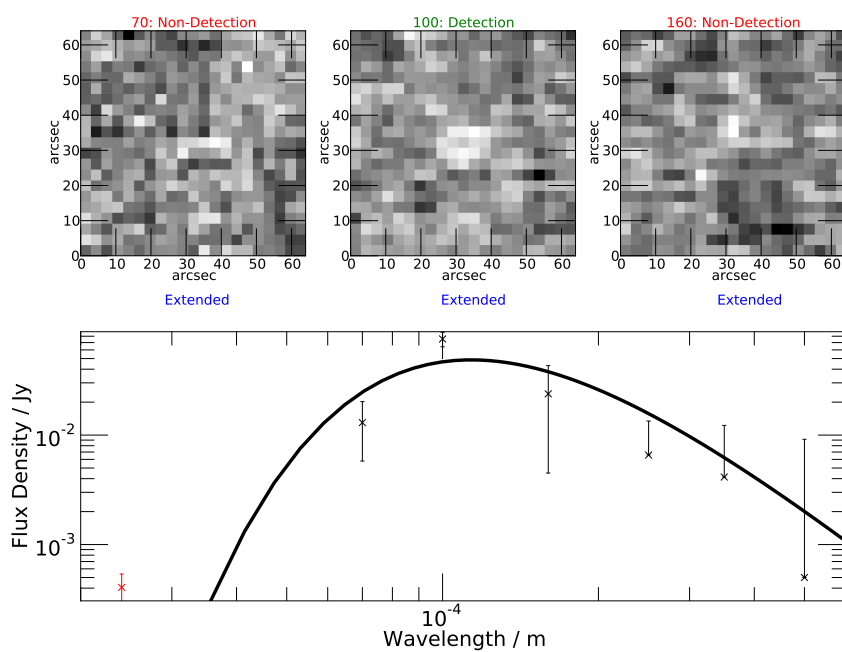


Figure A.26: Object 26: $T = 25.5\text{K}$, $\log_{10} \left(\frac{M_{Dust}}{M_{\odot}} \right) = 5.8$, $\log_{10} \left(\frac{M_{*}}{M_{\odot}} \right) = 10.3$

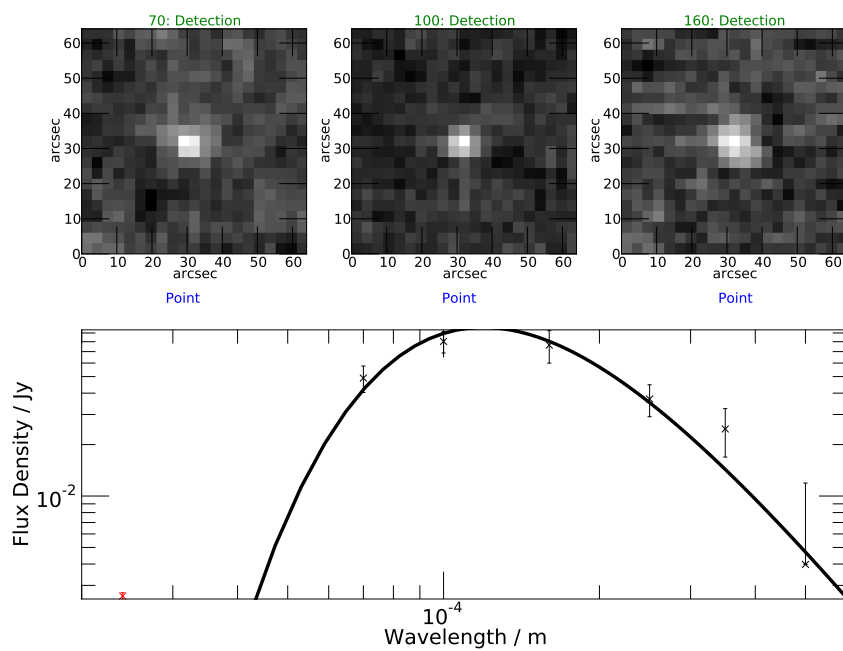


Figure A.27: Object 27: $T = 24.3\text{K}$, $\log_{10} \left(\frac{M_{Dust}}{M_{\odot}} \right) = 6.2$, $\log_{10} \left(\frac{M_{*}}{M_{\odot}} \right) = 10.6$

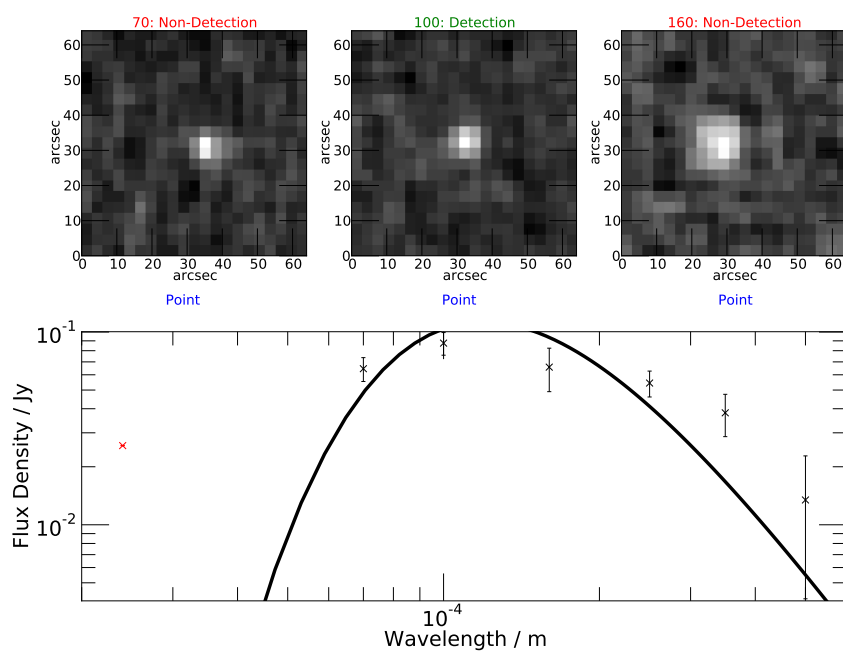


Figure A.28: Object 28: $T = 24.3\text{K}$, $\log_{10} \left(\frac{M_{Dust}}{M_{\odot}} \right) = 6.3$, $\log_{10} \left(\frac{M_{*}}{M_{\odot}} \right) = 8.5$

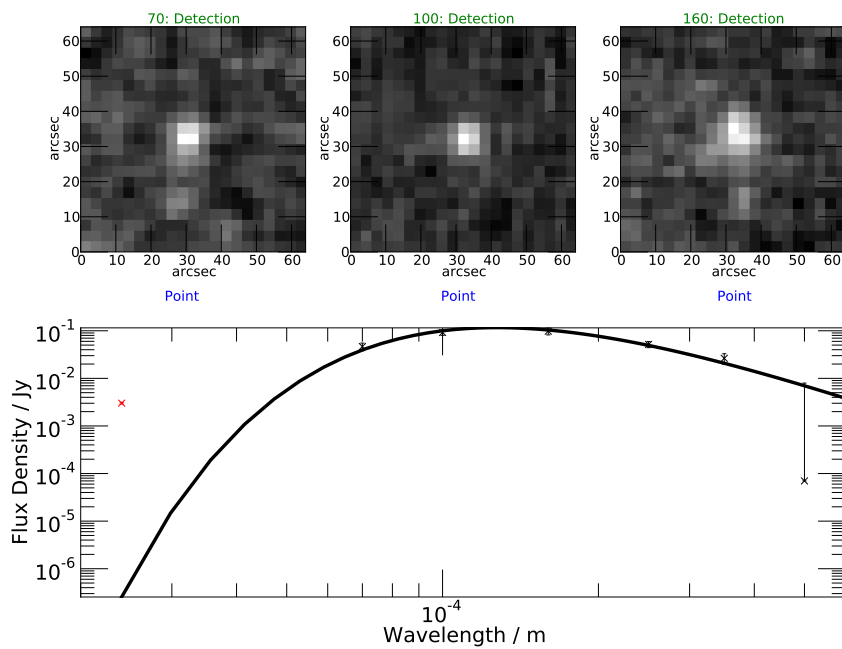


Figure A.29: Object 29: $T = 22.8\text{K}$, $\log_{10} \left(\frac{M_{Dust}}{M_{\odot}} \right) = 6.4$, $\log_{10} \left(\frac{M_{*}}{M_{\odot}} \right) = 9.4$

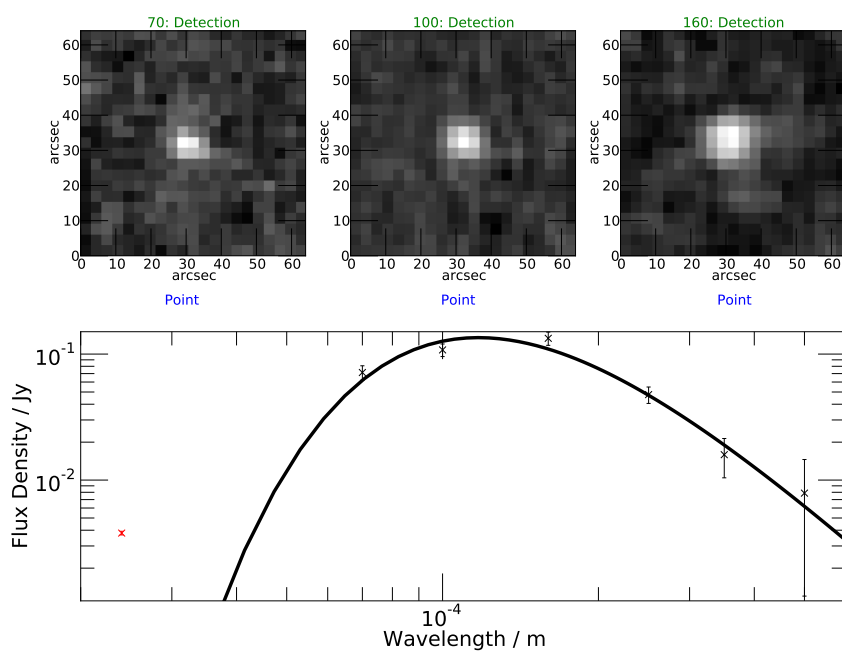


Figure A.30: Object 30: $T = 24.7\text{K}$, $\log_{10} \left(\frac{M_{Dust}}{M_{\odot}} \right) = 6.3$, $\log_{10} \left(\frac{M_{*}}{M_{\odot}} \right) = 9.1$

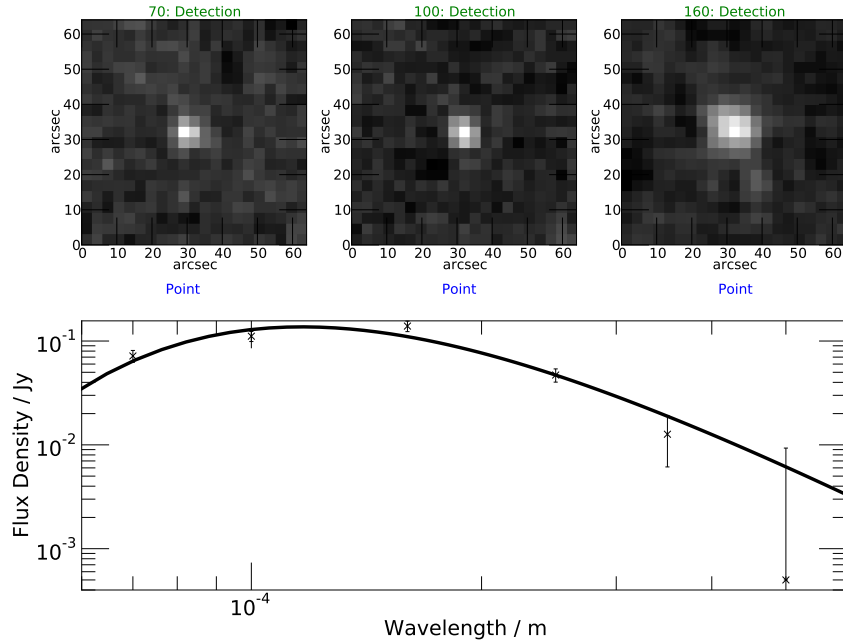


Figure A.31: Object 31: $T = 24.9\text{K}$, $\log_{10} \left(\frac{M_{Dust}}{M_{\odot}} \right) = 6.3$, $\log_{10} \left(\frac{M_{*}}{M_{\odot}} \right) = 9.3$

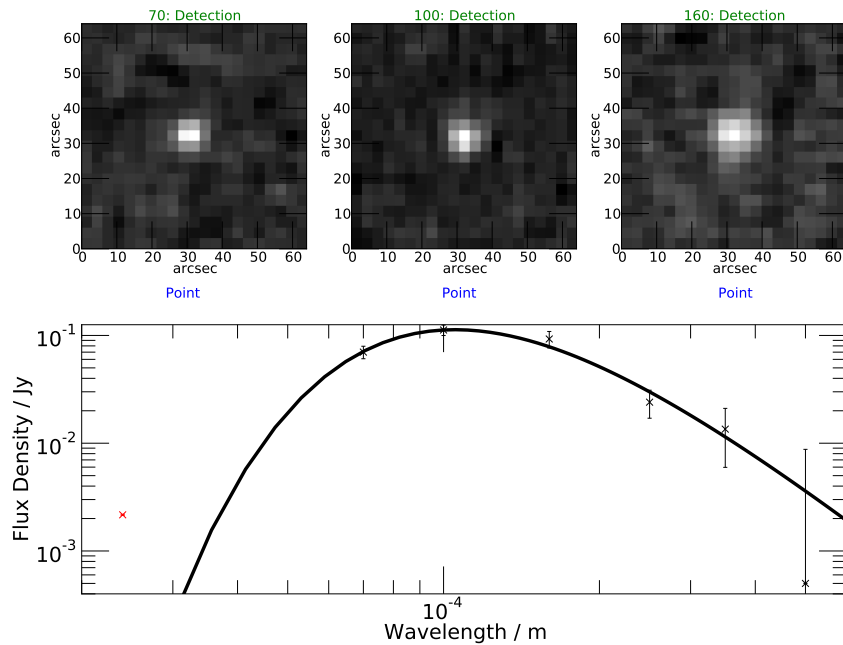


Figure A.32: Object 32: $T = 27.6\text{K}$, $\log_{10} \left(\frac{M_{Dust}}{M_{\odot}} \right) = 6.0$, $\log_{10} \left(\frac{M_{*}}{M_{\odot}} \right) = 10.4$

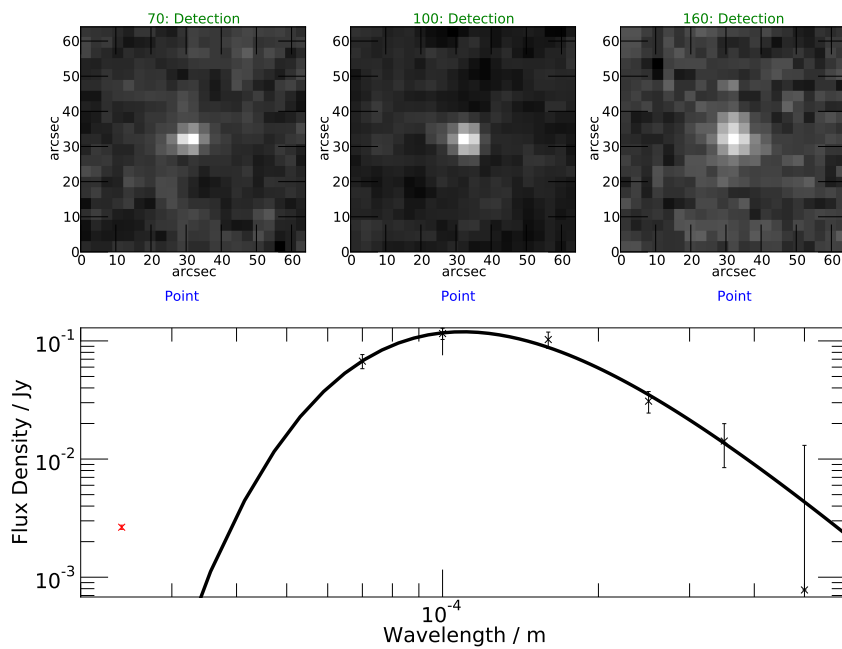


Figure A.33: Object 33: $T = 26.5\text{K}$, $\log_{10} \left(\frac{M_{Dust}}{M_{\odot}} \right) = 6.1$, $\log_{10} \left(\frac{M_{*}}{M_{\odot}} \right) = 10.4$

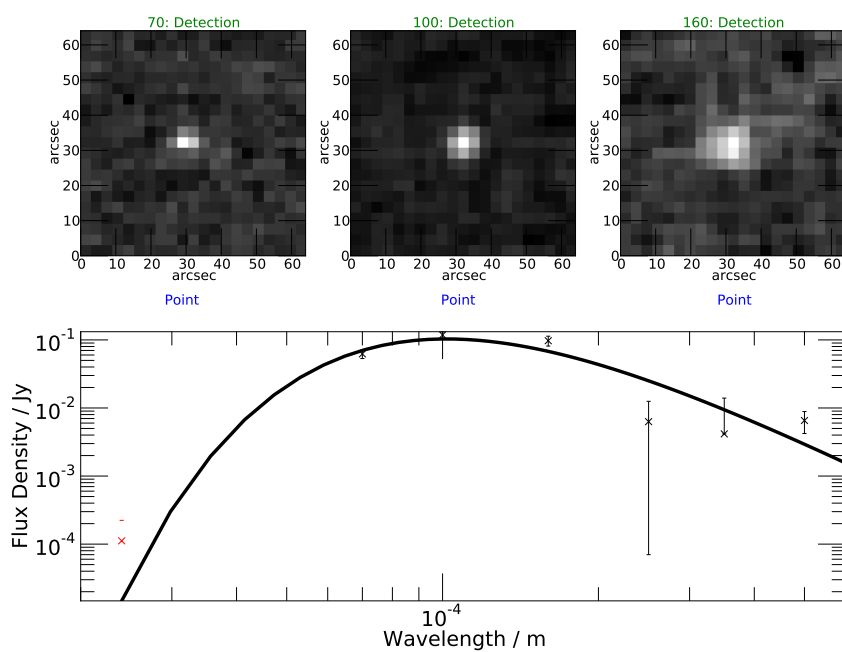


Figure A.34: Object 34: $T = 28.5\text{K}$, $\log_{10} \left(\frac{M_{Dust}}{M_{\odot}} \right) = 5.9$, $\log_{10} \left(\frac{M_{*}}{M_{\odot}} \right) = 10.4$

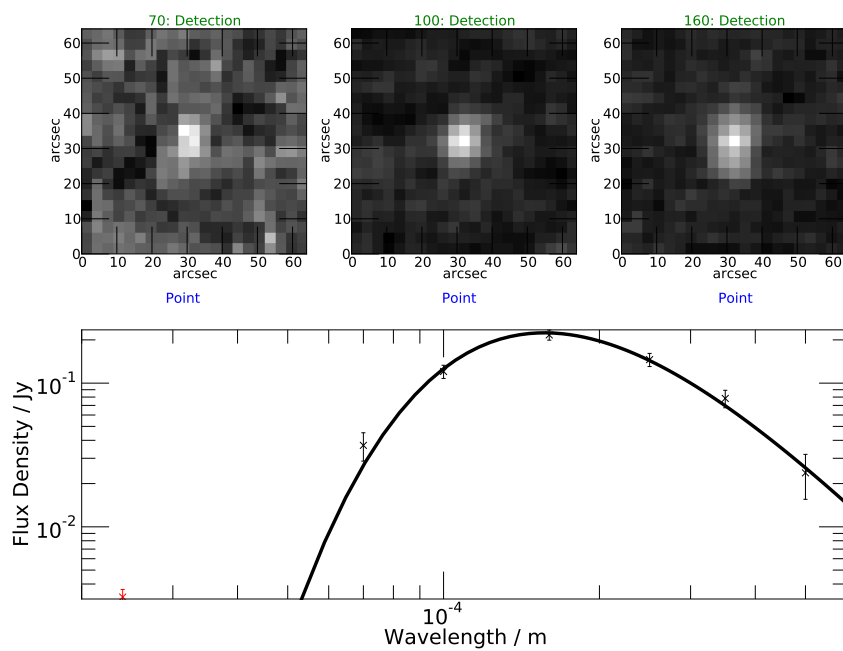


Figure A.35: Object 35: $T = 18.5\text{K}$, $\log_{10}\left(\frac{M_{Dust}}{M_{\odot}}\right) = 7.2$, $\log_{10}\left(\frac{M_{*}}{M_{\odot}}\right) = 10.3$

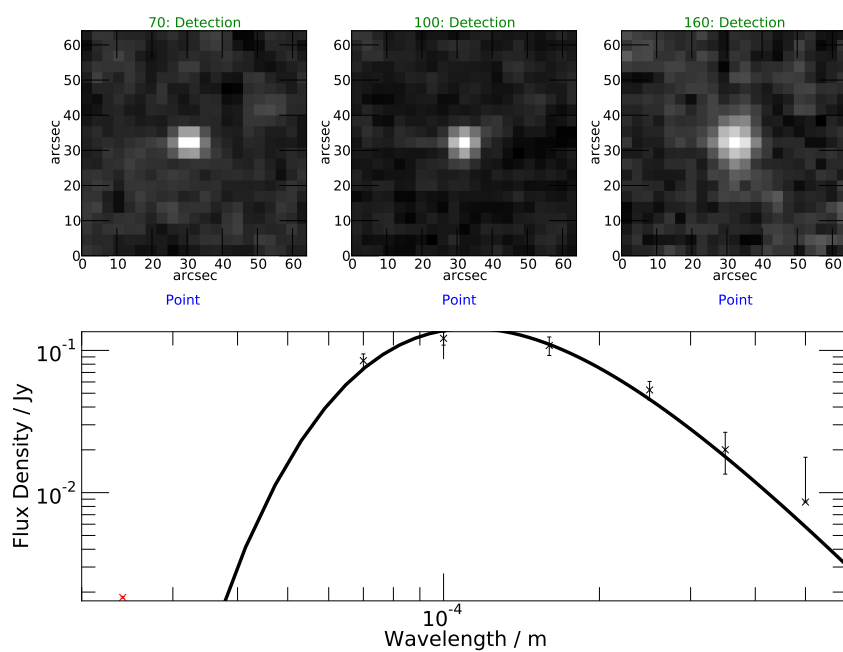


Figure A.36: Object 36: $T = 25.7\text{K}$, $\log_{10}\left(\frac{M_{Dust}}{M_{\odot}}\right) = 6.3$, $\log_{10}\left(\frac{M_{*}}{M_{\odot}}\right) = 10.4$

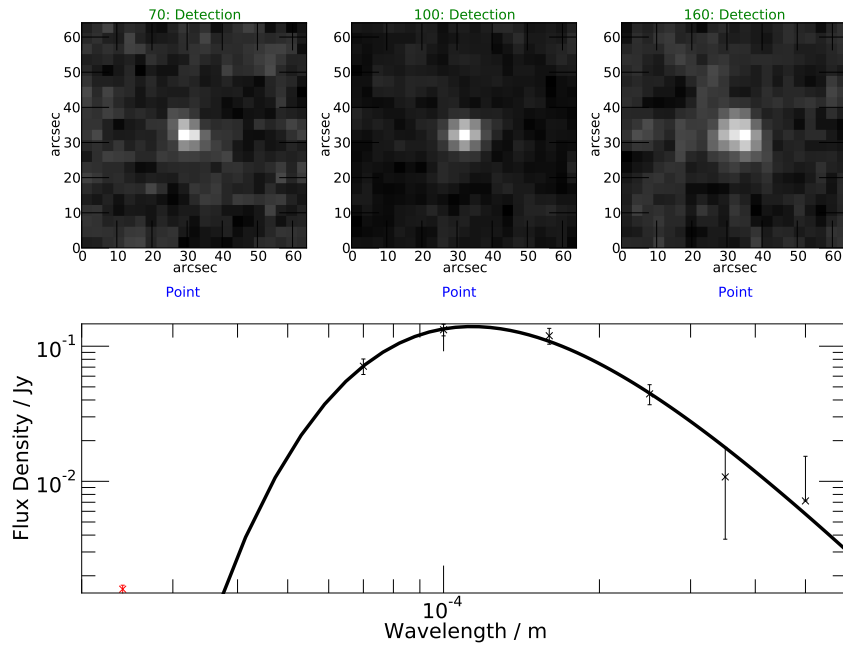


Figure A.37: Object 37: $T = 25.6\text{K}$, $\log_{10} \left(\frac{M_{Dust}}{M_{\odot}} \right) = 6.3$, $\log_{10} \left(\frac{M_{*}}{M_{\odot}} \right) = 10.4$

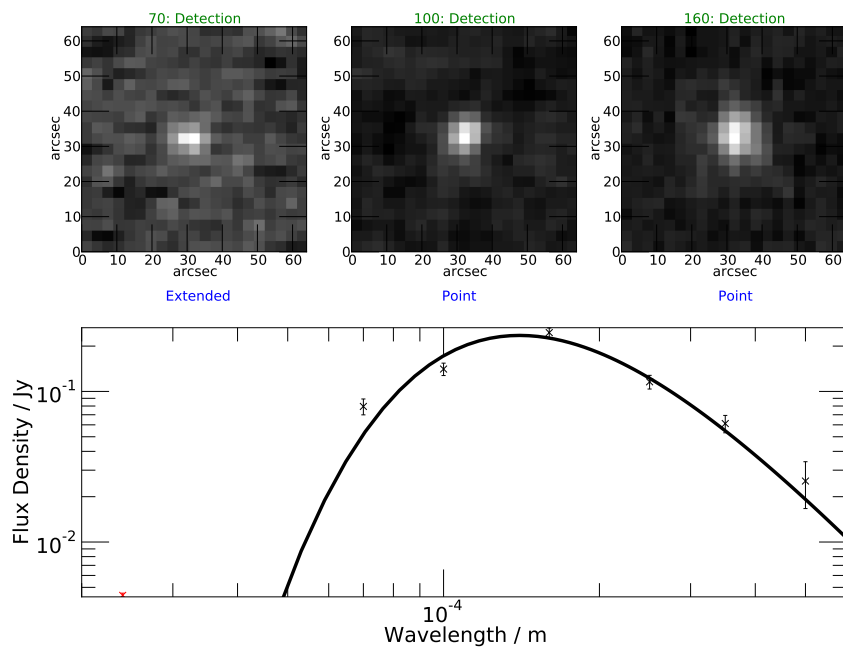


Figure A.38: Object 38: $T = 20.7\text{K}$, $\log_{10} \left(\frac{M_{Dust}}{M_{\odot}} \right) = 7.0$, $\log_{10} \left(\frac{M_{*}}{M_{\odot}} \right) = 9.9$

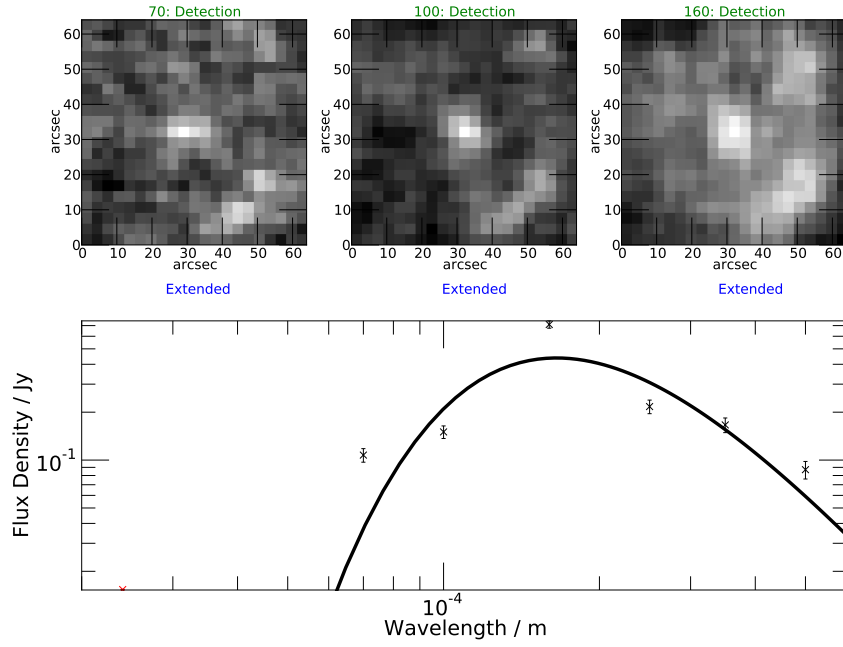


Figure A.39: Object 39: $T = 17.6\text{K}$, $\log_{10} \left(\frac{M_{Dust}}{M_{\odot}} \right) = 7.6$, $\log_{10} \left(\frac{M_{*}}{M_{\odot}} \right) = 11.1$

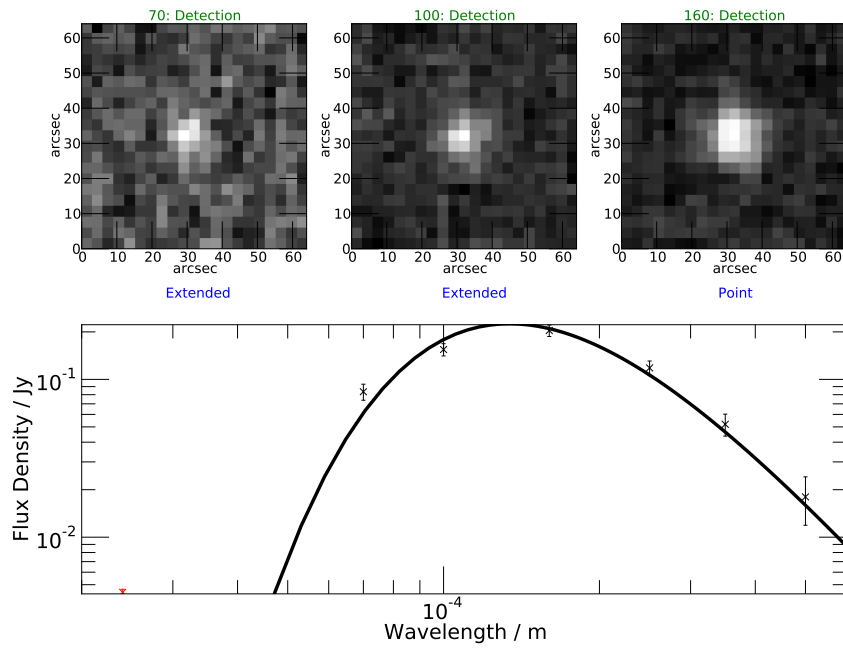


Figure A.40: Object 40: $T = 21.6\text{K}$, $\log_{10} \left(\frac{M_{Dust}}{M_{\odot}} \right) = 6.8$, $\log_{10} \left(\frac{M_{*}}{M_{\odot}} \right) = 9.7$

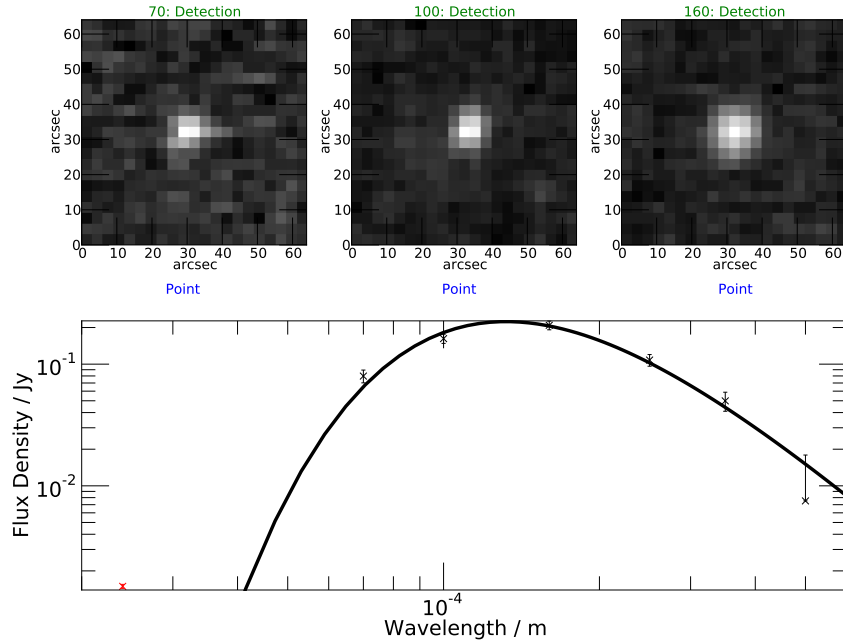


Figure A.41: Object 41: $T = 22.0\text{K}$, $\log_{10} \left(\frac{M_{Dust}}{M_{\odot}} \right) = 6.8$, $\log_{10} \left(\frac{M_{*}}{M_{\odot}} \right) = 9.4$

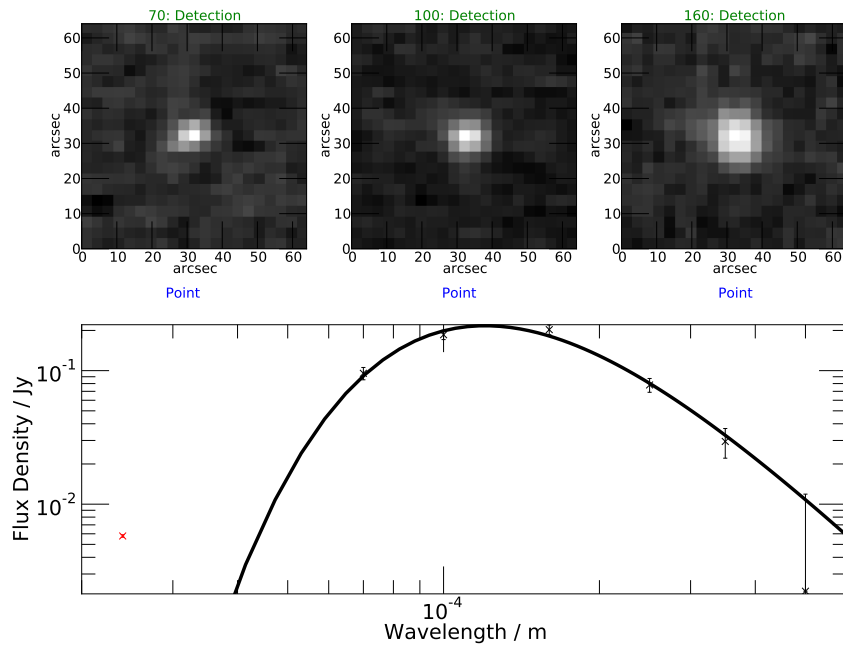


Figure A.42: Object 42: $T = 24.1\text{K}$, $\log_{10} \left(\frac{M_{Dust}}{M_{\odot}} \right) = 6.6$, $\log_{10} \left(\frac{M_{*}}{M_{\odot}} \right) = 9.4$

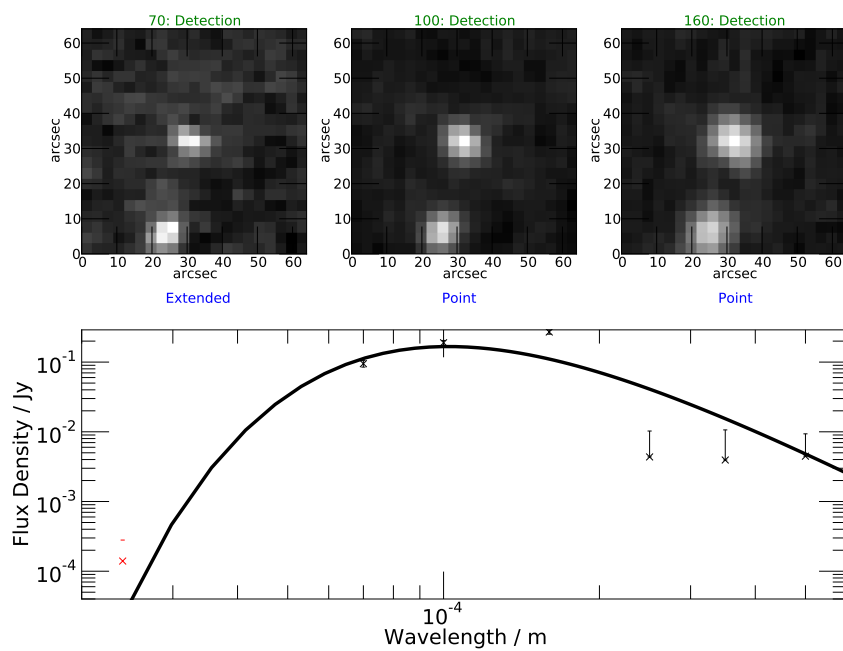


Figure A.43: Object 43: $T = 28.4\text{K}$, $\log_{10} \left(\frac{M_{Dust}}{M_{\odot}} \right) = 6.1$, $\log_{10} \left(\frac{M_{*}}{M_{\odot}} \right) = 9.7$

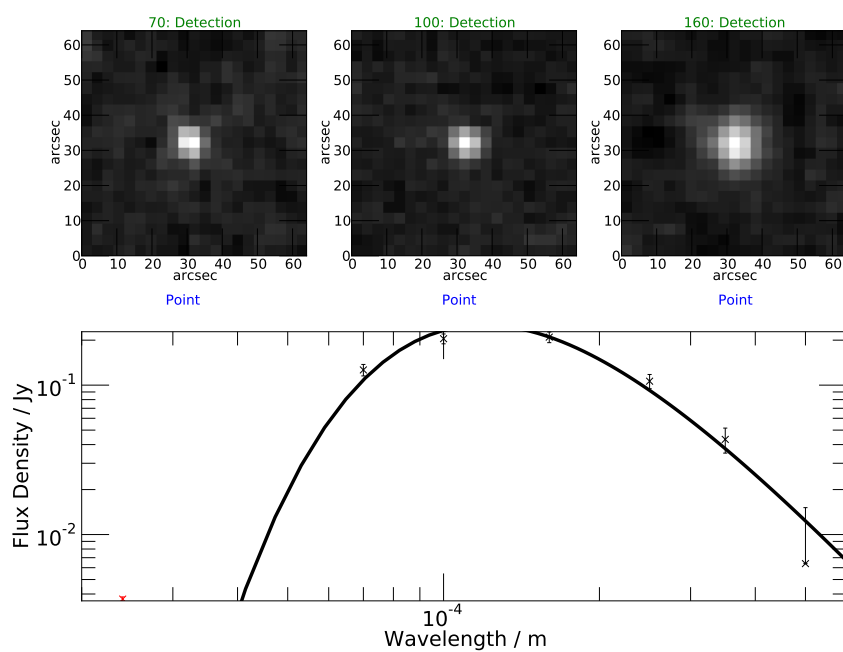


Figure A.44: Object 44: $T = 24.3\text{K}$, $\log_{10} \left(\frac{M_{Dust}}{M_{\odot}} \right) = 6.6$, $\log_{10} \left(\frac{M_{*}}{M_{\odot}} \right) = 10.6$

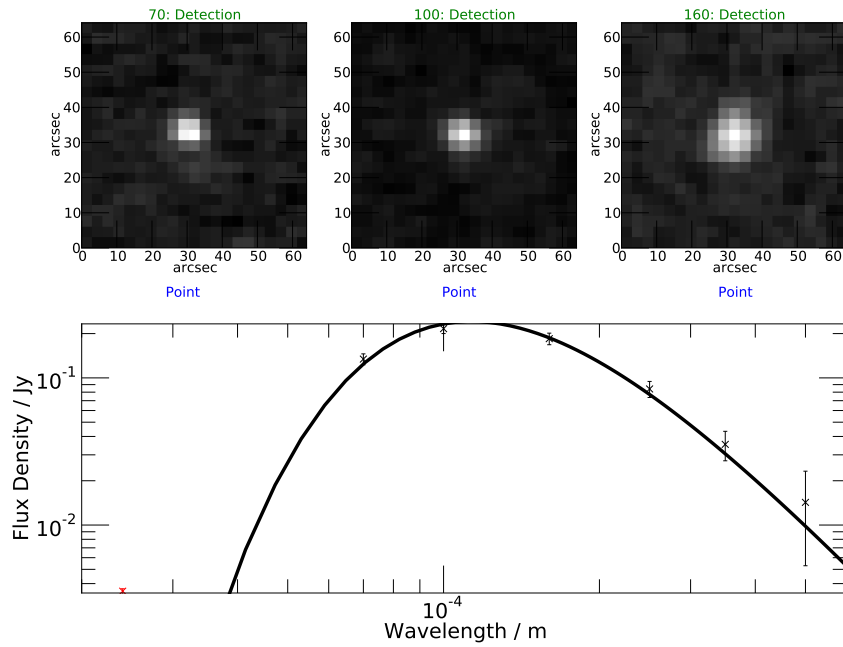


Figure A.45: Object 45: $T = 25.7\text{K}$, $\log_{10} \left(\frac{M_{Dust}}{M_{\odot}} \right) = 6.5$, $\log_{10} \left(\frac{M_{*}}{M_{\odot}} \right) = 10.5$

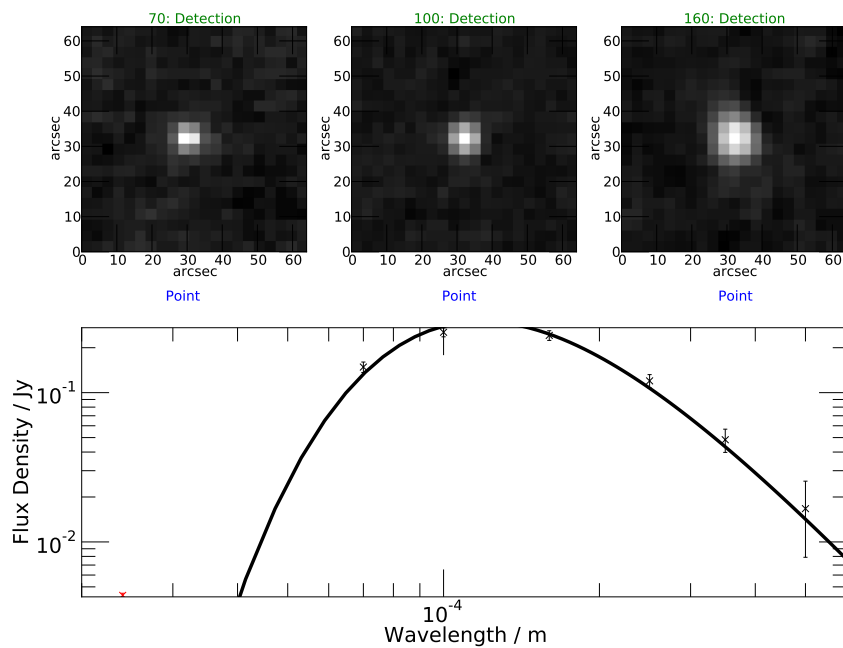


Figure A.46: Object 46: $T = 24.5\text{K}$, $\log_{10} \left(\frac{M_{Dust}}{M_{\odot}} \right) = 6.7$, $\log_{10} \left(\frac{M_{*}}{M_{\odot}} \right) = 10.6$

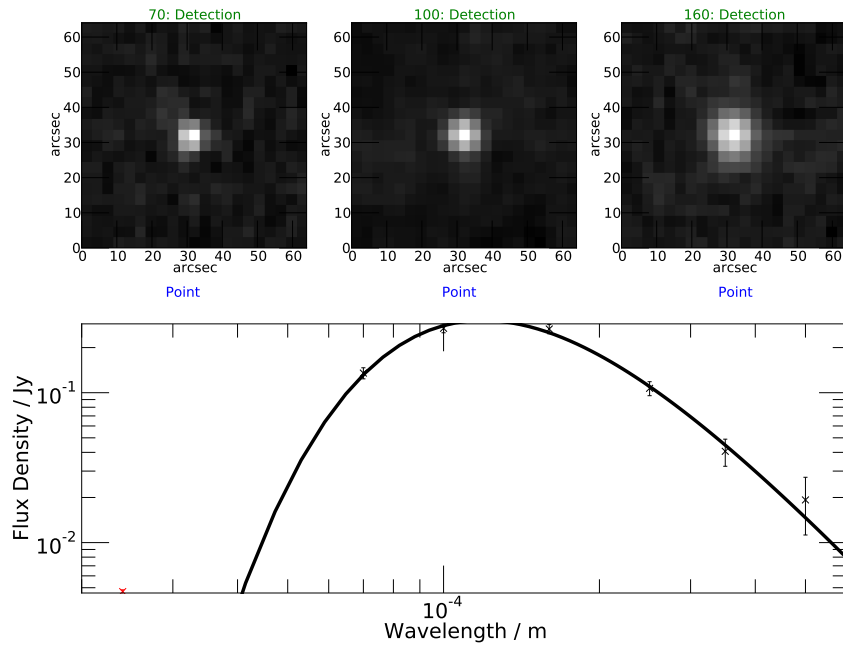


Figure A.47: Object 47: $T = 24.3\text{K}$, $\log_{10} \left(\frac{M_{Dust}}{M_{\odot}} \right) = 6.7$, $\log_{10} \left(\frac{M_{*}}{M_{\odot}} \right) = 10.5$

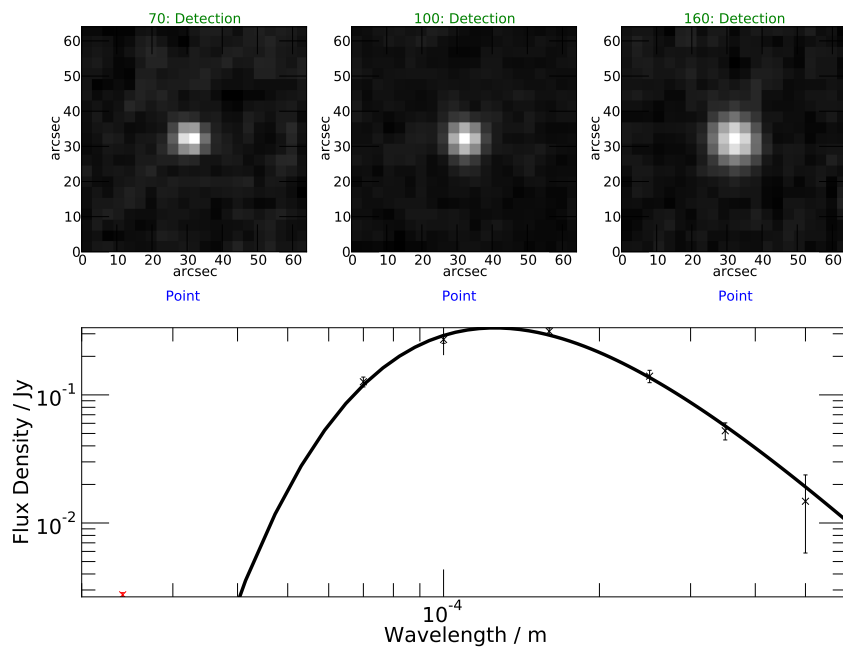


Figure A.48: Object 48: $T = 23.1\text{K}$, $\log_{10} \left(\frac{M_{Dust}}{M_{\odot}} \right) = 6.9$, $\log_{10} \left(\frac{M_{*}}{M_{\odot}} \right) = 10.7$

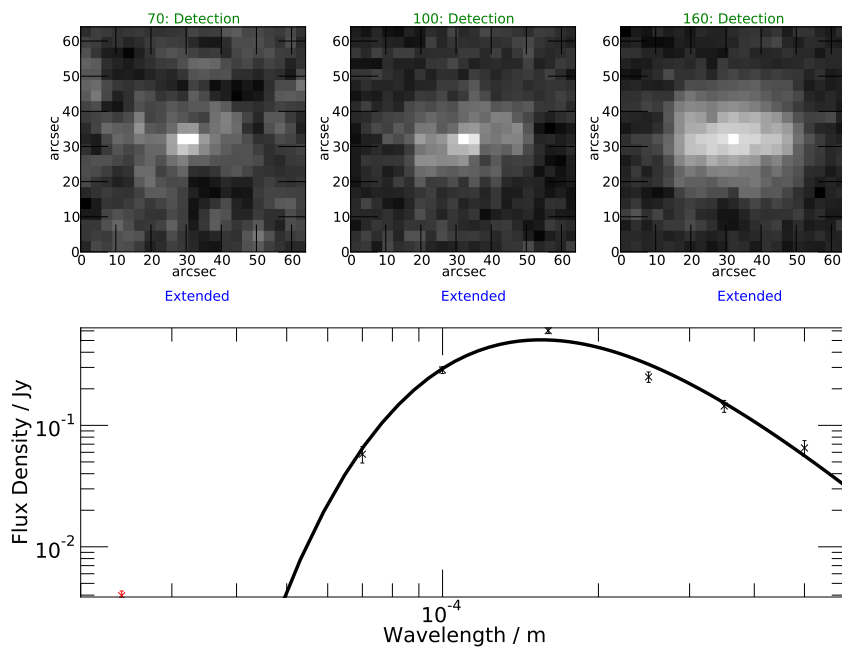


Figure A.49: Object 49: $T = 18.7\text{K}$, $\log_{10} \left(\frac{M_{Dust}}{M_{\odot}} \right) = 7.5$, $\log_{10} \left(\frac{M_{*}}{M_{\odot}} \right) = 10.8$

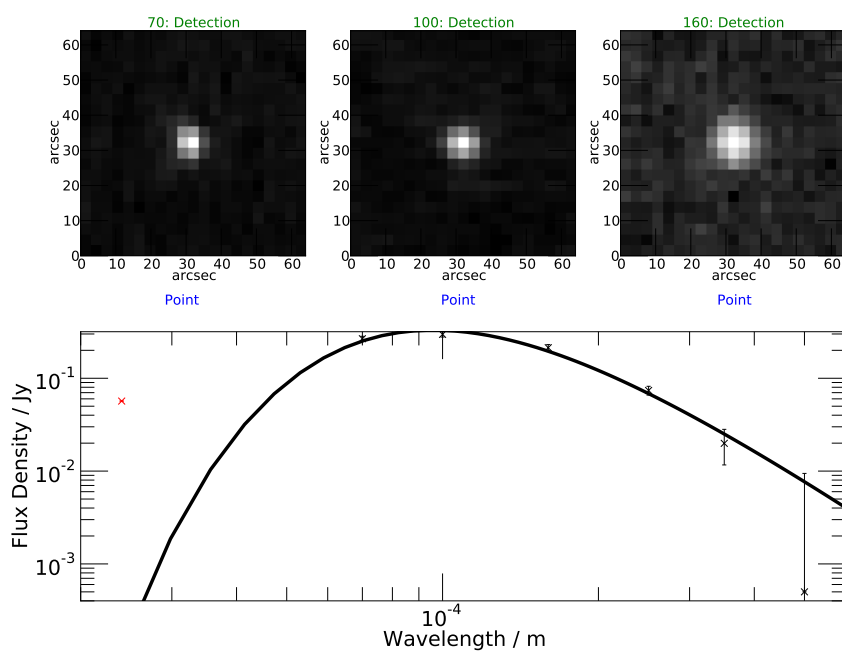


Figure A.50: Object 50: $T = 30.2\text{K}$, $\log_{10} \left(\frac{M_{Dust}}{M_{\odot}} \right) = 6.3$, $\log_{10} \left(\frac{M_{*}}{M_{\odot}} \right) = 9.6$

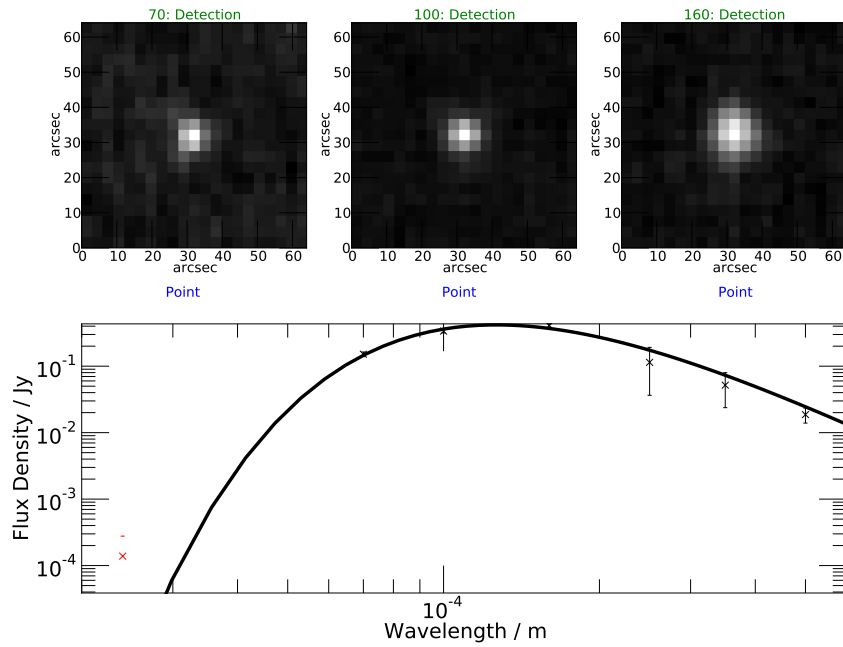


Figure A.51: Object 51: $T = 23.0\text{K}$, $\log_{10} \left(\frac{M_{Dust}}{M_{\odot}} \right) = 7.0$, $\log_{10} \left(\frac{M_{*}}{M_{\odot}} \right) = 10.8$

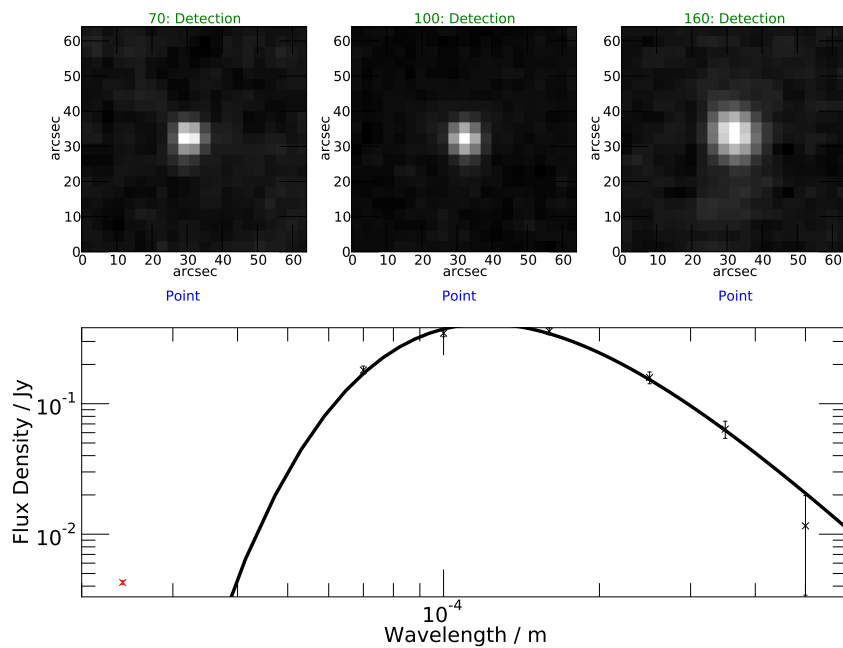


Figure A.52: Object 52: $T = 24.1\text{K}$, $\log_{10} \left(\frac{M_{Dust}}{M_{\odot}} \right) = 6.9$, $\log_{10} \left(\frac{M_{*}}{M_{\odot}} \right) = 10.7$

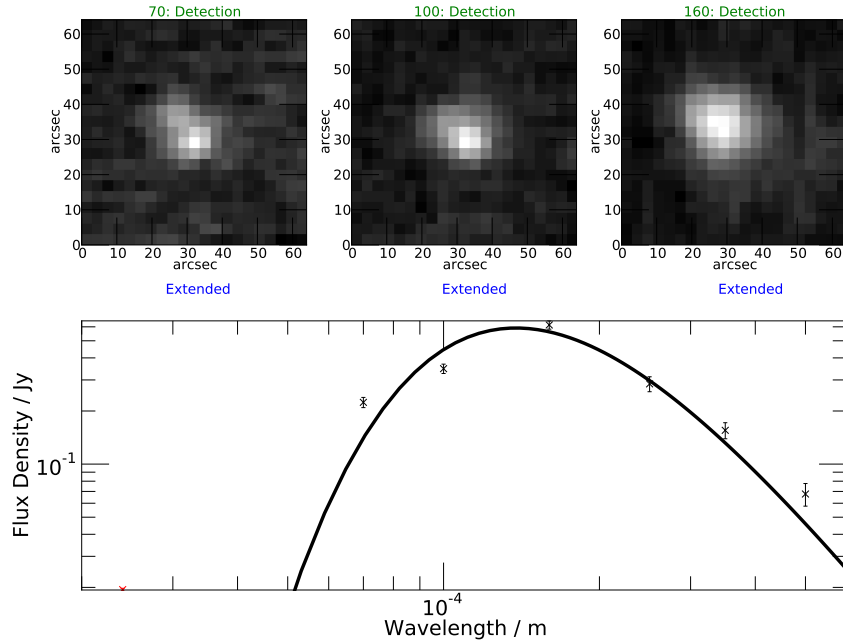


Figure A.53: Object 53: $T = 21.0\text{K}$, $\log_{10} \left(\frac{M_{Dust}}{M_{\odot}} \right) = 7.3$, $\log_{10} \left(\frac{M_{*}}{M_{\odot}} \right) = 9.9$

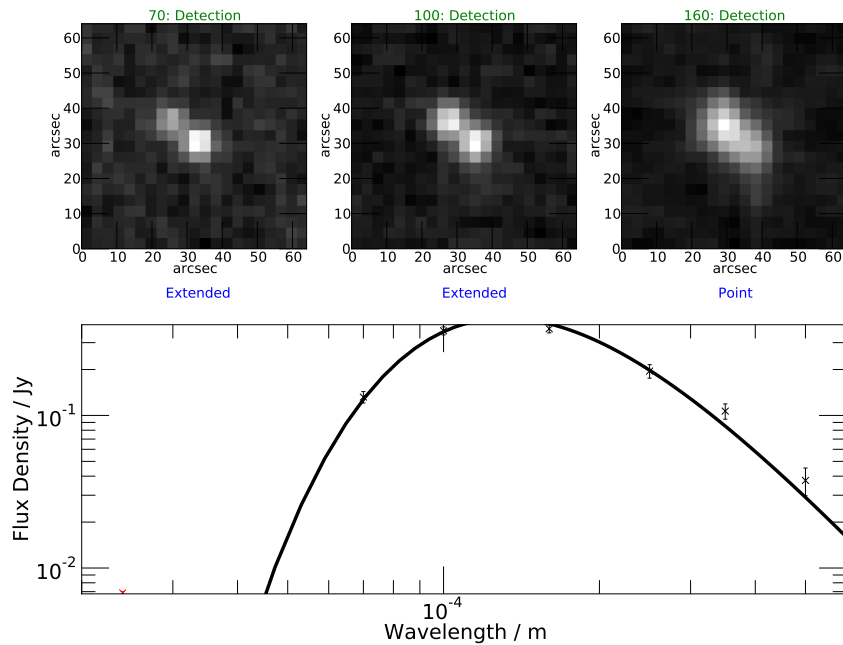


Figure A.54: Object 54: $T = 22.0\text{K}$, $\log_{10} \left(\frac{M_{Dust}}{M_{\odot}} \right) = 7.1$, $\log_{10} \left(\frac{M_{*}}{M_{\odot}} \right) = 9.7$

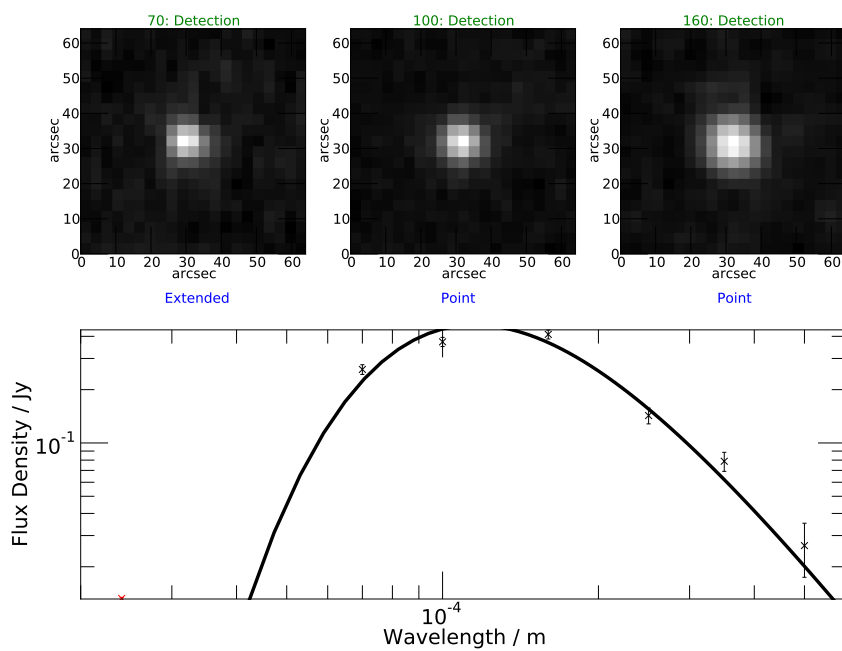


Figure A.55: Object 55: $T = 25.1\text{K}$, $\log_{10} \left(\frac{M_{Dust}}{M_{\odot}} \right) = 6.8$, $\log_{10} \left(\frac{M_{*}}{M_{\odot}} \right) = 9.5$

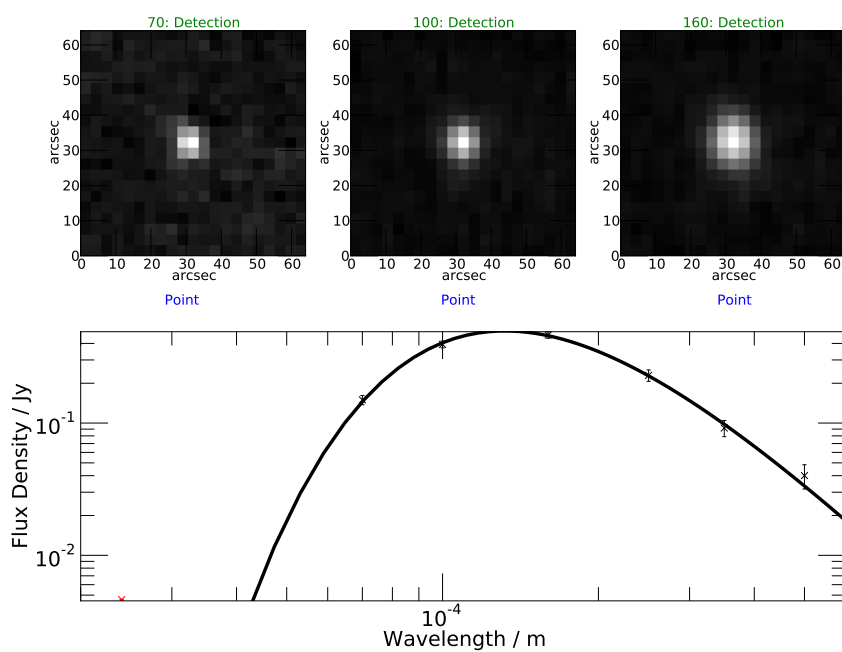


Figure A.56: Object 56: $T = 22.0\text{K}$, $\log_{10} \left(\frac{M_{Dust}}{M_{\odot}} \right) = 7.2$, $\log_{10} \left(\frac{M_{*}}{M_{\odot}} \right) = 10.9$

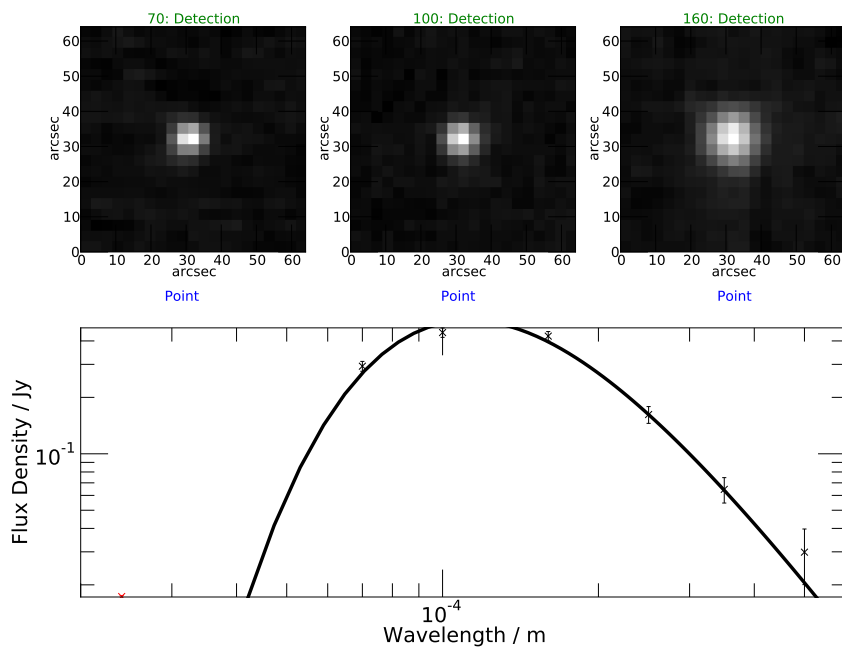


Figure A.57: Object 57: $T = 25.8\text{K}$, $\log_{10} \left(\frac{M_{Dust}}{M_{\odot}} \right) = 6.8$, $\log_{10} \left(\frac{M_{*}}{M_{\odot}} \right) = 9.4$

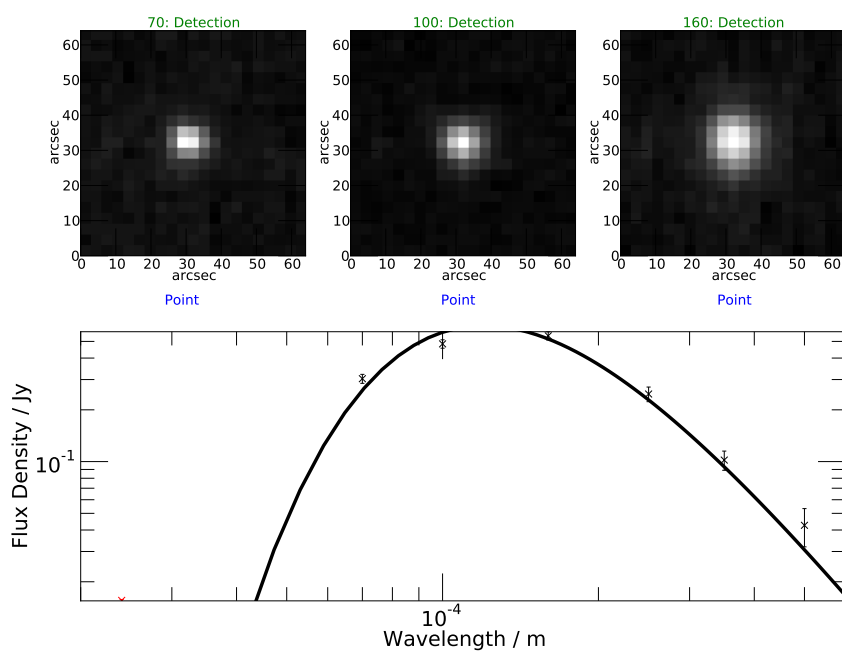


Figure A.58: Object 58: $T = 24.1\text{K}$, $\log_{10} \left(\frac{M_{Dust}}{M_{\odot}} \right) = 7.0$, $\log_{10} \left(\frac{M_{*}}{M_{\odot}} \right) = 9.6$

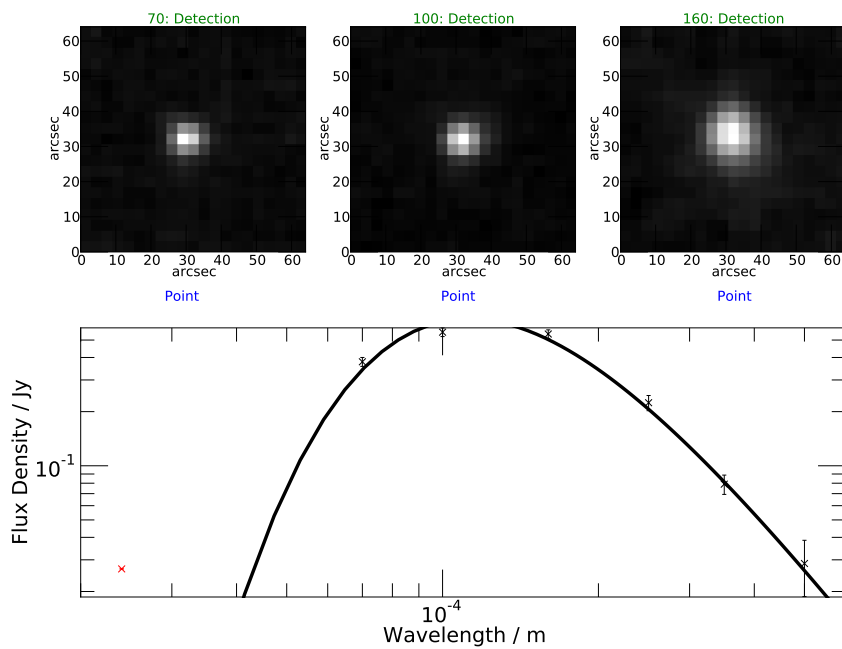


Figure A.59: Object 59: $T = 25.8\text{K}$, $\log_{10} \left(\frac{M_{Dust}}{M_{\odot}} \right) = 6.9$, $\log_{10} \left(\frac{M_{*}}{M_{\odot}} \right) = 9.9$

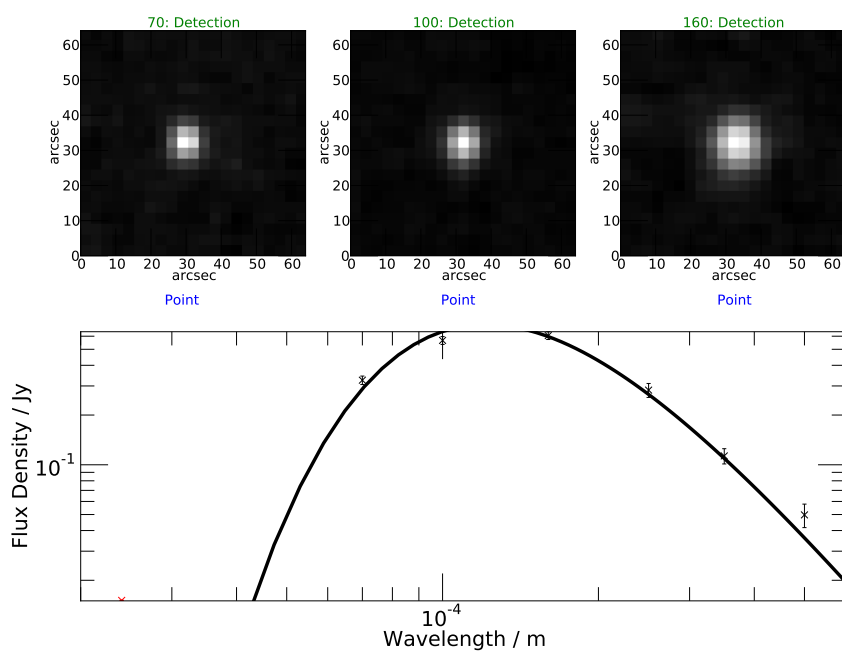


Figure A.60: Object 60: $T = 23.9\text{K}$, $\log_{10} \left(\frac{M_{Dust}}{M_{\odot}} \right) = 7.1$, $\log_{10} \left(\frac{M_{*}}{M_{\odot}} \right) = 9.7$

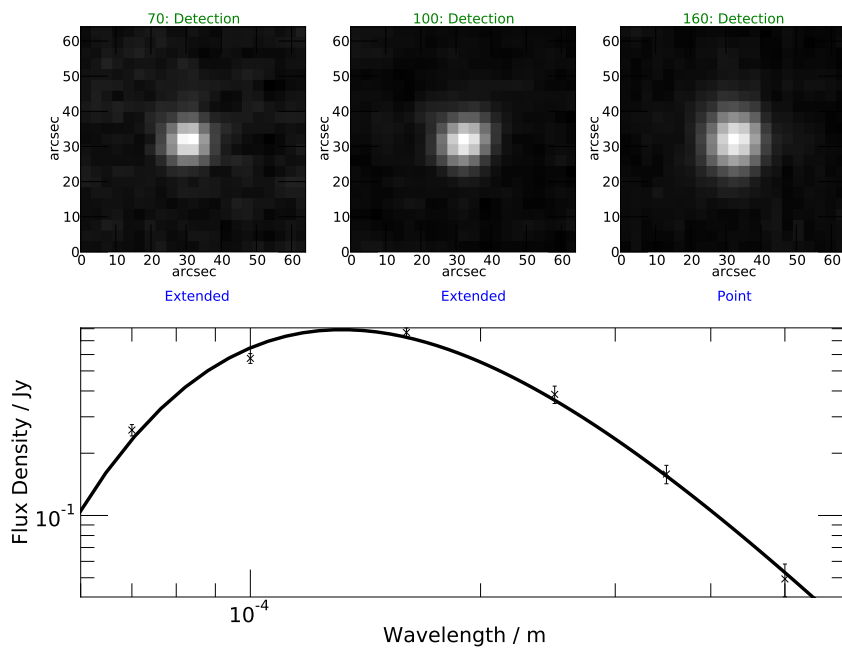


Figure A.61: Object 61: $T = 22.0\text{K}$, $\log_{10} \left(\frac{M_{Dust}}{M_{\odot}} \right) = 7.3$, $\log_{10} \left(\frac{M_{*}}{M_{\odot}} \right) = 10.2$

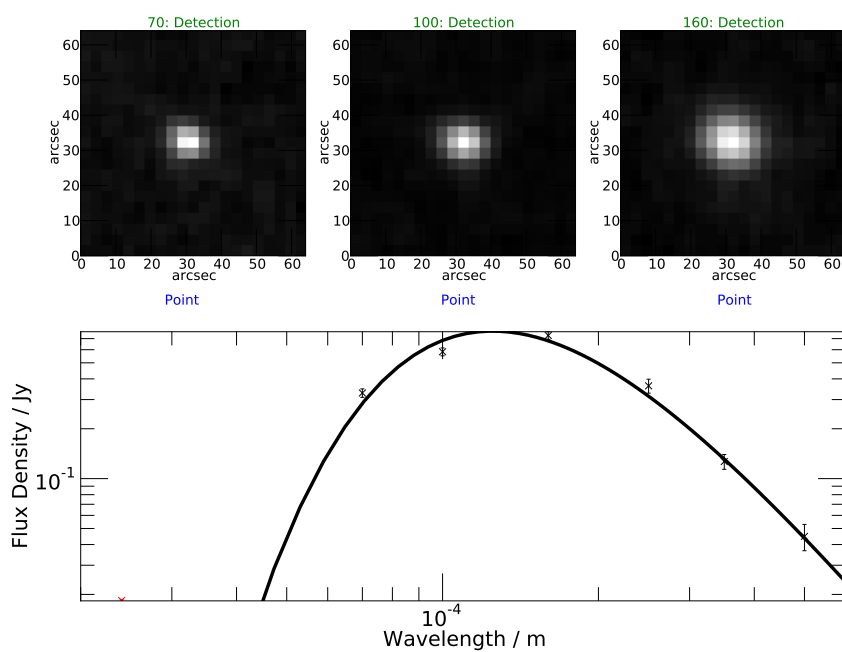


Figure A.62: Object 62: $T = 23.2\text{K}$, $\log_{10} \left(\frac{M_{Dust}}{M_{\odot}} \right) = 7.2$, $\log_{10} \left(\frac{M_{*}}{M_{\odot}} \right) = 10.0$

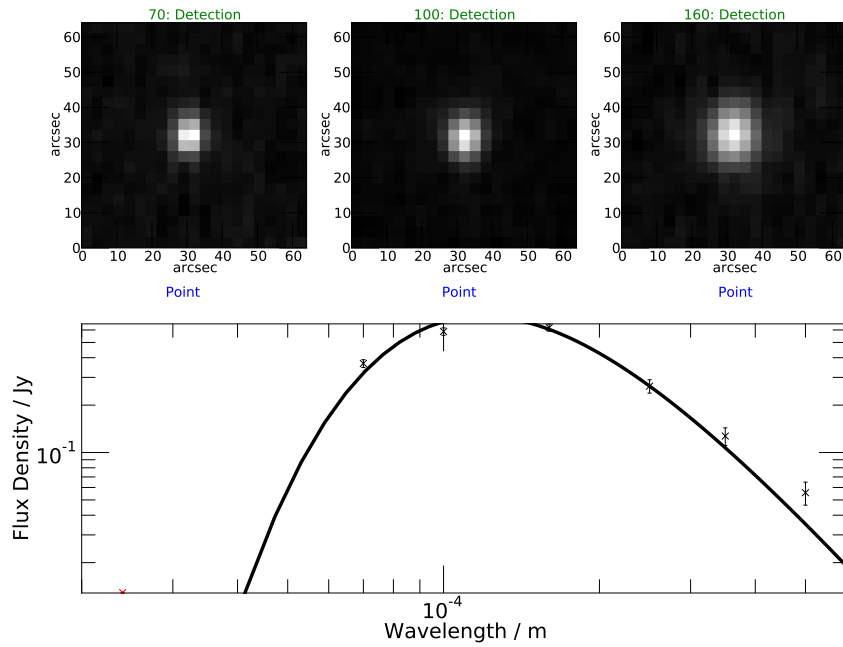


Figure A.63: Object 63: $T = 24.4\text{K}$, $\log_{10} \left(\frac{M_{Dust}}{M_{\odot}} \right) = 7.1$, $\log_{10} \left(\frac{M_{*}}{M_{\odot}} \right) = 9.3$

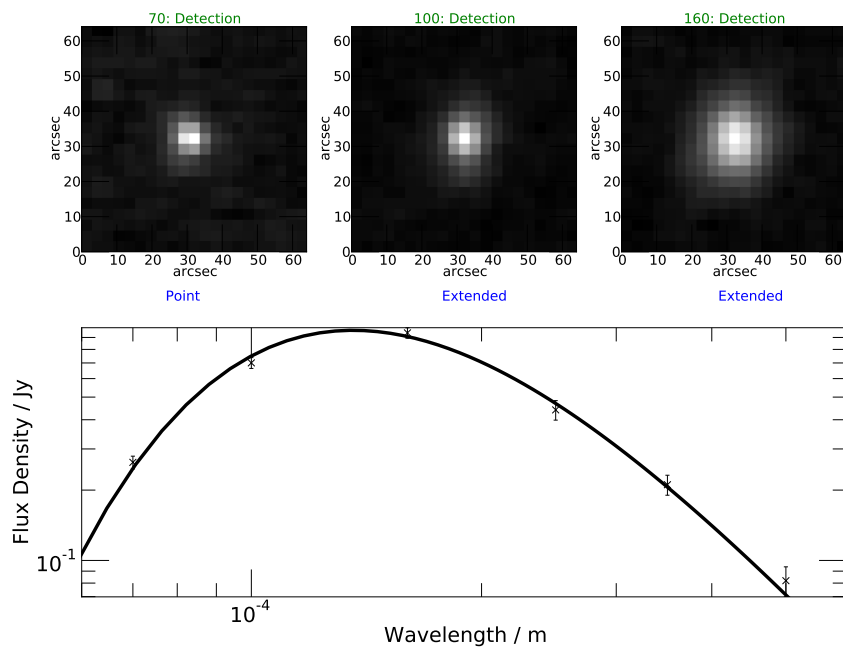


Figure A.64: Object 64: $T = 21.4\text{K}$, $\log_{10} \left(\frac{M_{Dust}}{M_{\odot}} \right) = 7.5$, $\log_{10} \left(\frac{M_{*}}{M_{\odot}} \right) = 10.9$

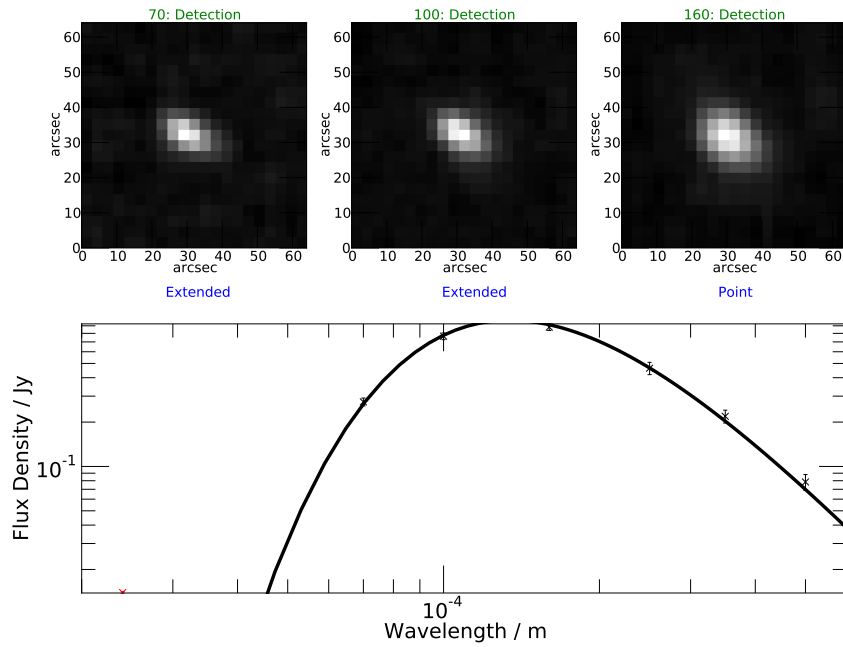


Figure A.65: Object 65: $T = 21.6\text{K}$, $\log_{10} \left(\frac{M_{Dust}}{M_{\odot}} \right) = 7.5$, $\log_{10} \left(\frac{M_{*}}{M_{\odot}} \right) = 10.4$

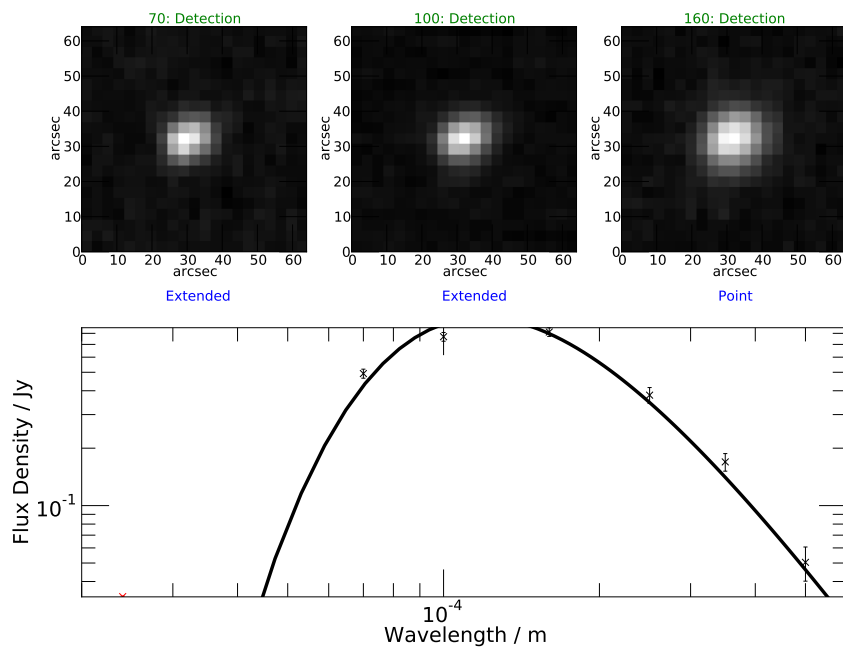


Figure A.66: Object 66: $T = 24.4\text{K}$, $\log_{10} \left(\frac{M_{Dust}}{M_{\odot}} \right) = 7.2$, $\log_{10} \left(\frac{M_{*}}{M_{\odot}} \right) = 9.6$

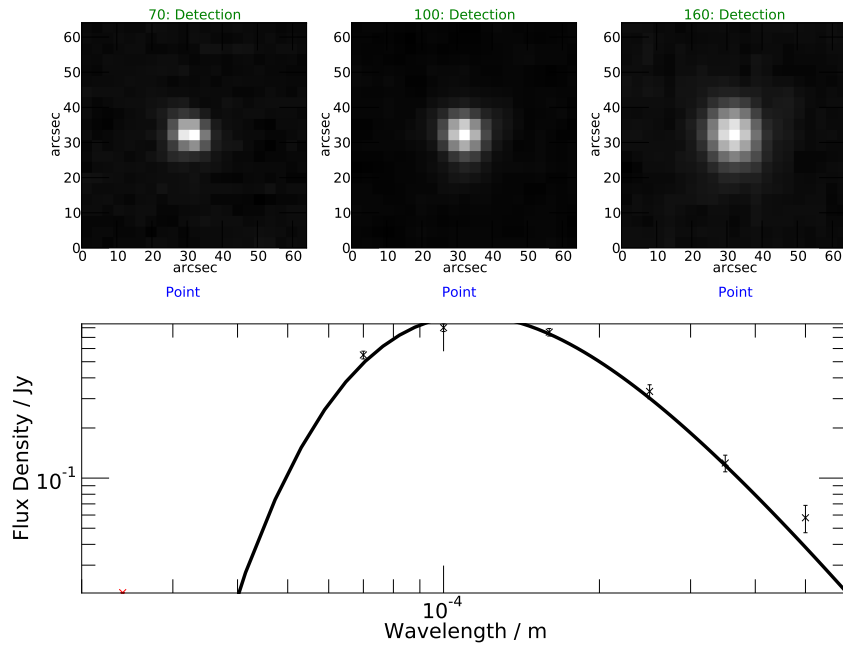


Figure A.67: Object 67: $T = 25.7\text{K}$, $\log_{10} \left(\frac{M_{Dust}}{M_{\odot}} \right) = 7.1$, $\log_{10} \left(\frac{M_{*}}{M_{\odot}} \right) = 9.7$

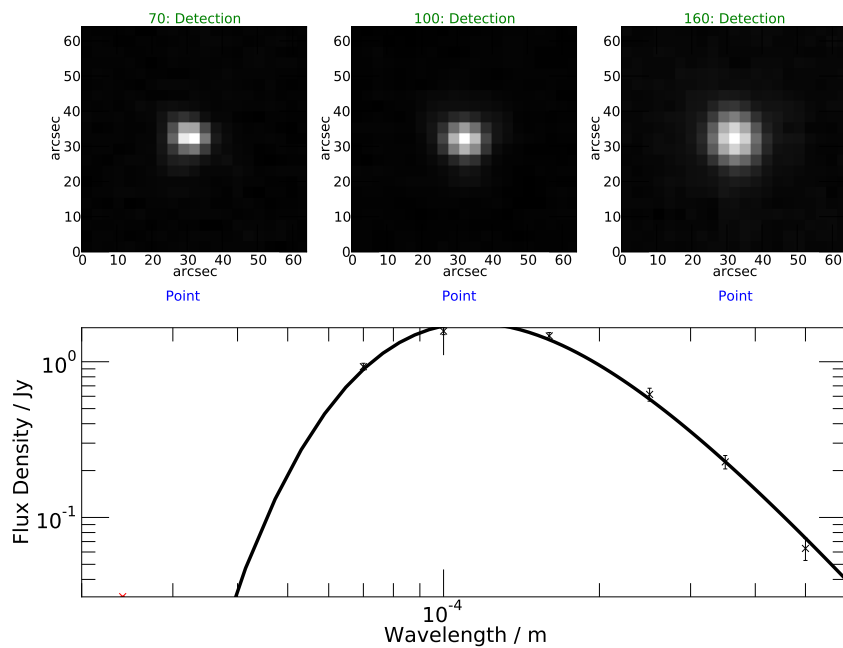


Figure A.68: Object 68: $T = 25.5\text{K}$, $\log_{10} \left(\frac{M_{Dust}}{M_{\odot}} \right) = 7.4$, $\log_{10} \left(\frac{M_{*}}{M_{\odot}} \right) = 10.5$

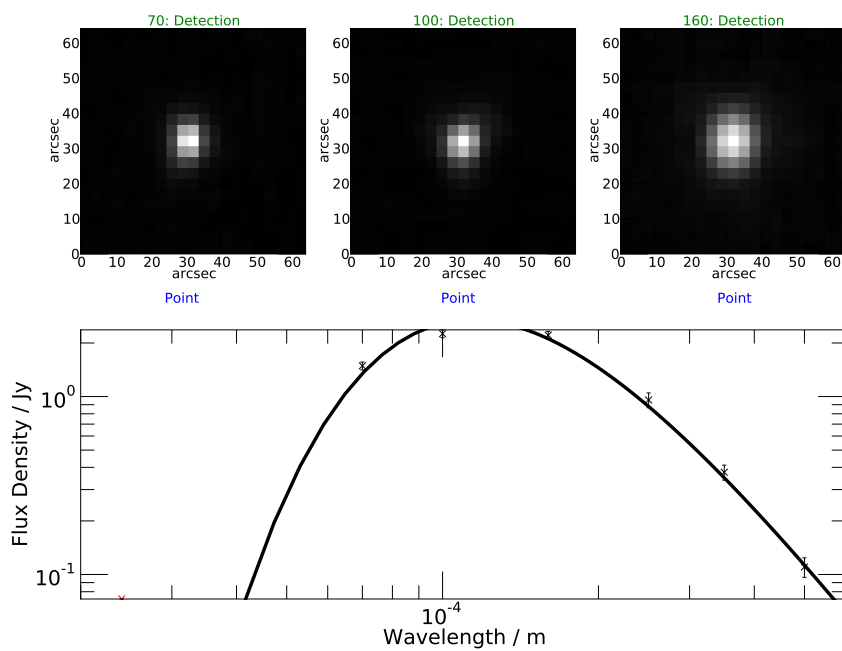


Figure A.69: Object 69: $T = 25.4\text{K}$, $\log_{10} \left(\frac{M_{Dust}}{M_{\odot}} \right) = 7.6$, $\log_{10} \left(\frac{M_{*}}{M_{\odot}} \right) = 9.8$

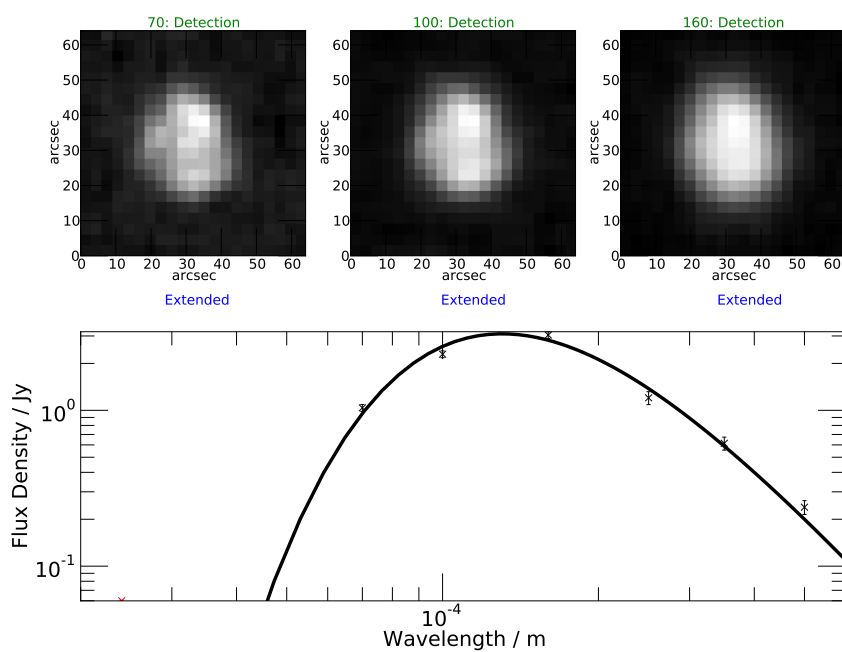


Figure A.70: Object 70: $T = 22.3\text{K}$, $\log_{10} \left(\frac{M_{Dust}}{M_{\odot}} \right) = 7.9$, $\log_{10} \left(\frac{M_{*}}{M_{\odot}} \right) = 11.1$

Appendix B

Data table: measured parameters

HeCoCS Object ID	SDSS PhotoObjID	RA (J2000)	Dec (J2000)	70 μ m Flux (mJy)	70 μ m Error (mJy)	100 μ m Flux (mJy)	100 μ m Error (mJy)	160 μ m Flux (mJy)	160 μ m Error (mJy)	Redshift
1	1237667323797766144	195.006	27.731	-8.160	28.500	3.430	8.680	55.000	17.070	0.0269
2	1237667443511656704	194.586	27.429	30.900	8.040	23.400	10.020	26.820	18.950	0.0252
3	1237667442437849088	194.362	26.694	7.690	6.790	34.100	10.360	14.700	20.820	0.0243
4	1237667444048658432	194.847	27.912	12.870	7.200	34.800	10.380	44.600	17.570	0.0227
5	1237667324334637312	195.038	28.170	16.330	7.400	36.000	10.410	14.540	20.850	0.0225
6	1237667324334571776	194.983	28.035	-33.500	28.500	36.800	10.440	65.100	16.720	0.0272
7	1237667442974851328	194.613	27.023	21.040	7.640	37.200	10.450	41.000	17.780	0.0252
8	1237667444048855296	195.459	27.894	-35.360	28.500	38.540	10.490	7.190	23.330	0.0252
9	1237667442974654464	194.181	27.179	21.350	7.650	39.300	10.510	29.240	18.700	0.0253
10	1237667443511656448	194.484	27.581	33.600	8.130	39.500	10.510	52.800	17.160	0.0166
11	1237667444048658432	194.887	27.984	19.470	7.560	40.300	10.530	46.600	17.460	0.0194
12	1237667444048658688	194.908	27.907	22.760	7.710	45.600	10.680	31.660	18.470	0.0267
13	1237667324334637056	195.019	27.988	29.500	7.980	45.900	10.690	35.060	18.190	0.0213
14	1237667444048723968	195.023	27.808	32.400	8.090	47.200	10.720	16.320	20.480	0.0219
15	1237667444048592896	194.775	27.997	12.720	7.190	47.900	10.740	16.800	20.380	0.0256
16	1237667323797504000	194.387	27.610	17.270	7.450	48.000	10.740	33.440	18.320	0.0201
17	1237667444048462080	194.487	27.992	14.130	7.280	48.800	10.760	43.800	17.610	0.0152
18	1237667442974851328	194.661	27.013	13.340	7.230	53.900	10.890	68.100	16.640	0.0234
19	1237667443511591168	194.295	27.405	31.200	8.050	55.200	10.930	47.100	17.430	0.0207
20	1237667444048592896	194.703	27.810	39.800	8.350	58.100	11.000	34.250	18.260	0.0197
21	1237667324334637056	195.033	28.079	45.700	8.540	61.300	11.090	49.100	17.330	0.0241
22	1237667444048658432	194.875	27.956	40.100	8.360	70.500	11.320	68.100	16.640	0.0227
23	1237667444048658688	194.935	27.912	-4.900	28.500	70.500	11.320	7.700	23.070	0.0224
24	1237667443511656448	194.477	27.491	44.400	8.500	75.000	11.440	60.600	16.870	0.0166
25	1237667324334637056	195.061	28.041	49.000	8.640	75.200	11.450	66.700	16.680	0.0191
26	1237667444048789760	195.247	27.900	13.000	7.210	75.500	11.450	23.800	19.300	0.0229
27	1237667324334702592	195.203	28.091	49.000	8.640	80.300	11.580	76.400	16.440	0.0232
28	1237667324334768384	195.400	28.151	64.520	9.130	87.600	11.770	65.750	16.700	0.0201
29	1237667324334440704	194.606	28.129	46.600	8.570	92.000	11.890	98.000	16.130	0.0274
30	1237667443511853312	195.140	27.504	71.400	9.350	107.900	12.330	133.400	16.070	0.0186
31	1237667322723827968	194.530	26.787	71.800	9.360	111.300	12.430	139.300	16.110	0.0240
32	1237667444048658688	194.878	27.884	70.100	9.300	112.300	12.460	92.700	16.180	0.0157
33	1237667444048658432	194.892	27.947	67.400	9.220	115.400	12.550	102.700	16.090	0.0240
34	1237667444048593152	194.814	27.971	62.300	9.060	118.300	12.630	97.300	16.130	0.0161
35	1237667442974654720	194.207	27.094	36.900	8.250	120.500	12.700	216.500	17.330	0.0231

Table B.1: Measured far-infrared parameters, objects 1 - 35

HeCoCS Object ID	SDSS PhotoObjID	RA (J2000)	Dec (J2000)	70 μ m Flux (mJy)	70 μ m Error (mJy)	100 μ m Flux (mJy)	100 μ m Error (mJy)	160 μ m Flux (mJy)	160 μ m Error (mJy)	Redshift
36	1237667444048658688	194.873	27.850	84.700	9.760	121.600	12.730	108.200	16.060	0.0226
37	1237667444048593152	194.783	27.855	71.100	9.340	132.300	13.050	119.500	16.040	0.0219
38	1237667442974785792	194.486	27.038	79.500	9.600	140.800	13.320	245.800	18.080	0.0247
39	1237667444048855040	195.359	27.886	107.500	10.510	150.300	13.620	711.400	37.290	0.0183
40	1237667323260567808	194.144	27.228	83.500	9.730	154.600	13.760	204.000	17.050	0.0240
41	1237667443511721984	194.658	27.464	79.800	9.610	162.100	14.000	208.700	17.150	0.0209
42	1237667323797700608	194.916	27.576	95.500	10.110	185.600	14.800	202.700	17.020	0.0167
43	1237667323797438720	194.269	27.773	94.830	10.090	189.500	14.940	270.200	18.790	0.0251
44	1237667324334702592	195.178	27.971	126.400	11.150	204.500	15.470	209.600	17.170	0.0213
45	1237667444048527360	194.591	27.968	134.200	11.430	216.000	15.890	184.700	16.680	0.0201
46	1237667444048723968	195.074	27.955	148.400	11.940	253.900	17.320	241.800	17.970	0.0230
47	1237667444585463808	194.758	28.225	135.200	11.460	269.000	17.920	266.000	18.670	0.0268
48	1237667324334702592	195.215	28.043	126.600	11.160	270.800	17.990	313.300	20.200	0.0291
49	1237667324334702592	195.203	28.158	57.900	8.920	285.900	18.590	601.900	32.220	0.0194
50	1237667444048724224	195.038	27.866	266.600	16.640	297.200	19.050	213.400	17.260	0.0177
51	1237667324334768128	195.490	28.006	151.500	12.050	337.000	20.700	408.400	23.800	0.0257
52	1237667324334571520	194.833	28.084	181.100	13.160	347.000	21.130	359.400	21.880	0.0153
53	1237667323260567552	194.119	27.291	223.900	14.860	347.500	21.150	614.800	32.810	0.0251
54	1237667443511591168	194.355	27.405	132.000	11.350	358.800	21.630	369.900	22.280	0.0162
55	1237667323797831680	195.140	27.638	260.100	16.370	372.400	22.210	410.200	23.880	0.0250
56	1237667444585594880	195.075	28.202	149.600	11.980	393.300	23.120	463.300	26.080	0.0284
57	1237667323260764160	194.647	27.265	293.300	17.790	443.300	25.330	424.400	24.460	0.0245
58	1237667324334440448	194.490	28.062	303.400	18.230	483.700	27.150	538.900	29.380	0.0271
59	1237667323797635328	194.772	27.644	378.500	21.570	553.100	30.330	540.200	29.430	0.0181
60	1237667442974916864	194.819	27.106	325.100	19.180	565.900	30.930	605.300	32.370	0.0280
61	1237667322723696896	194.213	26.899	258.800	16.310	575.100	31.350	766.600	39.890	0.0208
62	1237667323797831680	195.149	27.574	328.700	19.340	583.000	31.720	731.200	38.220	0.0170
63	1237667323260698624	194.578	27.311	367.600	21.080	586.900	31.900	621.900	33.130	0.0247
64	1237667322723696640	194.116	26.987	262.900	16.490	700.500	37.250	941.300	48.270	0.0215
65	1237667444048592896	194.733	27.833	274.200	16.970	765.000	40.320	881.400	45.380	0.0251
66	1237667323260764160	194.655	27.177	492.300	26.820	767.900	40.460	813.000	42.100	0.0256
67	1237667324334505984	194.759	28.116	549.100	29.490	801.000	42.040	752.600	39.230	0.0314
68	1237667323797635072	194.647	27.596	929.600	47.860	1572.800	79.780	1465.400	73.950	0.0256
69	1237667324334637312	195.158	28.057	1487.600	75.340	2255.600	113.620	2214.100	111.100	0.0262
70	1237667444048789504	195.234	27.791	1037.400	53.140	2291.300	115.390	3040.900	152.300	0.0266

Table B.2: Measured far-infrared parameters, objects 36 - 70

Appendix C

Data table: derived parameters

HeCoCS Object ID	Temperature (K)	Temperature Error (K)	Total Infrared Luminosity $\left(\log_{10}\left(\frac{L}{L_{\odot}}\right)\right)$	Total Infrared Luminosity Error	Dust Mass $\left(\log_{10}\left(\frac{M_{\text{dust}}}{M_{\odot}}\right)\right)$	Dust Mass Error	Stellar Mass (M_{\odot})
1	17.23	3.34	8.17	0.89	6.35	0.38	9.38
2	26.28	3.86	8.57	0.76	5.66	0.37	9.16
3	22.74	2.16	8.42	0.48	5.89	0.23	9.44
4	23.23	1.15	8.52	0.25	5.93	0.12	10.75
5	23.97	2.17	8.53	0.47	5.85	0.23	10.20
6	18.34	1.22	8.66	0.30	6.68	0.13	10.52
7	22.68	1.63	8.61	0.36	6.08	0.17	8.61
8	0.00	0.00	N/A	N/A	N/A	N/A	10.31
9	24.61	1.21	8.59	0.25	5.85	0.12	10.98
10	27.90	2.00	8.68	0.36	5.61	0.18	8.96
11	24.98	1.12	8.59	0.23	5.81	0.11	10.49
12	25.99	0.40	8.63	0.08	5.74	0.04	10.31
13	28.40	0.57	8.67	0.10	5.55	0.05	10.43
14	26.27	1.93	8.70	0.37	5.79	0.18	10.20
15	22.50	1.33	8.60	0.30	6.09	0.14	10.49
16	23.56	1.19	8.63	0.26	6.00	0.12	10.75
17	21.45	0.50	8.66	0.11	6.27	0.05	8.47
18	19.91	0.55	8.74	0.13	6.55	0.06	8.88
19	20.16	1.70	8.79	0.41	6.57	0.19	10.06
20	31.01	2.05	8.78	0.33	5.43	0.16	10.51
21	24.94	2.16	8.85	0.44	6.07	0.22	10.29
22	22.63	1.10	8.88	0.24	6.36	0.12	10.59
23	0.00	0.00	N/A	N/A	N/A	N/A	10.45
24	24.84	1.69	8.89	0.34	6.12	0.17	9.90
25	27.90	1.06	8.89	0.19	5.82	0.09	10.22
26	25.54	3.59	8.66	0.74	5.82	0.37	10.29
27	24.32	0.97	8.93	0.20	6.22	0.10	10.58
28	24.28	1.99	9.00	0.42	6.29	0.20	8.52
29	22.79	0.68	8.99	0.15	6.44	0.07	9.36
30	24.74	0.95	9.09	0.19	6.33	0.09	9.08
31	24.90	1.06	9.09	0.21	6.32	0.10	9.30
32	27.59	0.77	9.06	0.14	6.01	0.07	10.44
33	26.53	0.57	9.06	0.11	6.12	0.05	10.39
34	28.53	2.73	9.03	0.48	5.90	0.23	10.36
35	18.52	0.36	9.18	0.10	7.18	0.05	10.34

Table C.1: Derived far-infrared parameters, objects 1 - 35

HeCoCS Object ID	Temperature (K)	Temperature Error (K)	Total Infrared Luminosity $\left(\log_{10}\left(\frac{L}{L_{\odot}}\right)\right)$	Total Infrared Luminosity Error	Dust Mass $\left(\log_{10}\left(\frac{M_{\text{dust}}}{M_{\odot}}\right)\right)$	Dust Mass Error	Stellar Mass (M_{\odot})
36	25.73	0.84	9.13	0.16	6.27	0.08	10.41
37	25.59	0.51	9.12	0.10	6.27	0.05	10.39
38	20.70	0.89	9.25	0.21	6.96	0.10	9.92
39	17.55	1.63	9.45	0.48	7.59	0.24	11.12
40	21.64	0.76	9.25	0.18	6.84	0.08	9.71
41	21.98	0.59	9.25	0.14	6.81	0.07	9.39
42	24.13	0.51	9.28	0.11	6.59	0.05	9.36
43	28.42	4.65	9.24	0.82	6.12	0.39	9.74
44	24.26	0.77	9.35	0.16	6.64	0.08	10.57
45	25.65	0.51	9.35	0.10	6.50	0.05	10.49
46	24.50	0.55	9.43	0.11	6.70	0.05	10.60
47	24.35	0.30	9.43	0.06	6.72	0.03	10.53
48	23.10	0.37	9.45	0.08	6.87	0.04	10.69
49	18.73	0.57	9.54	0.16	7.51	0.08	10.79
50	30.23	0.87	9.56	0.14	6.28	0.06	9.59
51	22.95	0.56	9.54	0.13	6.98	0.07	10.85
52	24.05	0.41	9.56	0.09	6.87	0.04	10.71
53	21.02	1.23	9.66	0.30	7.32	0.15	9.94
54	22.02	0.42	9.54	0.10	7.09	0.05	9.67
55	25.14	0.97	9.63	0.19	6.83	0.09	9.48
56	21.99	0.18	9.60	0.04	7.15	0.02	10.89
57	25.80	0.63	9.69	0.12	6.82	0.06	9.41
58	24.14	0.78	9.74	0.16	7.04	0.08	9.63
59	25.79	0.69	9.79	0.13	6.92	0.06	9.92
60	23.92	0.60	9.79	0.13	7.12	0.06	9.66
61	22.02	0.43	9.80	0.10	7.35	0.05	10.16
62	23.24	0.68	9.82	0.15	7.22	0.07	10.02
63	24.39	0.80	9.81	0.17	7.09	0.08	9.35
64	21.37	0.26	9.88	0.06	7.50	0.03	10.86
65	21.61	0.19	9.89	0.05	7.48	0.02	10.40
66	24.44	0.77	9.94	0.16	7.21	0.08	9.61
67	25.69	0.74	9.95	0.14	7.09	0.07	9.66
68	25.48	0.39	10.22	0.08	7.38	0.04	10.52
69	25.42	0.60	10.40	0.12	7.57	0.06	9.79
70	22.27	0.47	10.40	0.11	7.92	0.06	11.06

Table C.2: Derived far-infrared parameters, objects 36 - 70

Bibliography

- Abadi, M. G., Moore, B., & Bower, R. G. 1999, MNRAS, 308, 947
- Abell, G. O. 1977, ApJ, 213, 327
- Ahn, C. P., Alexandroff, R., Allende Prieto, C., et al. 2014, ApJS, 211, 17
- Arnaud, M., Pointecouteau, E., & Pratt, G. W. 2005, A&A, 441, 893
- Atek, H., Kneib, J.-P., Pacifici, C., et al. 2014, ApJ, 789, 96
- Auld, R., Bianchi, S., Smith, M. W. L., et al. 2013, MNRAS, 428, 1880
- Bai, L., Rieke, G. H., Rieke, M. J., Christlein, D., & Zabludoff, A. I. 2009, ApJ, 693, 1840
- Bai, L., Rieke, G. H., Rieke, M. J., et al. 2006, ApJ, 639, 827
- Baldry, I. K., Balogh, M. L., Bower, R. G., et al. 2006, MNRAS, 373, 469
- Baldry, I. K., Glazebrook, K., Brinkmann, J., et al. 2004, ApJ, 600, 681
- Ball, N. M., Loveday, J., Brunner, R. J., Baldry, I. K., & Brinkmann, J. 2006, MNRAS, 373, 845
- Balog, Z., Müller, T., Nielbock, M., et al. 2014, Experimental Astronomy, 37, 129
- Bendo, G. J., Joseph, R. D., Wells, M., et al. 2003, AJ, 125, 2361
- Bernstein, R. A., Freedman, W. L., & Madore, B. F. 2002, ApJ, 571, 107
- Berta, S., Magnelli, B., Lutz, D., et al. 2010, A&A, 518, L30

- Bertin, E., & Arnouts, S. 1996, *A&AS*, 117, 393
- Bianchi, L., & GALEX Team. 1999, *Mem. Societa Astronomica Italiana*, 70, 365
- Bianchi, S., Davies, J. I., & Alton, P. B. 1999, *A&A*, 344, L1
- Biermann, P. 1976, *A&A*, 53, 295
- Binggeli, B., Popescu, C. C., & Tammann, G. A. 1993, *A&AS*, 98, 275
- Binggeli, B., Sandage, A., & Tammann, G. A. 1985, *AJ*, 90, 1681
- Binney, J. 1976, *MNRAS*, 177, 19
- . 1978a, *Comments on Astrophysics*, 8, 27
- . 1978b, *MNRAS*, 183, 501
- Blanton, M. R., Schlegel, D. J., Strauss, M. A., et al. 2005, *AJ*, 129, 2562
- Bluck, A. F. L., Conselice, C. J., Almaini, O., et al. 2011, *MNRAS*, 410, 1174
- Boselli, A., & Gavazzi, G. 2006, *PASP*, 118, 517
- Boselli, A., Gavazzi, G., Donas, J., & Scodreggio, M. 2001, *AJ*, 121, 753
- Boselli, A., Gavazzi, G., Lequeux, J., et al. 1997, *A&A*, 327, 522
- Boselli, A., Gavazzi, G., & Sanvito, G. 2003, *A&A*, 402, 37
- Boselli, A., Eales, S., Cortese, L., et al. 2010, *PASP*, 122, 261
- Bravo-Alfaro, H., Cayatte, V., van Gorkom, J. H., & Balkowski, C. 2000, *AJ*, 119, 580
- . 2001, *A&A*, 379, 347
- Briel, U. G., Henry, J. P., Lumb, D. H., et al. 2001, *A&A*, 365, L60
- Brinchmann, J., Charlot, S., White, S. D. M., et al. 2004, *MNRAS*, 351, 1151
- Broadhurst, T. J., Ellis, R. S., & Glazebrook, K. 1992, *Nature*, 355, 55
- Buat, V., & Xu, C. 1996, *A&A*, 306, 61

- Carter, D., Goudfrooij, P., Mobasher, B., et al. 2008, *ApJS*, 176, 424
- Casoli, F., Dickey, J., Kazes, I., et al. 1996, *A&AS*, 116, 193
- Cassarà, L. P., Piovan, L., Weiss, A., Salaris, M., & Chiosi, C. 2013, *MNRAS*, 436, 2824
- Clark, C. J. R., Dunne, L., Gomez, H. L., et al. 2015, *MNRAS*, 452, 397
- Clemens, M. S., Negrello, M., De Zotti, G., et al. 2013, *MNRAS*, 433, 695
- Colless, M., & Dunn, A. M. 1996, *ApJ*, 458, 435
- Conroy, C., Wechsler, R. H., & Kravtsov, A. V. 2007, *ApJ*, 668, 826
- Cortese, L., Davies, J. I., Pohlen, M., et al. 2010, *A&A*, 518, L49
- Cowie, L. L., & Songaila, A. 1977, *Nature*, 266, 501
- Daddi, E., Dickinson, M., Morrison, G., et al. 2007, *ApJ*, 670, 156
- Davies, J. I., Baes, M., Bendo, G. J., et al. 2010, *A&A*, 518, L48
- Davies, J. I., Bianchi, S., Cortese, L., et al. 2012, *MNRAS*, 419, 3505
- Davies, J. I., Bianchi, S., Baes, M., et al. 2013, *MNRAS*, 428, 834
- de Graauw, T., Helmich, F. P., Phillips, T. G., et al. 2010, *A&A*, 518, L6
- de Vaucouleurs, G. 1948, *Annales d'Astrophysique*, 11, 247
- . 1959, *Handbuch der Physik*, 53, 275
- Domínguez Sánchez, H., Mignoli, M., Pozzi, F., et al. 2012, *MNRAS*, 426, 330
- Draine, B. T. 2003, *ARA&A*, 41, 241
- Draine, B. T., & Li, A. 2001, *ApJ*, 551, 807
- Draine, B. T., Dale, D. A., Bendo, G., et al. 2007, *ApJ*, 663, 866
- Dressler, A. 1980, *ApJ*, 236, 351

- Dressler, A., Oemler, Jr., A., Couch, W. J., et al. 1997, *ApJ*, 490, 577
- Drinkwater, M. J., Gregg, M. D., & Colless, M. 2001, *ApJ Let.*, 548, L139
- Dunne, L., Eales, S., Edmunds, M., et al. 2000, *MNRAS*, 315, 115
- Eales, S., Dunne, L., Clements, D., et al. 2010, *PASP*, 122, 499
- Edwards, L. O. V., & Fadda, D. 2011, *AJ*, 142, 148
- Elbaz, D., Dickinson, M., Hwang, H. S., et al. 2011, *A&A*, 533, A119
- Fabricant, D., Fata, R., Roll, J., et al. 2005, *PASP*, 117, 1411
- Fuller, C., Davies, J. I., Auld, R., et al. 2014, *MNRAS*, 440, 1571
- Gavazzi, G., Boselli, A., Donati, A., Franzetti, P., & Scodreggio, M. 2003, *A&A*, 400, 451
- Gavazzi, G., Boselli, A., Scodreggio, M., Pierini, D., & Belsole, E. 1999, *MNRAS*, 304, 595
- Gehrels, N. 1986, *ApJ*, 303, 336
- Griffin, M. J., Abergel, A., Abreu, A., et al. 2010, *A&A*, 518, L3
- Gruppioni, C., Pozzi, F., Rodighiero, G., et al. 2013, *MNRAS*, 432, 23
- Gunn, J. E., & Gott, III, J. R. 1972, *ApJ*, 176, 1
- Hickinbottom, S., Simpson, C. J., James, P. A., et al. 2014, *MNRAS*, 442, 1286
- Hildebrand, R. H. 1983, *QJRAS*, 24, 267
- Hollenbach, D. J., Werner, M. W., & Salpeter, E. E. 1971, *ApJ*, 163, 165
- Holmberg, E. 1958, *Meddelanden fran Lunds Astronomiska Observatorium Serie II*, 136, 1
- Hoyle, F. 1949, Dayton: Central Air Documents Office, 195

- Ibar, E., Ivison, R. J., Cava, A., et al. 2010, *MNRAS*, 409, 38
- Iono, D., Yun, M. S., & Mihos, J. C. 2004, *ApJ*, 616, 199
- Jansen, F., Lumb, D., Altieri, B., et al. 2001, *A&A*, 365, L1
- Jenkins, L. P., Hornschemeier, A. E., Mobasher, B., Alexander, D. M., & Bauer, F. E. 2007, *ApJ*, 666, 846
- Jones, O. C., McDonald, I., Rich, R. M., et al. 2015, *MNRAS*, 446, 1584
- Karim, A., Schinnerer, E., Martínez-Sansigre, A., et al. 2011, *ApJ*, 730, 61
- Kauffmann, G., & Charlot, S. 1998, *MNRAS*, 297, L23
- Kennicutt, R. C., & Evans, N. J. 2012, *ARA&A*, 50, 531
- Kennicutt, Jr., R. C. 1998a, *ARA&A*, 36, 189
- . 1998b, *ApJ*, 498, 541
- Kennicutt, Jr., R. C., Roettiger, K. A., Keel, W. C., van der Hulst, J. M., & Hummel, E. 1987, *AJ*, 93, 1011
- Kessler, M. F., Steinz, J. A., Anderegg, M. E., et al. 1996, *A&A*, 315, L27
- Kormendy, J. 1993, in *IAU Symposium*, Vol. 153, *Galactic Bulges*, ed. H. Dejonghe & H. J. Habing, 209
- Larson, R. B., Tinsley, B. M., & Caldwell, C. N. 1980, *ApJ*, 237, 692
- Lavezzi, T. E., Dickey, J. M., Casoli, F., & Kazès, I. 1999, *AJ*, 117, 1995
- Leitherer, C., & Heckman, T. M. 1995, *ApJS*, 96, 9
- Lilly, S. J., Le Brun, V., Maier, C., et al. 2009, *ApJS*, 184, 218
- Lintott, C. J., Schawinski, K., Slosar, A., et al. 2008, *MNRAS*, 389, 1179
- Łokas, E. L., & Mamon, G. A. 2003, *MNRAS*, 343, 401

- Lonsdale Persson, C. J., & Helou, G. 1987, *ApJ*, 314, 513
- Lutz, D., Poglitsch, A., Altieri, B., et al. 2011, *A&A*, 532, A90
- Madore, B. F., Freedman, W. L., Silbermann, N., et al. 1999, *ApJ*, 515, 29
- Magnelli, B., Popesso, P., Berta, S., et al. 2013, *A&A*, 553, A132
- Mahajan, S., Haines, C. P., & Raychaudhury, S. 2010, *MNRAS*, 404, 1745
- Marshall, H. L., Tananbaum, H., Avni, Y., & Zamorani, G. 1983, *ApJ*, 269, 35
- Mihos, C. 2003, *ArXiv Astrophysics e-prints*, astro-ph/0305512
- Moore, B., Katz, N., Lake, G., Dressler, A., & Oemler, A. 1996, *Nature*, 379, 613
- Moore, B., Lake, G., & Katz, N. 1998, *ApJ*, 495, 139
- Murante, G., Giovalli, M., Gerhard, O., et al. 2007, *MNRAS*, 377, 2
- Neugebauer, G., Habing, H. J., van Duinen, R., et al. 1984, *ApJ Let.*, 278, L1
- Nulsen, P. E. J. 1982, *MNRAS*, 198, 1007
- Ott, S. 2010, in *Astronomical Society of the Pacific Conference Series*, Vol. 434, *Astronomical Data Analysis Software and Systems XIX*, ed. Y. Mizumoto, K.-I. Morita, & M. Ohishi, 139
- Patel, H., Clements, D. L., Vaccari, M., et al. 2013, *MNRAS*, 428, 291
- Peng, Y.-j., Lilly, S. J., Kovač, K., et al. 2010, *ApJ*, 721, 193
- Pilbratt, G. L., Riedinger, J. R., Passvogel, T., et al. 2010, *A&A*, 518, L1
- Poglitsch, A., Waelkens, C., Geis, N., et al. 2010, *A&A*, 518, L2
- Quilis, V., Moore, B., & Bower, R. 2000, *Science*, 288, 1617
- Rigby, E. E., Maddox, S. J., Dunne, L., et al. 2011, *MNRAS*, 415, 2336
- Roberts, M. S., & Haynes, M. P. 1994, *ARA&A*, 32, 115

- Rodighiero, G., Daddi, E., Baronchelli, I., et al. 2011, *ApJ Let.*, 739, L40
- Salim, S., Rich, R. M., Charlot, S., et al. 2007, *ApJS*, 173, 267
- Salpeter, E. E. 1955, *ApJ*, 121, 161
- Sargent, M. T., Béthermin, M., Daddi, E., & Elbaz, D. 2012, *ApJ Let.*, 747, L31
- Saunders, W., Rowan-Robinson, M., Lawrence, A., et al. 1990, *MNRAS*, 242, 318
- Schechter, P. 1976, *ApJ*, 203, 297
- Sellgren, K. 1994, in *Astronomical Society of the Pacific Conference Series*, Vol. 58, *The First Symposium on the Infrared Cirrus and Diffuse Interstellar Clouds*, ed. R. M. Cutri & W. B. Latter, 243
- Sellwood, J. A., & Wilkinson, A. 1993, *Reports on Progress in Physics*, 56, 173
- Sérsic, J. L. 1963, *Boletin de la Asociacion Argentina de Astronomia La Plata Argentina*, 6, 41
- Shen, S., Mo, H. J., White, S. D. M., et al. 2003, *MNRAS*, 343, 978
- Simionescu, A., Werner, N., Urban, O., et al. 2013, *ApJ*, 775, 4
- Smith, M. W. L., Gomez, H. L., Eales, S. A., et al. 2012, *ApJ*, 748, 123
- Smith, R. J., Lucey, J. R., Hammer, D., et al. 2010, *MNRAS*, 408, 1417
- Soifer, B. T., Neugebauer, G., & Houck, J. R. 1987a, *ARA&A*, 25, 187
- Soifer, B. T., Sanders, D. B., Madore, B. F., et al. 1987b, *ApJ*, 320, 238
- Strauss, M. A., Weinberg, D. H., Lupton, R. H., et al. 2002, *AJ*, 124, 1810
- Struble, M. F., & Rood, H. J. 1999, *ApJS*, 125, 35
- Tasca, L. A. M., Le Fevre, O., Hathi, N. P., et al. 2014, *ArXiv e-prints*, arXiv:1411.5687
- Taylor, E. N., Hopkins, A. M., Baldry, I. K., et al. 2011, *MNRAS*, 418, 1587

-
- Toomre, A. 1977, in *Evolution of Galaxies and Stellar Populations*, ed. B. M. Tinsley & R. B. G. Larson, D. Campbell, 401
- Urban, O., Werner, N., Simionescu, A., Allen, S. W., & Böhringer, H. 2011, *MNRAS*, 414, 2101
- Valluri, M. 1993, *ApJ*, 408, 57
- Vollmer, B., Cayatte, V., Balkowski, C., & Duschl, W. J. 2001, *ApJ*, 561, 708
- Walterbos, R. A. M., & Greenawalt, B. 1996, *ApJ*, 460, 696
- Wang, G., Leggett, S. K., Clowes, R. G., MacGillivray, H. T., & Savage, A. 1991, *MNRAS*, 248, 112
- Werner, M. W., Roellig, T. L., Low, F. J., et al. 2004, *ApJS*, 154, 1
- White, S. D. M., Briel, U. G., & Henry, J. P. 1993, *MNRAS*, 261, L8
- Whitmore, B. C., Gilmore, D. M., & Jones, C. 1993, *ApJ*, 407, 489
- Wuyts, S., Förster Schreiber, N. M., van der Wel, A., et al. 2011, *ApJ*, 742, 96